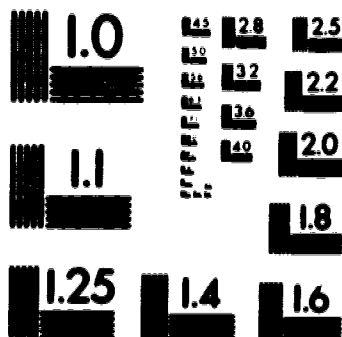


1

PM-1 3½"x4" PHOTOGRAPHIC MICROCOPY TARGET
NBS 1010a ANSI/ISO #2 EQUIVALENT



PRECISION™ RESOLUTION TARGETS



National Library
of Canada

Acquisitions and
Bibliographic Services Branch

395 Wellington Street
Ottawa, Ontario
K1A 0N4

Bibliothèque nationale
du Canada

Direction des acquisitions et
des services bibliographiques

395, rue Wellington
Ottawa (Ontario)
K1A 0N4

For further information, contact:

Cherchez plus d'information à:

NOTICE

The quality of this microform is heavily dependent upon the quality of the original thesis submitted for microfilming. Every effort has been made to ensure the highest quality of reproduction possible.

If pages are missing, contact the university which granted the degree.

Some pages may have indistinct print especially if the original pages were typed with a poor typewriter ribbon or if the university sent us an inferior photocopy.

Reproduction in full or in part of this microform is governed by the Canadian Copyright Act, R.S.C. 1970, c. C-30, and subsequent amendments.

AVIS

La qualité de cette microforme dépend grandement de la qualité de la thèse soumise au microfilmage. Nous avons tout fait pour assurer une qualité supérieure de reproduction.

S'il manque des pages, veuillez communiquer avec l'université qui a conféré le grade.

La qualité d'impression de certaines pages peut laisser à désirer, surtout si les pages originales ont été dactylographiées à l'aide d'un ruban usé ou si l'université nous a fait parvenir une photocopie de qualité inférieure.

La reproduction, même partielle, de cette microforme est soumise à la Loi canadienne sur le droit d'auteur, SRC 1970, c. C-30, et ses amendements subséquents.

UNIVERSITY OF ALBERTA

**Micromachining, Capillary Electrophoresis, Polymers,
and Their Applications to Chemical Sensors**

BY



Zhonghui H. Fan

**A thesis submitted to
the Faculty of Graduate Studies and Research
in partial fulfillment of the requirements for the degree of**

Doctor of Philosophy

Department of Chemistry

Edmonton, Alberta

SPRING 1994



National Library
of Canada

Acquisitions and
Bibliographic Services Branch

395 Wellington Street
Ottawa, Ontario
K1A 0N4

Bibliothèque nationale
du Canada

Direction des acquisitions et
des services bibliographiques

395, rue Wellington
Ottawa (Ontario)
K1A 0N4

Author's Acknowledgement

Author's Acknowledgement

The author has granted an irrevocable non-exclusive licence allowing the National Library of Canada to reproduce, loan, distribute or sell copies of his/her thesis by any means and in any form or format, making this thesis available to interested persons.

L'auteur a accordé une licence irrévocable et non exclusive permettant à la Bibliothèque nationale du Canada de reproduire, prêter, distribuer ou vendre des copies de sa thèse de quelque manière et sous quelque forme que ce soit pour mettre des exemplaires de cette thèse à la disposition des personnes intéressées.

The author retains ownership of the copyright in his/her thesis. Neither the thesis nor substantial extracts from it may be printed or otherwise reproduced without his/her permission.

L'auteur conserve la propriété du droit d'auteur qui protège sa thèse. Ni la thèse ni des extraits substantiels de celle-ci ne doivent être imprimés ou autrement reproduits sans son autorisation.

ISBN 0-612-11203-9

Canada

UNIVERSITY OF ALBERTA

RELEASE FORM

NAME OF AUTHOR: **Zhonghui H. Fan**

TITLE OF THESIS: **Micromachining, Capillary Electrophoresis,
Polymers, and Their Applications to Chemical
Sensors.**

DEGREE: **Doctor of Philosophy**

YEAR THIS DEGREE GRANTED:

1994

Permission is hereby granted to the University of Alberta Library to reproduce single copies of this thesis and to lend or sell such copies for private, scholarly or scientific research purposes only.

The author reserves all other publication and other rights in association with the copyright in the thesis, and except as hereinbefore provided neither the thesis nor any substantial portion thereof may be printed or otherwise reproduced in any material form whatever without the author's prior written permission.

Author's Signature: _____

Zhonghui Fan

Address: **Department of Chemistry
Iowa State University
Ames, Iowa 50011
USA**

Date: *Dec. 9, 1993*

UNIVERSITY OF ALBERTA

FACULTY OF GRADUATE STUDIES AND RESEARCH

The undersigned certify that they have read, and recommend to the Faculty of Graduate Studies and Research for acceptance, a thesis entitled **Micromachining, Capillary Electrophoresis, Polymers, and Their Applications to Chemical Sensors** submitted by **Zhonghui Fan** in partial fulfillment of the requirements for the degree of **Doctor of Philosophy**.

Supervisor:


Dr. D. Jed Harrison


Dr. Norman J. Dovichi


Dr. James A. Plambeck


Dr. Monica M. Palcic


Dr. Michael J. Brett

External Examiner:


Dr. Richard M. Cassidy

Date: November 24, 1993

**To Lei Huang, Kevin Y. Fan, and my parents
for their love and support**

Abstract

Chemical sensors have found considerable applications in biotechnology, process control, environmental and medical sciences, as they can be used to make measurements rapidly, repetitively, or even outside the lab. Unlike bench-top instruments, however, they critically require selectivity for the concerned species, because chemical sensors do not involve sample pretreatments such as separation. Selectivity may be obtained through the use of membranes, as has been shown for Nafion (perfluorosulphonated ionomer) coated glucose sensors intended for implantation in diabetic patients. Rotating disc electro-chemistry was used to measure the selectivity of Nafion to glucose and against interfering species. The effects of membrane preparation parameters, such as thickness, on selectivity have also been investigated.

An alternative approach to selectivity is to integrate separation techniques, such as capillary electrophoresis (CE), within a chemical sensor. Using integrated circuit fabrication technology called micromachining, micron-scale capillaries and sample injection systems have been fabricated in small glass chips, which resemble miniaturized instruments in terms of size and operations. Pumping of samples and mobile phase is performed electrokinetically by application of a high voltage. Electrophoresis, which occurs at the same time, effects the separation of components since they have different mobilities under an electric field. A laser-induced fluorescence detector is used for the detection. Three fluorophore tagged amino acids can be separated within 3 seconds in such a device. The configuration of the injectors demonstrated an influence on defining injected sample volume and separation efficiency. Leaking, or mixing, at the intersection increased the background and decreased the dynamic range of detection, but it can be suppressed by applying appropriate voltages to multiple reservoirs. A

chamber integrated in a device has been used for mixing, suggesting sample pretreatment or post-column derivatization may be performed on such devices. These results, as well as linear calibration curves obtained over 3 orders of magnitude, indicate the potential of such devices for chemical analysis in the future.

Acknowledgements

I would like to express my sincere gratitude to all of them who have provided me assistance during the course of my Ph. D. program at the University of Alberta. In particular, I wish to mention the following.

First and uppermost, my sincere, eternal thanks go to my supervisor, professor D. Jed Harrison. He introduced me into exciting research fields and guided me in accomplishing this work. His encouragement, patience, and friendship made my time here enjoyable. I feel very rewarding by working with him and I am very proud of being one of his students.

I am indebted to all other members of professor Harrison's research group for their support and sharing experiences and knowledge. Especially, I wish to thank Kwok-keung Shiu and Dan Raymond for teaching me to use electrochemical instruments, Kurt Seiler for setting up the apparatus used for the experiments on μ -TAS devices and writing the initial programs for instrument control and data acquisition. I am grateful to Paul Glavina, Rob Turner, Xizhong Li, Songcheng Sun, Andy Chan, Alebachew Demoz, Zhong Li, Francis Moussy, and Karl Fluri for their assistance and friendship.

Thanks are extended to the Alberta Microelectronic Center (AMC) for accessing the facilities for measuring thin film thicknesses and fabricating μ -TAS devices. The assistance of Graham McKinnon and Yan Loke at AMC in developing μ -TAS fabrication technology is also appreciated. The kind gifts, poly(vinylpyridine) from Reilly Tar and Chemicals, and Glass samples from Corning Glass and John's Scientific, are also acknowledged.

I wish to express my thanks to Dr. N. Dovichi, Dr. R. Cassidy, and other members of my examining committee for their useful comments and suggestions in the preparation of this thesis.

The scholarships from AMC during Sep. 1989--Aug. 1992 and from the Department of Chemistry, University of Alberta during Sep. 1992--

Aug. 1993 are greatly appreciated. Financial support for the research projects I have involved from Ciba-Geigy in Switzerland, National Sciences and Engineering Research Council (NSERC) of Canada, and University of Alberta is also acknowledged.

Table of Contents

Chapter 1	Introduction.....	1
1.1	Glucose Sensor.....	2
1.1.1	A brief history review.....	2
1.1.2	Implantable glucose sensors.....	4
1.1.3	Profilometry and ellipsometry.....	7
1.1.4	Present Nafion study.....	11
1.2	Miniaturized Total Chemical Analysis System (μ -TAS).....	13
1.3	Micromachining.....	19
1.4	Capillary Electrophoresis (CE).....	22
1.5	CE-based μ -TAS.....	28
1.6	References.....	32
Chapter 2	Glucose Permeability and Selectivity in Nafion Films.....	37
2.1	Introduction.....	37
2.2	Theoretical considerations.....	39
2.3	Experimental Section.....	42
2.3.1	Solutions and Reagents.....	42
2.3.2	Substrate Surface and Film Preparation.....	43
2.3.3	Electrochemical Measurements.....	44
2.3.4	Film thickness measurements.....	45
2.4	Results and Discussion.....	47
2.4.1	Measurement of Film Thickness.....	47
2.4.2	Permeability of Room Temperature Cured Nafion.....	52
2.4.3	Effect of Solvent and Temperature on Permeabilities.....	62
2.5	Conclusions.....	67
2.6	References.....	68

Chapter 3	Micromachined Capillary Electrophoresis Systems: Fabrication, Cross Injectors, and Rapid Separation.....	71
3.1	Introduction.....	71
3.2	Experimental Section.....	74
3.2.1	Device Fabrication.....	74
3.2.2	Apparatus	77
3.2.3	Materials and Reagents.....	79
3.2.4	Procedures.....	80
3.3	Results and Discussion.....	80
3.3.1	Device Fabrication.....	80
3.4.2	Electrical Characteristics.....	83
3.4.3	Rapid Separation.....	86
3.4.4	Effect of Injection Parameters.....	88
3.4.5	Separation Efficiency.....	90
3.4.6	Leakage Phenomena.....	97
3.5	Conclusions.....	103
3.6	References.....	103

Chapter 4	Micromachined Capillary Electrophoresis Systems: Double T Injectors, Leakage Suppression, and Calibration Curves..	106
4.1	Introduction.....	106
4.2	Experimental Section.....	108
4.2.1	Device.....	108
4.2.2	Instrument.....	110
4.2.3	Materials and reagents.....	111
4.2.4	Procedures.....	111
4.3	Results and Discussion.....	112
4.3.1	Device Fabrication.....	112
4.3.2	Resistance Simulation.....	112
4.3.3	Geometrically defined injection.....	119
4.3.4	Fast separation of 6 amino acids.....	131
4.3.5	Channel dimension change.....	131
4.3.6	Leakage suppression.....	134

	4.3.7 Calibration curve and the use of a standard...	139
4.4	Conclusions.....	142
4.5	References.....	143
Chapter 5	A Micromachined Mixing Chamber in a Miniaturized Capillary Electrophoresis System.....	145
5.1	Introduction.....	145
5.2	Experimental Section.....	147
5.3	Results and Discussion.....	148
	5.3.1 Device.....	148
	5.3.2 Mixing.....	151
	5.3.3 Leakage.....	157
	5.3.4 Dispersion in the chamber.....	160
5.4	Conclusion.....	166
5.5	References.....	167
Chapter 6	Conclusions and Future Directions.....	169
6.1	An implantable glucose sensor.....	169
	6.1.1 A summary of the study on Nafion.....	169
	6.1.2 Future directions.....	170
6.2	Miniaturized capillary electrophoresis systems.....	171
	6.2.1 A summary.....	171
	6.2.2 Future directions.....	173
6.3	References.....	175
Appendix 1	Computer Programs (Virtual Instruments).....	177
	VI 1 A Virtual Instrument for Controlling a Relay Switch System.....	178
	VI 2 A Virtual Instrument for the Jet-3 Device.....	189
	VI 3 A Virtual Instrument for Differentiating Frontal Electropherograms.....	204
Appendix 2	The Layout of Jet-1 and Jet-3 devices.....	207

List of Tables

Table		Page
2.1	Refractive indices and extinction coefficients of substrates.	48
2.2	Effect of curing temperature on effective diffusion coefficients in recast Nafion films.	57
2.3	Permeability, thickness and effective diffusion coefficient for hydroquinone in Nafion cured at room temperature.	59
2.4	Effect of pH and electrolyte on ascorbic acid diffusion in room temperature cured Nafion.	60
2.5	Effect of DMF on effective diffusion coefficients in Nafion.	66
3.1	Etch quality of several types of glass.	81
4.1	Ratios of channel resistances and distances in a Jet-1 device.	115

List of Figures

Figure	Page
1.1 (a) The probe end configuration of an implantable glucose sensor. (b) The molecular structure of Nafion monomer.	6
1.2 (a) The schematic diagram of μ scanning process by a profilometer. (b) The surface profile of a Nafion membrane coated on a Pt foil.	9
1.3 The optical system of an ellipsometer.	12
1.4 The sequence of a typical chemical analysis.	14
1.5 Layout of a complex μ -TAS device and the exploded view of FIA system of the device.	16
1.6 A gas chromatograph on a silicon chip.	18
1.7 The sequence of one mask microfabrication process.	20
1.8 Schematic of a capillary electrophoresis system.	23
1.9 (a) The formation of double-layer at a silica-solution interface and the generation of electroosmosis under an electric field. (b) The nearly flat electroosmotic flow profile. (c) A generic electropherogram.	25
1.10 Layout of a simple μ -TAS device called "Airport".	29
1.11 The three dimensional structure of "Airport" devices.	30

1.12	Illustration of sample injection using electroosmotic pumping and FIA, and separation using CE.	31
2.1a	Comparison of thickness measured by ellipsometry and by profilometry. Multiple layer coatings was used.	50
2.1b	Comparison of thickness measured by ellipsometry and by profilometry. Single layer coating was used.	51
2.2a	Levich plot of current <i>versus</i> rotation rate in rpm for several permeating species in Nafion films coated on Pt.	54
2.2b	A Koutecky-Levich plot of the inverse of current <i>versus</i> the inverse of the square root of rotation rate ($\text{rpm}^{-1/2}$) for the same set of data in Figure 2.2a.	55
2.3	The experimental relationship between the permeability of hydroquinone in Nafion and the coating thickness.	56
2.4	Comparison of the anodic peak current for FcTMA^+ in 0.1 M KCl in a Nafion membrane cured at room temperature with a membrane cured at 120°C.	64
3.1	(a) Dimensions and layout of the various Airport devices. (b) The intersection dimensions for Airport-30 and Airport-70.	75
3.2	The sequence of photolithographic fabrication process.	76
3.3	Block diagram of the apparatus.	78
3.4	Electron micrographs of Airport-70 fabricated in (a) Type I Pyrex and (b) Type II Pyrex (not annealed).	82

3.5	Electron micrograph of the intersection of channels etched in Type III Pyrex.	84
3.6	Current voltage curves in an Airport-70:70 device.	85
3.7	Electropherograms of FITC labelled 10 μM arg, phe and glu in pH 8.0 buffer.	87
3.8	Rapid separation of 50 μM fluorescein from 50 μM fluorescein sulfonate in device Airport-30.	89
3.9	Number of theoretical plates, N , as a function of injection time between separation steps for a 50 μM fluorescein sample in pH 8.0 buffer.	91
3.10	A plot of V_{ap} versus $1/t_m$ for 50 μM fluorescein in an Airport-70 device.	93
3.11	A plot of height equivalent to a theoretical plate, HETP, versus $1/V_{ap}$ for 50 μM fluorescein, pH 8.0.	95
3.12	Background fluorescence intensity without leakage, background with leakage, and the intensity of the 50 μM fluorescein.	98
3.13	(a) A 50 μM fluorescein solution, pH 8.0, is present in all reservoirs except 4. (b) The fluorescence intensity is shown versus time while the potential applied between reservoirs 1 and 2 was increased stepwise. (c) The fluorescence intensity versus time while V_{ap} between reservoirs 3 and 1 (ground) was increased stepwise.	99
3.14	The fluorescence intensity is plotted versus linear flow velocity that depends on the potential applied between reservoirs 3 and 4.	101

3.15	Plots of the flow rate in the side channel (3-4) <i>versus</i> electrical field applied to channel 1-2 or 1-3.	102
4.1	(a) The top view of layout and dimensions of Jet-1 devices. (b) Cross section view of the device.	109
4.2	Scanning electron micrograph of the sloped section jointing two channels with different width.	113
4.3	(a) The simulated resistance circuit of Jet-1 devices. (b) The potential scheme used for leakage suppression.	116
4.4a	Geometrically defined injections on a Jet-1 device. Injection times were varied.	120
4.4b	Non-geometrically defined injections on a Jet-1 device.	121
4.5	Geometrically defined injections on a Jet-3 device. Injection voltages were varied.	123
4.6	Photomicrographs of the injection area of the Jet-1 device. (a) The buffer was flowing in the channel 3-4 before the injection. (b) ~ 2 s after the injection was started.	125
4.6	Photomicrographs of the injection area of the Jet-1 device. (c) ~ 7 s after the injection was started. (d) After a 50 s injection.	126
4.7	Comparison of angle injection with double T injection.	128
4.8	The relationship between theoretical plate numbers and injection voltages.	130
4.9	Repetitive injections and the resulting electropherograms.	132

4.10	Electropherograms of separations of a mixture of 6 amino acids in pH 8.0 TRIS/boric acid buffer.	131
4.11	Separation efficiency loss over a channel dimension change.	135
4.12	Separation of 20 μ M Arg-FITC and 40 μ M Tyr-FITC in 0.064 M carbonate buffer, pH 9.1 with voltage control of background leakage from the sample channel.	136
4.13	The effect of the active voltage control on the background signal.	138
4.14a	Linear relationship between peak areas and amino acid concentrations up to 20 μ M. The inset shows the deviation at higher concentrations.	140
4.14b	Peak areas in figure 4.14a have been normalized to the response for aniline standard and linear relationship has been extended to 100 μ M.	141
5.1	(a) The top view of the layout and dimensions of Jet-3 devices. (b) The cross section view of the device.	149
5.2	The scanning electron micrograph of a part of the mixing chamber in a Jet-3 device.	150
5.3	Electropherograms of separation of two amino acids without mixing with fluorescein and with mixing.	152
5.4	The relationship between peak areas and mixing voltages applied to reservoir 1.	154
5.5	The simulated resistance circuit of mixing chamber configuration.	155

5.6	Comparision of leakage magnitudes between a T injector and the chamber.	159
5.7	The effect of voltages applied between reservoirs 1 and 5 on the magnitude of the leakage at the inlet of the mixing chamber from the channel connected to reservoir 2.	161
5.8	The frontal analysis electropherograms of 50 μM fluorescein through the chamber and a T injector.	163
5.9	The migration electropherograms by differentiating two frontal electropherograms in figure 5.8.	164

Chapter 1

Introduction

A chemical sensor, defined by the International Union of Pure and Applied Chemistry (IUPAC), is a device that transforms chemical information, ranging from the concentration of a specific sample component to total composition analysis, into an analytically useful signal. The chemical information may originate from a chemical reaction of the analyte or from a physical property of the system investigated (1).

IUPAC states that a chemical sensor contains two basic functional units: a receptor and a transducer (1). The receptor transforms the chemical information about the sample into a form of energy which may be measured by the transducer. The transducer then transforms the energy into a useful analytical signal. Most chemical sensors contain a separator which is, for example, a membrane. The selectivity of a sensor is usually contributed by this separator.

Chemical sensors may be classified according to the operating mechanism of the transducer. J. Janata has divided them into four groups: thermal sensors, mass sensors, electrochemical sensors, and optical sensors (2). Another term, biosensors, is often seen in the literature. However, the principle of the transducer on which they are based is, in general, common to these four groups of chemical sensors. Biosensors are differentiated due to the use of biological elements, e.g., enzymes, in their receptors, and to the fact that they are used for biologically important analytes.

The first part of this thesis describes work involving a glucose sensor. The transducer of the glucose sensor is an electrode, while the receptor is an enzyme, glucose oxidase. Membranes are needed to screen out interferences in complex matrix samples, as this sensor is designed to measure glucose in blood as discussed in the next section.

The second part of the thesis delineates a new concept of chemical sensor, which is miniaturized total chemical analysis systems (μ -TAS). As in a typical chemical analysis, a μ -TAS device may perform the following functions: sample pretreatment, injection, separation and detection. However, its short analysis time and small size due to miniaturization, and the ability to measure a specific analyte in a complex sample matrix, make it resemble a chemical sensor. The advantages over both bench-top instruments and conventional chemical sensors render the μ -TAS worthy of attention.

1.1 Glucose Sensor

There are about 30 million people throughout the world affected by diabetes (3). In Canada, diabetes is the third largest contributing cause of death by disease. Moreover, there is no known cure for diabetes, and all therapeutic measures are aimed at limiting the disease and relieving the patient's symptoms (4). The most powerful and reliable antidiabetic agent known is insulin, which facilitates the metabolism of glucose that is the major end product of carbohydrate digestion. Because the glucose level in the bloodstream of a diabetic fluctuates considerably in response to ingestion of foodstuffs, activity level, and so on, the amount of insulin injected has to be adjusted accordingly or the patient may suffer severe reactions. For those insulin-dependent diabetics, therefore, it is very important to know the glucose concentration in the blood before each injection. This has spurred the development of glucose sensors.

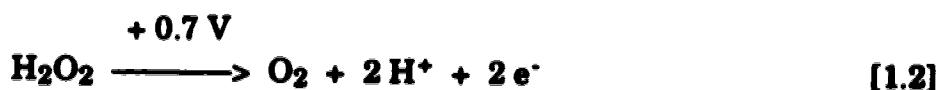
1.1.1 A brief history review

As early as in 1962, Clark and Lyons described the determination of glucose by oxidizing it using glucose oxidase enzyme (5), which is the basis of virtually all glucose sensors and analyzers. As shown in equation [1.1], glucose is catalyzed by the enzyme to gluconic acid in the presence of dissolved oxygen.



The concentration of glucose was determined by electrochemically measuring the extent of oxygen consumption with a Clark-type oxygen electrode (6). The oxygen electrode consisted of a Ag anode and a Pt cathode coated with a hydrophobic gas selective membrane. Oxygen in the sample diffuses through the membrane and is reduced at the cathode. A few years later, Updike and Hicks developed a miniature glucose sensing electrode immobilized with glucose oxidase enzyme using the same principle (7). Although the method was extended by Gough *et al.* (8) and others (9), it suffered from two drawbacks. First, the method had a high background, because the detected O₂ signal was from high to low when glucose was present. Secondly, the relationship between the signal and the concentration of glucose became nonlinear when a large amount of glucose was present, because oxygen transport through the membrane was the limiting factor of the reaction at that time.

Another approach is to determine the rate of hydrogen peroxide production in reaction [1.1], reported by Guilbault *et al.* (10, 11) and others (12, 13). Hydrogen peroxide was electrochemically measured at a potential of about +0.7 V *versus* a saturated calomel electrode (SCE), as shown in equation [1.2].



This is the least complicated and most commonly employed detection mechanism for miniaturized glucose sensors (14).

In 1974, Albisser *et al.* reported the implementation of a closed-loop glycaemic control system, which consisted of a glucose analyzer, a minicomputer and peripherals, an insulin delivery pump, and intravenous catheters to interface with a patient (15, 16). The system had been improved by Shichiri *et al.* in the 1980's (17, 18).

Considerable efforts in this field have been directed toward the design of implantable glucose sensors. Harrison *et al.* have implanted their miniature glucose sensors in dogs and the sensors functioned for more than a week (19). Implantation of glucose sensors in dogs and rats has also been performed by Reach and Wilson (20). Pickup has even implanted glucose sensors in humans (21).

1.1.2 Implantable glucose sensors

The devices used in clinics for glucose concentration measurement fall into three main categories (22). The first type is the dip-stick that performs *in vitro* measurement in blood samples or urine specimens. The glucose level can be read by comparing the colour developed due to the reagents on the strip with a chart or from the electrical current generated. The second type is the bench-top analyzers, most of which are based on the amperometric detection of hydrogen peroxide formed at an electrode coated with a glucose oxidase membrane. The glucose analyzers are very reliable and are used in routine clinical practice. The third type is the implantable sensor for continuous monitoring of glucose concentration. The implantable glucose sensor is a goal for the future rather than an existing product.

The use of a long term implantable glucose sensor can eliminate the need for diabetic patients to prick their fingers several times every day to obtain blood samples. Moreover, glucose sensors could lead to an artificial pancreas, which includes not only a glucose sensor but also an insulin delivery system that automatically administers the amount of insulin based on the feedback signal from the sensor (14-18). The need for such a closed loop system has spurred research interest.

Implantable glucose sensors also rely on the electrochemical measurement of hydrogen peroxide generated by oxidation of glucose, which is catalyzed by the glucose oxidase enzyme as shown in equations [1.1] and [1.2]. The configuration of many implantable glucose sensors comprises a Pt electrode, inner membrane, an enzyme layer, and outer membrane (20). Ideally both inner membrane and outer membrane are selective, i.e., permeable to the concerned chemical while eliminating interferences. In

fact, it is impossible to find a membrane that is absolutely selective in a very complex sample like blood. This is why two types of membranes are often used for inner and outer membranes to reduce interferences from different species. One example of a glucose sensor is shown at the top of figure 1.1 in which a needle shape is used (19, 23).

When this sensor is implanted, glucose in the body first diffuses through the outer membrane, is catalyzed by the enzyme into hydrogen peroxide, which then permeates through the inner membrane and is detected on the Pt electrode. The inner layer needs to be selective to H_2O_2 , while the outer layer must be selective to glucose and oxygen. The membrane used for the outer layer is especially important, because it must also prevent degradation of the enzyme and electrode in the biological environment, and be biocompatible as well. Biocompatibility has been defined as the ability to perform with an appropriate host response in a specific application (20). In other words, after implantation, a biostable environment should be rapidly formed that will be compatible with the sensor's function (20).

Several materials have been suggested for the outer membrane of implantable glucose sensors, including polyurethane (17, 24-28), cellulose and cellulose acetate (12, 29-31), and the perfluorinated ionomer Nafion (14, 19, 23, 32, 33). Nafion-encapsulated glucose sensors were pioneered by Harrison *et al.* and have demonstrated superior performance both *in vitro* and *in vivo* to others in terms of response time, reproducibility and biocompatibility.

The molecular structure of the Nafion monomer is shown at the bottom of figure 1.1. It is quite similar to that of Teflon except for its sulfonate groups. In fact sulfonate groups play an important role in the selectivity of Nafion membrane, as its negative charge attracts cations and expels anions. Many interfering compounds in blood such as ascorbic acid are anions at physiological pH, thus being rejected by Nafion.

In order to systematically design Nafion-encapsulated glucose sensors, a few critical parameters related to the membrane must be quantitatively characterized. These parameters include the diffusion coefficient and permeability of glucose in Nafion, selectivity of the

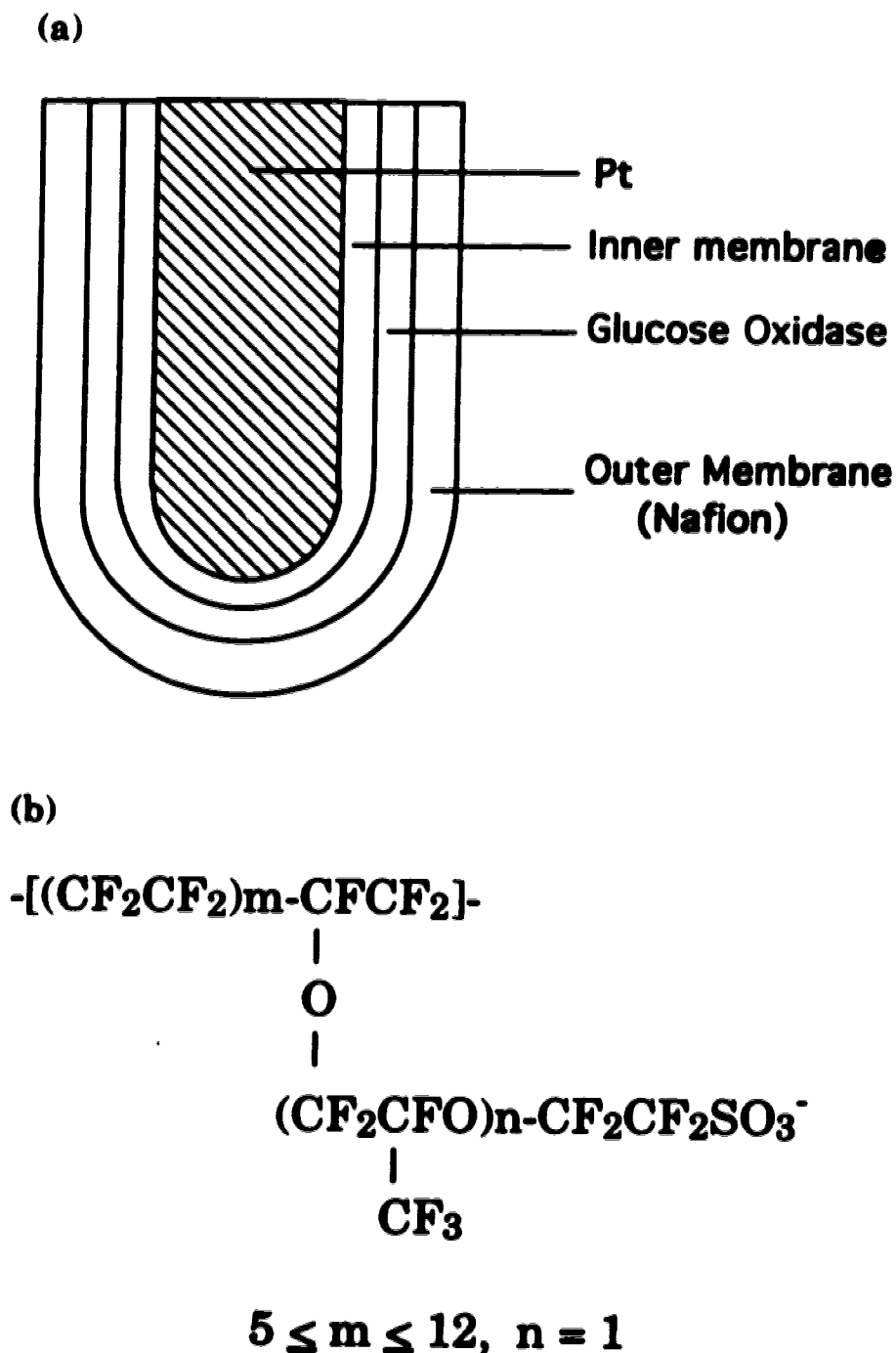


Figure 1.1 (a) The probe end configuration of an implantable glucose sensor (adapted from reference 23 with modification). (b) The molecular structure of Nafion monomer.

membrane against interfering species, and the effects of membrane thickness on these parameters. A membrane-coated rotating disk electrode was used to evaluate these parameters. The method and the results will be presented in chapter 2. However, the techniques used for measuring the membrane thickness, profilometry and ellipsometry, are introduced here.

1.1.3 Profilometry and Ellipsometry

The thickness of Nafion membranes is a critical parameter because it plays an important role in the performance of Nafion-encapsulated glucose sensors (32). The determination of the diffusion coefficient of glucose in Nafion also required the knowledge of the thickness of Nafion membrane as discussed in chapter 2. However, the thickness measurement of so thin a membrane is always problematic in polymer modified electrochemistry.

There are several reported methods for the estimation of film thickness. One of them is an electrochemical method, which was used for membranes containing ions (32, 34). The following procedures are usually performed. A redox ion is first exchanged into the membrane, then oxidized or reduced using cyclic voltammetry. The charge integrated from the resulting voltammogram indicates the amount of redox ions retained in the membrane. These ions are present as counter ions to the charged polymer moieties so that the total amount of polymer on the electrode can be determined according to stoichiometric relationship between these two ions. If the polymer density is known one can calculate the volume of the solid film. The thickness of membrane can then be obtained by dividing the calculated volume of the film by the electrode area. The drawback of this method is that the thickness obtained is not accurate due to the uncertainty in the estimated film density and complexity of the redox process.

Alternatively, a simple calculation has also been used to estimate the membrane thickness as well (35, 36). The volume of the solid film was calculated from the molar concentration and the volume of casting solution, molecular weight of the monomer, and the density of the film. The thickness of the film was again obtained by dividing the calculated volume of the film by the electrode area. This method is not accurate, either,

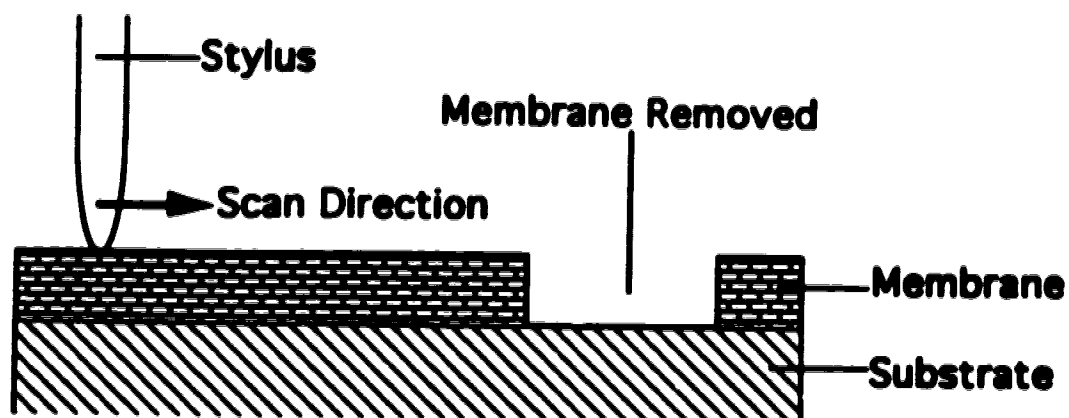
because it also involves the uncertainty in the film density. Besides, the assumption is not often true that all solvent has been evaporated.

Apart from being not accurate, both methods discussed above only tell the average thickness without knowing the uniformity of the film. However, both profilometry (37, 38) and ellipsometry (39, 40) can accurately measure the film thickness, as well as indicate the uniformity of the film. Below is the introduction of these two methods.

A profilometer, also called an alpha-stepper, consists of a scanner and a monitor. The scanner has a stylus, which scans along the surface of a sample with its ultrasmall tip. The scanning process is schematically shown in figure 1.2a. A step is made by removing a part of the membrane, so that the thickness of the membrane can be obtained from the difference of height between the film surface and the substrate surface. The surface profile of the sample, including the step, is then displayed on the monitor or printed out. Figure 1.2b shows the profile of a Nafion membrane coated on a Pt foil. In the Y axis, the height is arbitrarily chosen as zero at the starting point of the scanner. The thickness of this particular Nafion membrane is 254 μm , determined by subtracting the average height of the substrate surface from the average height of the film surface. The film is uniform, as evidenced by the flat profile of the film surface.

Profilometry is an accurate method for measuring film thickness, however, it is not completely satisfactory when it is used for electrochemistry. First, most electrodes can not be placed in a profilometer because of the limitation resulting from the geometry of the sample stage. For the Tencor alpha-step[®] 200 profilometer (Mountain View, CA) we used, the maximum height of a sample that can fit onto the rotary sample stage is 17 mm (41). Even though the stage of a profilometer can be modified to have enough space to place electrodes, there is another disadvantage that is impossible to overcome. Profilometry is a destructive method, as a step in the sample has to be created for the thickness measurement. This makes following electrochemical experiments inaccessible. The typical practice is to coat a membrane on a substrate rather than an electrode. The thickness measured using a profilometer is then assumed to be the same as the

(a)



(b)

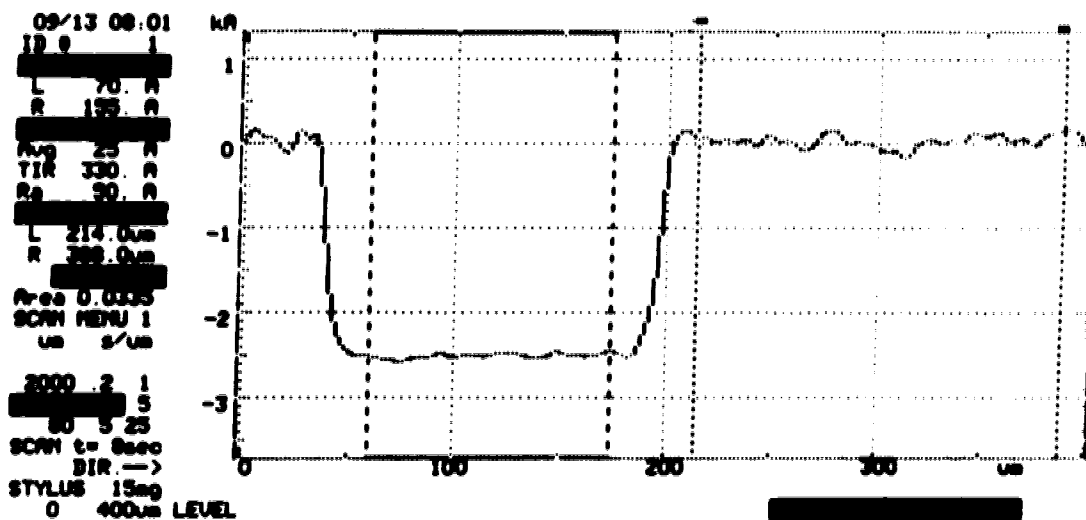


Figure 1.2 (a) The schematic diagram of a scanning process by a profilometer. (b) The surface profile of a Nafion membrane coated on a Pt foil. A step was created by removing a part of film.

thickness of membrane on electrodes when using the same coating procedures. However, using the same coating procedures does not guarantee the same thickness, as evidenced by the data in chapter 2.

Ellipsometry has been recommended for film thickness measurements because it is non-destructive and can be accurate with thin films (39, 40). Semi-conductor industries have used it routinely for measuring the thickness of thin films on silicon wafers. It has also been used to study the growth of surface oxides during corrosion, passivation and electrodeposition. The application of ellipsometry has also been extended to medical and biological science, such as for studies on adsorption of proteins on a surface (40).

As an optical technique, ellipsometry involves illuminating the surface of a sample with a monochromatic light of known wavelength and polarization. The state of polarization changes after reflection from the surface of a sample. The change in the state of polarization can be measured and used to determine the thickness of the film on the sample.

Two parameters, $\tan\psi$ and Δ , are used to represent the polarization state of light (42). $\tan\psi$ is the ratio of the reflection coefficient for the light component polarized in the plane of incidence to that for the component polarized normal to the plane of incidence. The reflection coefficients can be calculated from the incidence angle and the optical properties of the media. Δ is the relative phase difference between the light component polarized in the plane of incidence and the component polarized normal to the plane of incidence. The relationship between these two parameters and film thickness can be described by the Drude equations [1.3] and [1.4] (43).

$$\Delta - \Delta' = \frac{4\pi}{\lambda} \frac{\cos\varphi \sin^2\varphi (\cos^2\varphi - \alpha)}{(\cos^2\varphi - \alpha)^2 + \alpha_1^2} \left(1 - \frac{1}{n^2}\right) d \quad [1.3]$$

$$\psi - \psi' = \frac{2\pi}{\lambda} \frac{\sin 2\psi' \cos\varphi \sin^2\varphi \alpha_1}{(\cos^2\varphi - \alpha)^2 + \alpha_1^2} \left(1 - n^2 \cos\varphi\right) \left(1 - \frac{1}{n^2}\right) d \quad [1.4]$$

In these equations, Δ , ψ are the values obtained in the presence of the film whereas Δ' , ψ' are the values obtained on the bare substrate. φ , λ , n , d are

the angle of the incidence, the wavelength of the incident light, refractive index of the film, and the thickness of the film respectively. α and α_1 are defined by equations [1.5] and [1.6].

$$\alpha = \frac{n_f^2 - k_f^2}{(n_f^2 + k_f^2)^2} \quad [1.5]$$

$$\alpha_1 = \frac{2n_1 k_1}{(n_f^2 + k_f^2)^2} \quad [1.6]$$

Where n_1 and k_1 are the refractive index and extinction coefficient of the substrate.

The optical system of an ellipsometer is shown in figure 1.3 (40, 44). A monochromatic, polarized laser beam is projected onto the surface of a sample after being converted into circularly polarized light by a quarter-wave plate (QWP). The reflected beam is elliptically polarized because of the changes occurred in the amplitude and phase of both the parallel and perpendicular oscillating light components. After polarization by an analyzer, the signal is detected by a photomultiplier tube (PMT) and then sent to a computer. In fact, the instrument is even more complicated and its detail is too great to be discussed here. However, interested readers can refer to the classic ellipsometry textbook written by Azzam and Bashara (45).

1.1.4 Present Nafion study

There are many reported studies on Nafion as discussed in the next chapter. However, transport of neutral molecules in Nafion is poorly understood, and the effect of the film morphology on their permeability is unknown. As a part of the overall glucose sensor research plan, we needed to obtain this information. Ellipsometry and the rotating disk electrode provided a means to measure quantitatively permeability and diffusion coefficients in Nafion, the selectivity of the membrane against interfering species, and the effects of membrane thickness and membrane preparation

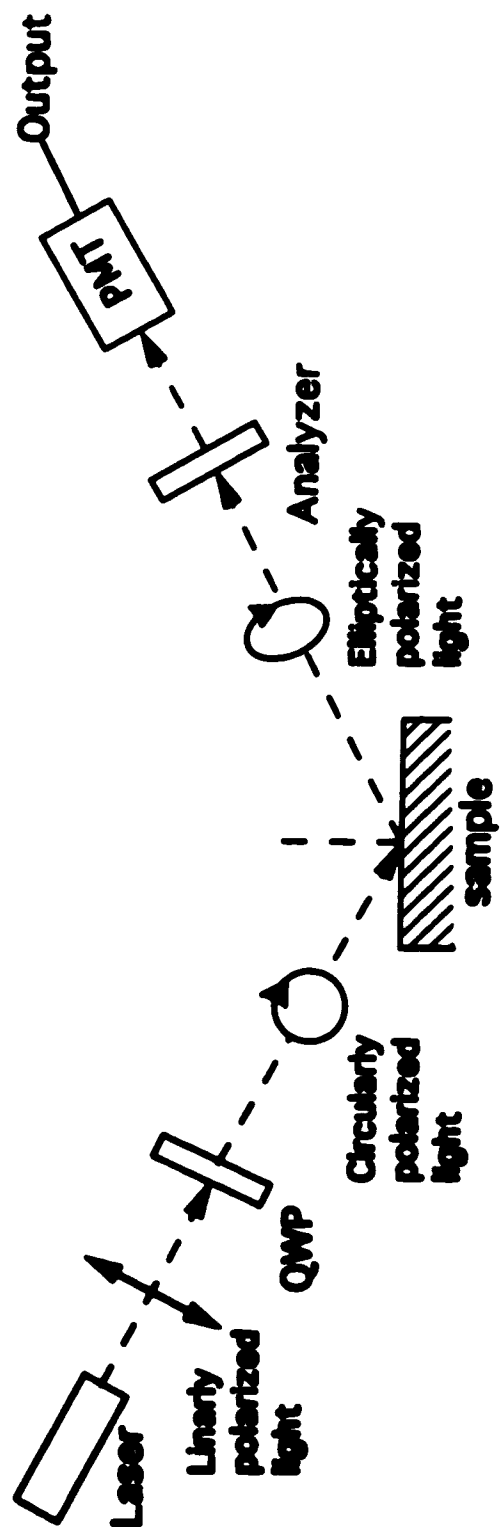


Figure 1.3 The optical system of an ellipsometer

procedures on these parameters, all of which will be detailed in the next chapter.

1.2 Miniaturized Total Chemical Analysis System (μ -TAS)

Chemical sensors are, at best, selective; few, if any, are truly specific. This results from the fact that a chemical sensor may response to several species at once because they have similar physical and/or chemical properties. As a consequence, a chemical sensor can not compete with bench-top instruments in terms of specificity and accuracy, especially when a sample is complex.

If we look at the bench-top chemical analysis, a separation procedure is often performed prior to the final measurement. A typical analysis operation includes the following steps: sampling and sample transport; sample pretreatment; separation; measurement; data analysis and interpretation, as shown in figure 1.4 (46). The extensive automation and combination of all sample handling and measurement steps result in the concept of the Total Chemical Analysis System (TAS) (46, 47). Automation here refers to the overall design of flow systems which facilitate more efficient manipulation and analysis of samples than robotics. Examples of TAS include many commercially available analyzers using flow injection analysis (FIA) (48), and those more sophisticated systems that incorporating FIA with either a chromatograph or a selective enzyme reactor (46, 49, 50).

TAS offers a major economic advantage, for considerable labor costs can be saved due to automation. Another advantage is its increased speed, which can arise from efficient automation and rapid repetition of the operation. Indeed, this speed often makes possible continuous monitoring during process control. Besides, reproducibility and accuracy could be enhanced due to less human involvement.

As shown in figure 1.4, today's chemical sensors represent only a part of the analysis sequence in TAS. If a chemical sensor can perform all or most procedures, its specificity and accuracy will be significantly enhanced. Such chemical sensors have been called miniaturized total chemical analysis systems (μ -TAS), since they consist of virtually all components of a TAS (51).

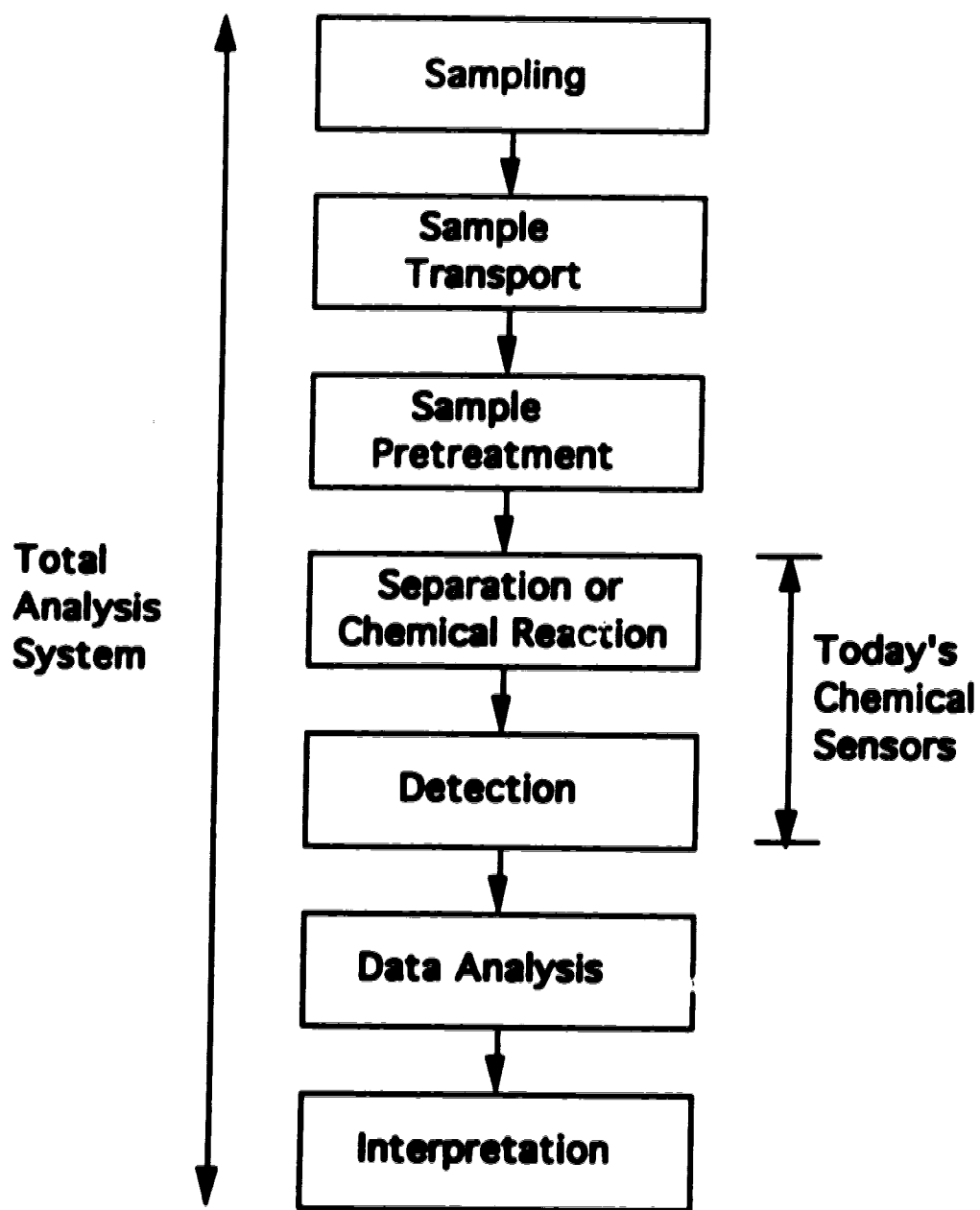


Figure 1.4 The sequence of a typical chemical analysis. (Adapted from reference 46)

μ -TAS would resemble a chemical sensor due to its small size and easy operation, at least from the operator's perspective, although its performance may be under his dynamic control. On the other hand, μ -TAS offers advantages over chemical sensors. It not only enhances specificity and accuracy, but also increases durability because each element in the system can be designed to protect those downstream from components of the sample matrix.

A separation method could be incorporated as a part of μ -TAS devices. Among all separation techniques, capillary electrophoresis (CE) is one method that has been chosen to explore the μ -TAS concept (52). The principle of CE will be introduced in section 1.4 below. Capillary electrophoresis not only gives efficient separation, but also the electroosmotic flow that is induced can be used to pump fluids during sample transport, injection and pretreatment. In contrast, conventional pumps are not well suited to delivery of nanolitre or lower volumes and the use of them develops extremely high back pressures in small capillaries.

Flow injection analysis (FIA) is also integrated as a convenient means for sample injection in μ -TAS devices. FIA is very easy to automate, and leads to rapid analysis due to ready repetition. It can not only be used to inject samples into a separation system, but also to control various pretreatment steps.

One example of such μ -TAS devices has been discussed by Manz *et al.* (53), which demonstrates a miniaturized chemical analysis system containing most procedures of a typical analysis operation performed manually or with a flow injection instrument. The layout of the device is shown in figure 1.5, in which injection, dilution, derivatization, and separation can be performed consecutively by the following four steps.

- Step 1: A voltage is first applied between reservoirs 1 and 3 (3 is grounded), the sample in reservoir 1 is then injected through the first injector to waste reservoir 3.
- Step 2: After turning off the first voltage, another voltage is applied between reservoirs 2 and 5 (5 is grounded). Carrier in reservoir 2 takes the sample plug in the first injector into the

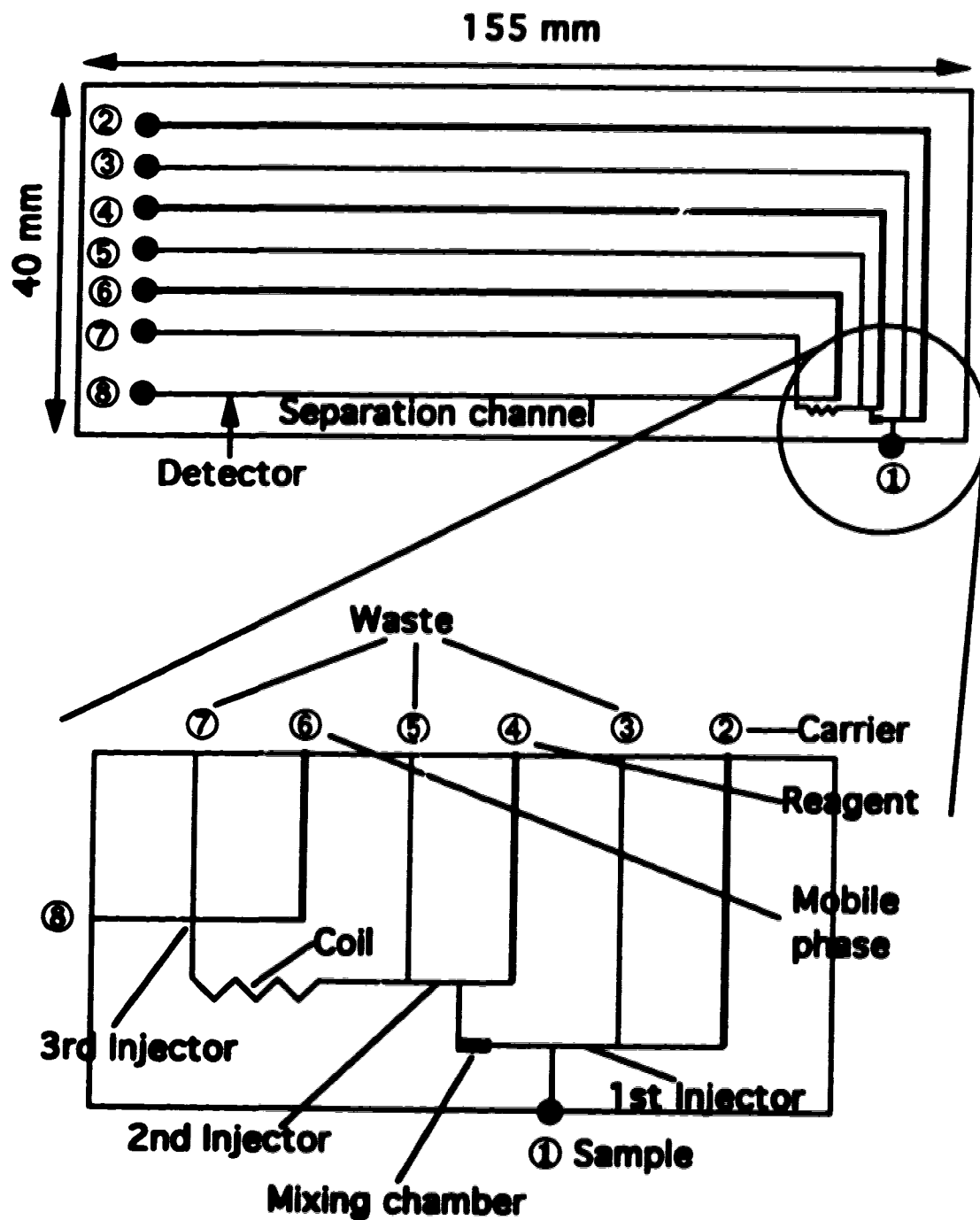


Figure 1.5 Layout of a complex μ -TAS device and the exploded view of FIA system of the device. (Adapted from reference 53 with modifications)

mixing chamber, where dilution takes place, and then through the second injector to waste reservoir 5.

Step 3: When the third voltage is applied between reservoirs 4 and 7 (7 is grounded), the reagent in reservoir 4 takes the diluted sample plug in the second injector into a mixing coil, where the sample is derivatized, and then through the third injector to waste reservoir 7.

Step 4: The application of the final voltage between reservoirs 6 and 8 (8 is grounded) enables the mobile phase in reservoir 6 to carry the sample in the intersection (third injector) into the separation channel, where analytes in the sample are separated, towards the detector and then waste reservoir 8.

While this device concept has been presented in the literature, there have been no reports on its performance to date. Nevertheless, the power of such a system for chemical analysis is clear.

Although μ -TAS is in its infancy stage, it has recently received a lot of attention. A very early example of μ -TAS is a gas chromatograph made in a silicon chip using micromachining technology. Fabricated by Terry *et al.* at Stanford University, the gas chromatograph had a sample injection valve and a 1.5 m long, 200 μ m wide, 30 μ m deep separation capillary column etched in a single 5 cm diameter Si wafer (54). The column was hermetically sealed by a Pyrex glass cover plate, and a micromachined thermal conductivity detector (TCD) was integrally mounted on the same wafer. Combined with a carrier gas supply and a data processing unit, the miniaturized system was used to analyze a gaseous hydrocarbon mixture. Figure 1.6 shows the schematic diagram of this gas chromatograph. Other μ -TAS examples include an *in situ* blood pH analyzer (55), a microphysiometer (56, 57), a titrator based on an ion-selective field effect transistor (ISFET) (58), an integrated FIA system on Si chips (59), and a liquid chromatograph in a Si wafer (60). In addition, Harrisson *et al.* and their collaborators at CIBA-GEIGY in Switzerland have presented recent advances in this field (51-53, 61-64).

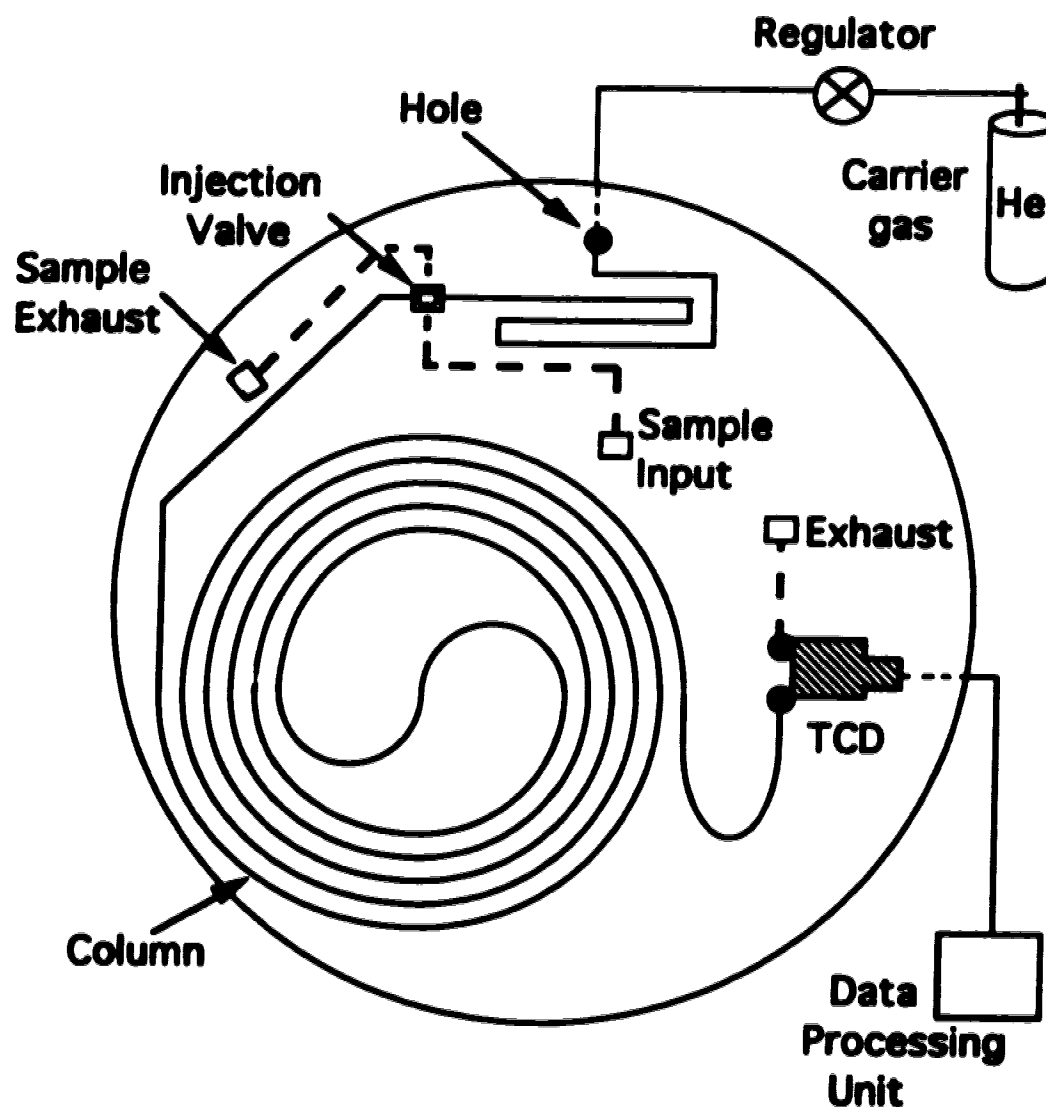


Figure 1.6 A gas chromatograph on a silicon chip. The big circle represents the Si wafer. The dashed lines indicate those are not etched in the wafer and out of the plane. (Adapted from reference 54 with modification.)

In the next two sections, the basic principle of micromachining used to make these devices, and electrophoresis on which they are based will be presented.

1.3 Micromachining

Micromachining refers to the fabrication of three dimensional micromechanical structures and related devices in silicon or other materials using microelectronics fabrication technology (65). Micromachining involves the processes of film deposition, photolithography, etching, diffusion or ion implantation, and bonding, all of which have been used in integrated circuit manufacture (66, 67).

A standard, one mask fabrication process is outlined in figure 1.7. It starts with the deposition of a layer of silicon dioxide on a Si wafer using thermal oxidation (figure 1.7a). Other film deposition methods used are spin coating, physical vapor deposition (PVD), chemical vapor deposition (CVD), low pressure CVD, plasma enhanced CVD, and sputtering (67). SiO_2 or Si_3N_4 is mostly used as a mask when Si is the substrate to be etched. A photoresist (PR), which is light sensitive, is usually spin coated on the surface (figure 1.7a). Residue solvent in the photoresist is removed by so-called soft-baking at a certain temperature. Photolithographic patterning is then performed as shown in figure 1.7b. The desired pattern is made in the master mask and ultraviolet (UV) light is usually used as the radiation source. The exposed area of photoresist undergoes photochemical reactions, which change the physical and/or chemical property of the film.

There are two types of photoresist: positive and negative (68). Positive PR consists of a photosensitizer molecule, i.e., diazonaphthoquinone or its substitute, and a polymer, both of which are dissolved in an organic solvent. The polymer acts as a matrix to form a film. Upon radiation exposure, the reaction represented by equation [1.7] takes place.

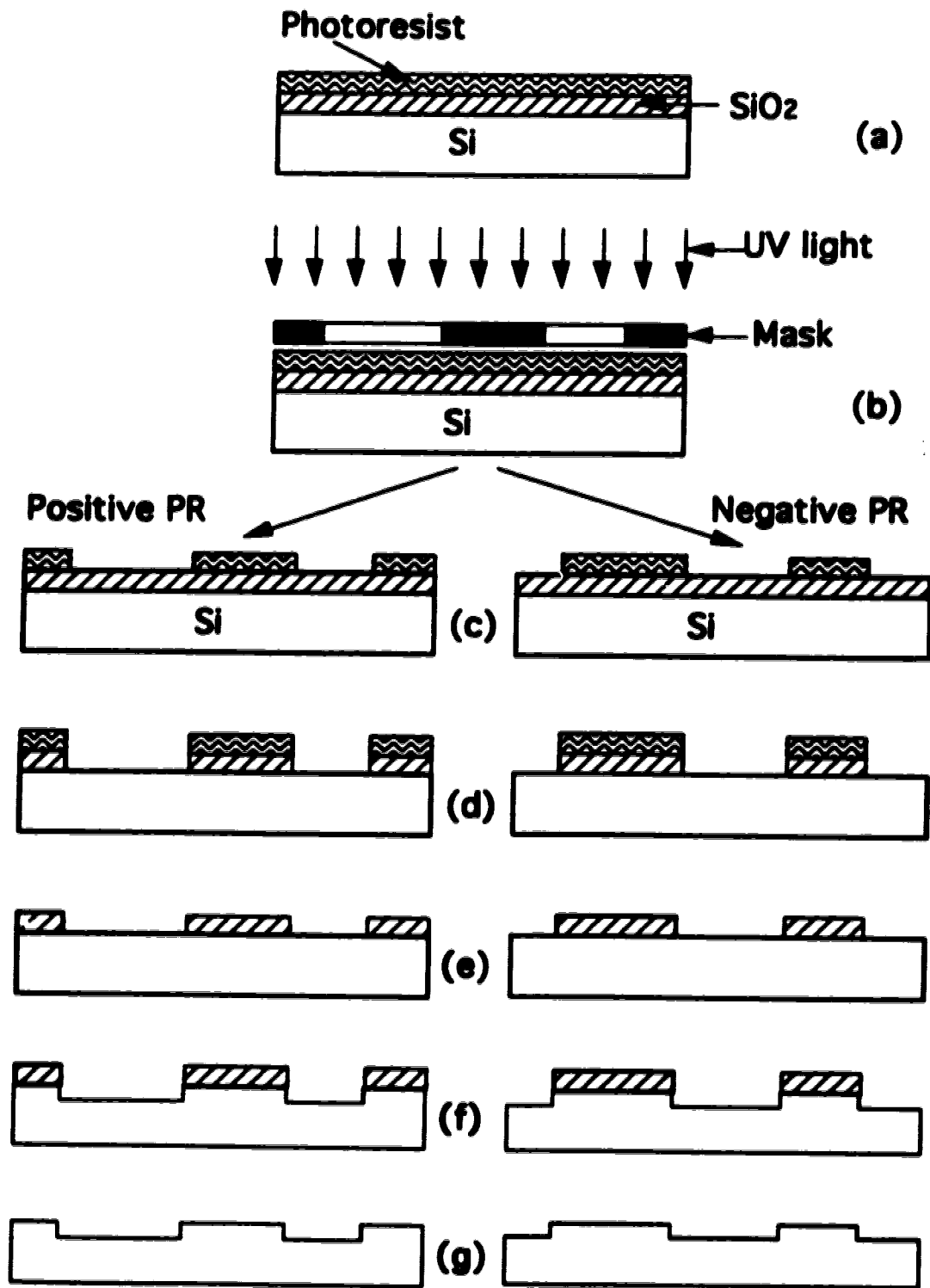
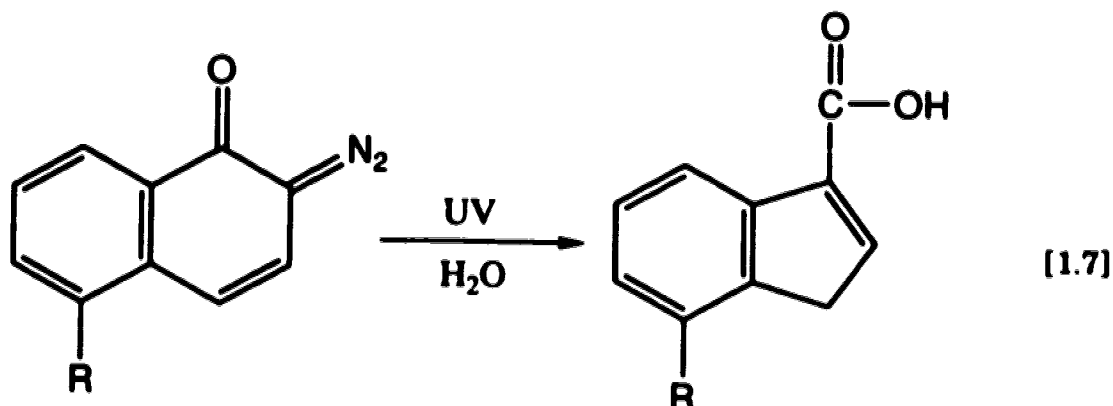


Figure 1.7 The sequence of one mask microfabrication process.



The R group in diazonaphthoquinone varies with the product and the manufacturer. The carboxylic acid produced accelerates the film dissolution (development) by a basic developer, and then the exposed area is stripped off as shown in the left side of figure 1.7c.

In contrast, the sensitizer of negative PR is an arylazide whose photoreaction produces a nitrene, as expressed by equation [1.8].



The intermediate nitrene then undergoes polymerization reactions, which result in covalent linkages with another polymer. Therefore, the exposed area resists the solvent during development and unexposed area is stripped off instead, as shown in the right side of figure 1.7c.

After development, hard-baking at a high temperature is often carried out to improve polymer-wafer adhesion. The next step is to etch the exposed silicon oxide layer (figure 1.7d), followed by removing the rest of the photoresist (figure 1.7e). Si substrate is then etched while the remaining SiO₂ functions as a mask layer (figure 1.7f). Different channel shapes can be obtained by choosing anisotropic or isotropic etching, which depends on etchants (69). After the SiO₂ layer is removed, the desired pattern appears in the Si wafer (figure 1.7g). To complete the fabrication of a device, bonding and packaging procedures are needed, although they are not shown in the figure.

Using micromachining technology, many micromechanical structures have been fabricated and reported in the literature. For example, micromachined pumps and valves have been designed, and even integrated into chemical sensors to handle liquid or gas flows (55, 59). Other examples include micromachined motors, rotators, mass flow meters, neural probes, atomic force microscopes, etc. (65, 69, 70). Many of the applications are not related to chemistry.

The strength of this technology lies in the ability to make miniaturized 3-dimensional structures integrated together or with electronics in large batch processes. Mass production can result in excellent reproducibility, and potentially inexpensive devices.

1.4 Capillary Electrophoresis (CE)

Electrophoresis has been widely used for several decades as a method for separating ionized compounds (71, 72). However, only about a decade ago was capillary electrophoresis (CE) pioneered by Virtanen (73) and Mikkers *et al.* (74). Jorgenson and Lukacs, with their contributions (75, 76), are often credited for popularizing this method, which is also called capillary zone electrophoresis (CZE) or high performance capillary electrophoresis (HPCE) (77). Characterized by low sample consumption, high resolution and efficient separation, CE has occupied its own niche in scientific research, and will become more popular in industry as well in the near future, due to the fact that a variety of CE instruments have been commercially available in recent years (78).

As shown in figure 1.8, capillary electrophoresis is carried out in a capillary tube with a typical inner diameter of 10-100 μm and a total length of 30-100 cm. Capillaries that are used in modern CE are almost exclusively made of fused silica. Both ends of the buffer-filled capillary are placed in electrolyte reservoirs that contain electrodes. A high voltage (HV) connected to electrodes is typically in the range of 10-30 kV and furnished by a high voltage power supply. On-column detection is often used to avoid loss of separation efficiency caused by detector dead volume.

Under an electrical field a phenomenon called electroosmosis occurs,

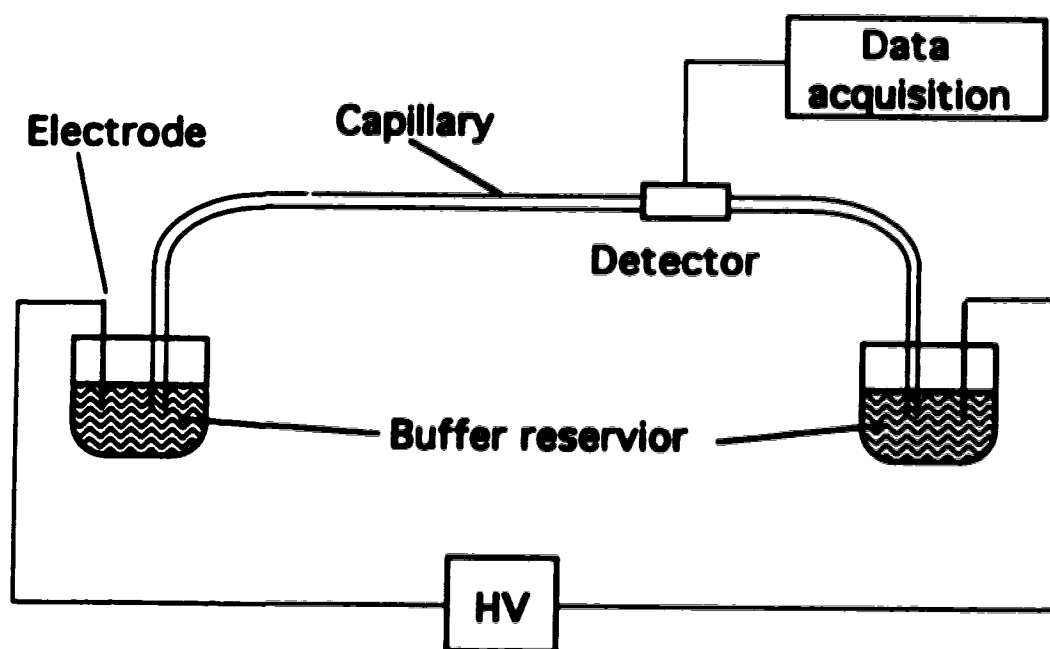


Figure 1.8 Schematic of a capillary electrophoresis system.

in which the solvent typically moves from the anode through the capillary to the cathode. The generation of electroosmosis, which is occasionally called electroendosmosis (72, 79), is schematically demonstrated in figure 1.9 (80). The walls of a fused silica capillary are usually negatively charged in the aqueous solution at a pH above 3 due to the ionization of surface silanol groups (81). The charges on the wall surface attract positive ions from the buffer solution, thus giving a typical double-layer structure. These mobile positive ions in the diffuse layer carry solvent molecules with them and are attracted to the cathode under an electric field. The resulting electroosmosis has a unique feature, a nearly flat flow profile across the capillary, as shown in the figure. This feature makes electroosmosis contribute very little to bandbroadening, so that separation efficiencies as high as a few million plates have been achieved (82). A flat flow profile in capillary gel electrophoresis also results in high separation efficiency, although there is no electroosmosis. Such high separation efficiency offers CE advantages over column chromatography.

While electroosmosis moves both solutes and solvents in the same direction and at the same speed, the separation of solutes is generated from electrophoresis that occurs at the same time and is caused by the difference in mobility between ions. Although electrophoresis simultaneously moves cations to the cathode and anions to the anode, both cations and anions migrate to the cathode and are detected at one end of the capillary because electroosmotic mobility is usually larger than electrophoretic mobility.

The overall ionic mobility, μ_{all} , also called apparent ionic mobility, can be expressed by equations [1.9-1.11].

$$\mu_{all} = \mu_{eo} + \mu_{ep} \quad [1.9]$$

$$\mu_{eo} = \frac{\epsilon \zeta_{eo}}{6\pi\eta} \quad [1.10]$$

$$\mu_{ep} = \frac{q}{6\pi\eta\gamma} \quad [1.11]$$

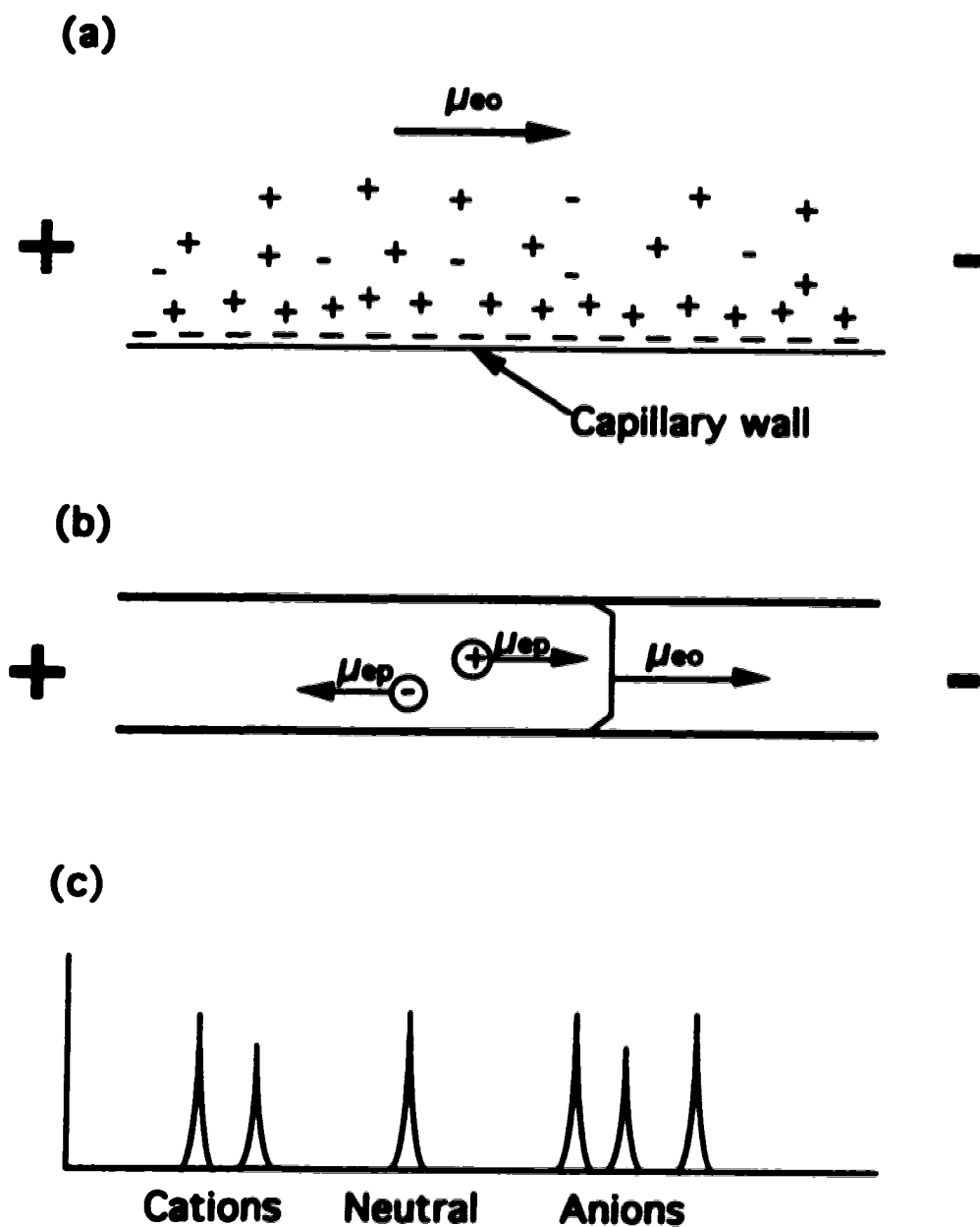


Figure 1.9 (a) The formation of double-layer at a silica-solution interface and the generation of electroosmosis under an electric field. (Adapted from reference 80) (b) The nearly flat electroosmotic flow profile. Both cations and anions have electrophoretic flow at the same time. (c) A generic electropherogram.

Where μ_{eo} and μ_{ep} are the electroosmotic mobility and electrophoretic mobility; ζ_{eo} is the zeta potential created by the double-layer at the wall surface and defined by the potential difference across the diffuse layer; ϵ and η are the dielectric constant and the viscosity of the solution; and q and γ are the charge and the hydrodynamic radius of an ion (80, 83).

A generic electropherogram is shown in Figure 1.9c, in which cations first migrate out of the capillary, then neutral molecules, with anions last. This is because for cations both electrophoretic and electroosmotic mobilities are in the same direction, neutral molecules experience only electroosmosis, while for anions electroosmotic and electrophoretic mobilities are in the opposition direction.

As mentioned above, the separation of solutes, in principle, depends only on electrophoresis. Therefore, the charge and size of analyte species determine the separation as indicated in equation [1.11]. The viscosity of the medium in the equation has the same effect on the mobilities of all analytes. However, other solvent properties, such as ionic strength, pH, dielectric constant, are also important because they control the effective charge on the analyte ions and, for larger molecules, their shape and hydrodynamic radius.

Electroosmosis has an indirect influence on the separation (80). Because of the flat electroosmotic flow profile, longitudinal diffusion should theoretically be the main source of band broadening (75, 76). The amount of time a solute resides in the capillary therefore affects both separation efficiency and resolution. Both the migration velocity (v) and the migration time (t) of each analyte ion depend not only on electrophoretic mobility but also on the electroosmotic mobility, as expressed in equations [1.12] and [1.13] (75, 76).

$$v = (\mu_{ep} + \mu_{eo}) E = \frac{(\mu_{ep} + \mu_{eo}) V}{L} \quad [1.12]$$

$$t = \frac{L^2}{(\mu_{ep} + \mu_{eo}) V} \quad [1.13]$$

Where E , V , L are the electrical field, the total applied voltage, and the length of the capillary, respectively. Both equations assume that the detection is at the end of the capillary. In fact, equation [1.14], which is used to calculate the separation efficiency of the capillary, clearly suggests the separation efficiency is dependent on electroosmosis (75, 76).

$$N = \frac{(\mu_{ep} + \mu_{eo}) V}{2 D} \quad [1.14]$$

N and D in this equation are the theoretical plate number and the diffusion coefficient. This equation can hold only when longitudinal diffusion is the major source of band broadening and other sources are negligible.

The resolution (R) of two components in capillary electrophoresis can be given by equation [1.15] (80).

$$R = \frac{\sqrt{N}}{4} \left(\frac{\Delta v}{\bar{v}} \right) \quad [1.15]$$

Where Δv is the difference in component flow velocity and \bar{v} is the average velocity. Using equations [1.12] and [1.14] and substituting into equation [1.15], the resolution can be expressed as

$$R = \frac{(\mu_{e,1} - \mu_{e,2}) \sqrt{\frac{V}{D(\mu_e + \mu_{eo})}}}{4\sqrt{2}} \quad [1.16]$$

where $\mu_{e,1}$ and $\mu_{e,2}$ are the electrophoretic mobilities for the two components and μ_e is the average electrophoretic mobility.

Another fundamental point worthy of mention is Joule heating, which results from the ionic current inside the capillary. Joule heating is a limitation of normal or larger scale electrophoresis, because it can result in density gradients and temperature gradients that increase band broadening, affect electrophoretic mobilities, and can even lead to breakdown of the electrophoretic process due to boiling of the solvent (75, 80). However, the large ratio of surface area to volume of the small bore capillary used in CE

provides efficient heat dissipation, which is another unique feature of CE. A typical electrical field used in CE is 300 V/cm (80), and maximum power dissipation without affecting efficiency is typically said to be 1 W/m (84).

1.5 CE-based μ -TAS

To understand the principle of CE-based μ -TAS, it is useful to consider the modes of operation envisioned to effect an analysis. Figure 1.10 shows the layout of a simple μ -TAS device, called "Airport", that will be discussed in detail in chapter 3. The three dimensional structure of the "Airport" devices is shown in figure 1.11. The device consists of two capillaries or channels intersecting with each other. Each channel end is connected to a reservoir. These are numbered in the figure 1.10 for reference in the following discussion. Suppose a buffer is present in the two channels and reservoirs 2, 3, 4, while a sample is present in reservoir 1. The sample is then driven from reservoir 1 through the injection channel to reservoir 2 by applying a voltage between reservoirs 1 and 2. Electroosmotic motion pumps the sample through the whole injection channel and the composition inside the channel should be the same as that in reservoir 1 after a certain time. After turning off the voltage on reservoirs 1 and 2, another voltage is applied to reservoirs 3 and 4. The buffer in reservoir 3 flows in the direction of reservoir 4 and the sample in the intersection is carried into the separation channel. After electrophoretic separation, analytes in the sample are detected on the separation channel as in conventional CE. Figure 1.12 illustrates the whole process.

The two examples of CE-based μ -TAS devices given in figures 1.5 and 1.10 illustrate the principles of the μ -TAS concept. The realization of amino acid separations and solution mixing in the μ -TAS devices described in chapters 3-5 indicates the feasibility of using relatively complex miniaturized chemical analysis systems for the analysis of real samples. Such μ -TAS devices have potential to be used in continuous monitoring of chemical concentrations in industrial processes. Since μ -TAS devices offer a rapid and sophisticated analysis, they have been called "laboratories on a

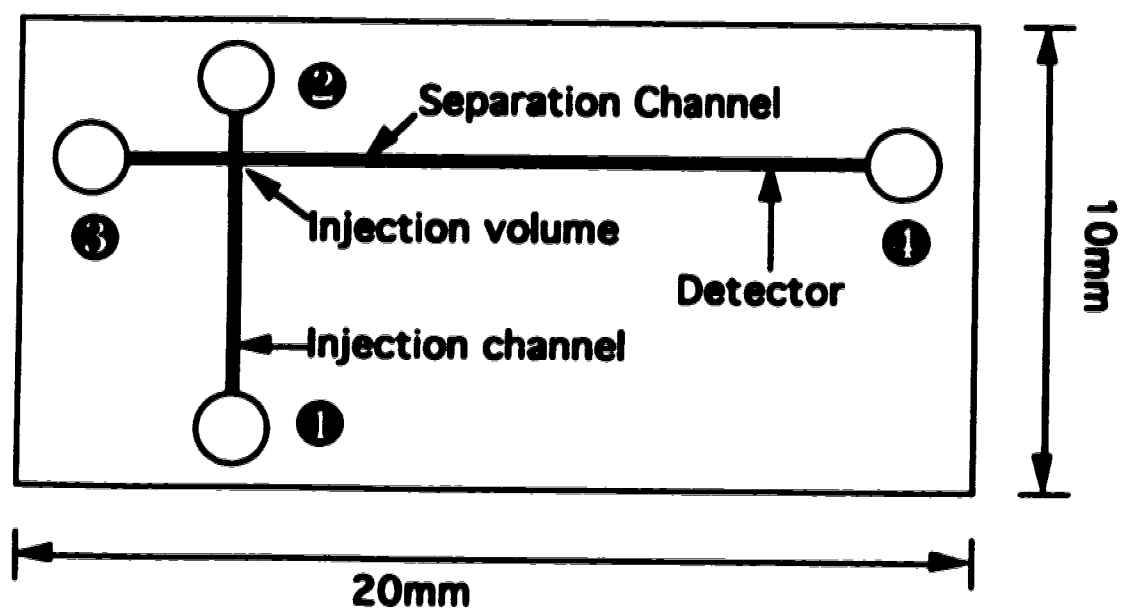


Figure 1.10 Layout of a simple μ -TAS device called "Airport". Reservoirs referred to in the text are identified by numbers.

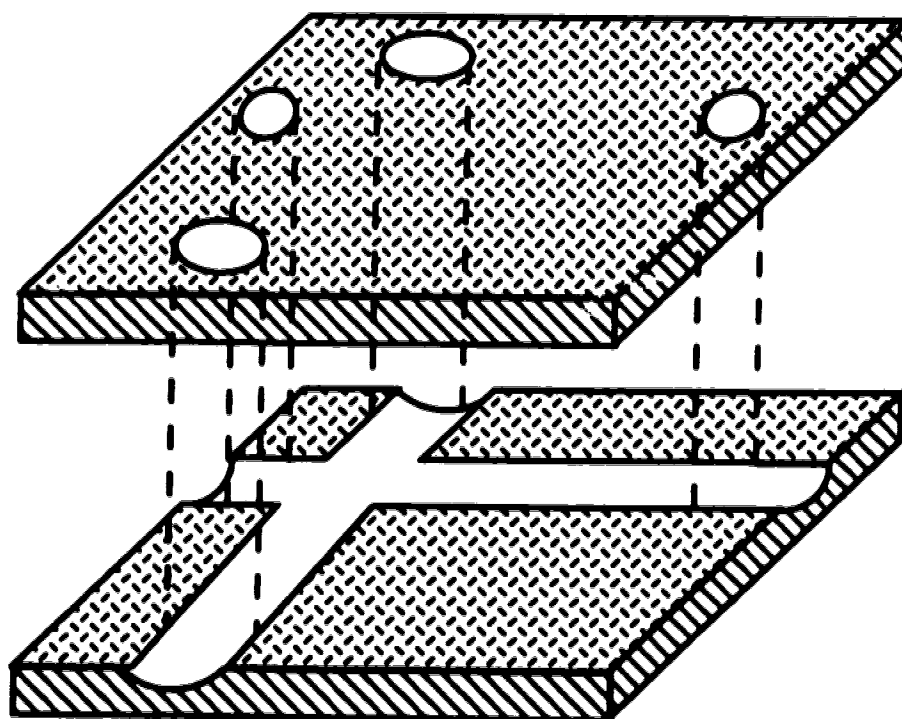


Figure 1.11 The three dimensional structure of "Airport" devices. The bottom plate has two channels intersecting with each other. Four holes in the cover plate are aligned with the channels and connected with reservoirs for introducing solutions and applying voltages. The ends of channels are plugged with epoxy. Two plates are separated here for clarity, but they are bonded together in actual devices.

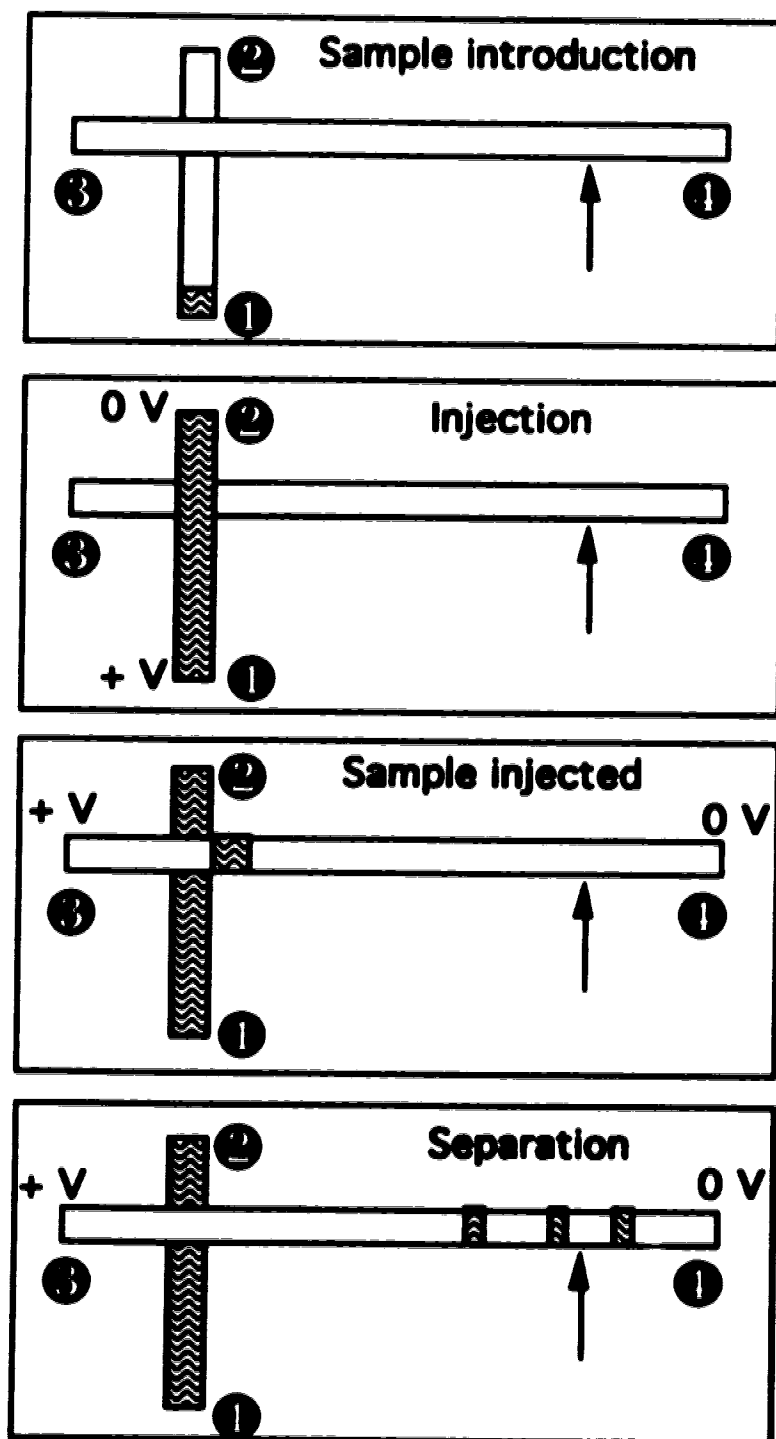


Figure 1.12 Illustration of sample injection using electroosmotic pumping and FIA, and separation using CE.

chip". In their final form they will be sufficiently portable to be used in the field (63).

1.6 References

1. Hulanicki, A.; Glab, S.; Ingman, F., *Pure & Appl. Chem.*, **1991**, *63*, 1247-1250.
2. Janata, J., *Principles of Chemical Sensors*, Plenum Press: New York, **1989**.
3. Powers, M. A., *Handbook of Diabetes Nutritional Management*, Aspen Publishers: Rockville, MD, **1987**, 3.
4. Solomon, I., in *The Encyclopedia Americana*, International Edition, Vol. 9, Grolier Inc.: Danbury, CT, **1981**, 51-53.
5. Clark, L. C.; Lyons, C., *Ann. New York Acad. Sci.*, **1962**, *102*, 29-35.
6. Clark, L. C., *Trans. Am. Soc. Artif. Intern. Organs*, **1956**, *2*, 41-47.
7. Updike, S. J.; Hicks, G. P., *Nature*, **1967**, *214*, 986-988.
8. Gough, D. A.; Leyboldt, J. K.; Armour, J. C., *Diabetes Care*, **1982**, *5*(3), 190-198.
9. Kondo, T.; Ito, K.; Ohkura, K.; Ito, K.; Ikeda, S., *Diabetes Care*, **1982**, *5*(3), 218-221.
10. Guilbault, G. G.; Lubrano, G. J., *Anal. Chim. Acta*, **1972**, *60*, 254-255.
11. Guilbault, G. G.; Lubrano, G. J., *Anal. Chim. Acta*, **1973**, *64*, 439-455.
12. Clark, L. C.; Duggan, C., *Diabetes Care*, **1982**, *5*, 174-180.
13. Yao, T., *Anal. Chim. Acta*, **1983**, *148*, 27-33.
14. Turner, R. F. B., *Toward an Implantable Glucose Sensor for the Artificial Beta Cell*, Ph. D. thesis, University of Alberta, **1980**.
15. Albisser, A. M.; Leibel, B. S.; Ewart, T. G.; Davidovac, Z.; Botz, C. K.; Zingg, W., *Diabetes*, **1974**, *23*, 389-396.
16. Albisser, A. M.; Leibel, B. S.; Ewart, T. G.; Davidovac, Z.; Botz, C. K.; Zingg, W.; Schipper, H.; Gander, R., *Diabetes*, **1974**, *23*, 397-404.
17. Shichiri, M.; Kawamori, R.; Goriya, Y.; Yamasaki, Y.; Nomura, M.; Hakui, N.; Abe, H., *Diabetologia*, **1983**, *24*, 179-184.
18. Shichiri, M.; Kawamori, R.; Hakui, N.; Yamasaki, Y.; Abe, H., *Diabetes*, **1984**, *33*, 1200-1202.

19. Moussy F.; Harrison, D. J.; O'Brien, D. W.; Rajotte, R. V., *Anal. Chem.*, **1993**, *65*, 2070-2077.
20. Reach, G.; Wilson, G. S., *Anal. Chem.*, **1992**, *64*, 381A-386A.
21. Pickup, J., *TIBTECH*, **1993**, *11*, 285-291.
22. Pickup, J. C.; Shaw, G. W.; Claremont, D. J., *Biosensors*, **1987**, *3*, 335-346.
23. Turner, R. F. B.; Harrison, D. J.; Rajotte, R. V.; Baltes, H. P., *Sensors and Actuators*, **1990**, *B1*, 561-564.
24. Yamasaki, Y. *Medical Journal of Osaka University* **1984**, *35*, 25-34.
25. Velho, G.D.; Reach, G.; Thevenot, D. In: *Biosensors: Fundamentals and applications*, Turner, A.P.F.; Karube, I.; Wilson, G.S. (Eds) Elsevier **1987**, pp 390-408.
26. Schichiri, M.; Asakawa, N.; Yamasaki, Y.; Kawamori, R.; Abe, H. *Diabetes Care* **1986**, *9*, 298-301.
27. Bindra, D.S.; Zhang, Y.; Wilson, G.; Sternberg, R.; Thevenot, D.R.; Moatti, D.; Reach, G. *Anal. Chem.* **1991**, *63*, 1692-1696.
28. Moatti-Sirat, D.; Capron, F.; Poitout, V.; Reach, G.; Bindra, D.S.; Zhang, Y.; Wilson, G.S.; Thevenot, D.R. *Diabetologia* **1992**, *35*, 224-230.
29. Thevenot, D.R. *Diabetes Care* **1982**, *5*, 184-189.
30. Ikeda, S.; Ito, K.; Kondo, T.; Ichikawa, T.; Yukawa, T.; Ichihashi, H. *Proc. Chem. Sensors* **1983**, *17*, 620-625.
31. Gough, D.A.; Lucisano, J.Y.; Tse, P.H.S. *Anal. Chem.* **1985**, *57*, 2351-2357.
32. Harrison, D. J.; Turner, R. F. B.; Baltes, H. P., *Anal. Chem.*, **1988**, *60*, 2002-2007.
33. Turner, R. F. B.; Harrison, D. J.; Rajotte, R. V., *Biomaterials*, **1991**, *12*, 361-368.
34. Harrison, D. J.; Daube, K. A.; Wrighton, M. S., *J. Electroanal. Chem.*, **1984**, *163*, 93-115.
35. Whiteley, L. D.; Martin, C. R., *Anal. Chem.* **1987**, *59*, 1746-1751.
36. Martin, C. R.; Dolland, K. A., *J. Electroanal. Chem.*, **1983**, *159*, 127-135.

37. White, H. S.; Leddy, J.; Bard, A. J., *J. Am. Chem. Soc.* **1982**, *104*, 4811-4817.
38. Szentirmay, M. Z.; Martin, C. R., *Anal. Chem.*, **1984**, *56*, 1898-1902.
39. Carlin, C. M.; Kepley, L. J.; Bard, A. J. *J. Electrochem. Soc.* **1985**, *132*, 353-359.
40. Collins, R. W.; Kim, Y.-T. *Anal. Chem.* **1990**, *62*, 887A-900A.
41. Tencor Instruments, *The manual of alpha-step® 200*, Mountain View, CA, **1985**.
42. Passaglia, E., in *Ellipsometry in the Measurement of Surface and Thin Films*, Passaglia E; Stromberg, R. R.; Kruger, J., Eds.; National Bureau Standards: Washington, D.C., **1963**, 1-4.
43. Heavens, O. S., *Optical Properties of Thin Solid Films*, Dover Publications: New York, **1965**, Chapter 5, 96-154.
44. Gaertner Scientific Corp., *User Manual of Two Wavelength Ellipsometers L125B and L126B*, Chicago, IL.
45. Azzam, R. M. A.; Bashara, N. M., *Ellipsometry and Polarized Light*, North-Holland: Amsterdam, **1977**.
46. Graber, N.; Lüdi, H.; Widmer, H. M., *Sensors and Actuators*, **1990**, *B1*, 239-243.
47. Manz, A.; Harrison, D. J.; Verpoorte, E.; Widmer, H. M., in *Advances in Chromatography*, Brown, P. R.; Grushka, E. Eds.; Marcel Dekker, Inc: New York, **1993**, 1-66.
48. Skoog, D. A.; Leary, J. J., *Principles of Instrumental Analysis*, 4th Ed, Saunders College Publishing: Orlando, FL, **1992**, Chapter 28, 681-700.
49. Gisin, M.; Thommen, C., *Anal. Chim. Acta*, **1993**, *190*, 165-176.
50. Garn, M.; Cevy, P.; Gisin, M.; Thommen, C., *Biotechnol. Bioeng.*, **1999**, *34*, 423-428.
51. Manz, A.; Graber, N.; Widmer, H. M., *Sensors and Actuators*, **1990**, *B1*, 244-248.
52. Harrison, D. J.; Manz, A.; Fan, Z.; Lüdi, H.; Widmer, H. M., *Anal. Chem.*, **1992**, *64*, 1926-1932.
53. Manz, A.; Fettingner, J. C.; Verpoorte, E.; Lüdi, H.; Widmer, H. M.; Harrison, D. J., *Trends Anal. Chem.* **1991**, *10*, 144-149.

54. Terry, S. C.; Jerman, J. H.; Angell, J. B., *IEEE Transactions on Electron Devices*, **1979**, ED-26, 1880-1886.
55. Shoji, S.; Esashi, M.; Matsuo, T., *Sensors and Actuators*, **1988**, *14*, 101-107.
56. Parce, J. W.; Owicki, J. C.; Kercso, K. M.; Sigal, G. B.; Wada, H. G.; Muir, V. C.; Bousse, L. J.; Ross, K. L.; Sikic, B. I.; McConnell, H. M., *Science*, **1989**, *246*, 243-247.
57. McConnell, H. M.; Owicki, J. C.; Parce, J. W.; Miller, D. L.; Baxter, G. T.; Wada, H. G.; Pitchford, S., *Science*, **1992**, *257*, 1906-1912.
58. Olthuis, W.; van der Schoot, B. H.; Chavez, F.; Bergveld, P., *Sensors and Actuators*, **1999**, *17*, 279-283.
59. van der Schoot, B. H.; Jeanneret, S.; van den Berg, A.; de Rooij, N. F., *Sensors and Actuators*, **1992**, *B6*, 57-60.
60. Manz, A.; Miyahara, Y.; Miura, J.; Watanabe, Y.; Miyagi, H.; Sato, K., *Sensors and Actuators*, **1992**, *B1*, 249-255.
61. Harrison, D. J.; Glavina, P. G.; Manz, A., *Sensors and Actuators*, **1993**, *B10*, 107-116.
62. Seiler, K.; Harrison, D. J.; Manz, A., *Anal. Chem.*, **1993**, *65*, 1481-1488.
63. Harrison, D. J.; Fluri, K.; Seiler, K.; Fan, Z.; Effenhauser, C. S.; Manz, A., *Science*, **1993**, *261*, 895-897.
64. Manz, A.; Harrison, D. J.; Verpoorte, E.; Fettingner, J. C.; Lüdi, H.; Widmer, H. M., *J. Chromatogr.*, **1992**, *593*, 253-258.
65. Delapierre, G. *Sensors and Actuators*, **1999**, *17*, 123-138.
66. Gise, P. E.; Blanchard, R. B., *Semiconductor and Integrated Circuit Fabrication Techniques*, Peston Publishing Co.: Reston, VA, **1979**.
67. Ko, W. H.; Suminto, J. T., in *Sensors: A Comprehensive Survey*, Grandke, T.; Ko, W. H., Eds; VCH Press: Weinheim, Germany, **1999**, *1*, 107-168.
68. Weill, A., in *The Physics and Fabrication of Microstructures and Microdevices*, Kelly, M. J.; Weisbuch, C., Eds; Springer-Verlag: Berlin, **1996**, 59-64.
69. Petersen, K. E., *Proceedings of the IEEE*, **1992**, *70*, 420-457.
70. Wise, K. D.; Najafa, K., *Science*, **1991**, *254*, 1335-1342.

71. Tiselius, A., *Trans. Faraday Soc.*, **1937**, *33*, 524-531.
72. Hjertén, S., *Chromatogr. Rev.*, **1967**, *9*, 122-224.
73. Virtanen, R., *Acta Polytech. Scand. Chem. Incl. Metall. Ser.*, **1974**, *123*, 1-67.
74. Mikkers, F. E. P.; Everaerts, F. M.; Verheggen, Th. P. E. M., *J. Chromatogr.*, **1979**, *169*, 11-20.
75. Jorgenson, J.; Lukacs, K. D., *Anal. Chem.* **1981**, *53*, 1298-1302.
76. Jorgenson, J.; Lukacs, K. D., *Science*, **1983**, *222*, 266-272.
77. Gordon, M. J.; Huang, X.; Pentoney, S. L.; Zare, R. N., *Science*, **1988**, *242*, 224-228.
78. Terabe, S. *Anal. Chem.* **1990**, *62*, 605A-607A.
79. Grossman, P. D.; Colburn, J. C., Eds, *Capillary Electrophoresis: Theory and Practice*, Academic Press: San Diego, CA, **1992**.
80. Ewing, A.; Wallingford, R. A.; Olefirowicz, T. M., *Anal. Chem.* **1989**, *61*, 292A-303A.
81. Lukacs, K. D.; Jorgenson, J., *J. HRC & CC* **1985**, *8*, 407-411.
82. Swerdlow, H.; Wu, S.; Harke, H.; Dovichi, N. J., *J. Chromatogr.*, **1990**, *516*, 61-67.
83. Chien, R.; Burgi, D. S., *Anal. Chem.* **1992**, *64*, 489A-496A.
84. Monnig, C. A.; Jorgenson, J., *Anal. Chem.* **1991**, *63*, 802-807.

Chapter 2

Glucose Permeability and Selectivity in Nafion Films [†]

2.1 Introduction

The use of semipermeable polymeric overcoatings to protect electrodes in complex sample matrices, or to otherwise tailor their reactivity and selectivity characteristics, is an attractive and successful approach to electrode design (1). The DuPont perfluorinated sulfonate ionomer Nafion has been used as a protective or selective coating material for a number of applications. These include coating of C electrodes used for neurotransmitter determination in cerebral fluids (2, 3) and for metal ion analysis in whole blood (4), enzyme electrodes used for glucose assays in whole blood (5), Cu^{2+} ion selective electrodes used in seawater (6), and a number of other applications (7-12). These applications often utilize Nafion recast from its dissolved form due to the ease of film preparation. It is now generally recognized that Nafion prepared in this manner has substantially different characteristics than the solid form supplied by the manufacturer (13-17). Differences in the morphology of the films, such as crystallinity and long range order, are observed, as well as significant solubility of recast films in aqueous and organic solvents (13, 14). It is also believed there are differences in the uptake of solvent and ions between the two forms (18-20). Importantly, the diffusion coefficients in recast films

[†] A version of this chapter has been published as:

Zhonghui Fan; D. Jed Harrison, "Permeability of Glucose and Other Neutral Species Through Recast Perfluorosulfonated Ionomer Films", *Analytical Chemistry*, 1992, 64, 1304-1311.

appear to be greater than in the solid form received from Dupont (16). Thermal curing of the recast films, and judicious choice of casting solvent, have been found to increase order in the films and decrease or eliminate their solubility (13, 14, 17). Yet, many of the applications of Nafion coatings are likely to rely on the less ordered structure of recast Nafion and the larger diffusion coefficients. Consequently, it is of considerable importance to understand how treatments used to affect Nafion's stability will affect transport characteristics in the films.

Nafion coatings were shown to be very effective as protective coatings for glucose oxidase based glucose sensors (5, 21, 22), as discussed in chapter 1. This application involves transport of neutral substrates and supporting electrolyte across the Nafion coating. The study of neutral molecule transport in Nafion has been very limited, and the effect of the film morphology on their permeability is unknown. One report giving the average fluxes of the protonated form of a number of organic acids in the solid form of Nafion has appeared (23). The authors indicated quantitative comparisons could not be made, but concluded that molecular size influenced transport rates in the expected manner. The transport rates of neutral species were lower than those of simple cations such as Na^+ and Li^+ , but much higher than those of anions (23, 24). Transport of O_2 in the solid form of Nafion has also been studied and it is quite rapid, exhibiting a diffusion coefficient approaching that of ions in solution (25, 26). Transport of O_2 in the recast form was found to be about 10 fold faster than in the solid form (16). It has also been shown that ferrocene will extract into a Nafion film (27), that glucose can be transported across a film in aqueous solution (5), and that ferrocene and catechols are transported in wet films in supercritical CO_2 (20). Only the O_2 studies provide quantitative information on permeability or diffusion coefficients of neutrals in recast Nafion.

It is also important to understand how thermal curing of recast films affects transport. Whiteley and Martin (28) have studied transport of a charged ferrocene derivative present at less than 10% of the saturation content in Nafion films cured at 180°C . A high ionic strength was used to induce breakdown of anion exclusion (Donnan failure) and increase the

ion content in the films. These conditions are substantially different from those of sensor applications, and are in fact argued (28) to result in different rate limiting steps for the transport process. Quantitative data for O₂ transport in recast Nafion cured at room temperature (16) and 180°C (29) shows little difference in permeability. However, the solvation state of O₂ is likely to be much different than glucose or other larger molecules in Nafion, so the generality of this observation is not clear.

Transport of electroactive molecules to the surface of a rotating disk electrode (RDE) through a coating of Nafion film can be used to obtain quantitative data on the films permeability (30, 31). In order to determine the effective diffusion coefficients and the effect of film thickness, it is necessary to know the thickness of the polymer coating. Film thickness measurements of films on polymer modified electrodes have often been problematic (1). Bard and coworkers have discussed the drawbacks of various methods and recommended that ellipsometry be used for the study of polymer modified electrodes (32). They applied it to measuring film growth during the electrodeposition of several polymers. Ellipsometry has previously been used to study the growth of surface oxides during corrosion and passivation, and others have since studied the deposition of conducting polymers (33-35), as discussed in chapter 1. It is non-destructive, and easily adapted to various electrode geometries, and is also well suited to *in situ* measurements so can be used to measure thickness in solution, although we have not done so in our study. Despite these advantages, to our knowledge ellipsometry has not been used to determine the thickness of polymer coatings that are not electrodeposited such as Nafion and poly(vinylpyridine). We report here on the effectiveness of ellipsometry for film thickness measurements on polymer coated electrodes.

2.2 Theoretical considerations

A Nafion membrane coated, rotating disk electrode was used to measure permeabilities and effective diffusion coefficients of several electroactive compounds in the films. The dependence of current on

rotation rate is given by a modified form of the Levich equation [2.1], as shown by the derivation of Gough and Leypoldt (30). Since that work there have been numerous developments in describing current flow across a modifying film for electroactive species, and these consider much more complex situations (28, 29, 31). In our analysis we have employed the formalism of Savéant and colleagues (31) in which the overall current, i , through a passive film is represented by several characteristic currents.

$$\frac{1}{i} = \frac{1}{i_A} + \frac{1}{i_s} + \frac{1}{i_p} \quad [2.1]$$

$$i_A = 0.62nFAC_0D_s^{2/3}\nu^{-1/6}\omega^{1/2} \quad [2.2]$$

$$i_s = nFAC_0P_m \quad [2.3]$$

$$i_p = nFAC_0\chi_m \quad [2.4]$$

where i_A is the solution mass transport limited current; n , F , and A are electron transfer number, Faraday constant, and electrode area respectively; C_0 is the bulk concentration; D_s is the diffusion coefficient in solution; ν is the kinematic viscosity; and ω is the angular velocity of the disk. The limiting current through the film is given by i_s , and depends on the permeability of the polymer membrane, P_m .

$$P_m = \alpha D_m / \delta_m \quad [2.5]$$

where α is the extraction coefficient of solute between the solution and the film, D_m is the diffusion coefficient in the film, and δ_m is the film thickness. If the extraction of solute is not at equilibrium then another term, i_p , is present, where χ_m is the heterogeneous rate of mass transfer across the interface, as discussed by Leddy *et al.* (31).

Equations [2.1]-[2.4] show that a plot of $1/i$ versus $1/\omega^{1/2}$ should be linear, with a slope dependent on the solution diffusion coefficient and substrate concentration. The intercept is a function of the permeability of

the film and the rate of mass transfer at the interface. Leddy *et al.* (31) have shown that a plot of the intercepts of the Koutecky-Levich plots *versus* δ_m should give an intercept of i_p^{-1} , if it is significant. Consequently both χ_m and P_m can be evaluated from these analyses. If the membrane thickness δ_m is determined independently then the product αD_m , referred to as the effective diffusion coefficient in the membrane (30), can be obtained from the Koutecky-Levich intercept. For applications to chemical sensing, knowledge of the effective diffusion coefficient should be sufficient to predict the membrane characteristics, if α does not vary significantly in the concentration range of interest.

It must be noted that when the electroactive substrate undergoes reversible reactions the situation becomes more complex than originally described by Leypoldt and Gough, or equations [2.1]-[2.4]. Electron self exchange between species in the film can contribute to the apparent diffusion coefficient, as described by the Dahms-Ruff equation (10), when the species is present at high concentrations due to ion exchange equilibria. We have avoided this issue by using redox couples with relatively slow self exchange kinetics for which mass transport is the dominant factor, or by using neutral or anionic redox couples that have low values of α and will not be present at high concentrations in the film. If mass exchange at the surface is slower than self exchange between species in the polymer and the solution then this effect may contribute to the Koutecky-Levich intercept (31). If so a plot of these intercepts *versus* δ_m would have a non-zero intercept since this is a surface phenomenon.

Diffusion coefficients in polymer films can also be determined from potential-step chronoamperometric experiments (1, 36, 37), for which the current in the membrane obeys the Cottrell equation at short times:

$$i = nFAC_m \sqrt{\frac{D_m}{\pi t}} \quad [2.6]$$

C_m is the concentration of electroactive species in the membrane, t is the time, and the other terms have the same meanings as above. The value of C_m can be determined using equation [2.7],

$$C_m = N_m / (A \delta_m) \quad [2.7]$$

in which N_m is the number of moles of the electroactive species determined by coulometry, and the film thickness (δ_m) is determined independently. Because the membrane phase is finite, a plot of i versus $t^{-1/2}$ will be linear only at short times, when the concentration perturbation has not yet propagated to the membrane edge. These experiments are normally done in a solution containing little or no electroactive species in solution to avoid the need to separate the different diffusion processes. Consequently, this method is only applied to the analysis of diffusion of cations in Nafion for which there is a strong electrostatic interaction leading to a large value of α . For this case the chronoamperometric experiment yields D_m and the RDE study gives αD_m , thus allowing α to be determined.

2.3 Experimental Section

2.3.1 Solutions and Reagents

A commercial Nafion solution (5%, 1100 equivalent weight (EW), Solution Technology Inc., Mendenhall, PA) was used for most of the work described. A Nafion solution of 1100 EW was also obtained from Aldrich. A sheet of Du Pont Nafion-117 membrane (thickness 0.20 mm, EW 1100, Electrosynthesis Co., East Amherst, N.Y.) was dissolved in 1:1 water-isopropanol to give a 1% solution, following the method of Martin *et al.* [38]. Nafion solutions in *N,N*-dimethylformamide (DMF) (Fisher, Reagent Grade) were prepared by adding an appropriate volume of DMF to commercial Nafion solutions, and then removing the alcohol and water with a Roto-vap (Bucher) (13, 17).

Quarternized poly(vinylpyridine) (QPVP) was synthesized (39) from poly(vinylpyridine) (500,000 MW, a kind gift from Reilly Tar and Chemicals). A stock 0.2 M QPVP (expressed as moles of vinylpyridine monomer), 0.05 mM α , α' -dibromo-*p*-xylene solution in methanol was

prepared and diluted with methanol to give other concentrations. Addition of α , α' -dibromo-p-xylene gave more durable films (39).

N,N,N-trimethyl-N-ferrocene methylammonium chloride (FcTMA⁺) was prepared from N,N-dimethyl-aminomethylferrocene methiodide (Strem Chemicals, Newburyport, MA) by ion-exchange using Rexyn 201 (Fisher Scientific) and eluting with 20 mM NaCl. The eluent was rotary evaporated to remove solvent, re-crystallized twice from acetonitrile and dried overnight *in vacuo*. Removal of I⁻ was confirmed by cyclic voltammetry.

A buffer solution of pH 7.4 was prepared from phosphate salts (ionic strength $\mu = 0.05$ M), with 5 mM sodium benzoate and 1 mM ethylenediaminetetraacetic acid (EDTA) as preservatives, and 0.1 M NaCl as additional electrolyte. All other chemicals were reagent grade and were used as received. Aqueous solutions were prepared from doubly-distilled, deionized water.

2.3.2 Substrate Surface and Film Preparation

Silicon slides (1cm x 2 cm) were scribed from 3" diameter n-type (100) Si wafers (S. E. H., Malaysia) with a resistivity of 1-2 Ω -cm. The slides were sonicated in turn in 5% aqueous Sparkleen (Fisher), distilled methanol, and doubly-distilled water. Flat Pt foil substrates (1cm x 1cm) were prepared from Pt foil (0.004" thick, Johnson Matthey) glued onto 2 cm x 2 cm glass slides with epoxy. These were polished with alumina (to 0.3 μ m) until flat, and rinsed in doubly-distilled water in an ultrasonic bath. Flat gold foil substrates were prepared by electroplating Au onto clean Pt substrates (40). The Pt foil and RDE were cleaned by anodizing at +1.9 V (5 min) in 0.5 M H₂SO₄, and cycling from -0.28 V to +1.1 V (5 min). The Pt RDE was then anodized at +1.1 V (5 min). When coated with Nafion it was first exposed to 5% N-(trimethoxysilylpropyl)-N,N,N-trimethylammonium chloride (Petrarch Systems) in anhydrous methanol, following the procedure described by Szentirmay *et al.* (41) to enhance Nafion adhesion. The electroplated Au foils were used directly after electroplating and

rinsing with water. The Au RDE was polished with alumina (0.3 μm), ultrasonicated, and cycled from -1.4 V to +0.9 V for 15 min in 0.1 M NaOH.

Nafion solutions were spin coated on the substrates at 2000 RPM, most commonly. For the Pt or Au RDE's 100 or 50 μL was deposited, respectively; the volume varied for the other substrates. The film edge needed for surface profilometry was generated by cutting the film with a plastic knife. Non-uniformity was evidenced by variation in the colored thin film interference pattern that developed and such films were discarded. Film thickness could be controlled by varying the concentration of the Nafion solution (0.5-5%), or the number of coatings. Multiple coating showed a greater tendency to produce visibly non-uniform films and so was used less often. This was unfortunate since multiple coating is the best way to reduce the effect of pinholes, and the spin coating method, while giving more uniform films on average, is prone to pinhole formation (1). Nafion films were cured at room temperature for about 1 to 2 hr. High temperature curing of Nafion membrane was done by placing coated electrodes in an oven at 80 or 120°C for 1 hr, after first air drying for 1 to 2 hr.

2.3.3 Electrochemical Measurements

Cyclic voltammetry, rotating disk voltammetry, and amperometry were performed with a Pine RDE-4 Potentiostat, Pine MSR rotator, and a Kipp and Zonen BD 90 X-Y recorder. A three-electrode system was used with a Pt or Au rotating disk electrode (RDE), a platinum gauze counter electrode, and a saturated calomel electrode (SCE). All potentials are reported *versus* SCE. Chronoamperometry was done using a PAR 273 potentiostat with an IBM-PC-XT interfaced as a controller and data acquisition system. The software was written in-house in BASIC.

The Pt RDE was obtained from Pine instruments. The Au RDE was prepared by Ag soldering a 3 mm diameter, 2 mm long Au cylinder (Johnson Matthey) to a brass piece machined to fit the Pine MSR Rotator. The assembly was sealed in a teflon sleeve and the electrode surface was then polished. The active area of the Au and Pt RDE's was determined

from the slope of Levich plots (i vs $\omega^{1/2}$) for the oxidation of ferrocyanide in 0.1 M KCl. Using a diffusion coefficient of $D_s = 6.50 \times 10^{-6} \text{ cm}^2/\text{s}$ (42), and $\nu = 0.997$ centistokes (cs) (43) the area was found to be 0.306 cm^2 for the Pt RDE and 0.0673 cm^2 for the Au RDE, in reasonable agreement with the geometric areas.

Rotating disk measurements of the oxidation of hydroquinone (QH_2), the ferrocene derivative (FcTMA^+), ferrocyanide, and ascorbic acid (AA) were performed on naked and Nafion coated Pt RDE's. The pH 7.4 buffer ($\nu = 1.011$ cs (43)) was used for QH_2 and AA, and 0.1 M KCl for FcTMA^+ and $\text{Fe}(\text{CN})_6^{4-}$. The electroactive solute concentrations were 1 mM except where specified. For these compounds the Levich plots were obtained at potentials well into the mass transport limited region: +0.70 V for QH_2 and AA, +0.60 V for FcTMA^+ , and +0.40 V for $\text{Fe}(\text{CN})_6^{4-}$. Rotating disk measurements of glucose oxidation were made using a naked or Nafion coated Au RDE and the method developed by Larew and Johnson (44). The peak current obtained near +0.15 V in a potential sweep between -0.80 and +0.50 V at 100 mV/s was determined as a function of rotation rate. Larew and Johnson have shown this gives a mass transport, i.e. Levich, controlled current. A 0.1 M NaOH supporting electrolyte ($\nu = 1.019$ cs (43)) with 1 mM glucose was used.

Chronoamperometry was performed on a Nafion coated Pt RDE in 0.1 M KCl after the electrode was first immersed for 10 min in 7.3 mM FcTMA^+ , 0.1 M KCl and then rinsed briefly. The potential was stepped from 0 to +0.6 V, and the current was acquired every 1 ms. The amount of FcTMA^+ in the film was determined by integration of the current obtained from a cyclic voltammetric scan at 10 mV/s between -0.2 and 0.8 V.

2.3.4 Film thickness measurements

Polymer film thickness was measured using a Gaertner L125B two wavelength ellipsometer equipped with a rotating analyzer. Ellipsometer control, data acquisition and data analysis were done with an IBM PS-2 system and software provided by Gaertner. Microspot optics gave a sample area of 0.002 mm^2 at a 70° incident angle and 0.001 mm^2 at a 50°

incident angle. The 632.8 nm He:Ne laser and an angle of 70 ° were used most frequently. Measurements at both 50 ° and 70 ° were used to determine the period or order of the ellipsometric parameters, so as to obtain the thickness unambiguously. Occasionally the 441.6 nm He:Cd laser was used to cross-check the results. Pt or Au RDE's were fixed with a screw in a holder made to fit into a notch in the sample stage. The optical parameters for the naked substrates were obtained after using the cleaning procedures described above. The polymer thickness and its refractive index, N_i , were determined for coating thicknesses greater than 350 Å. For thinner films the value of N_i so determined was input to the programs to allow the thickness to be calculated. For silicon substrates the native oxide thickness was measured on each sample. This parameter was then input into a two, non-absorbing layer program provided by Gaertner, to evaluate the thickness of the polymer layer. On the Pt PDE (trimethylaminopropyl)trimethoxy silane was deposited as an adhesion promotion layer. The combined thickness of the Nafion/silane layer was used in calculations of the substrate diffusion coefficients.

The ellipsometer used allowed the surface to be aligned with respect to the incident beam and the analyzer by observation of a crosshair through a microscope eyepiece. The alignment was easy for the foil samples, however, initially we could not observe the crosshair for the RDE's mounted on the sample stage. The problem proved to be due to rounding of the electrode surface during polishing, which caused the image to diverge upon reflection from the surface. Considerable care was required to insure the RDE surface was truly planar and not just smooth, which resolved the problem.

All of the film thickness measurements were made on films in air, not in solution. Solvent swelling can be expected to have some effect on the thickness following immersion. However, we have previously found (5) that films cured at room temperature swell by no more than 15% after 1 h in water. Consequently, any systematic errors introduced by studying the films in air should be of this magnitude or less.

Surface profilometry was conducted using an Alpha-step Surface Profilometer (Tencor Industries) on flat metal foils or silicon wafers. The

same samples were then examined by ellipsometry to cross calibrate the two methods.

2.4 Results and Discussion

2.4.1 Measurement of Film Thickness

To evaluate the reliability and accuracy of ellipsometry for measuring the thickness of polymer films coated on electrodes a comparison between ellipsometry and surface profilometry was undertaken. Both Nafion and quaternized poly(vinylpyridine) (QPVP) were used as the coating film to gain some insight into the generality of the method. Initially, silicon/silicon dioxide substrates were used since the substrate parameters for these materials are extremely well known, and the method is so well characterized for Si that its use has become routine. Results using Pt and Au substrates were then evaluated by both ellipsometry and surface profilometry.

Optical properties of the substrates Si, SiO₂, Au, and Pt obtained in this work, or from the literature (46) are given in Table 2.1. The values were measured by ellipsometry several times over a period of days, and the errors given are the standard deviations (as are other errors given in the text). The differences between optical parameters for the metal foils and the RDE's, as well as the discrepancies relative to the literature values reflect one of the difficulties in using ellipsometry for the purpose we intend. They also underscore the need to calibrate the technique against another method if it is to be used. The variations observed are most likely due to differences in the surface oxides arising from different anodization procedures, as well as differences in planarity and surface roughness. Also, for the Pt substrates the difference relative to literature values must arise in part from the different wavelengths used for the measurements. This is supported by the fact that the literature values at 589 nm lie between those we found at 632.8 and 441.8 nm.

Table 2.1 Refractive indices and extinction coefficients of substrates.

Substrate	Source	Wavelength (nm)	Refractive Index (N_s)	Extinction Coefficient (K_s)
Si	Gaertner^a	632.8	3.850	-0.020
SiO₂	Gaertner^a	632.8	1.46	0.00
Pt foil	This work	632.8	1.89 ± 0.07	-4.09 ± 0.20
Pt RDE	This work	632.8	2.261 ± 0.022	-4.411 ± 0.186
Pt RDE	This work	441.8	1.760 ± 0.040	-3.235 ± 0.125
Pt bulk	Ref. 46	589	2.06	-4.26
Pt electrolytic	Ref. 46	589	2.63	-3.54
Au foil	This work	632.8	0.6	-3.3
Au RDE	This work	632.8	0.749 ± 0.046	-2.564 ± 0.090
Au evaporated	Ref. 46	650	0.142	-3.374
Au crystalline	Ref. 46	640	0.1667	-3.6902

a) Parameters used in Gaertner ellipsometer software.

Ellipsometric measurements of polymer coatings on the silicon substrates gave a value of 1.32 ± 0.03 for the refractive index of Nafion, and 1.62 ± 0.02 for that of QPVP. Using the substrate parameters we determined for Pt and Au foils, the refractive indices of the polymer coatings were the same within experimental error. For Pt the average parameters given in Table 2.1 were acceptable, however, because the Au substrate parameters showed more variability between samples, the values for each substrate were determined immediately before coating with Nafion. The N_s and K_s substrate values differ slightly even for different spots on the same electrode, but this does not cause a big difference in estimates of the film thickness. For example, the optical parameters measured for naked Pt varied over several days from $N_s = 2.178$ and $K_s = -4.014$ to $N_s = 2.261$ and $K_s = -4.411$. Subsequent coating of the electrode with 1% and then 3% Nafion solutions gave a film with a thickness of 1000 Å based on the former parameters, and 980 Å based on the latter.

Figure 2.1a shows a compilation of the results for Nafion and QPVP films on Si, Pt and Au substrates for which a multiple layer coating technique was used. The thickness determined by ellipsometry is plotted *versus* that measured by surface profilometry for thicknesses ranging up to 13,000 Å (or 1,300 nm). Membranes with a range of thicknesses can also be obtained by application of a single layer using different concentrations of polymer solutions. The plot of the thickness by ellipsometry *versus* the thickness by profilometry for those single layer coatings is shown in figure 2.1b. The intercepts are close to zero within experimental error. While there is some scatter in the data of both figure 2.1a and figure 2.1b the slopes of the two plots are 1, indicating that there is no systematic bias between the two methods for measuring membrane thickness. Consequently, ellipsometry can be used as a non-invasive method to measure polymer film thickness on electrodes. The quality of the agreement is particularly striking for the Au foil substrate given the discrepancy in its optical substrate parameters relative to the literature. However, it is clear that careful attention must be paid to measurement of the substrate parameters on the specific electrode surfaces used. It

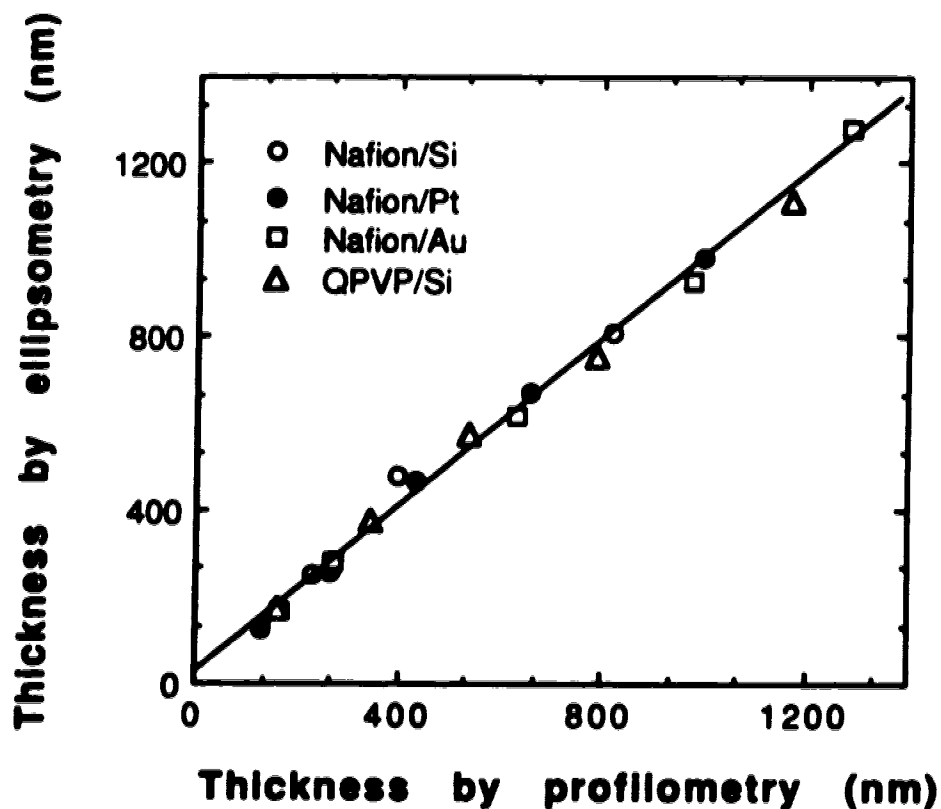


Figure 2.1a Comparison of thickness measured by ellipsometry and by profilometry for Nafion coated on silicon (○), Pt (●), and Au (□), and quaternized poly(vinylpyridine) (QPVP) coated on silicon substrates (Δ). All membranes were made by multiple layer coatings with one concentration of polymer solution. The number of coating layers is from 1 to 5. The concentration of Nafion solution used is 3%, while that of QPVP is 0.12 M.

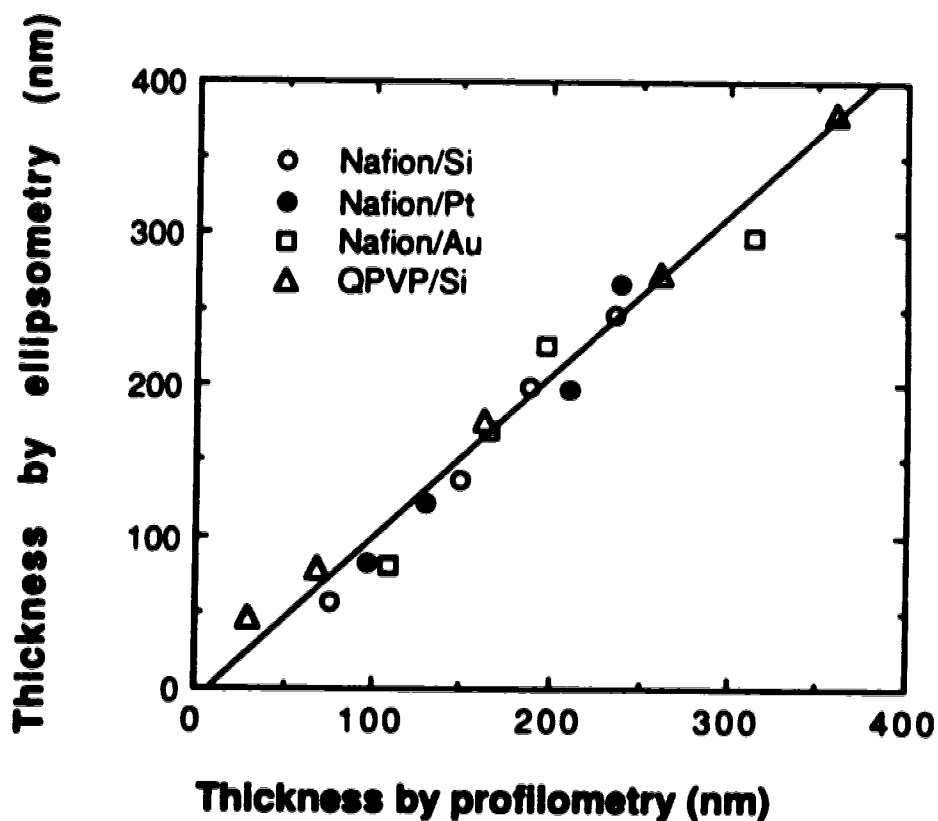


Figure 2.1b Comparison of thickness measured by ellipsometry and by profilometry for Nafion coated on silicon (○), Pt (●), and Au (□), and quaternized poly(vinylpyridine) (QPVP) coated on silicon substrates (Δ). All membranes were made by one layer coating with several concentrations of polymer solutions. The concentrations of Nafion solution used are 1%, 2%, 3%, 4%, and 5%; while those of QPVP are 0.04 M, 0.08 M, 0.12 M, 0.16 M, and 0.20 M.

should also be mentioned that errors due to variation in the substrate parameters will increase if the coating film is very thin ($< 100 \text{ \AA}$).

2.4.2 Permeability of Room Temperature Cured Nafion

To evaluate the permeability of Nafion films, the current for several different redox couples was examined at coated rotating disk electrodes as a function of rotation rate and film thickness. Studies were initially performed on solution-cast Nafion cured at room temperature (RT) to establish a baseline for comparison for the other curing procedures. The redox couples were chosen to allow a comparison between possible permeation routes in the polymer. The highly charged anion $\text{Fe}(\text{CN})_6^{4-}$ was used to test for pinholes, although it also has some limited permeability, despite electrostatic repulsion or Donnan exclusion by the sulfonic acid sites in the polymer. The cation $\text{N,N,N-trimethyl-N-ferrocene-methyl-ammonium chloride}$ (FcTMA^+) has been previously used to study diffusion in Nafion (10), and it has been shown that electron self exchange does not play a role for this species within Nafion films. Uptake and transport of this ion in the polymer film occurs via the ionic clusters that form in the Nafion polymer. These clusters represent the principal pathway for transport of solvated ions in the film, and so this ion gives a measure of transport in these domains (24). Neutral molecules should be transported along the same pathways as the other ions, but obviously will not exhibit any ionic interactions that dominate their uptake in the film, and may also enter the interphase region of the Nafion structure (24). Hydroquinone (QH_2) was chosen because its structure and functional groups are somewhat similar to those of glucose, making it a reasonable model, and its electrochemistry is far less complex, making it much easier to study. Glucose was also evaluated in order to compare it to the hydroquinone model. Finally, ascorbic acid (AA) was examined since it is a common interfering species in biological samples (2, 3), and it could be studied in both its neutral and anionic form, providing a comparison with very little difference in molecular size and structure of the diffusing species.

Figure 2.2a demonstrates the typical relationship between current and rotation rate on membrane-coated electrodes. A Koutecky-Levich plot of i^{-1} versus $\text{rpm}^{-1/2}$ is shown in Figure 2.2b. The data is linearized, as expected based on equations [2.1]-[2.4], and the non-zero intercept indicates the magnitude of the permeability for each redox couple. Three curves are shown for 1 mM QH_2 with increasing film thickness. The slopes are parallel and give a solution diffusion coefficient of $5.0 \times 10^{-6} \text{ cm}^2/\text{s}$, in agreement with that obtained at a naked electrode. The intercepts increase with increasing film thickness, indicating the permeability is decreasing as anticipated. The cation FcTMA^+ exhibits a larger intercept value, indicating a lower permeability, and a different slope due to its solution diffusion coefficient. Data for glucose, obtained using a Au RDE of different area is also shown, and the Koutecky-Levich plot can be seen to be linear. Using values of ν (43) and D_s (44) from the literature an electron transfer number of 7 is obtained from the slope, in agreement with Larew and Johnson (44).

Plots of the Koutecky-Levich intercept *versus* film thickness were linear for each of the various redox couples. The intercepts of these plots were not statistically different than zero, on the basis of the standard deviation of the intercepts and the magnitude of the residuals for points on the curves. Consequently, there was no evidence for a limitation to mass or electron transfer at the film/solution interface. Figure 2.3 shows a plot of the permeability of QH_2 , P_m , determined from the intercept of the Koutecky-Levich plots, as a function of Nafion film thickness. The solid line shown is a fit to equation [2.5], and demonstrates that the effective diffusion coefficient is independent of film thickness over the range studied. These results confirm that the RDE can be used to determine the permeability of Nafion coatings, and so give effective diffusion coefficients when the film thickness is determined by ellipsometry.

Table 2.2 indicates the permeabilities and effective diffusion coefficients of glucose, hydroquinone, and FcTMA^+ in RT cured Nafion prepared from the commercial Nafion solution. A value is also given for ferrocyanide, however, as discussed below, it may reflect the pinhole density. The permeabilities and effective diffusion coefficients in RT cured

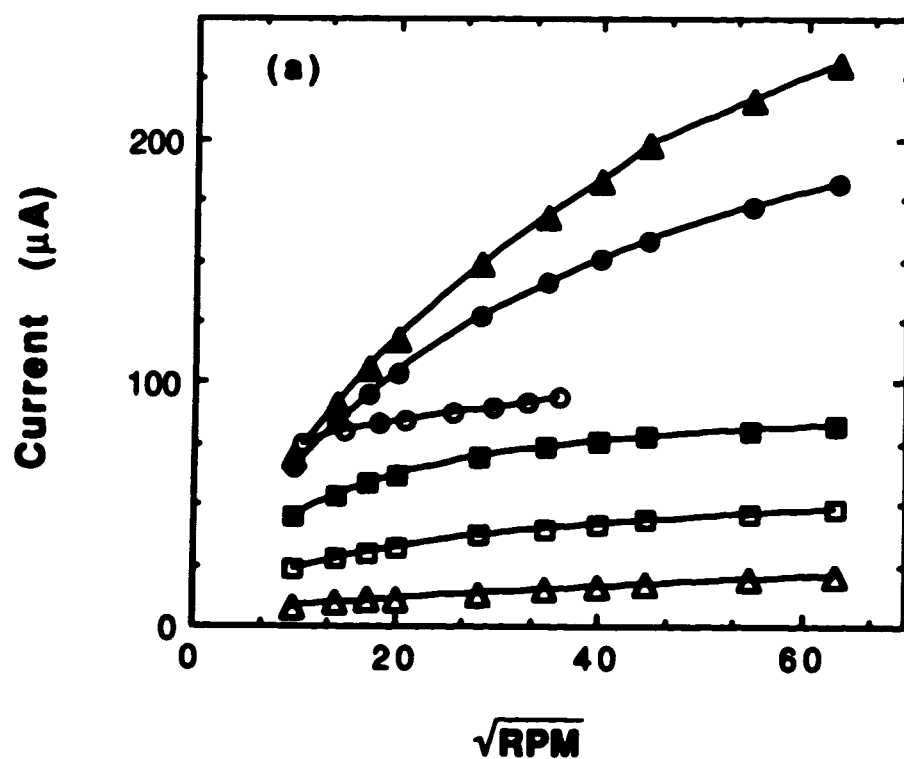


Figure 2.2a Levich plot of current *versus* rotation rate in rpm for several permeating species in Nafion films coated on Pt: 1 mM QH_2 through 65.8 nm film (▲), 111.4 nm film (●), 335.7 nm film (■); 1 mM FcTMA^+ through 65.8 nm film (□); 1 mM $\text{Fe}(\text{CN})_6^{4-}$ through 65.8 nm film (Δ). Data is also shown for 1 mM glucose transport through 128.6 nm of Nafion (○) coated on a Au electrode. Smooth curves were drawn for clarity.

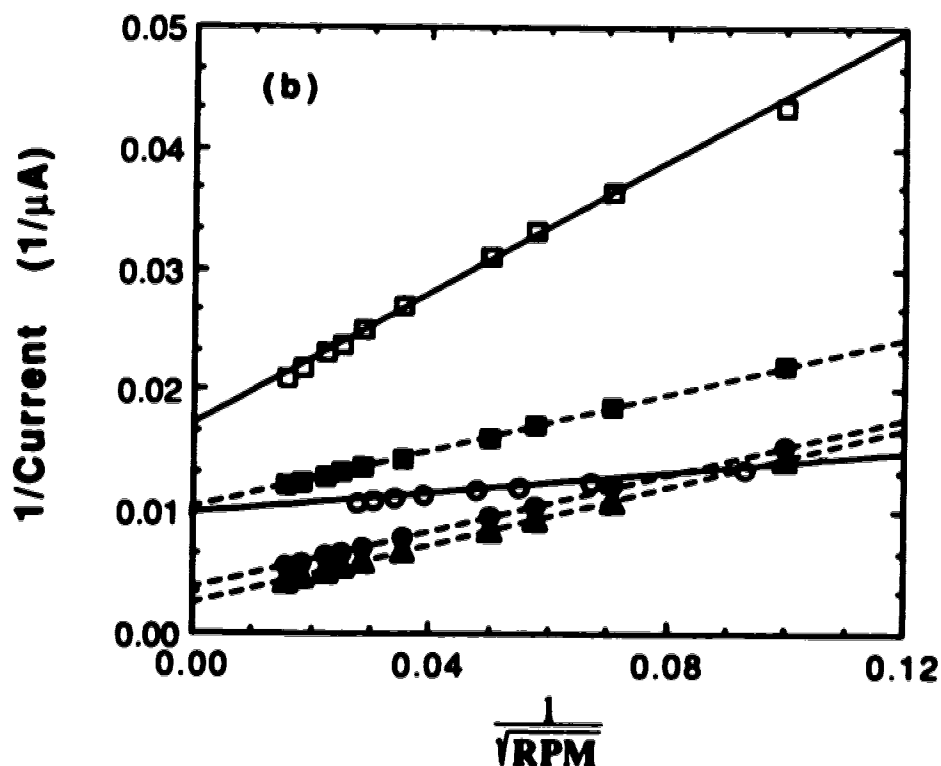


Figure 2.2b A Koutecky-Levich plot of the inverse of current *versus* the inverse of the square root of rotation rate ($\text{rpm}^{-1/2}$) for the same set of data in Figure 2.2a. The species and films again are: 1 mM QH_2 through 65.8 nm film (▲), 111.4 nm film (●), 335.7 nm film (■); 1 mM FcTMA^+ through 65.8 nm film (□); 1 mM glucose through 128.6 nm of film (○). Data for $\text{Fe}(\text{CN})_6^{4-}$ is not shown since their larger values of $1/i$ make others too small to be seen in the same figure. Straight lines were determined by least square linear regression.

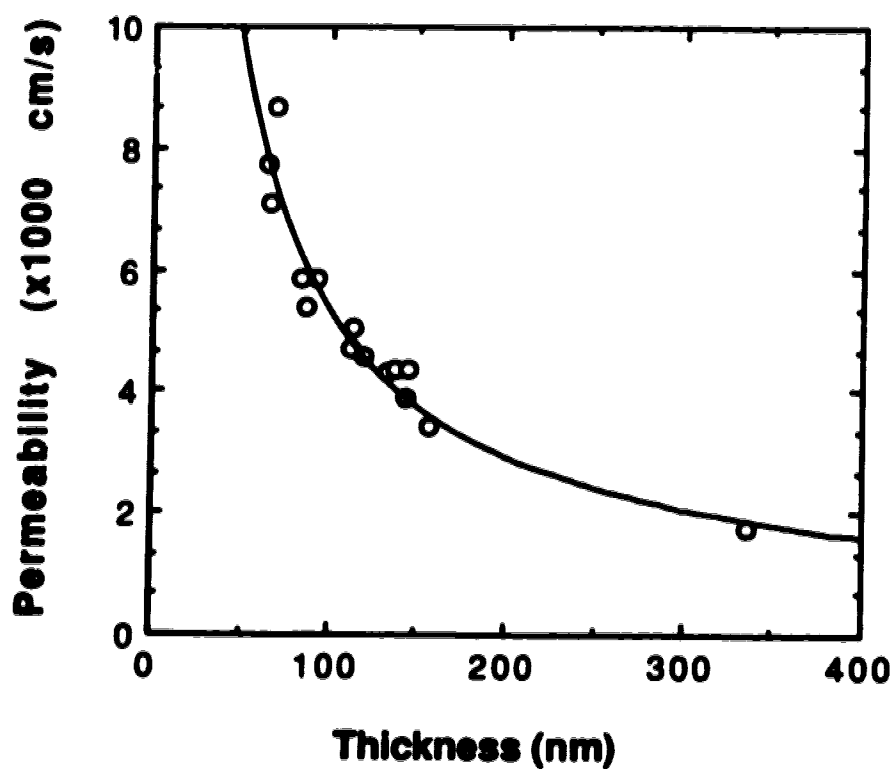


Figure 2.3 The experimental relationship (○) between the permeability of hydroquinone in Nafion and the coating thickness, and a theoretical curve obtained using equation [2.5] (solid line) and $D = 5.4 \times 10^{-8} \text{ cm}^2/\text{s}$ are shown. The Nafion was cast from aqueous alcohol and cured at room temperature.

Table 2.2 Effect of curing temperature on effective diffusion coefficients in recast Nafion films.^a

Substrate ^{b,c}	Effective diffusion coefficients ($\times 10^8 \text{ cm}^2/\text{s}$) ^d	
	Room temperature cure	120°C cure
glucose	3.4 ± 0.5	—
QH ₂	5.4 ± 0.5	2.6 ± 0.4
FcTMA ⁺	1.8 ± 0.5	1.1 ± 0.2
Fe(CN) ₆ ⁴⁻	$\leq 0.5 \pm 0.1^e$	$\leq 0.2 \pm 0.1^e$

- a) Films were cast from Solution Technologies' commercially available aqueous alcoholic solution.
- b) QH₂ is hydroquinone, FcTMA⁺ is a trimethylammonium substituted ferrocene (see text).
- c) Solution pH values varied, see experimental for electrolytes. Glucose pH 13, QH₂ pH 7.4, FcTMA⁺ and Fe(CN)₆⁴⁻ pH 7.
- d) The results are the average of 3 to 15 separate measurements.
- e) This is an upper limit, since this value likely reflects the presence of pinholes, as discussed in the text.

Nafion were measured most extensively for hydroquinone, and these are shown as a function of thickness and the number of coatings in Table 2.3. The concentration of the coating solution, the number of coatings applied, and the thickness determined by ellipsometry are also given. It can be seen that the film thickness is not proportional to the number of coating applications. The effective diffusion coefficient of ascorbate, and the effect of pH and supporting electrolyte on its αD_m are shown in Table 2.4.

It is noteworthy that the neutral compounds show a higher permeability than any of the ions studied, indicating differences in their transport through the polymer. Their much larger permeability relative to anions is clearly due to Donnan exclusion of the latter. The increased permeability relative to FcTMA^+ is more difficult to interpret, since several factors are involved. Differences in the extraction coefficient are likely to be very significant, since the cation is coulombically attracted to the Nafion matrix, while the neutral molecules probably have an extraction coefficient that is less than 10. In fact neutral ferrocene appears to have a value of α in Nafion relative to aqueous solution that is close to one (27). In contrast we obtain a value of 300 for FcTMA^+ , by comparison of αD_m and D_m measured with the rotating disk and chronoamperometric methods, respectively. This value of α means the difference in diffusion coefficients is even larger than the difference in αD_m . Differences in molecular size could play a role, but the greatest effect probably arises from the electrostatic interaction between the cation and the sulfonic acid sites in the ionic clusters (24), which enforce a form of site-to-site hopping (11) for the cations. It is also possible that the neutral molecules can permeate a larger volume of the polymer by entering the "interfacial zones" that are thought to exist between the fluorocarbon backbone phase and the ionic pockets in the polymer (24).

In evaluating the data in Tables 2.2-2.4 in detail several points must be considered. The values of αD_m for $\text{Fe}(\text{CN})_6^{4-}$ are surprisingly high. We have previously reported that thicknesses of 0.25 or 0.8 μm will reduce the $\text{Fe}(\text{CN})_6^{4-}$ cyclic voltammetric peak current to 1% or 0.1% of its value at a naked electrode, respectively (5). The αD_m of $0.53 \times 10^{-8} \text{ cm}^2/\text{s}$ obtained in this study indicates a thickness of at least 10 μm would be required to

Table 2.3 Permeability, thickness and effective diffusion coefficient for hydroquinone in Nafion cured at room temperature.^a

Nafion^b (coatings x conc.)	Permeability (x 10³ cm/s)	Thickness (nm)	αD_m (x 10⁸ cm²/s)
1 x 1%	8.67	69.2	5.99
1 x 1%	7.72	63.5	4.90
1 x 1%	7.10	65.8	4.66
2 x 1%	5.37	86.0	4.62
2 x 1%	5.84	83.0	4.84
4 x 1%	5.84	91.9	5.38
4 x 1%	4.56	118.7	5.41
10 x 1%	4.70	111.4	5.24
1 x 2%	4.38	138.0	6.06
1 x 2%	4.32	132.6	5.73
1 x 3%	5.06	112.9	5.72
2 x 3%	4.35	145.0	6.31
3 x 3%	3.40	156.9	5.33
4 x 3%	3.88	142.7	5.54
1 x 5%	1.74	335.7	5.83

a) Films were cast from commercial Solution Technologies' solution.

b) The number of coatings and the wt% concentration of the Nafion solution are given.

Table 2.4 Effect of pH and electrolyte on ascorbic acid diffusion in room temperature cured Nafion.^a

Electrolyte	Effective diffusion coefficient^b (x 10⁸ cm²/s)
pH 7.4 buffer	0.6 ± 0.1
0.1 M HCl	19 ± 7
0.05 M HCl	24 ± 7
0.05 M HCl, 0.1 M NaCl	20 ± 7

- a) Films were cast from commercial Solution Technologies solution.**
b) The results are the average of 2 to 4 separate measurements.

achieve these reductions in current. This discrepancy far exceeds the errors associated with the thickness measurement method we used previously. It is also much higher than the value for αD_m of 4×10^{-10} cm²/s reported for the trianion ferricyanide in solid Nafion (47). Consequently, we interpret the data for $\text{Fe}(\text{CN})_6^{4-}$ as an indication of the presence of pinholes in the polymer coatings. The apparent difference in pinhole density between this work and our previous study may reflect the fact that here we have used spin-coating methods, with only a limited number of coating applications. The results indicate that values of αD_m for other species will be distorted. Given the low currents observed for $\text{Fe}(\text{CN})_6^{4-}$ the error in αD_m will be less than 10% for QH_2 and other neutral species. However, at pH 7.4 the ascorbate anion exhibits an αD_m similar to that of ferrocyanide, which suggests that it too may be affected by the presence of pinholes.

We note that the values of D_m and α for FcTMA^+ are not in good agreement with the results of White *et al.* for 1 mM FcTMA^+ in Nafion with an equivalent weight per sulfonate, EW, of 970. The discrepancies may result from the difference in equivalent weights, which has been reported to have a significant effect on D_m for Dow perfluorinated ionomers (28). In addition the value of α near saturation of the film will decrease with increasing solution concentration (12), and our study was done at 7.3 mM.

Of necessity, glucose and QH_2 were studied at different pH values. A NaOH electrolyte was used to obtain satisfactory glucose kinetics at a Au electrode, while a pH of 7.4 was used to ensure QH_2 was in its neutral form. Diffusion coefficients in Nafion are a function of pH and electrolyte composition (24) and this makes a truly quantitative comparison between αD_m for the two compounds difficult. However, since transport in Nafion varies substantially only at high ionic strengths (24) the comparison should be satisfactory in this case. Given that the effective diffusion coefficient for glucose is 60% of that for QH_2 , we conclude that the neutral quinone is a reasonable model for glucose.

Comparison of the results for neutral AA with those for QH_2 suggests that appreciable differences exist between neutral molecules.

Again the comparison is not quantitative because of the difference in pH and electrolytes. The difference in pH is likely to be the greatest cause of any discrepancy, and so AA was evaluated at two different pH values. A comparison with NaCl as the electrolyte was also made since Na^+ is more strongly bound in Nafion than H^+ , so that any polymer swelling effects due to H^+ should have been minimized. As shown in Table 2.4 the results for AA were not sensitive to pH, or the concentration of NaCl, within the relatively large scatter obtained. This suggests the comparison in effective diffusion coefficients under these differing conditions of pH remains informative.

Solutions of Nafion can be purchased commercially or obtained by dissolving solid Nafion sheets. Since it has been suggested that these solutions are colloidal (14, 17) they may have history dependent properties, and so produce different film characteristics when used to cast films. To check this we prepared RT cured films from commercial solutions of EW 1100 Nafion obtained from Solution Technologies and Aldrich, as well as a solution of EW 1100 Nafion we dissolved. The effective diffusion coefficients measured in these films for QH_2 and FcTMA^+ were independent of the source of the polymer.

2.4.3 Effect of Solvent and Temperature on Permeabilities

It has been shown that solution-cast Nafion membranes are at least partially soluble in a variety of polar organic solvents and even water (13, 17), whereas the solid form commercially available is not. Martin and Moore have recommended that re-cast films be cured at elevated temperatures in the presence of high boiling point solvents, and shown that a temperature of about 130°C should be met or exceeded (13, 17). Michael and Wightman have recently stated that curing at 80°C using the original low boiling solvent gives sufficiently stable films (20). They also reported that redox couples in these films showed cyclic voltammetry closer to the ideal than in films prepared in DMF solutions and cured at 120°C or more, at least in the highly resistive solvent, supercritical CO_2 . However, the effect of these treatments on transport in Nafion has been

examined quantitatively only for very low concentrations of electroactive cations (28).

The simplest curing procedure involves casting solvent films at room temperature from the alcohol-water mixture Nafion is prepared in, and then curing at elevated temperatures. This method has some advantages if a component of the film is an enzyme, since aprotic organic solvents often promote denaturing. (Of course with an enzyme present the temperature range may also be severely restricted.) Figure 2.4 compares the stability of a film cast from the commercial Solution Technologies solution cured at room temperature, and at 120°C for 1 h. FcTMA⁺ was ion exchanged into the films, and cyclic voltammograms were recorded at 15 min. intervals in solutions free of the redox couple. Between scans the electrodes were resoaked in the FcTMA⁺ solutions. The shape of the cyclic voltammograms was not affected by the curing procedure. However, for room temperature cured films the peak currents and peak areas began to decrease after about 30 min., while those cured at 120°C exhibited a constant peak current over the period of the study. These results are consistent with loss of polymer cured at room temperature, as has been reported by Moore and Martin, and with substantially decreased solubility following curing, as suggested by Michael and Wightman. Our results indicate that the stability of Nafion films can be enhanced by curing at elevated temperatures without introducing an intermediate step involving the use of a high boiling point solvent. We can not say that the films prepared in this manner are completely insoluble, since the test we have used is not as rigorous as others (17).

The permeabilities and effective diffusion coefficients of QH₂, FcTMA⁺, and Fe(CN)₆⁴⁻ in Nafion films cured at 120°C are listed in Table 2.2. Comparison to the room temperature data in Table 2.2 shows that the effective diffusion coefficients decrease by a factor of about two for the compounds studied. The currents for the anion are much lower than for the other two species, so that for the latter two any current due to pinholes is only a small fraction of the total current. Therefore, the decrease in αD_m for QH₂ and the cation must be ascribed to changes in the bulk properties of the film, which is further supported by the fact αD_m changes

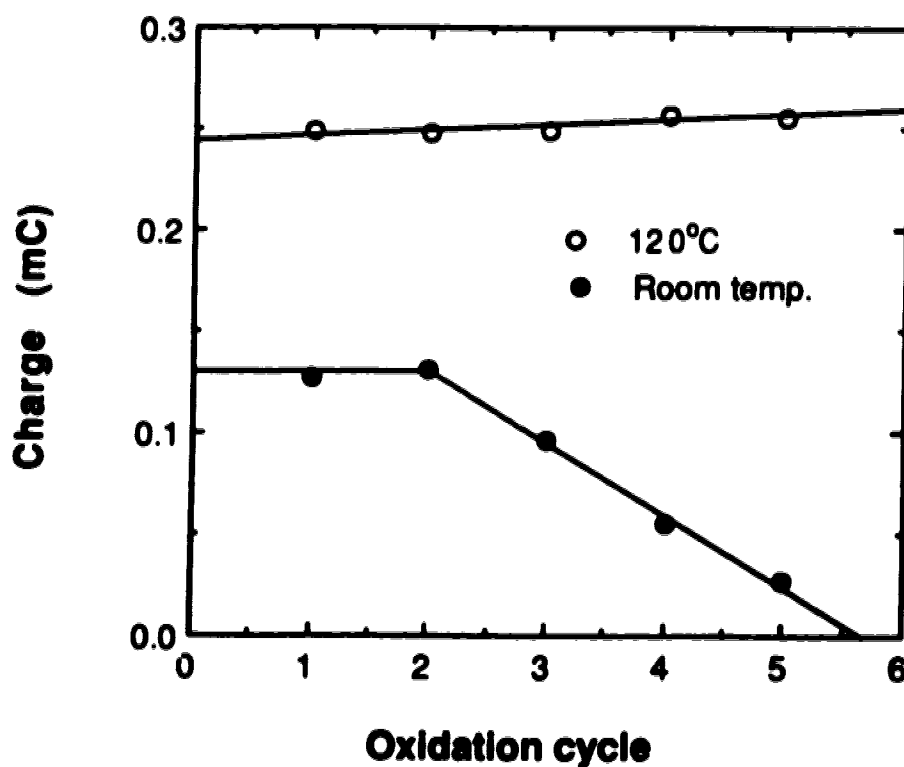


Figure 2.4 Comparison of the integrated anodic peak current for FcTMA⁺ in 0.1 M KCl in a membrane recast from aqueous alcohol solution, cured at room temperature (●), with a membrane cast from the same solvent and cured at 120°C (○), as a function of the number of test cycles. The electrode was soaked in 7 mM FcTMA⁺ between cycles in a 0.1 M KCl electrolyte. Each test cycle represents 15 min in aqueous solution.

by the same amount for both species. The effect of curing films cast from alcohol solutions at 80°C was also examined. For QH₂ a value of 3.84×10^{-8} cm²/s was obtained. This value is intermediate between the values for room temperature and 120°C cured films, and indicates a gradual change in permeability is effected with curing temperature. Curing has been suggested to reduce the disorder in the polymer (17), and may decrease the solvent uptake, and these effects could be expected to reduce the effective diffusion coefficients. A simple densification of the film can be ruled out since the film thicknesses were not changed within experimental error following curing at 120°C. Overall, the results indicate the films become less permeable as a result of curing, but ionic conductivity and transport in the film is not changed dramatically.

Replacing the low boiling alcohol component of solutions of Nafion with a high boiling solvent such as dimethylformamide (DMF) or dimethylsulfoxide before curing at elevated temperatures has been recommended, and studied in detail by several authors (13, 14, 17). We have evaluated the effect of using DMF as a solvent on the permeability of the films as a function of temperature. Films prepared from DMF solutions cured at room temperature were intended to establish the "baseline" behaviour, but yielded a surprising result. Table 2.5 shows that the use of DMF lowers αD_m twofold compared to films prepared from the alcohol solution (Table 2.2), even without curing at elevated temperatures. The change is equivalent to the effect of curing films prepared from alcohol at elevated temperature. Curing films cast from DMF at 120°C caused a further 2 to 4-fold decrease in permeability. The effect of curing at 130°C was also studied since Moore and Martin (17) have suggested there is a difference in the film solubility when prepared at 120 *vs* 130°C. However, we saw no further change in the permeability within experimental error.

Whiteley and Martin studied transport of FcTMA⁺ in recast Nafion cured at 180°C, and found that the diffusion coefficient increased on

Table 2.5 Effect of DMF on effective diffusion coefficients in Nafion.^a

Substrate ^b	Effective diffusion coefficient ($\times 10^8 \text{ cm}^2/\text{s}$)	
	Room temperature cure	120°C cure
QH ₂	2.7 ± 0.4	0.7 ± 0.2
FcTMA ⁺	1.6 ± 0.4	0.8 ± 0.3

a) Films were cast from dimethylformamide (DMF) as solvent.

b) Symbols, electrolytes and pH are the same as identified for Table 2.2.

curing at loadings of FcTMA⁺ of less than 1% per sulfonate equivalent (28). At 10% loading the results were independent of curing procedure. As discussed in the introduction the experimental conditions were significantly different than those used here. In fact Whiteley and Martin discuss the differences in transport mechanism with solution conditions extensively. It seems clear that the factors controlling transport rates are complex in Nafion, and will best be resolved by further experimentation.

2.5 Conclusions

Our results show that ellipsometry is an effective method for determining the thickness of Nafion and quaternized poly(vinylpyridine) coatings on Pt, Au, and Si substrates. The usefulness of the method for electrode geometries that are not well suited to profilometry measurements has been demonstrated.

The effect of thermally curing recast Nafion films on transport in the films is significant. Compared to films cast from aqueous alcohol solutions cured at room temperature, effective diffusion coefficients are reduced 4 to 8 fold on curing films cast from DMF at 120 to 130°C. The results indicate that the changes in crystallinity and order observed for the latter procedure have a substantial effect on transport in the films (13-15, 17). Comparing the data for films cured at 120°C with either aqueous alcohol or DMF as the casting solvents shows that the solvent must play a role in the polymer reorganization. Presumably this effect arises from both the solvating strength, or plasticizing efficiency, of the solvent, and from differences in the percent of solvent retained in the film at a given temperature. It is noteworthy that the magnitude of the decrease in diffusion rates can be controlled by the choice of casting solvent and curing temperature, allowing the transport properties of a film to be tailored by the film preparation procedure.

The reduction in effective diffusion coefficients observed when room temperature cured films were cast from DMF instead of alcoholic solutions is surprising. It indicates that considerable differences can be induced in the film morphology by the solvent even at room temperature.

The effect may arise from differences in the form of the Nafion colloid in solution (14, 17), the efficiency of plasticizing of the film by the solvent during drying, or the role of hydration in the curing process when using the aqueous alcohol solvent.

Neutral molecules permeate recast Nafion films significantly, and appear to diffuse much more rapidly than cations of similar size. High temperature curing causes some change in the permeability of the neutrals and cations studied relative to each other, but the changes relative to room temperature curing are more significant. From the perspective of sensor design these results indicate that using thermal curing or "solution processing" (13, 17) to enhance Nafion film stability will affect the design parameters. For a constant thickness the permeability will decrease, thus decreasing the sensitivity to the substrate and increasing the response time. However, these changes occur in a predictable fashion, and could in fact be used to fine tune sensor characteristics.

2.6 References

1. Murray, R. W. in *Electroanal. Chem. Vol. 13*; Bard, A. J., Ed.; Marcel Dekker: New York, 1984, 191-368.
2. Gerhardt, G. A.; Oke, A. F.; Nagy, G.; Moghaddam, B.; Adams, R. N. *Brain Res.* 1984, 290 , 390-395.
3. Kristensen, E. W.; Kuhr, W. G.; Wightman, R. W. *Anal. Chem.* 1987, 59, 1752-1757.
4. Hoyer, B.; Florence, T. M. *Anal. Chem.* 1987, 59 , 2839-2842.
5. Harrison, D. J.; Turner, R. F. B.; Baltes, H. P. *Anal. Chem.* 1988, 60, 2002-2007.
6. Hoyer, B.; Loftager, M. *Anal. Chem.* 1988 , 60 , 1235-1237.
7. Enea, O. *J. Electrochem. Soc.* 1988 , 135 , 1601-1602.
8. Matsue, T.; Akiba, U.; Osa, T. *Anal. Chem.* 1988, 58 , 2096-2097.
9. Wang, J.; Tuzhi, P. *Anal. Chem.* 1988, 58 , 3257-3261.
10. White, H. S.; Leddy, J.; Bard, A. J. *J. Am. Chem. Soc.* 1983, 104 , 4811-4817.

11. Buttry, D. A.; Anson, F. C. *J. Am. Chem. Soc.* **1983**, *105* , 685-689.
12. Whiteley, L. D.; Martin, C. R. *Anal. Chem.* **1987**, *59* , 1746-1751.
13. Moore, R. B.; Martin, C. R. *Anal. Chem.* **1986**, *58* , 2569-2570.
14. Gebel, G.; Aldebert, P.; Pineri, M. *Macromolecules* **1987**, *20* , 1425-1428.
15. Redepenning, J.; Anson, F. C. *J. Phys. Chem.* **1987**, *91* , 4549-4553.
16. Gottesfeld, S.; Raistrick, I. D.; Srinivasan, S. *J. Electrochem. Soc.* **1987**, *134* , 1455-1462.
17. Moore, R. B.; Martin, C. R. *Macromolecules* **1988**, *21* , 1334-1339.
18. Rubinstein, I.; Bard, A. J. *J. Am. Chem. Soc.* **1981**, *103* , 5007-5013.
19. Lopez, M.; Kipling, B.; Yeager, H. L. *Anal. Chem.* **1976**, *48* , 1120-1122.
20. Michael, A. C.; Wightman, R. M. *Anal. Chem.* **1989**, *61* , 2193-2200.
21. Turner, R. F. B.; Harrison, D. J.; Rajotte, R. V.; Baltes, H. P. *Sens. Actuators* **1990**, *B1* , 561-564.
22. Turner, R. F. B.; Harrison, D. J.; Rajotte, R. V. *Biomaterials* **1991**, *12* , 361-368.
23. Sikdar, S. K. *J. Membrane Sci.* **1985**, *23* , 83-92.
24. Eisenberg, A.; Yeager, H. L., Ed., *Perfluorinated Ionomer membranes* , ACS symposium series 180, American Chemical Society: Washington, D. C. **1982**.
25. Ogumi, Z.; Takehara, Z.; Yoshizawa, S. *J. Electrochem. Soc.* **1984** , *131* , 769-773.
26. Sakai, T.; Takenaka, H.; Torikai, E. *J. Electrochem. Soc.* **1986**, *133* , 88-92.
27. Rubinstein, I. *J. Electroanal. Chem.* **1984**, *176* , 359-362.
28. Whiteley, L. D.; Martin, C. R. *J. Phys. Chem.* **1989**, *93* , 4650-4658.
29. Lawson, D. R.; Whiteley, L. D.; Martin, C. R. *J. Electrochem. Soc.* **1988**, *135* , 2247-2253.
30. Gough, D. A.; Leyboldt, J. K. *Anal. Chem.* **1979**, *51* , 439-444.
31. Leddy, J.; Bard, A. J.; Maloy, J. T.; Savéant, J. M. *J. Electroanal. Chem.* **1985**, *187* , 205-227.
32. Carlin, C. M.; Kepley, L. J.; Bard, A. J. *J. Electrochem. Soc.* **1985**, *132* , 353-359.

33. Collins, R. W.; Kim, Y.-T. *Anal. Chem.* **1990**, *62* , 887A-900A.
34. Kruger, J.; Hillman, A.R. *J. Electrochem. Soc.* **1988**, *135*, 2517-2524.
35. Kruger, J. in *Advances in Electrochemistry and Electrochemical Engineering*, Ed. Delahay, P.; Tobias, C.W., John Wiley and Sons; New York, **1973**, Vol. 9, 227-280.
36. Bard, A. J.; Faulkner, L. R. *Electrochemical methods, fundamentals and applications* , Wiley: New York, **1980**.
37. Kuo, K.; Murray, R. W. *J. Electroanal. Chem.* **1982**, *131*, 37-60.
38. Martin, C. R.; Rhoades, T. A.; Ferguson, J. A. *Anal. Chem.* **1982**, *54* , 1639-1641.
39. Shiu, K. K.; Harrison, D. J. *J. Electroanal. Chem.* **1989**, *262* , 145-160.
40. Lainer, V. I. *Modern Electroplating* , Keter Preccs: Jerusalem, **1970**, 262.
41. Szentirmay, M. N.; Campbell, L. F.; Martin, C. R. *Anal. Chem.* **1986**, *58* , 661-662.
42. Adams, R. N. *Electrochemistry at solid electrodes* , Marcel Dekker, Inc.: New York, **1969**, 219.
43. Weast, R. C., Ed. *C. R. C. Handbook of chemistry and physics* , 59th Ed., CRC Press, Inc., **1978/1979**, D-289, D-299, F-62, D-303, D-202.
44. Larew, L. L.; Johnson, D. C. *J. Electroanal. Chem.* **1989** , *262* , 167-182.
45. Finklea, H. O.; Robinson, L. R.; Blackburn, A.; Richter, B.; Allara, D.; Bright, T. *Langmuir* **1986**, *2* , 239-244.
46. Gray, D. E., Ed. *American Institute of Physics handbook* , 3rd Ed., McGraw-Hill Book Co., **1972**, 6-244, 6-136.
47. DeWulf, D.; Bard, A. J. *J. Macromol. Sci-Chem.* **1989**, *A26*, 1205-1209.

Chapter 3

Micromachined Capillary Electrophoresis Systems: Fabrication, Cross Injectors, and Rapid Separation.[†]

3.1 Introduction

Most successful analyses in the laboratory involve a complete *system* of sample treatment, separation and analysis, designed to circumvent the complexities of a sample and its matrix. These methods are often time consuming or labor intensive. To overcome this, the analysis process may be automated, increasing its speed, precision and reproducibility. The use of flow injection analysis (FIA), and its coupling to separation methods such as gas or liquid chromatography, or selective chemical sensors is one route to achieve this. High levels of automation have resulted in total chemical analysis systems (TAS) that can be used to monitor chemical concentrations continuously in industrial chemical and biochemical processes [1-3]. The miniaturization of a TAS onto a monolithic structure could produce a device (a μ -TAS) that would resemble a sensor in many ways [4-9]. Such a device could be configured as a dip-type probe, giving out a reading for the analyte of interest, so that it behaved as a sensor from the perspective of the user. Separation methods such as liquid chromatography and capillary electrophoresis, as well as other

[†] A version of this chapter has been accepted for publication as:

Zhonghui H. Fan, D. Jed Harrison, "Micromachining of Capillary Electrophoresis Injectors and Separators on Glass Chips and Evaluation of Flow at Capillary Intersections", *Analytical Chemistry*, January, 1994.

bench-top analytical approaches such as FIA may also benefit from the μ -TAS approach. It has been made clear that smaller dimensions result in improved performance for these analytical methods [10-13]. The benefits of miniaturization, though, are complicated by problems of detection, and dead volumes associated with coupling capillaries to detectors and injectors. Several authors have noted that the use of microlithographic techniques to fabricate systems would be beneficial [13-15]. The ease of fabrication of small structures should facilitate coupling of capillary separation systems to each other for 2-dimensional separations, or to injectors and detectors, with minimum dead volume. Increased speed of analysis, decreased sample and solvent consumption, or increased detector efficiency could also be realized, as have been discussed in detail elsewhere (4,5).

Micromachining of silicon or other planar materials provides a path to development of liquid phase μ -TAS devices [16]. The combination of microlithography with isotropic and anisotropic etching techniques, as well as controlled thin film deposition, allows for the fabrication of micron scale, three-dimensional structures [17-22]. Terry *et al.* [17] developed a gas chromatograph on a silicon wafer, but there have been relatively few extensions of this technology to solution phase systems. Bergveld's group have designed micron-scale coulometric titration systems [23], and Shoji *et al.* [24] have developed a dissolved O_2 sensor based on a micromachined device. Both of these systems are based on the pH sensitive field effect transistor (pH FET), but because the FET is integrated as a part of system they offer better performance than the stand-alone pH FET does. A micro-machined liquid chromatograph has been reported, and the theoretical behavior of such a system discussed, but no data from the system has been presented [25].

Capillary electrophoresis (CE) has been chosen as a separation method to be coupled with FIA on a planar substrate to explore the μ -TAS concept, as discussed in Chapter 1. CE provides a route to very rapid sample injection and separation schemes, since very short separation distances can be achieved using lithographic fabrication techniques. Very rapid separations are of general interest, but have specific application if

the integrated CE device is intended to compete with a chemical sensor, or be used as the second stage of a two dimensional separation scheme (26). This chapter will report a 3 second separation of amino acids on a device with dimensions of 1 x 2 cm.

The integrated injector design reported previously (6-8) was based on straightforward electrokinetic injection of the sample into the separation channel, but is subject to biasing of the sample composition due to differences in the electrophoretic mobilities of sample components (27). In a manifold of integrated capillaries it should prove possible to design injectors that inject a well-defined sample volume that is defined geometrically within the structure. As a consequence, electrokinetic biasing of the sample composition could be eliminated. The simplest of such designs is the intersection defined by the crossing of two perpendicular capillaries, for which, simplistically, the intersection volume would define the injection volume (9). The behavior of such an injection design is reported here.

It has been shown that fluid flow in a manifold of intersecting capillaries can be directed in the desired manner by the appropriate application of potentials to various channels in the manifold (6, 7). This valveless control of fluid flow is subject to leakage between channels at the intersection points due to diffusive effects (7). However, we have also observed some evidence for a convective contribution to leakage. This issue is of considerable importance to understanding the behavior of fluid flow in the integrated CE devices. The evidence will be presented here that leakage at intersections is largely due to hydrodynamic effects, which lead to convective flow from side channels into a channel in which electro-osmotic flow has been induced.

While μ -TAS devices reported previously were fabricated under contract using a commercially available microlithographic process, the devices used in the experiments described in this chapter were made by ourselves. The studies on selecting the glass type and on device fabrication process, and the detailed procedures will be presented here. In addition, the possible advantage of using a planar glass structure with

high thermal conductivity and mass relative to air and fused silica capillaries is also examined.

3.2 Experimental Section

3.2.1 Device Fabrication

Figure 3.1 shows the layout and dimensions of the glass devices studied, which consisted of two capillary channels intersecting at right angles. For device Airport-30 both channels were 30 μm wide, while for device Airport-70 the shorter channel was 70 μm wide and the longer channel was 30 μm wide. A few devices, Airport-70:70, were prepared with both channels 70 μm wide. The short channel between reservoirs 1 and 2 was used to supply sample solutions while the long channel was used for separations. A cover plate, with 0.3 mm holes drilled ultrasonically (Bullen Ultrasonics, Cincinnati) to provide channel access points, was thermally bonded to a glass plate in which channels were etched (6).

Devices were fabricated at the Alberta Microelectronic Centre (AMC) using a modification of bulk silicon micromachining methods (16, 28), following the steps illustrated in Figure 3.2. Glass plates (2" x 2", 3" x 3", or 1.5" x 3") were used as received, thermally annealed, or polished mechanically before proceeding. They were cleaned ultrasonically in detergent (5% Sparkleen, Fisher Scientific), methanol (Reagent Grade), acetone (Semiconductor Grade, Olin Hunt, NJ) and deionized water in an ultrasonic bath in a class 100 clean room environment. A H_2SO_4 , H_2O_2 etch was also used on occasion. A metal mask, nominally consisting of 200 Å Cr and 1000 Å Au was evaporatively deposited under vacuum ($<10^{-6}$ torr), and trace organics were then removed in H_2SO_4 , H_2O_2 mixture (3 volumes of 98% H_2SO_4 : 1 volume of 40% H_2O_2). A 1.4 μm thick positive photoresist (Waycoat HPR 504, Olin Hunt) was spin-coated on the metal with a Solitec photoresist coater/developer (3500 rpm), then soft-baked at 110°C for 5 min, as illustrated in Figure 3.2a.

Photomask layout was performed on a Princess CAD system, SUN

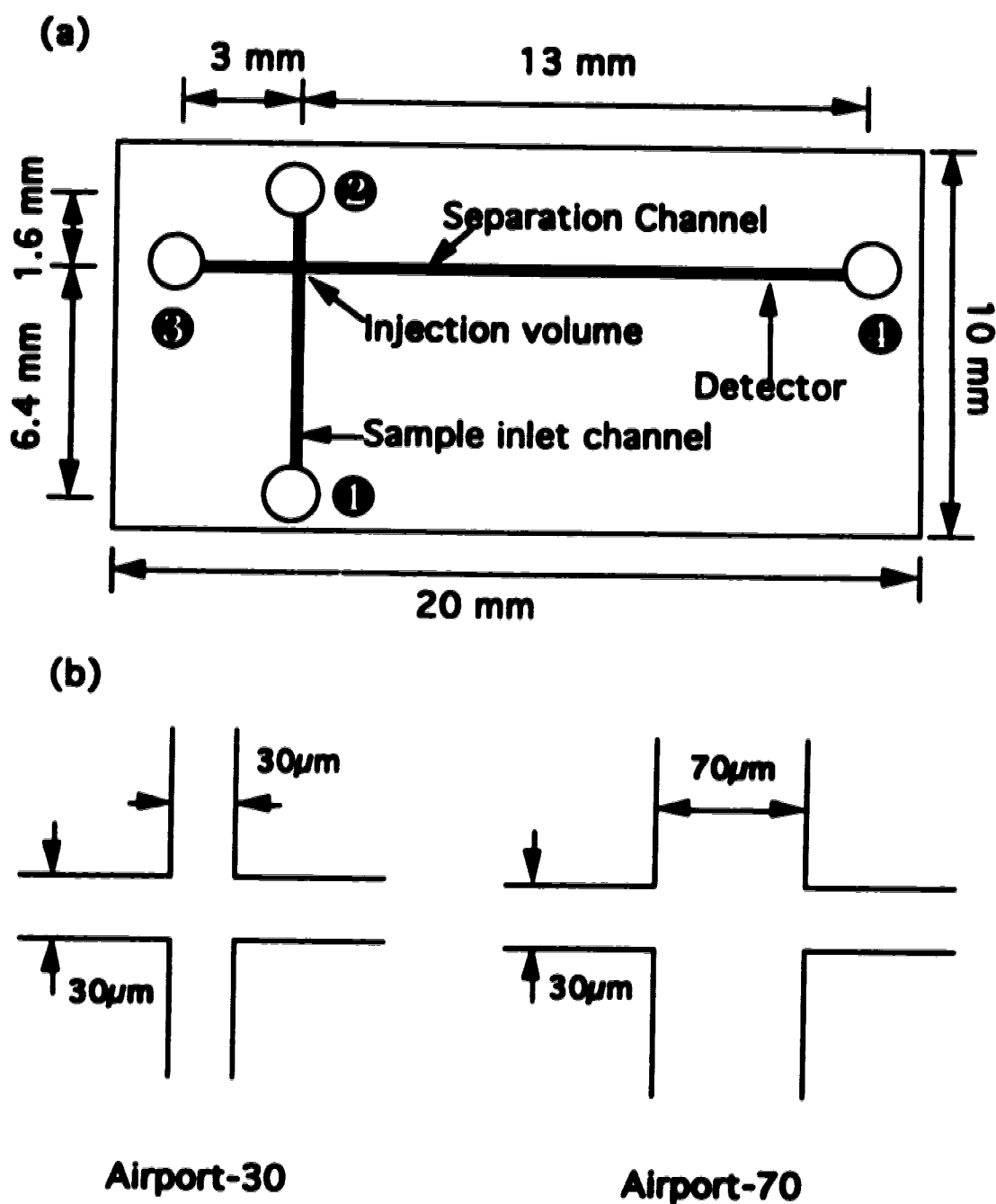


Figure 3.1 (a) Dimensions and layout of the various Airport devices are shown. Channels were 10 μ m deep. The reservoirs are numbered for reference in the text. (b) The intersection dimensions for Airport-30 and Airport-70.

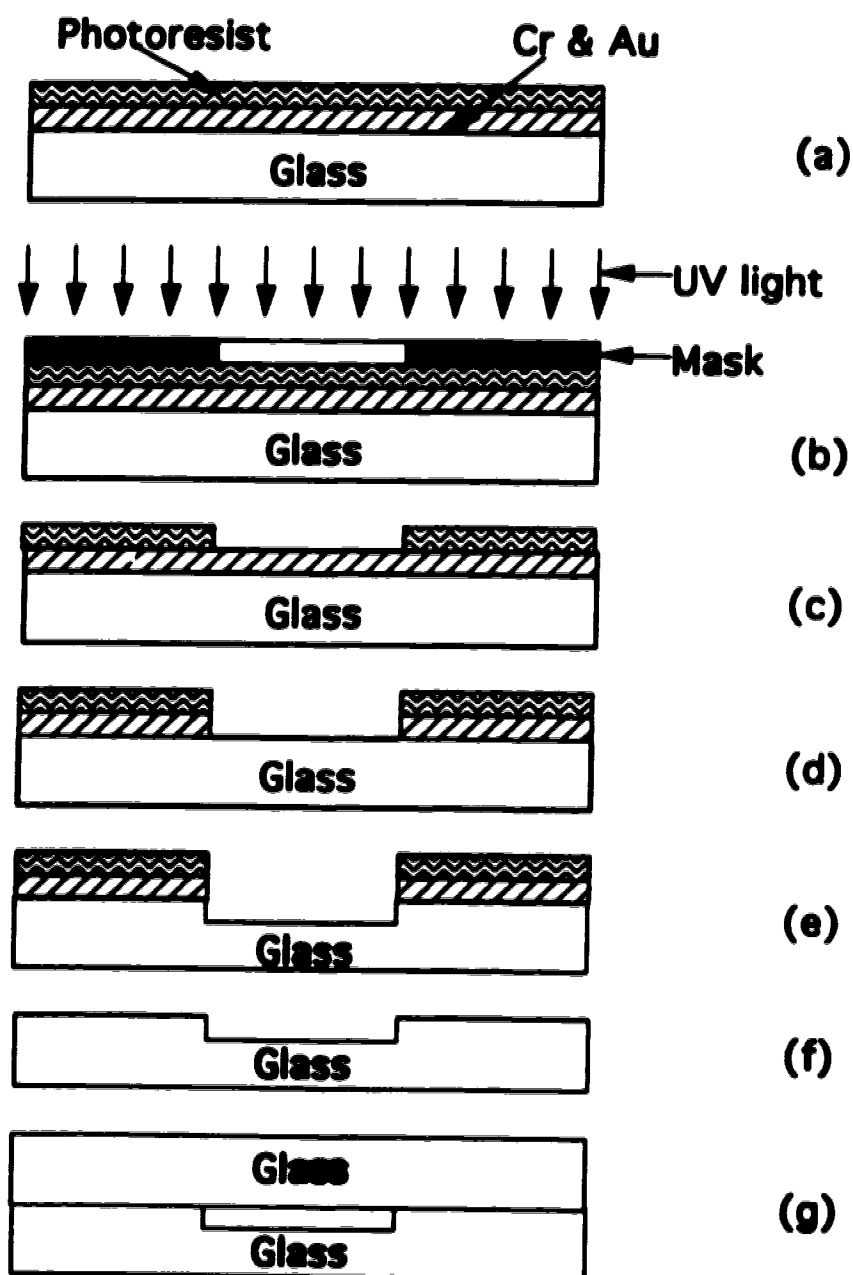


Figure 3.2 The sequence of photolithographic fabrication is shown: (a) Cr and Au masked glass plate is coated with photoresist; (b) Sample is exposed to light through a master mask; (c) Photoresist is developed; (d) Exposed metal mask is etched; (e) Exposed glass is etched; (f) Resist and metal are stripped; (g) Glass cover plate is bonded to form capillary.

3/160 Workstation, and the master mask was manufactured by Precision Photomask (Montreal, Canada). A Quintel contact mask aligner was used to expose the photoresist, Figure 3.2b, and Microposit 354 (Shipley, Newton, MA) was used as the developer to obtain a 10 or 50 μm line-width for channel definition, Figure 3.2c. Following a hard-bake at 120°C, 5 min, the metal layer was etched away with *aqua regia* and a commercial Cr etch (KTI Chemicals, Sunnyside, CA), Figure 3.2d.

The photoresist was not removed from the remaining metal layer, so as to reduce the impact of pinholes in the metal. The exposed glass was etched in a slowly stirred mixture of concentrated $\text{HF}:\text{HNO}_3:\text{H}_2\text{O}$ (20:14:66) (29), or a commercial buffered oxide etch (BOE 10:1, Olin-Hunt), Figure 3.2e. The channel depth during etching was monitored with an Alpha-step profilometer (Tencor Ind., Mountain View, CA) to establish the etch rate, and was then controlled by timing the etch period. The photoresist and metal masks were then removed with the etches described above, Figure 3.2f.

The etched glass plate was cut into individual 1 x 2 cm die using a Model 1100 wafer saw (Microautomation, Fremont, CA) with a spindle speed of 20,000 rpm, cutting speed of 0.64 mm/s, and a depth increment of 0.51 mm.

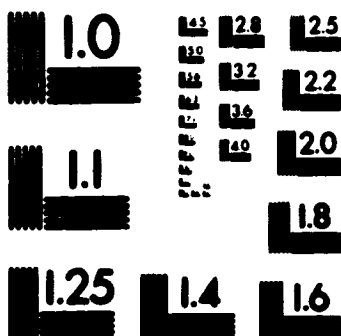
The etched plate and the cover plate were cleaned as described above, aligned under a microscope and thermally bonded in a Model 6-525 programmable furnace (J.M. Ney Co., Yucaipa, CA), Figure 3.2g. The temperature program was: 40°C/min to 550°C for 30 min total, 20°C/min to 610°C for 30 min, 20°C/min to 635°C for 30 min, 10°C/min to 650°C for 6 h, followed by natural cooling of the furnace to room temperature. Unbonded regions were evidenced by interference fringes and differences in optical clarity. The bonding cycle was repeated once or twice with weights (~90 g) placed over poorly bonded regions.

3.2.2 Apparatus

The block diagram in Figure 3.3 illustrates the apparatus used for the experiments reported here. FUG Elektronik Model HCN 2000 and

2

PM-1 3½"x4" PHOTOGRAPHIC MICROCOPY TARGET
NBS 1910a ANSI/ISO #2 EQUIVALENT



PRECISIONSM RESOLUTION TARGETS

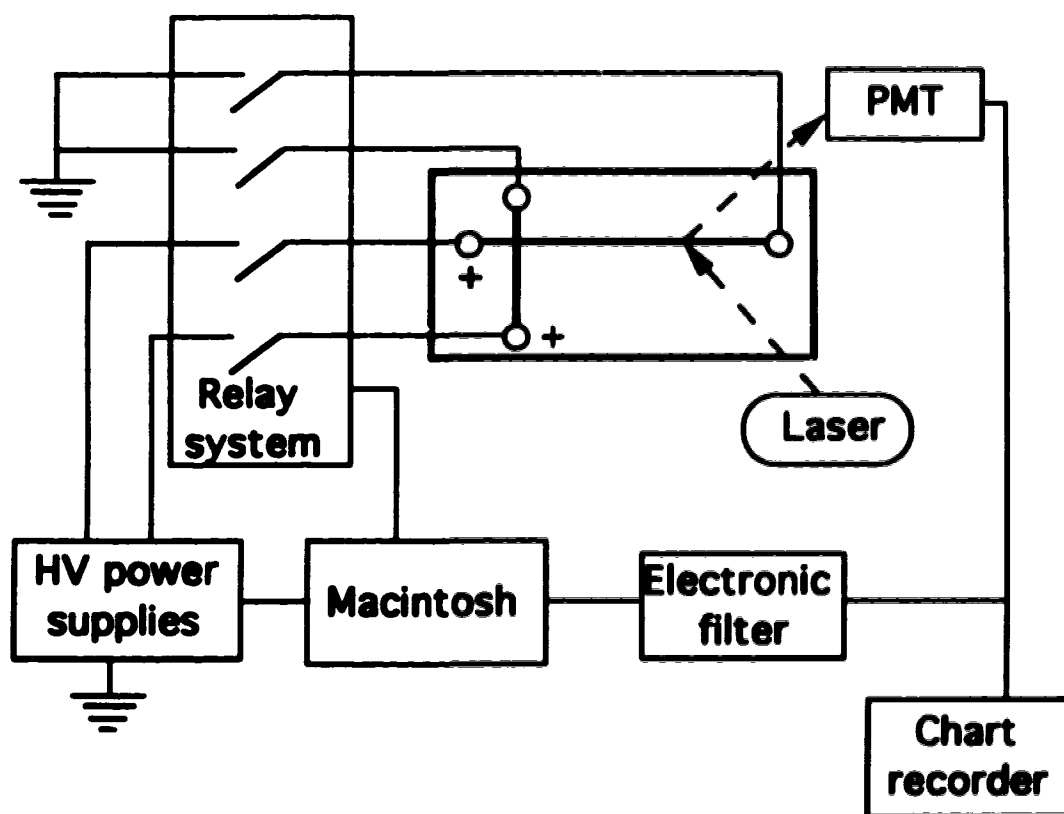


Figure 3.3 Block diagram of the high voltage relay controlled system for the capillary electrophoresis power supplies, with computer control and digital data acquisition of laser excited (488 nm) fluorescence.

HCN 12500 high voltage (HV) power supplies (Rosenheim, Germany) were connected with the electrodes in the device reservoirs via a relay system (Control 488/16, IOtech Inc., Cleveland, OH). Both HV power supplies and the relay system were controlled by a Macintosh IIfx computer with a NB-MIO-16 board (National Instruments Corp., Austin, TX). A 488 nm air-cooled argon ion laser (Uniphase/Ionics Model 2011) was used to excite fluorescence after focussing to about a 40 μm spot size in the device channel. The fluorescence emission was collected with a 7:1 microscope objective and directed onto a photomultiplier tube using a 100 μm slit at the image plane and an optical band pass filter (508 to 533 nm) as described elsewhere (7). The emission signal was electronically filtered with a Krohn-Hite Model 3342 6-pole Butterworth filter with a 200 Hz low pass cut-off frequency. The current in the channels was monitored from the potential drop across a 10 kW resistor located between the channel reservoir and the power supply ground, and recorded on a strip chart recorder. The peak parameters, such as area and the number of theoretical plates, were calculated using statistical moments analysis. Labview programs (National Instruments Corp., Austin, TX) written locally were used for calculations, data acquisition and instrument control.

3.2.3 Materials and Reagents

Corning 7740 (Pyrex) was obtained from I.G.S. (Sunnyvale, CA) and Paragon Optical Co. (Reading, PA). Corning 7059 was a gift from Corning Glass. Schott B270 and Tempax were gifts from John's Scientific (Toronto, ON), and Fisher 12-550C microscope slides (7.5 x 5.0 cm) were from Fischer Scientific. Some of the Pyrex glass was annealed at 570°C for 6 h.

Amino acids, fluorescein and fluorescein-5-isothiocyanate (FITC) were used as received (Sigma), as was fluorescein sulfonic acid (Molecular Probes, Eugene, OR). A pH 8.0 buffer of 0.05 M boric acid, 0.05 M tris(hydroxymethyl)amino methane (tris), as well as a pH 7.0 buffer (0.1 M in sodium salts of phosphate) were used. All chemicals were reagent grade; deionized, doubly-distilled water was used for all solutions.

Solutions were filtered using 0.22 μm pore size Miller-GV sterile filter units (Millipore, Bedford, MA) before injecting into the capillaries.

3.2.4 Procedures

Fluorescent labelling of amino acids with FITC followed the method of Sweedler *et al* (30). Five volumes of 10 mM single amino acid in the pH 8.0 buffer was mixed with 1 volume of 10 mM FITC in 95% acetone, 5% water, with 0.001% pyridine. The reaction took place overnight at room temperature, in the dark. The solutions were then diluted with the running buffer to the required concentration. Amino acid concentrations are given as the concentration of labelled acid, assuming complete reaction occurred.

Solutions were degassed with He to decrease problems with bubbles in the channels. Buffer was introduced by microsyringe into one reservoir and then flushed until all channels were filled. Fine Pt wires were insulated using glass sleeves and were inserted into the four reservoirs on the devices. Fluorescent samples were usually introduced through reservoir 1 (see Figure 3.1), and a potential was applied between reservoirs 1 and 2 (or 4) to drive the dye into the channels. After the potential applied to reservoirs 1 and 2 was turned off, another potential was applied between reservoir 3 and 4 to drive the sample at the intersection into the separation channel. The detector was aligned with dye present in the region of detection.

3.3 Results and Discussion

3.3.1 Device Fabrication

Both the type of glass and its pretreatment had a significant effect on the quality of results obtained by etching. Various borosilicate glasses were examined with differing results, as evidenced in Table 3.1. A "good" etch quality refers to results such as shown in Figure 3.4a and "poor" to results such as in Figure 3.4b. Even within one glass type (Corning 7740

Table 3.1 Etch Quality of Several Types of Glass.

Glass Type	Etchants	Etching Rate ($\mu\text{m}/\text{min}$)	Etch Quality
Pyrex I^(a)	HF:HNO₃	0.5	good
Pyrex II^(b)	HF:HNO₃	0.8	poor
Pyrex III^(c)	HF:HNO₃	0.5	good
Corning 7059	HF:HNO₃	5.0	good
Tempax	HF:HNO₃	0.5	some defects
Schott B270	HF:HNO₃	3.5	poor
Schott B270	BOE 10:1^(d)	0.4	poor
Microscope slides	HF:HNO₃	3.5	poor

- (a) Pyrex I was manufactured by Corning Glass to 2 mm thickness.
- (b) Pyrex II was polished to 2 mm thickness by I.G.S. or Paragon Glass.
- (c) Pyrex III was type II, following annealing at 570°C.
- (d) BOE is a commercial, buffered oxide etch (Olin-Hunt).

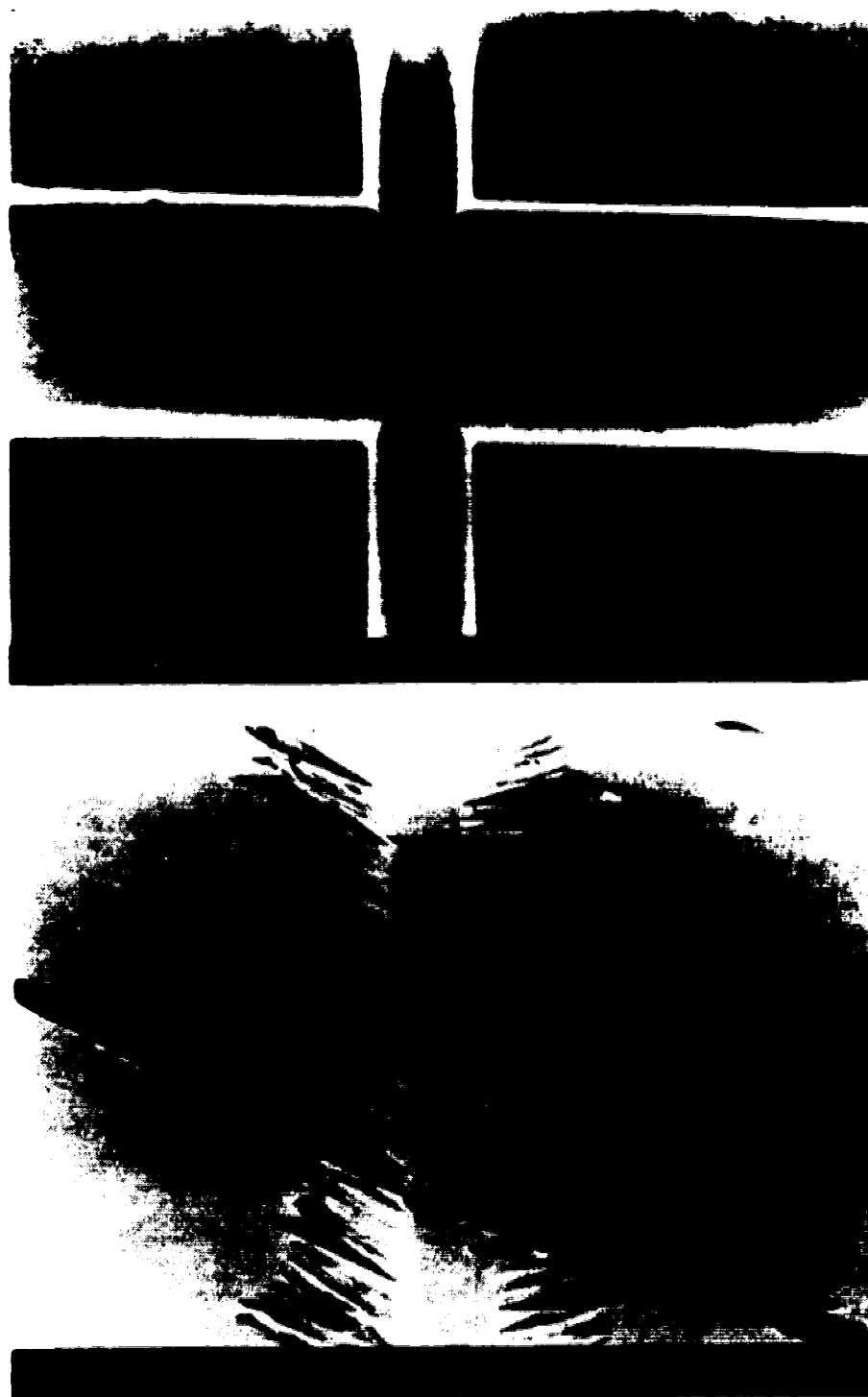


Figure 3.4 Electron micrographs of Airport-70 fabricated in (a) Type I Pyrex and (b) Type II Pyrex (not annealed).

Pyrex) the results depended on whether the glass was annealed after mechanical polishing. Figure 3.4 compares the etch quality of Pyrex I and Pyrex II. Pyrex II was polished to a 2 mm thickness, while Pyrex I was manufactured by Corning with a nominal 2 mm thickness. Annealing of Pyrex II gave a material, Pyrex III, which etched as well as Pyrex I. Subsequent re-polishing of Pyrex III again gave poor quality etching, suggesting mechanical stresses were introduced that could be relieved by annealing. Different etching solvents might produce different results, but did not within the selection we studied. Pyrex I was used for the work described below, except where noted, although we have had equal success with Pyrex III in subsequent studies.

Glass is etched isotropically, so that the metal mask is undercut during the etching step (29), giving curved side walls and a flat bottom, as illustrated in Figure 3.5. The degree of undercutting, specified by the ratio of the horizontal distance of etch back under the mask to the vertical etch depth, was close to 1:1. For a photomask feature width of 10 μm and a 10 μm etch depth this gave channels 30 μm wide at the surface, while a mask width of 50 μm gave a 70 μm wide channel.

With a commercially fabricated device we found that 30 μm channels were not distorted by the thermal bonding process, but 1 mm wide channels tended to collapse (6). With Pyrex I and III bonding occurred at 640°C, but the 30 μm channels collapsed at 700°C. At a temperature of 650°C bonding was effective and even 2 mm wide channels (10 μm deep) did not collapse.

3.4.3 Electrical Characteristics

The linear range of the current-voltage curves in Airport-70:70, with all channels 70 μm wide and 10 μm deep, extended up to about 2500 V/cm when using a low conductivity pH 8.0 buffer. This is an order of magnitude greater field than is typically used in CE, although Monnig and Jorgenson have used similar fields in a small capillary (15). Figure 3.6 shows the current-voltage curves obtained in Airport-70:70 with potentials applied between various pairs of reservoirs. Deviation from

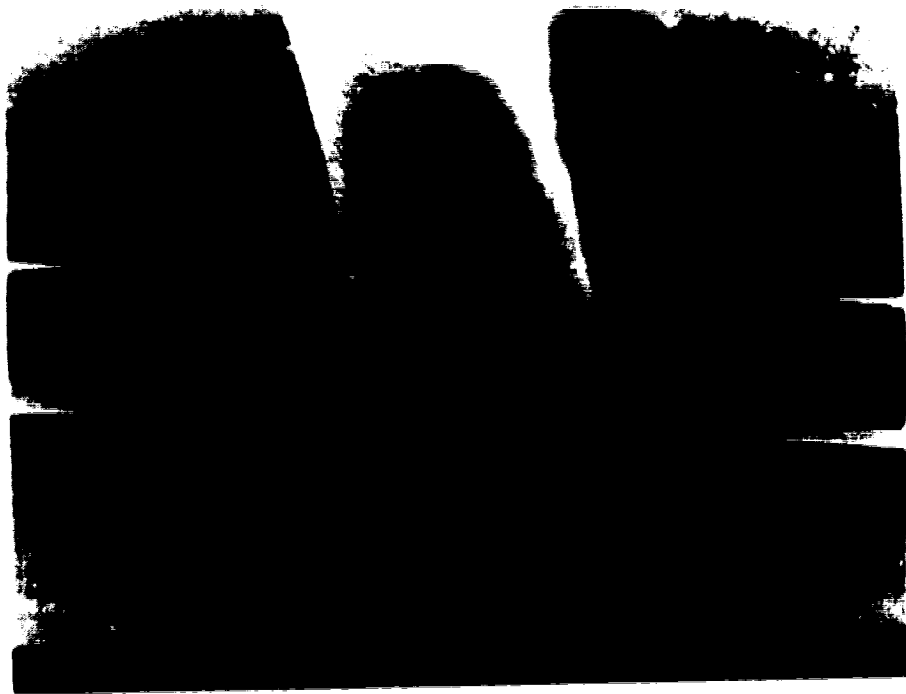


Figure 3.5 Electron micrograph of the intersection of channels etched in Type III Pyrex.

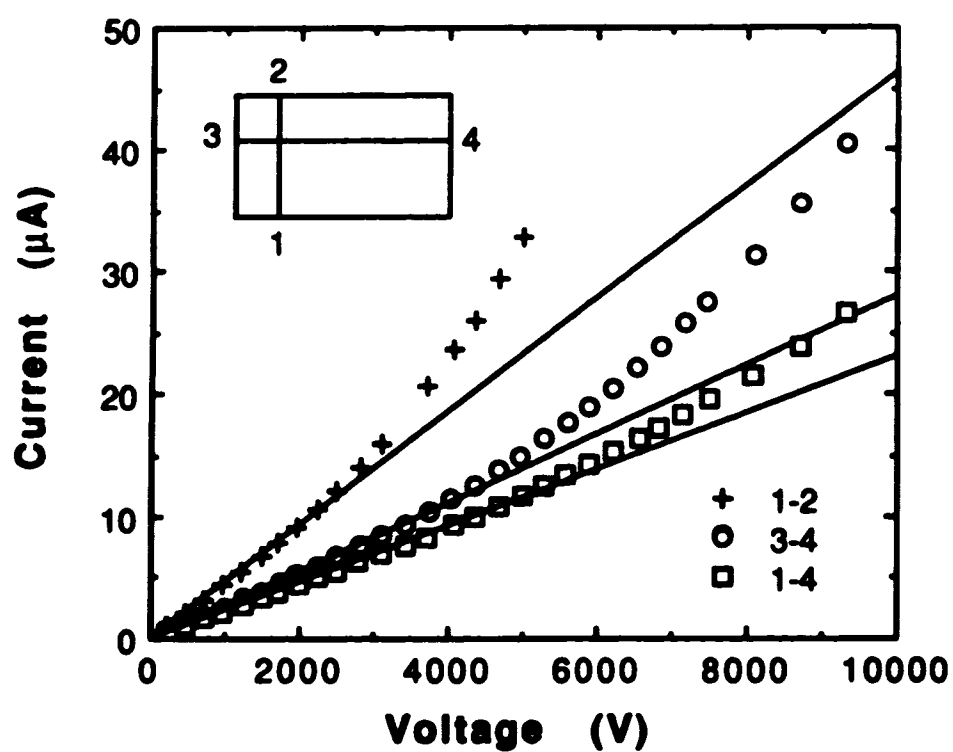


Figure 3.6 Current voltage curves in an Airport-70:70 device with pH 8.0, tris-boric acid buffer in all reservoirs. The inset shows the numbering scheme.

linearity occurred at about 2.8 W/m of power dissipation. A higher conductivity pH 7.0 phosphate buffer showed a similar deviation from linearity at about 1200 V/cm, corresponding to about 2.3 W/m. These results indicate the deviation is caused by Joule heating effects and show there is about a two-fold improvement over the 1 W/m limit typically used (15) for uncooled, conventional fused silica capillaries. The high thermal mass of the glass device relative to a fused silica capillary, and the 40-fold greater thermal conductivity of glass compared to stagnant air must be the source of this effect (31, 32). (In fact, at 2.6×10^{-3} cal/s·cm·°C at 0°C Pyrex is about twice as thermally conductive as water.)

The resistance, R , between any two reservoirs was determined from current-voltage curves. For all devices the magnitudes of R between different reservoirs were proportional to the channel cross-sections and lengths. This shows that the current passed through the capillary channels, indicating that the bonding process was effective, as we have found with glass devices fabricated commercially (6, 7).

3.4.3 Rapid Separation

Rapid separation is of considerable interest if CE-based devices are to be used as part of a chemical sensor system, or the second stage of a two-dimensional separation (15, 26). The high electric fields that can be obtained with a device having relatively short channel lengths should give rapid separation. Fluorescein isothiocyanate (FITC) labelled arginine (Arg-FITC), phenylalanine (Phe-FITC) and glutamic acid (Glu-FITC) were used in this study. Figure 3.7 shows that the complete separation of the three amino acids was performed in Airport-30 within 3 s using a potential of just 2500 V between reservoirs 3 and 4 (1560 V/cm). This potential corresponds to 1170 V between the injection point (the intersection) and the detector, which was located 0.75 cm away from the intersection in the direction of reservoir 4. The injection step described below required 1 s, giving a total cycle time for analysis of about 4 s. The time is clearly comparable to the response time of many chemical sensors.

The injection was effected by applying +500 V between reservoir 1

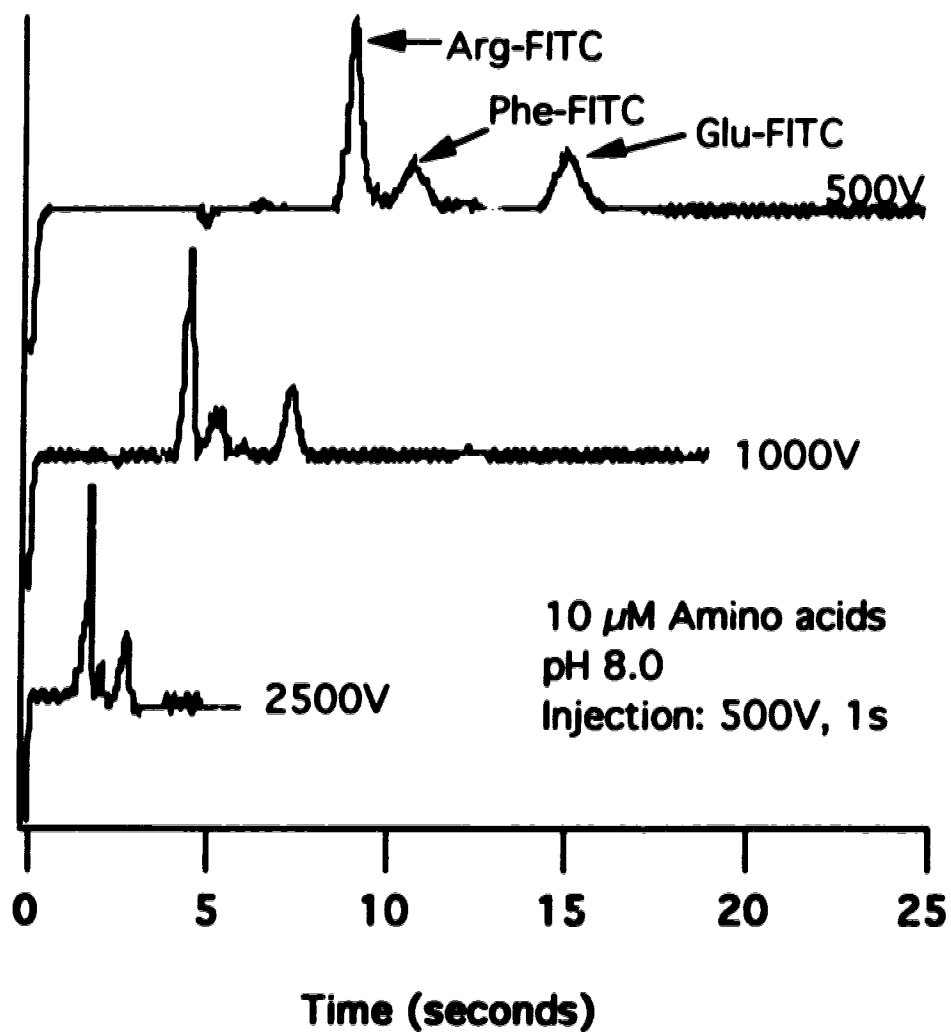


Figure 3.7 Electropherograms of FITC labelled 10 μM arg, phe and glu in pH 8.0 buffer. Separation voltages of 500, 1000 and 2500 V correspond to 234, 470 and 1170 V between the intersection and detector location, respectively. Sample was injected for 1 s with 500 V between reservoirs 1 and 2.

and reservoir 2 (at ground) for 1 s. This procedure drove sample in reservoir 1 across the intersection point, creating a sample plug in the path between reservoirs 3 and 4. Switching the potential to those two reservoirs (4 at ground) caused injection and separation to occur as the plug moved towards reservoir 4. On the basis of calibrations described below we estimate the injection plug length to be equivalent to 500 μm long. This plug size resulted in separation efficiencies, expressed as the number of plates, of 2100 at 500 V (234 V_{id} ; injector to detector voltage drop), 1900 at 1000 V (47 V_{id}) and 560 at 2500 V (1170 V_{id}) for glutamic acid. A small shoulder is apparent on the peaks at 2500 V, which became worse at higher potentials and further degraded efficiency. This effect may arise from artifacts induced by the injection method and injector design. At all potentials the size of the injected plug contributed significantly to the band broadening observed.

Figure 3.8 shows a rapid separation of a fluorescein and fluorescein sulfonate mixture in the same device. Sample was also introduced into reservoir 1 of the device and then driven along the channel to reservoir 2 with 500 V applied for 1 s. The plug of sample at the intersection of the channels (a geometric volume of 9 pL) was then separated by application of 3000 V (1875 V/cm) between reservoirs 3 and 4. The separation of the two dyes was completed within 3 s, leading to a total analysis cycle time of under 4 s. Further details of this study have been described elsewhere (33).

3.4.4 Effect of Injection Parameters

The cross formed at the intersection of the channels was intended to create a geometrically defined sample plug close to the volume of the intersection for injection into the separation channel. It proved not to be the case, however, the effect was too complex to be described as arising solely from diffusion effects. Cross injections were made by applying an "injection" potential of 500 V between reservoirs 1 and 2 for various periods, driving a 50 μM fluorescein, 50 μM fluorescein sulfonate solution across the intersection. The plug at the intersection was then directed

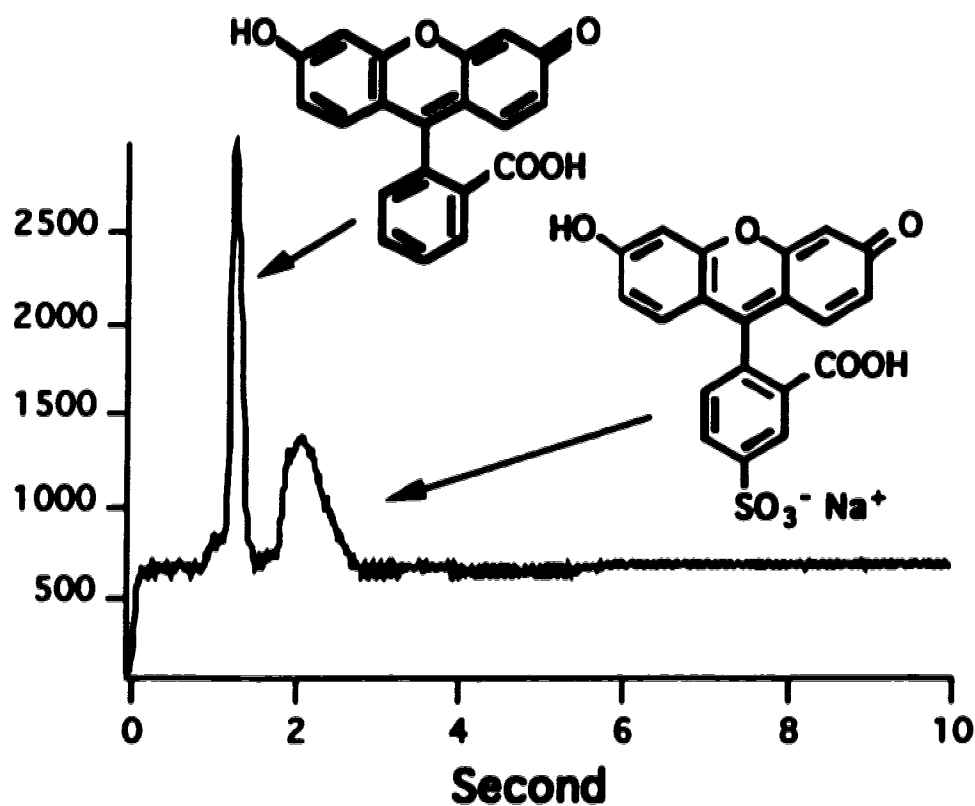


Figure 3.8 Rapid separation of 50 μM fluorescein from 50 μM fluorescein sulfonate in device Airport-30. Injection was accomplished by applying 500 V for 1 s between reservoirs 1 and 2, and then switching to apply 3000 V between reservoirs 3 and 4 in the pH 8.0 buffer.

towards reservoir 4, with 1500 V separation potential applied between reservoirs 3 and 4. A plot of peak area for fluorescein *versus* the square root of time was linear between 1 and 4 s of injection time. Similarly, if no injection voltage was used, but a delay period was allowed between separations, the peak area observed increased with delay time. These results appear consistent with diffusion of sample along the separation channel during the injection process (7, 34).

The complex nature of the cross injector's characteristics was made apparent by the effect of the injection voltage. For a 1 s injection and delay period the peak area increased linearly with the injection potential, varying from 250 to 1750 in arbitrary units as the injection potential was increased from 0 to 1000 V. This effect was unexpected, since the volume injected should have been defined by the intersection volume and diffusion into the side channels (7, 34) (fixed 1 s period) with no potential dependence. It is possible that significant depletion of the sample channel occurs due to leakage during the separation step (*vide infra*), which then requires a longer injection period to establish the nominal concentration. However, at 100 V injection potential the dye would travel about 400 μm in the sample channel, which should have compensated for any depletion of sample in the sample channel during the separation step. The result suggests there is some incursion of sample into the separation channel due to the applied field. This incursion may be related to distortions in the electric field lines at the intersection. An estimate of the effect on plug size was obtained from an analysis of the separation efficiencies, as discussed below.

3.4.5 Separation Efficiency

Optimization of the injection procedure was necessary to improve the separation efficiency, since the plug size was a significant contributor to band broadening (35). Figure 3.9 shows the results for a nominal injection voltage of 100 V, and various injection times. With a 500 V separation potential the maximum efficiency was achieved with a 115 ms injection time. The rise time of the power supplies was ~ 300 ms so that the

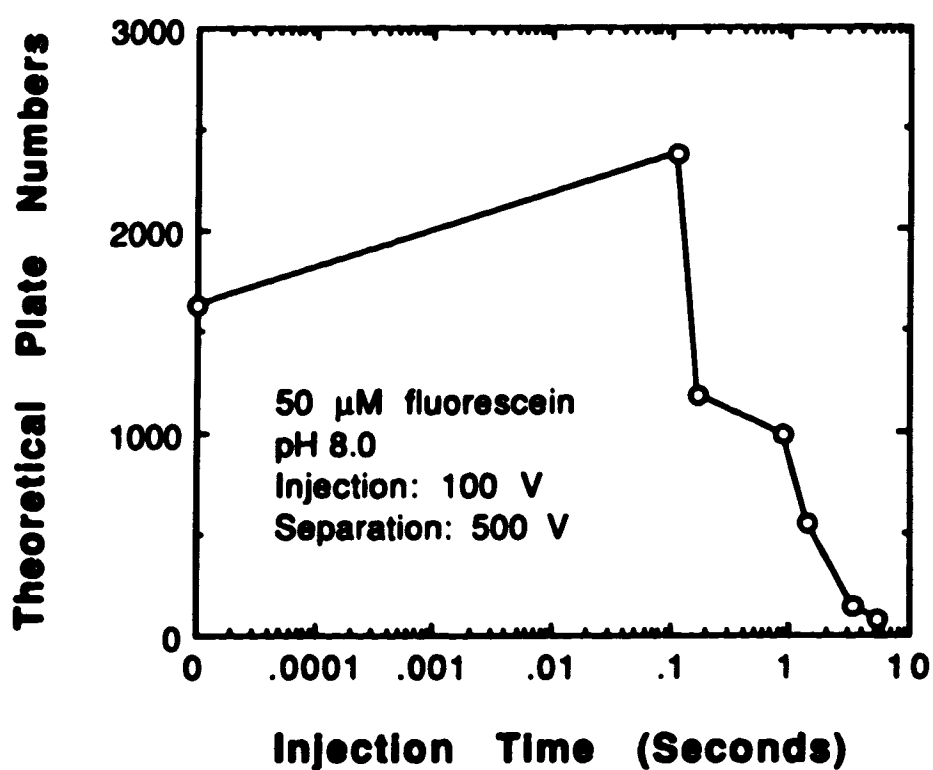


Figure 3.9 Number of theoretical plates, N , as a function of injection time between separation steps for a 50 μ M fluorescein sample in pH 8.0 buffer. A constant delay time of 2 s was added to the injection times. A separation potential of 500 V was used, and all injections used a nominal value of 100 V between reservoirs 1 and 2.

actual injection potential achieved was only 60 V for about the last 50 ms of the 115 ms injection period. We have since been able to program 50 msec injection periods and achieve a true square wave injection potential program that attains the nominal potential value, but the injector efficiency study was not repeated.

The separation potential impacts on the number of theoretical plates, and the height equivalent to a theoretical plate, H , through eq. [3.1] (7, 36),

$$H = \frac{2DL}{\mu V_{ap}} + \frac{w_{inj}^2}{12 d_{id}} + \frac{w_{det}^2}{12 d_{id}} + \frac{2 D t_{inj}}{d_{id}} \quad [3.1]$$

where D is the diffusion coefficient, μ is the apparent electroosmotic mobility, L is the distance across which the potential, V_{ap} , is applied, w_{inj} and w_{det} are the lengths of the injected plug and detector cell, respectively, d_{id} is the distance from injection to detection points, and t_{inj} is the time between applications of the separation voltage (*i.e.* period of injection plus any delay times). This expression assumes a rectangular shape for the injection plug and detector volume, but makes no allowance for possible absorption effects on the walls of the glass (37, 38).

The apparent electroosmotic mobility in equation [3.1], μ , was determined experimentally. As shown in figure 3.10, a plot of V_{ap} versus $1/t_m$ was linear. The slope of the plot was used to calculate μ according to equation [3.2] (36).

$$\mu \frac{V_{ap}}{L} = v = \frac{d_{id}}{t_m} \quad [3.2]$$

Where v is the linear flow velocity and t_m is the migration time of the compound. Based on experiments in both Airport-30 and Airport-70 devices, for example, μ of fluorescein in pH 8.0 tris-borate buffer was determined to be $(2.2 \pm 0.1) \times 10^{-4} \text{ cm}^2/\text{s}\cdot\text{V}$.

As discussed in chapter 1, the apparant electroosmotic mobility (μ) consists of the electrophoretic mobility (μ_{ep}) and the electroosmotic

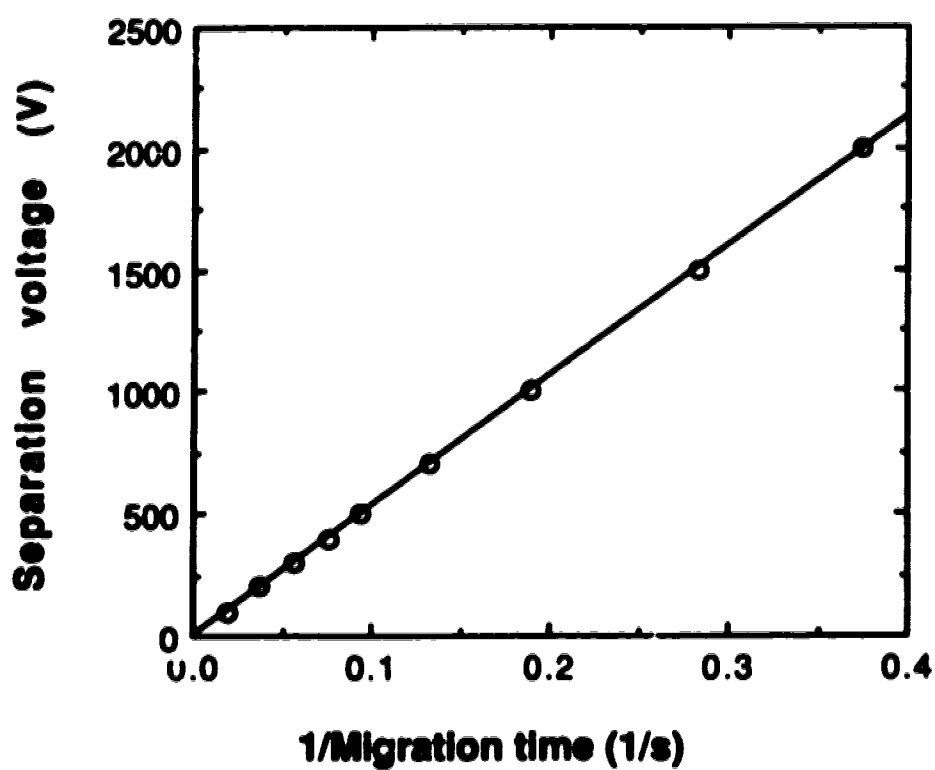


Figure 3.10 A plot of V_{ap} versus $1/t_m$ for 50 μM fluorescein, pH 8.0. While sample was injected for 115 ms at nominally 100 V between reservoirs 1 and 2, a variety of voltages were applied between reservoirs 3 and 4 for separation. An Airport-70 device was used.

mobility (μ_{eo}). To determine the μ_{ep} of fluorescein in pH 8.0 tris-borate buffer, a Quanta 4000 CE system (Millipore Waters, Milford, MA) was used with a 75 μm i.d. conventional silica capillary. A 254 nm UV absorbance detector was used for detection. The μ of fluorescein in pH 8.0 tris-borate buffer in the silica capillary was determined to be $4.12 \times 10^{-4} \text{ cm}^2/\text{s}\cdot\text{V}$, while μ_{eo} of the buffer was $7.04 \times 10^{-4} \text{ cm}^2/\text{s}\cdot\text{V}$, as determined from the mobility of a neutral marker, tryptophan (39). Therefore, the μ_{ep} of fluorescein in pH 8.0 tris-borate buffer can be calculated to be $-2.92 \times 10^{-4} \text{ cm}^2/\text{s}\cdot\text{V}$. It is reasonable to assume the same μ_{ep} of fluorescein in a silica capillary and a μ -TAS device, because the same buffer was used. As a result, the μ_{eo} of the buffer in μ -TAS devices can be calculated to be $5.12 \times 10^{-4} \text{ cm}^2/\text{s}\cdot\text{V}$.

Figure 3.11 shows the dependence of H on V_{ap}^{-1} for a 50 μM fluorescein sample injected with a nominal 100 V for 115 ms. A linear relationship was observed for separation potentials up to about 1000 V (625 V/cm), after which some curvature was seen. This is well below the field strength of 2500 V/cm at which Joule heating effects become apparent. The deviation may arise from interactions with the walls, as has been discussed by Liu *et al* (38). However, it may also be an artifact associated with the behavior of the cross injector, as discussed for the amino acid separation. The minimum plate height of about 1.2 μm , giving $N = 6800$ with 470 V between the injection and detection points ($V_{ap} = 1000 \text{ V}$), indicates the relatively high efficiencies that can be achieved within this small device.

According to equation [3.1], the slope of the plot in Figure 3.11 should give the diffusion coefficient of fluorescein, determined to be $3.3 \times 10^{-6} \text{ cm}^2/\text{s}$ by polarography, but a value of $4.5 \pm 0.2 \times 10^{-6} \text{ cm}^2/\text{s}$ was obtained. Huang *et al* (37) have previously suggested that interactions with the capillary walls could play a role in increasing the apparent value of D , although other effects may also play a role in our results. The intercept observed in Figure 3.11 can be described by the separation potential invariant terms in equation [3.1]. Given a detector cell length of 14 μm , a response time of 5 ms, and known values of the delay time it is instructive to estimate the length of the injected plug from the observed

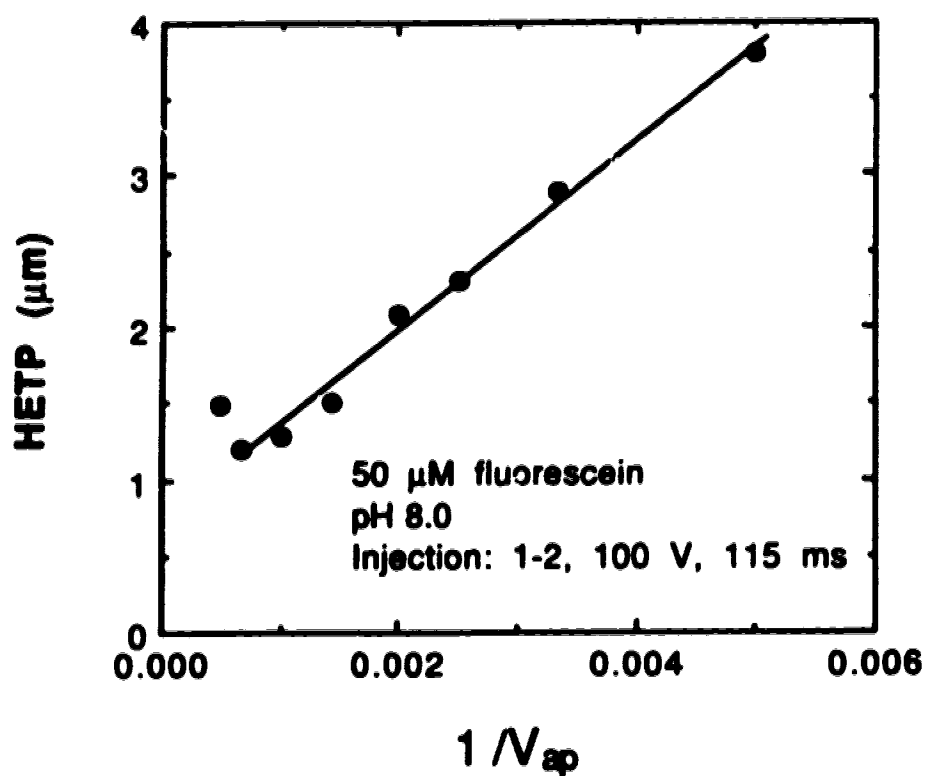


Figure 3.11 A plot of height equivalent to a theoretical plate, HETP, *versus* $1/V_{ap}$ for 50 μM fluorescein, pH 8.0. Conditions were the same as in Figure 3.10.

intercepts. Using the optimum injection conditions of Figure 3.9, nominally 100 V for 115 ms, the plug length calculated from the band broadening of fluorescein samples was 210 and $250 \mu\text{m} \pm 10\%$ for devices Airport-30 and 70, respectively. An increase to a 1 s injection period in Airport-30 gave $w_{\text{inj}} = 510 \mu\text{m} \pm 10\%$, which was essentially independent of injection voltage between 100 and 500 V. Since the amount injected was a function of injection voltage these results indicate that band broadening is not just a function of the plug size in the cross injector. Airport-70 showed a larger increase in band broadening than Airport-30 for a 1 s injection, giving $w_{\text{inj}} = 1000$ and $3300 \mu\text{m}$ at 100 and 500 V injection potentials, respectively. In this case band broadening did increase with plug size.

The data presented shows that the cross-injector design gives an injection that makes a significant contribution to band broadening and that the volume of the intersection plays a role. The reasons for this are not clear, but the size of the plugs is too large to be explained by diffusional broadening. Equation [3.1] is derived assuming a true plug injection leading to the factor $1/12$, but this may be inappropriate. The broadening introduced by a mixing chamber is given by w^2/d_{id} (40) and it is probable that mixing occurs at the intersection point while the injection takes place. Using this expression the size of the injection "plugs" given above is reduced by $\sqrt{12}$, giving $60\text{-}70 \mu\text{m}$ for the smallest plugs. These lower values are more consistent with the injection geometry and diffusional distances. The band broadening from mixing may be relatively constant during the injection and separation step. Eddies that flow at the sharp corners of the intersections and distortions of the field lines at the corners may give the greatest contribution to band broadening effects arising from mixing. Such effects would be relatively independent of the injector volume. This could explain why w_{inj} for Airport-30 was independent of the amount injected while a dependence was seen for Airport-70. In this case the volume of the Airport-70 injection would have to be large enough that band broadening due to the physical size of the sample plug was as large or larger than the broadening contributed by a constant effect from mixing.

3.4.6 Leakage Phenomena

In a manifold of capillary channels that has no valves, leakage of liquid between channels will occur at the intersections. In a previous study (6) we showed this amounted to about 3% contamination of the buffer by the sample during the separation step. However, this value is dependent on the layout of the channels, apparently due to the differences in resistance to fluid flow with capillary dimensions. Figure 3.12 shows the fluorescence intensity observed when fluorescein dye was present from reservoir 1 up to the intersection, with buffer in the other channels. A positive potential applied from reservoirs 4 to 3 (ground) caused buffer to flow past the detector and established the baseline. With the polarity reversed solution flowing past the detector was contaminated by sample leaking into the flowing stream at the intersection. This amounted to 3.5% of the signal observed when dye was intentionally driven past the detector with a potential between reservoirs 1 (sample) and 4 (ground).

The leakage was shown to arise from convective flow out of the side channels by introducing buffer into all the channels and reservoirs. Since the dye was photobleached by the laser the observed fluorescence intensity was a function of velocity, as determined by applying increasing potentials between reservoirs 3 and 4. Any flow induced in the separation channel could be monitored by the intensity of fluorescence while a potential was applied between reservoirs 1 and 2. Observation that the fluorescence intensity in the separation channel 3-4 increased in a stepwise fashion with stepwise increases in potential applied to the sample channel 1-2 confirmed the leakage was due to a convective effect, because the potential applied to the sample channel should have caused flow only in the sample channel.

The direction of convective leakage flow was determined by filling reservoir 1, 2 and 3 with dye and 4 with buffer. The dye was then directed a short distance past the detector with a potential between reservoirs 1 and 4, as indicated in Figure 3.13a. Since there was only a limited amount of dye between the detection point and reservoir 4 any convective flow in the direction of the intersection would eventually deplete the dye and cause a

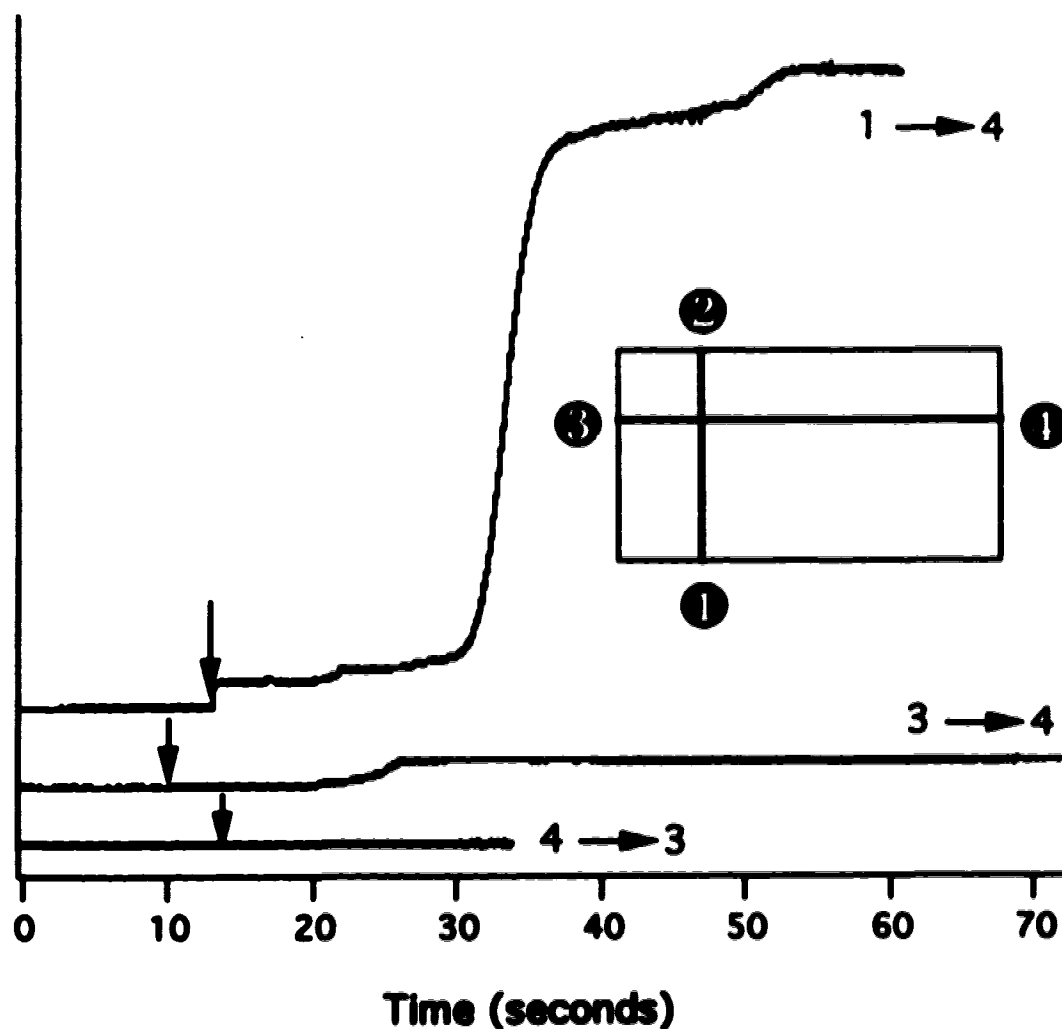


Figure 3.12 Bottom trace shows the background fluorescence intensity change when 500 V is applied to direct buffer from reservoir 4 to 3 is too small to measure on this scale. The arrows indicate the time when 500 V was applied. Central trace shows the increase in background due to leakage from reservoir 1 when 500 V is applied to direct flow from reservoir 3 to 4. Upper trace shows the intensity due to the 50 μM fluorescein in reservoir 1 when 500 V is applied to direct flow from reservoir 1 to 4. All other reservoirs contain buffer only.

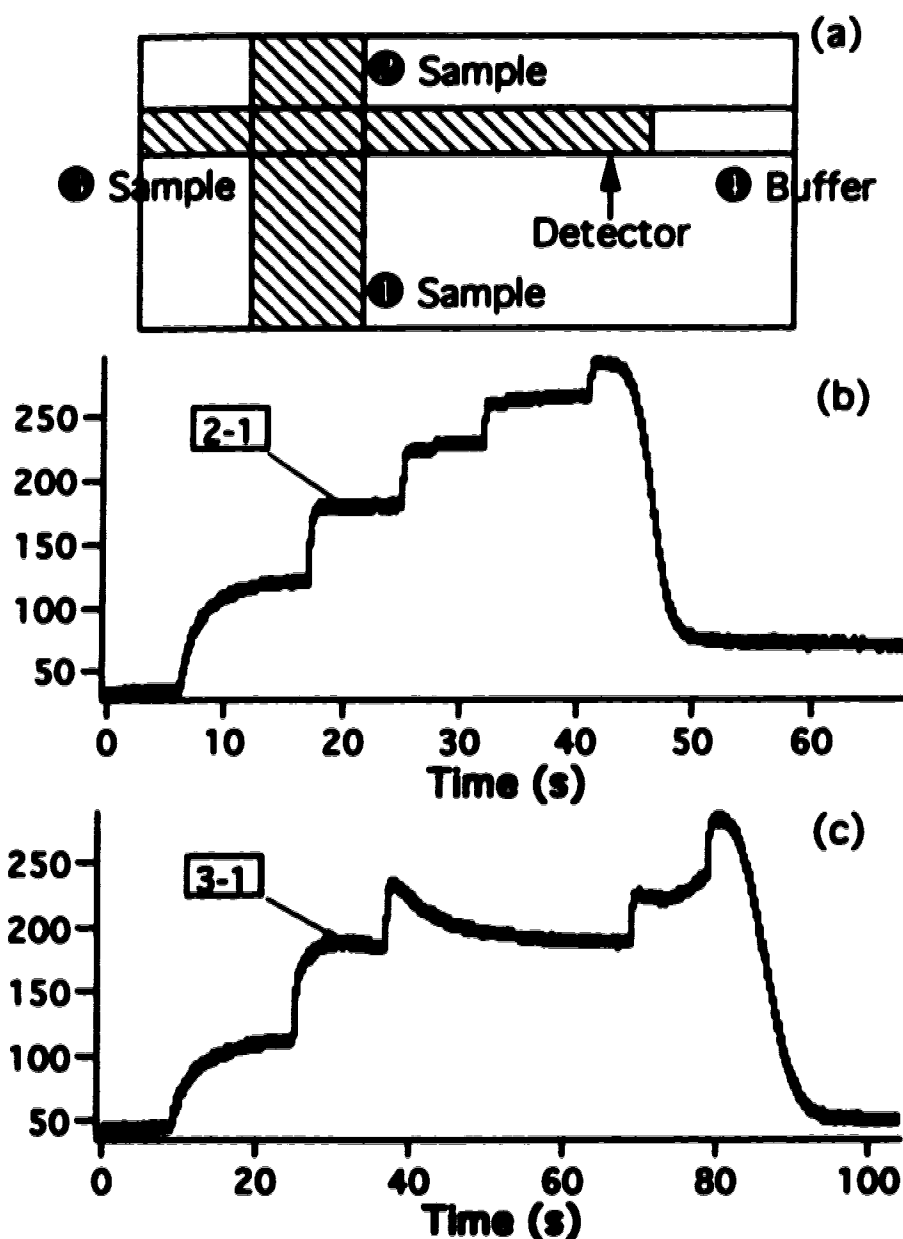


Figure 3.13 (a) A 50 μM fluorescein solution, pH 8.0, is present in all reservoirs except 4. The dye was moved a short distance past the detector electrokinetically. (b) The fluorescence intensity is shown *versus* time while the potential applied between reservoirs 1 and 2 was increased stepwise. The potential started from 0 V, and each step was 100 V. (c) The fluorescence intensity *versus* time while V_{ap} between reservoirs 3 and 1 (ground) was increased stepwise.

decrease in signal at the detector. Flow out of the intersection towards reservoir 4 would instead result in a steady supply of dye. Stepwise (100 V/step) increases of a potential applied between reservoirs 1 and 2 caused stepwise increases in fluorescence intensity, but the intensity then dropped to zero while the potential continued to increase, as shown in figure 3.13b. This indicated that electroosmotic flow along the sample channel caused convective flow out of the side (separation) channel. Figure 3.13c shows that convective flow was out of the detection/separation channel even when the electrokinetic flow was directed around a corner from reservoir 3 to 1. The convective flow most likely arises from frictional forces within the solvent that lead to a transfer of momentum from the flowing stream to the stagnant fluid in the side channel (40). This would be consistent with the observed leakage flow directions. Neither diffusion driven flow nor hydrostatic flow induced by differences in the fluid heads could account for the observations described above and shown in figure 3.13.

To determine actual leaking flow velocities a calibration curve of fluorescence intensity with flow rate was obtained in the following way. All reservoirs of the device were filled with the dye. Then stepwise potential increases were applied between reservoirs 3 and 4 to observe the stepwise increases in the intensity along that same channel. The flow velocity at each step was calculated from the mobility of fluorescein and the known electric field using equation [3.2]. Figure 3.14 shows the intensity as a function of dye velocity in both Airport-30 and Airport-70.

Using calibration curves in figure 3.14 the observed intensity changes due to leakage were translated into flow velocities. Plots of the flow rate in the side channel (intersection-4) as a function of the electrical fields applied to channel 1-2 or 1-3 were obtained, as shown in figure 3.15. Unfortunately, extrapolation of the calibration curves in figure 3.14 had to be used due to the small velocity in the side channel. Therefore, there could be a significant error in the calibrated flow rates in figure 3.15. Nevertheless, the figure provides an estimate of the flow rate due to leakage. It is approximately $(1.0 \pm 0.4)\%$ of the corresponding flow rate in the main channel at 300 V/cm.

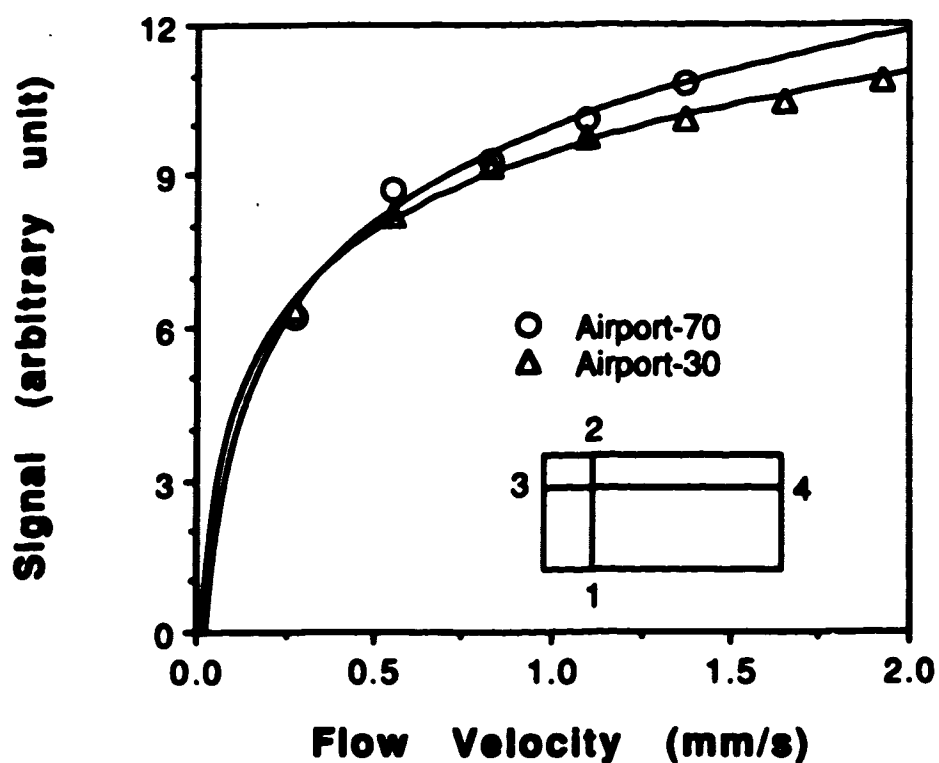


Figure 3.14 The fluorescence intensity is plotted *versus* linear flow velocity that depends on the potential applied between reservoirs 3 and 4. The stepwise potential (200 V/step) was used with 5 s for each step. A 50 μ M fluorescein solution, pH 8.0, is present in all reservoirs. Lines were empirically fitted using logarithmic regression.

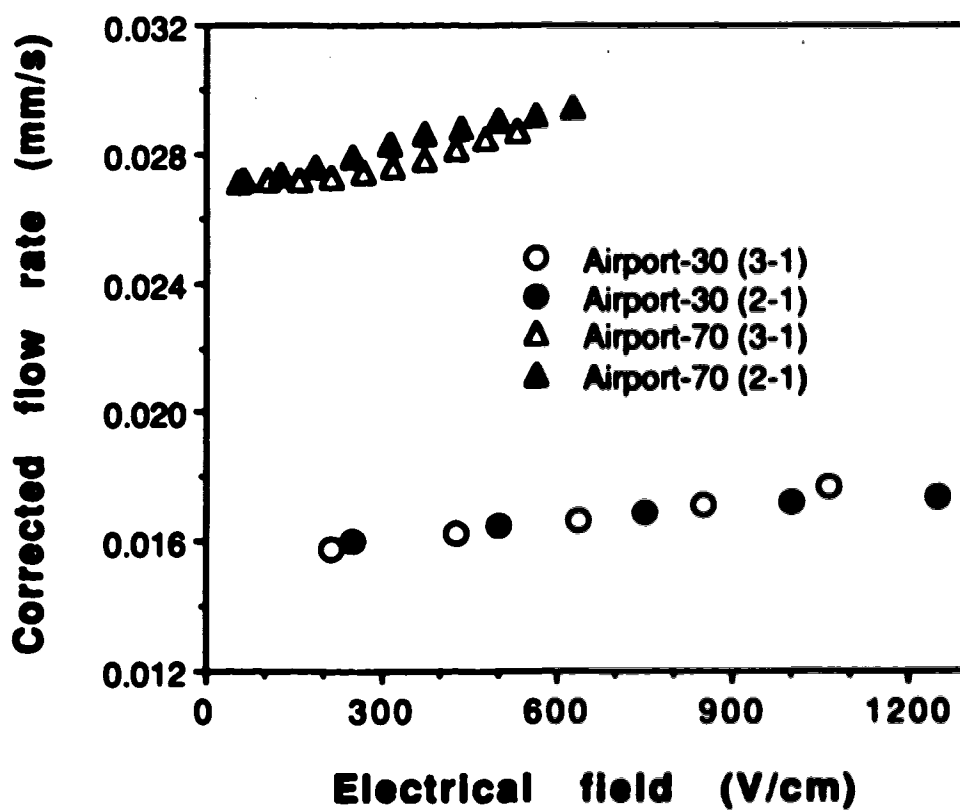


Figure 3.15 Plots of the flow rate in the side channel (intersection-4) *versus* electrical field applied to channel 1-2 or 1-3. Other conditions were the same as in figure 3.14.

3.5 Conclusions

This study shows that CE devices can be fabricated in a small format size in a planar configuration. The choice and treatment of the glass substrate proved to be of considerable importance to the quality of the channels formed by etching, and further improvements would still be advantageous in terms of improving device yields. The very rapid separation of amino acid and fluorescein samples demonstrates the potential of these micromachined CE systems to compete with chemical sensors in terms of total analysis time. It also establishes one advantage of these devices over conventional CE systems. The high thermal conductivity and mass of the glass substrate, which allows the use of higher electric fields is another.

The use of computer controlled high voltage relays to switch the channels to which potentials are applied, and so switch the direction of fluid flow, allows for sample injection on a 100 msec time scale. This approach offers the advantage of needing no moving parts other than the relays, and does not require the development of integrated valves for liquids. However, without valves there is the possibility of fluid mixing at the intersection of channels due to both diffusion and convection, as we have established in this work. The presence of convective effects indicates that the resistance of the intersecting channels to fluid flow must be considered, in order to balance the forces involved and minimize convective flow. Clearly, such effects must be taken into account in order to optimize the injector's design and improve the efficiency of the cross-injector tested here.

3.6 References

1. Graber, N.; Lüdi, H.; Widmer, H.M. *Sens. Actuat.* **1990**, *B1*, 239-243.
2. Gisin, M.; Thommen, C. *Anal. Chim. Acta* **1996**, *190*, 165-176.
3. Garn, M.; Cevy, P.; Gisin, M.; Thommen, C. *Biotechnol. Bioeng.* **1999**, *34*, 423-428.

4. Manz, A.; Graber, N.; Widmer, H.M. *Sens. Actuat.* **1990**, *B1*, 244-248.
5. Manz, A.; Fettingner, J.C.; Verpoorte, E.; Lüdi, H.; Widmer, H.M.; Harrison, D.J. *Trends Anal. Chem.* **1991**, *10*, 144-149.
6. Harrison, D. J.; Manz, A.; Fan, Z.; Lüdi, H.; Widmer, H. M. *Anal. Chem.* **1992**, *64*, 1926-1932.
7. Seiler, K.; Harrison, D. J.; Manz, A., *Anal. Chem.*, **1993**, *65*, 1481-1488.
8. Manz, A.; Harrison, D. J.; Verpoorte, E. M. J.; Fettingner, J. C.; Paulus, A.; Ludi, H.; Widmer, H. M. *J. Chromatog.* **1992**, *593*, 253-258.
9. Harrison, D. J.; Glavina, P. G.; Manz, A. *Sens. Actuat.* **1993**, *B10*, 107-116.
10. Small Bore Liquid Chromatography Columns: Their Properties and Uses, Scott, R.P.W., Ed.; Wiley, New York, **1984**.
11. Micro-Column High Performance Liquid Chromatography, Kucera, P., Ed., Elsevier, Amsterdam, **1984**.
12. Microcolumn Separations: Columns, Instrumentation and Ancillary Techniques. *J. Chrom. Library Vol. 30*, **1985**.
13. van der Linden, W.E. *Trends Anal. Chem.* **1987**, *6*, 37-40.
14. Ruzicka, J.; Hansen, E.H. *Anal. Chim. Acta* **1984**, *161*, 1-10.
15. Monnig, C.A.; Jorgenson, J.W. *Anal. Chem.* **1991**, *63*, 802-807.
16. Petersen, K.E. *Proc. IEEE* **1982**, *70*, 420-457.
17. Terry, S.C.; Jermon, J.H.; Angell, J.B. *IEEE Trans. Elect. Dev.* **1979**, *ED-26*, 1880-1886.
18. Muller, R.S. *Sens. Actuat.* **1990**, *A21*, 1-8.
19. Esashi, M.; Shoji, S.; Nakano, A. *Sens. Actuat.* **1989**, *20*, 163-169.
20. Fan, L-S.; Tai, Y-C.; Muller, R.S. *IEEE Trans. Elec. Dev.* **1988**, *ED-35*, 724-730.
21. Sato, K.; Kawamura, Y.; Tanaka, S.; Uchida, K.; Kohida, H. *Sens. Actuat.* **1990**, *A21*, 948-953.
22. Kittisland, G.; Stemme, G.; Norden, B. *Sens. Actuat.* **1990**, *A21*, 904-907.

23. Olthus, W.; van der Schoot, B.H.; Bergveld, P. *Sens. Actuat.* **1989**, *17*, 279-283.
24. Shoji, S.; Esashi, M.; Matsuo, T. *Sens. Actuat.* **1988**, *14*, 101-107.
25. Manz, A.; Miyahara, Y.; Miura, J.; Watanabe, Y.; Miyagi, H.; Sato, K. *Sens. Actuat.* **1990**, *B1*, 249-255.
26. Monnig, C.; Dohmeier, D. M.; Jorgenson, J. W. *Anal. Chem.* **1991**, *63*, 807-810.
27. Huang, X.; Gorgon, M. J.; Zare, R. N. *Anal. Chem.* **1988**, *60*, 375-377.
28. Ko, W. H.; Suminto, J. T. in *Sensors: A Comprehensive Survey*, Grandke, T.; Ko W. H. Ed., VCH Press:Weinheim, Germany, **1989**; Vol. 1, 107-168.
29. Kern, W.; Deckert, C. A. in *Thin Film Processes*, Vossen J. L., Kern, W., Eds.; Academic Press, Inc., San Diego, CA, **1978**, Chapter V-1, pp401-496.
30. Sweedler, J. V.; Shear, J. B.; Fishman, H. A.; Zare, R. N.; Scheller, R. H. *Anal. Chem.* **1991**, *63*, 496-502.
31. Weast, R. C., Ed. *C. R. C. Handbook of Chemistry and Physics*, 59th ed.; CRC Press, Inc.: Boca Raton, FL, **1978/1979**; ppE-6, E-2, E-11.
32. A. J. Chapman, *Fundamentals of Heat Transfer*, Macmillan publishing Co.: New York, **1987**; p14.
33. Harrison, D. J.; Fan, Z.; Seiler, K.; Manz, A.; Widmer, H. M. *Anal. Chim. Acta* **1993**, *283*, 361-366.
34. Dose, E. V.; Guiochon, G. *Anal. Chem.* **1992**, *64*, 123-128.
35. Delinger, S. L.; Davis, J. M. *Anal. Chem.* **1992**, *64*, 1947-1959.
36. Jorgenson, J. W.; Lukacs, K. D. *Anal. Chem.* **1981**, *53*, 1298-1302.
37. Huang, X.; Coleman, W. F.; Zare, R. N. *J. Chromatogr.* **1989**, *480*, 95-110.
38. Liu, J.; Dolnik, V.; Hsieh, Y.; Novotny, M. *Anal. Chem.* **1992**, *64*, 1328-1336.
39. Fluri, K.; Harrison, D. J., unpublished results.
40. Sternberg, J.C. *Adv. Chromatogr.* **1993**, *2*, 206-270.
41. Coulson, J.M.; Richardson, J.F. *Chemical Engineering*, Vol 1, 3rd Ed., Pergamon Press, New York, **1977**.

Chapter 4

Micromachined Capillary Electrophoresis Systems: Double T Injectors, Leakage Suppression, and Calibration Curves.

4.1 Introduction

Capillary electrophoresis (CE) has been a research interest for more than a decade. Since the pioneering work by Mikkers *et al.* (1) and Jorgenson and Lukacs (2, 3), considerable attention has been paid to biological applications of CE, e.g., separation and characterization of biopolymers such as peptides, proteins and DNA, as seen in a recent book (4). Many detection methods have been applied to CE, including UV-visible absorbance, fluorescence, electrochemistry, radioisotope, and mass spectrometry (5, 6). Another active area of CE lies in the various operation modes of CE, such as capillary zone electrophoresis (CZE), isotachopheresis, isoelectric focusing (IEF), capillary gel electrophoresis (CGE), and micellar electrokinetic capillary chromatography (MECC) (7). In addition, there is a fair amount of work to expand the boundary of CE by coupling it with other techniques. For example, Jorgenson *et al.* have investigated two dimensional separation systems in which CE was functioned as the second separation process in tandem with liquid chromatography (LC) (8-10). Ewing *et al.* have connected a CE capillary to a microinjector to allow direct sampling from a single cell in vivo (7, 11). CE has also been used by Harrison *et al.* and their collaborators in CIBA-GEIGY for miniaturized total chemical analysis systems (μ -TAS), in which electroosmotic motion was used for injection while electrophoresis was for separation (12-16). Separations of amino acids and other species have been realized in such μ -TAS devices.

There are two injection schemes, electromigration and

hydrodynamic injection, which are typically used in capillary electrophoresis (17, 18). In electromigration injection a high voltage is applied between two electrodes in the sample and buffer reservoirs for a short period of time. Both electroosmotic and electrophoretic motion occur due to the electrical field, so that a plug of sample flows into the capillary. In hydrodynamic injection the sample reservoir is raised to a certain height for an interval of time. The height difference created between the liquid levels in the sample and buffer reservoirs causes a hydrostatic pressure which drives sample into the capillary.

Although electromigration injection is more convenient and easier to automate, it gives a significant bias in the injected amount of each component, due to different ionic mobilities (18). Injection volume could also change over a period of time, as flow rate depends on the zeta potential, which changes with the column conditioning and effects such as surface adsorption (19). In this respect, hydrodynamic injection is a better choice, as it yields very little bias and better precision (17). However, the injection is taking place when sample reservoir is being raised or lowered, reducing the control of the injected volume (17). Corrections for these deviations must be made when CE is used for quantitative analysis. Besides, hydrodynamic injection could seriously distort the injection front in some cases because of the parabolic flow profile under hydrostatic pressure (18). Moreover, hydrodynamic injection is difficult to perform in the μ -TAS devices we investigated, because capillaries in those devices were etched in planar plates.

Because μ -TAS devices usually have several capillary channels intersecting with each other, it is possible to define an injection volume geometrically at an intersection, as in the cross in the Airport devices. Unfortunately, the studies on both Airport (20) and CETAS (12, 13) devices suggested that cross and T intersections are not wholly satisfactory in that respect due to diffusional leakage and convective mixing taking place in the intersection. To overcome this, we have designed a double T injector that can define injection volume geometrically, as reported in this chapter.

As discussed in chapter 3, diffusional leakage and convective

mixing taking place in the intersection cause sample in the injection capillary to contaminate the buffer in the separation capillary when effecting separation. This leakage phenomenon will increase background and decrease the dynamic range of detection (20). To solve this problem, all reservoirs involved were actively controlled by appropriate potentials so that sample in the injection capillary was pumped back at the same time when the separation was taking place. In fact, the active voltage control could prevent leakage and suppress background as shown in this chapter.

When the μ -TAS devices are to be used for quantitative chemical analysis, calibration curves must be made. For the device we described in this chapter, we obtained linear calibration curves over 3 orders of magnitude. Because fluorescence detection methods were used, quenching taking place caused non-linear calibration curves. To correct this, a standard was employed so that the linear range of the calibration curves was extended. Another advantage offered by the standard was that it could correct bias in the injection volume, since the standard and analytes were influenced by the same capillary history effects such as surface absorption.

4.2 Experimental Section

4.2.1 Device

Figure 4.1 shows the layout and dimensions of the glass device called Jet-1, studied in this chapter. The numbers of reservoirs in the figure will be referred to in the discussion. The channel connecting reservoir 1 is 25 μm wide, while the channel connecting reservoir 2 is 50 μm wide. The width of the blackened bulky lines connecting reservoirs 3 and 4 is 300 μm , whereas the width of the narrow line between them is 30 μm . The different size of the channel between 3 and 4 ensured a maximum potential drop over the effective separation distance between the injection point and the detector. The offset between the two side channels connected to reservoirs 1 and 2 was 150 μm . The offset was used for the double T injection scheme discussed below. The depth of all

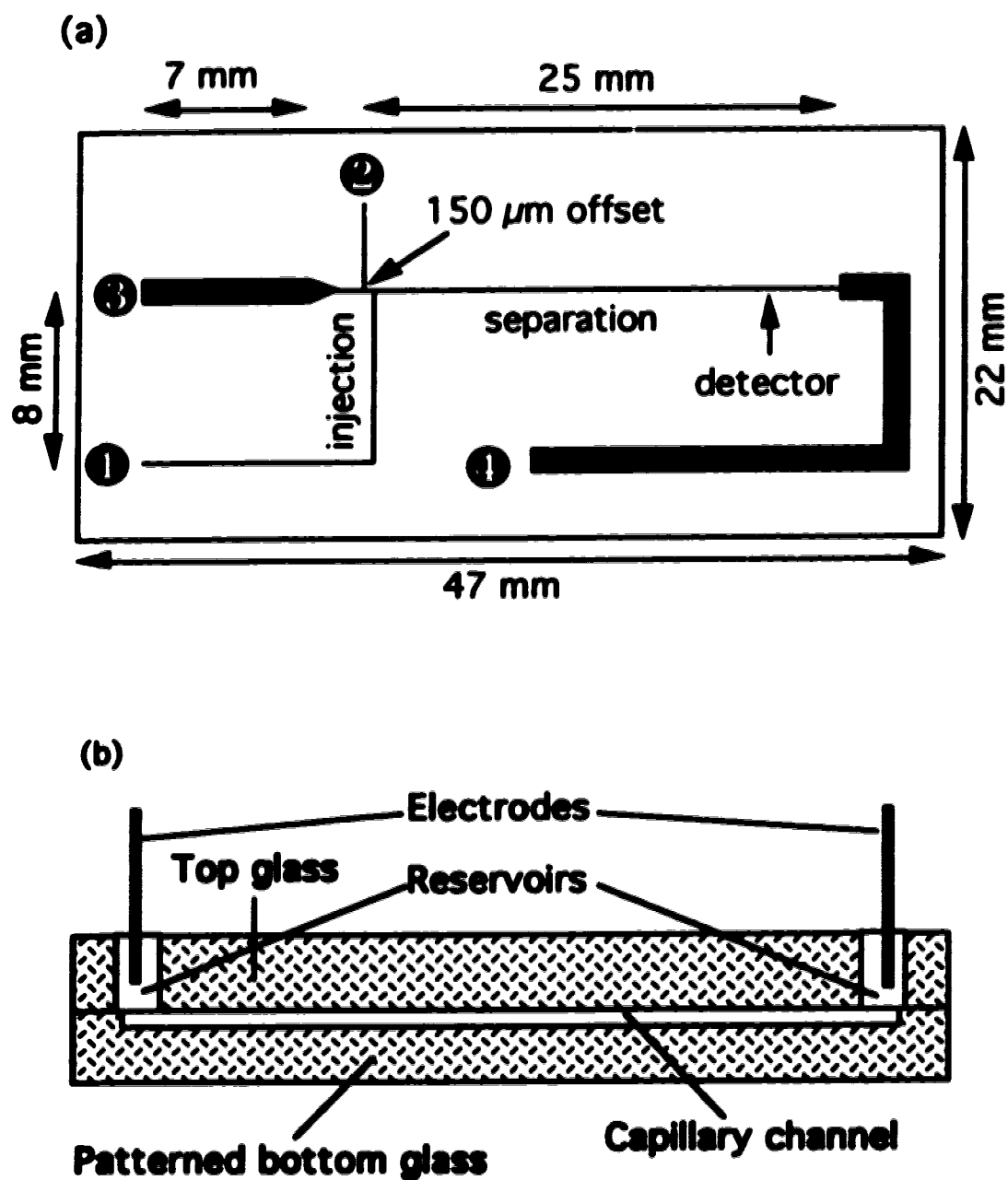


Figure 4.1 (a) The top view of layout and dimensions of Jet-1 devices. The numbers of the reservoirs are referred to in the text. (b) Cross section view of the device. See device fabrication section in the text for the detail.

channels was 10 μm . The size of the whole device was 2.2 cm x 4.7 cm. Four reservoirs were designed as far apart as possible to prevent current between the electrodes in reservoirs due to possible dielectric breakdown of air. The space in the region of detection was used for maneuvering the detector.

The glass devices were fabricated at the Alberta Microelectronic Centre (Edmonton, Canada) using the micromachining methods described in chapter 3 (20). Briefly, (a) A clean Pyrex glass plate was first coated with Cr and Au to be used as an etch mask. (b) A pattern was lithographically defined in the metal mask. (c) The glass was etched using a concentrated HF, HNO₃ and H₂O mixture (20 : 14 : 66). (d) The mask and photoresist coatings were then stripped off. (e) The patterned glass plate was then bonded to a cover glass plate by melting at 650 °C. The holes in the cover plate were ultrasonically drilled before bonding, and were aligned with the capillaries to provide access for sample and mobile phase introduction, as well as the access for electrodes with which to apply potentials. The diameter of the holes is 1.5 mm.

4.2.2 Instrument

The apparatus was assembled in house and has been described in chapter 3. A 488 nm air-cooled argon ion laser (Uniphase/Ionics, Model 2011) was used to excite fluorescence after focusing onto the device channel. The fluorescence emission was collected with a 10:1 microscope objective and directed onto a photomultiplier tube using a 1 mm diameter pinhole at the image plane and an optical band-pass interference filter (from 508 nm to 533 nm). The emission signal was electronically filtered with a Krohn-Hite Model 3342 6-pole Butterworth filter with a 50 Hz low pass cut-off frequency. The current in the channels was monitored from the potential drop across a 10 k Ω resistor located between the channel reservoir and the power supply ground, and recorded on a strip chart recorder. The peak parameters, such as peak area and the number of theoretical plates, were calculated from statistical moment analysis. Labview programs (National Instruments Corp., Austin, TX) written

locally were used for calculations, data acquisition and instrument control.

A Shimadzu RF 5000U spectrofluorophotometer was used to measure fluorescence quantum yield. The excitation wavelength was fixed at 488 nm, which agrees with the laser wavelength. The smallest excitation slit (1.5 nm) available on the machine was used. The largest emission slit (30 nm) was used to match the bandwidth of the emission filter used with the detector cell for the μ -TAS setup.

4.2.3 Materials and reagents

Corning 7740 (Pyrex) was obtained from Paragon Optical Co. (Reading, PA). Glass plates were annealed at 570 °C for 6 hours and slowly cooled down before fabrication. This released surface tension to ensure good etching quality (20). Amino acids, fluorescein and fluorescein-5-isothiocyanate (FITC) were used as received from Sigma. A pH 8.0 buffer of 0.05 M boric acid and 0.05 M tris(hydroxymethyl) aminomethane (TRIS), as well as a pH 9.1 buffer of 0.064 M sodium carbonate were used. All chemicals are of reagent grade and all solutions were prepared in deionized, double-distilled water. Solutions were filtered with Miller-GV sterilizing filter unit with 0.22 μ m membrane (Millipore, Bedford, MA) before injecting to capillaries.

4.2.4 Procedures

The derivatization of amino acids with FITC has been described in chapter 3. In brief, 5 volumes of 10 mM single amino acid in a buffer was mixed with 1 volume 10 mM FITC in 95% acetone, 5% water and 0.1% pyridine. The reactions took place overnight at room temperature, in the dark. The labelled single amino acids were then diluted to the desired concentration with the buffer solution. The concentration of each amino acid is given as the concentration of the labelled acid, assuming a complete reaction occurred.

Solutions were degassed with helium to decrease problems with

bubbles in channels. Buffer was introduced by a syringe into one reservoir, and then flushed until all channels were filled. Fine Pt wires were insulated using glass sleeves and inserted into reservoirs of the device. Fluorescent sample was usually introduced through reservoir 2 (see figure 4.1). A injection potential was then applied between reservoirs 2 and 1 to drive the sample through the intersection into reservoir 1. After the injection potential was turned off, separation was performed by applying another potential between 3 and 4. The detector was aligned with dye present in the region of detection.

4.3 Results and Discussion

4.3.1 Device Fabrication

We have reported that both the type of glass and its pretreatment had a significant effect on the quality of results obtained by etching (20). Fine annealing of glass plates before fabrication is necessary to acquire smooth channel walls. Isotropic etching of glass gave curved side walls and a flat bottom. The good etching quality is shown in figure 4.2, in which there is a gradual change in channel width from 30 μm to 300 μm . The length of the change is 1 mm, while the depth of the whole channel is 10 μm . This sloped section is used to connect 30 μm and 300 μm wide channels between reservoirs 3 and 4 in figure 4.1. The etching quality shown in figure 4.2 also suggests that there is room to manipulate the size of channels that function as connectors when we design new devices in the future.

4.3.2 Resistance Simulation

We have reported that the resistance of a channel is proportional to the channel length (12, 21). Because of the different size and shape of channels in Jet-1 device, as well as the curved side walls shown in figure 4.2, we need to re-evaluate the relationship between resistances and channel lengths so that the potential at a particular point under an

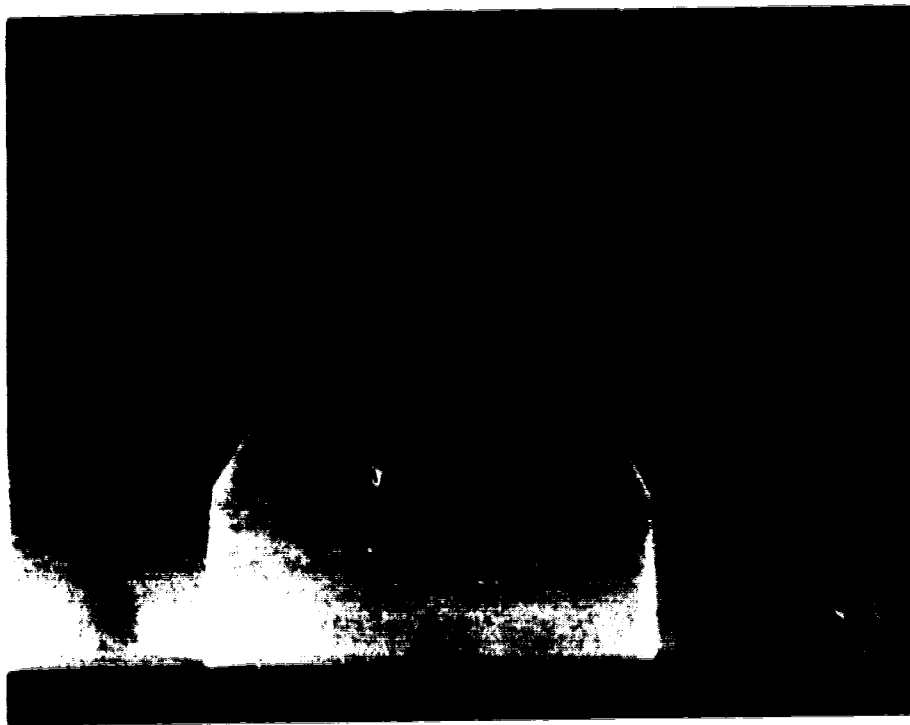


Figure 4.2 Scanning electron micrograph of the slope section jointing two channels with different width.

electrical field can be accurately predicted. The resistance of a channel was determined from the current-voltage curve, which was obtained by measuring currents in the channel when applying a series of voltages (21). The pH 8.0 TRIS and borate buffer was filled in all channels of the device. All distances, that is, equivalent lengths of channels, were calculated by converting the width of channels to 30 μm based on the cross sectional area. Table 4.1 shows the measured resistance, their ratios relative to the resistance between reservoirs 1 and 2, the distances, and their distance ratios. The good agreement between the ratios of the resistances with the ratios of the distances indicates a simulated resistance circuit will accurately predict the potential at a particular point under an electrical field.

The simulated resistance circuit is shown in figure 4.3a, in which the resistances are represented by the equivalent lengths of channels. The potential at a particular point under an electrical field can be calculated using a voltage divider equation. For example, the potential at point "a" in the figure can be obtained using equation [4.1] when 284 V and -3000 V were applied to reservoirs 3 and 4, and reservoirs 1 and 2 were left floating.

$$V_a = V_3 - V_{3a} = V_3 - V_{34} \frac{d_3}{d_3 + d_{inj} + d_4} \quad [4.1]$$

where, V_a and V_3 are the potentials at the point "a" in the figure and at the reservoir 3; V_{3a} is the potential drop over the distance between reservoirs 3 and point "a"; V_{34} is the potential differences between reservoirs 3 and 4; d_3 , d_{inj} and d_4 are the distances of each channel section represented by resistors in figure 4.3a. With the data in the figure, the potential at point "a" is calculated to be -45 V.

In fact, the resistance of each channel section can be obtained from the determined resistances of whole channels in table 4.1. For example, resistances for those channel sections indicated in figure 4.3b must observe the following equations.

Table 4.1 Ratios of channel resistances and distances in Jet-1 device

Channel^(a) reservoirs	Resistances^(b) (MΩ)	Resistance^(c) ratio	Distance^(d) (cm)	Distance^(c) ratio
1-2	384 ± 1.8	1	2.20 ± 0.09	1
1-3	406 ± 2.7	1.06 ± 0.01	2.31 ± 0.06	1.05 ± 0.05
1-4	819 ± 5.3	2.13 ± 0.02	4.80 ± 0.06	2.19 ± 0.09
2-3	81.4 ± 0.51	0.212 ± 0.002	0.42 ± 0.03	0.19 ± 0.02
2-4	502 ± 3.1	1.31 ± 0.01	2.96 ± 0.03	1.35 ± 0.06
3-4	526 ± 3.2	1.37 ± 0.01	3.08 ± 0.01	1.40 ± 0.06

- (a) The numbers of reservoirs are referred to in figure 4.1.
- (b) The standard deviation of the resistance was obtained from the uncertainty in the slope of the current-voltage plots.
- (c) Resistances or distances ratioed to the value between reservoirs 1 and 2. The standard deviations were calculated using the error propagation analysis.
- (d) The distances are converted to the equivalent lengths of 30 μm wide, 10 μm deep channels. The uncertainty in the position of each channel end was estimated to be 0.05 cm, as the channel end may not be in the center of the holes in the cover plate. The standard deviations have been converted in the same way.

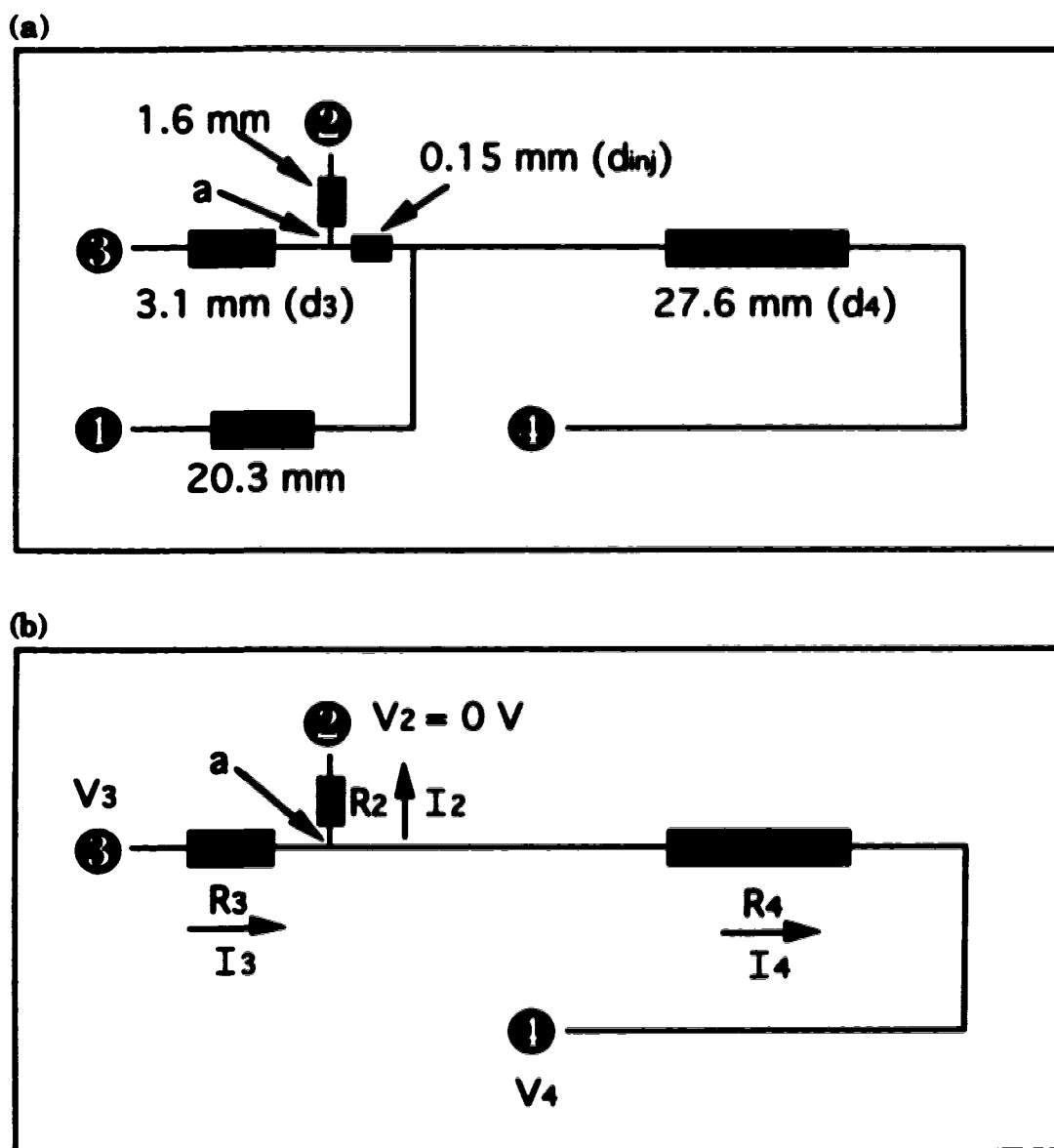


Figure 4.3 (a) The simulated resistance circuit of Jet-1 devices. The resistances are represented by the equivalent lengths of channels. The point "a" is the injection point when a sample is in reservoir 1. (b) The potential scheme used for leakage suppression discussed in section 4.3.6. Reservoirs 3 and 4 were applied with 284 V (V_3) and -3000 V (V_4), whereas 2 was grounded and 1 was not connected. R_4 is equivalent to the combination of d_{inj} and d_4 in (a).

$$R_{34} = R_3 + R_4 \quad [4.2]$$

$$R_{23} = R_2 + R_3 \quad [4.3]$$

$$R_{24} = R_2 + R_4 \quad [4.4]$$

Where R_{34} , R_{23} , R_{24} were resistances of channels 3-4, 2-3, 2-4, respectively; R_2 , R_3 , R_4 were the resistances of each channel section represented by resistors in the figure. Solution of these equations gave:

$$R_2 = \frac{R_{23} + R_{24} - R_{34}}{2} \quad [4.5]$$

$$R_3 = \frac{R_{23} - R_{24} + R_{34}}{2} \quad [4.6]$$

$$R_4 = \frac{-R_{23} + R_{24} + R_{34}}{2} \quad [4.7]$$

With data for R_{34} , R_{23} , R_{24} in table 4.1, R_2 , R_3 , R_4 were calculated to be 28.7 ± 2.2 , 52.7 ± 2.2 , 473.3 ± 2.2 M Ω , respectively. The standard deviation of each resistor was obtained from the error propagation equation [4.8] and the standard deviations of R_{34} , R_{23} , R_{24} in table 4.1.

$$\Delta R = \frac{\sqrt{\Delta R_{23}^2 + \Delta R_{24}^2 + \Delta R_{34}^2}}{2} \quad [4.8]$$

Using the resistances of R_3 and R_4 for d_3 and $(d_{inj} + d_4)$ in equation [4.1], the potential obtained for point "a" agrees with the result above.

However, calculations become more complicated when more than two reservoirs are actively controlled with potentials. The scheme shown in figure 4.3b was used for suppressing leakage, as discussed in section 4.3.6. Reservoirs 2, 3, 4 were biased at 284, 0, -3000 V, respectively, but reservoir 1 was floating. Figure 4.3b also indicates the resistors representing each channel section, currents flowing through each

resistor, and the assumed current directions. According to Kirchhoff's law, the following equations must be observed.

$$V_3 = I_3 R_3 + I_2 R_2 \quad [4.9]$$

$$V_4 = -I_4 R_4 + I_2 R_2 \quad [4.10]$$

$$I_3 = I_2 + I_4 \quad [4.11]$$

Where V_3 , V_4 are the voltages applied to reservoirs 3 and 4; I_2 , I_3 , I_4 are currents flowing through resistors R_2 , R_3 , R_4 . Solution of equations [4.5]-[4.7] gave:

$$I_2 = \frac{V_3 R_4 + V_4 R_3}{R_2 R_3 + R_3 R_4 + R_2 R_4} \quad [4.12]$$

$$I_3 = \frac{V_3 R_4 - V_4 R_2 + V_3 R_2}{R_2 R_3 + R_3 R_4 + R_2 R_4} \quad [4.13]$$

$$I_4 = \frac{V_3 R_2 - V_4 R_3 - V_4 R_2}{R_2 R_3 + R_3 R_4 + R_2 R_4} \quad [4.14]$$

Therefore, the potential at intersection point "a" was

$$V_a = V_3 - I_3 R_3 = \frac{V_3 R_2 R_4 + V_4 R_2 R_3}{R_2 R_3 + R_3 R_4 + R_2 R_4} \quad [4.15]$$

Substitution of data for V_3 , V_4 , R_2 , R_3 , R_4 gave -17 V for V_a , rather than -45 V using equation [4.1] when reservoir 2 was not connected to the ground. Its standard deviation is ± 12 V based on the error propagation analysis of the calculation in equation [4.15]. The absolute standard deviation in the voltage calculated at any point along the channel resulted from the error accumulation in the calculations. Note that while the relative standard deviation is large at point "a", it will be much smaller at most other locations in the channel, where an appreciable voltage is present.

Using equation [4.15], the potential at reservoir 3 required to make $V_a = 0$ V was calculated to be 334 ± 14 V. In this case, the net flow in the channel between reservoir 2 and point "a" is 0, as discussed in section 4.3.6.

4.3.3 Geometrically defined injection

Accurately defined injection volume is certainly critical in realizing μ -TAS devices as an alternative to chemical sensors. However, it is imprecise to define injection volume by timing electroosmotic flow, because the flow rates change with the zeta potential, which changes with the column conditioning and effects such as surface adsorption (19). It is also impractical to use a standard injection loop as in HPLC because of difficulties in connecting to small capillaries without dead volume. Therefore it is desired to have sample injections defined geometrically. However, the studies on both Airport and CETAS devices suggested that cross and T intersections are not wholly satisfactory in that respect, due to diffusional leakage and convective mixing at intersections (12, 13, 20).

Diffusional leakage and convective mixing should, in principle, be restricted to the area surrounding the intersection. Consequently, using a "double T" arrangement it should be possible to define the sample geometrically if the separation between the two stems of the T is significant. Figure 4.4a shows a study of the amount of sample injected at a double T intersection of a Jet-1 device as a function of injection time. The two "stems" of the double T were separated by a distance of 150 μ m, so that the amount of sample injected should be essentially independent of the injection time above a certain value. The peak area of FITC labeled arginine (Arg-FITC) initially increased with increasing injection time, but then leveled off after ~ 7 s. Glu-FITC (FITC labeled glutamic acid) took longer time to reach a plateau due to its smaller mobility. It can be concluded that the injection volume is geometrically defined.

It should be noted that the injection direction used in Figure 4.4a was from reservoir 1 to 2, i.e. 2 was grounded. A surprise result was observed when the injection direction was reversed. Figure 4.4b shows

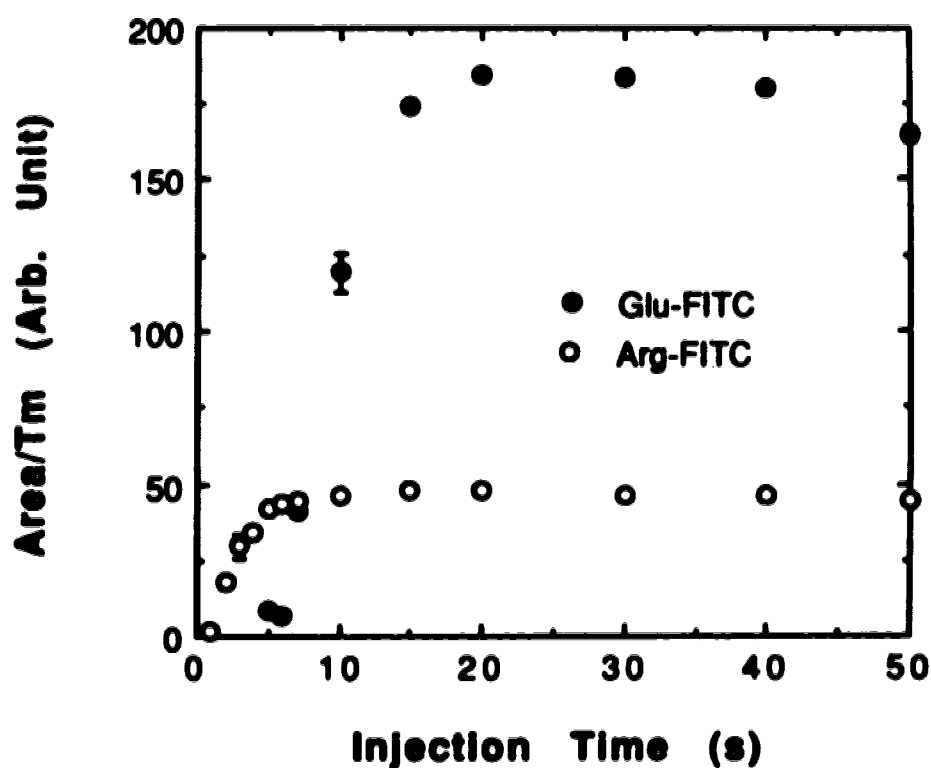


Figure 4.4a Geometrically defined injections on a Jet-1 device are shown. 10 μ M Arg-FITC and 10 μ M Glu-FITC in 0.05 M TRIS and boric acid buffer, pH 8.0 was used. Injection voltage of 500 V (228 V/cm) was applied between reservoirs 1 and 2 (2 was grounded), while a separation voltage of 3000 V (974 V/cm) was used between 3 and 4.

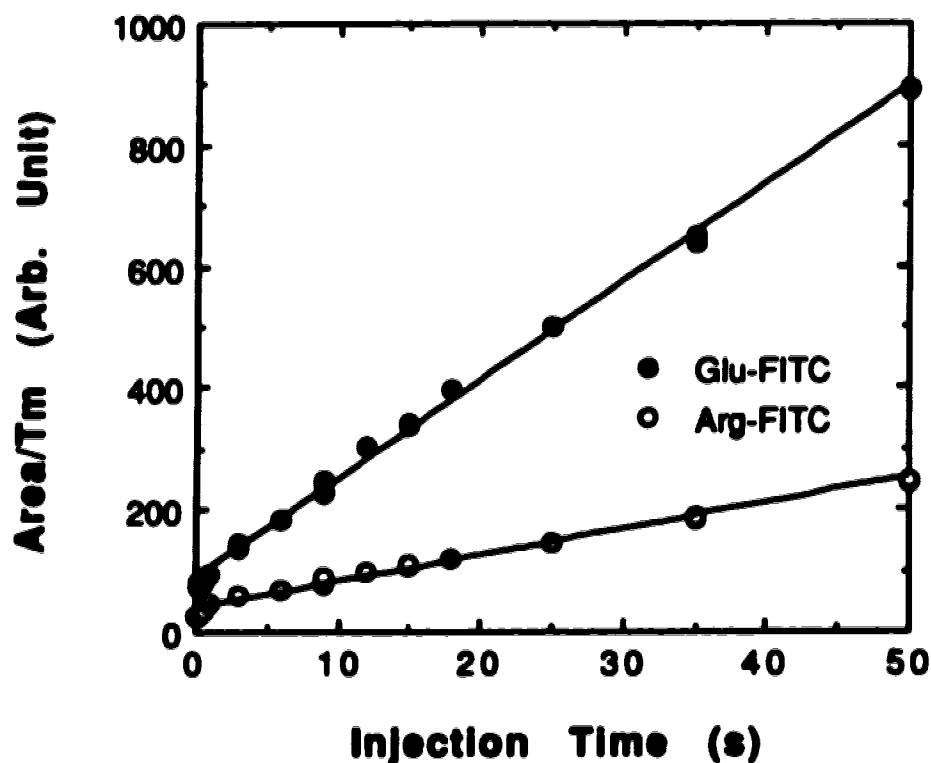


Figure 4.4b Non-geometrically defined injections on a Jet-1 device are shown when injections were directed from reservoir 2 to 1. 10 μM Arg-FITC and 10 μM Glu-FITC in 0.05 M TRIS and boric acid buffer, pH 8.0 was again used. Injection voltage of 500 V (228 V/cm) was applied between reservoirs 1 and 2 (1 was grounded), while a separation voltage of 4000 V (1230 V/cm) was used between 3 and 4.

that the amount of sample injected increased with the injection time over the time period studied when an injection voltage of 500 V (228 V/cm) was applied to reservoir 2 while reservoir 1 was grounded. This observation was confirmed by photomicrographs taken using the method discussed below. This abnormal result is probably related to the configuration of this double T injector. The two side channels connected to reservoirs 1 and 2 were 25 μm and 50 μm wide respectively, while the main channel was 30 μm wide. It appears that directing the sample flow from the large channel into the smaller one created a flow that could not be completely contained within the smaller channel.

Because of the complexity in the channel size of the double T injector of the Jet-1 device, there was a need to further study the double T injection using another device called Jet-3, which will be further discussed in chapter 5. The widths of the side and main channels of the double T injector in Jet-3 were all 30 μm . The depths of all channels in Jet-3 are the same as in Jet-1, 10 μm .

Figure 4.5 shows the relationship between the peak area and injection voltage measured in Jet-3. The device layout is shown at the top. The injections were run by applying voltages from 50 V to 1500 V (44 V/cm to 1332 V/cm) for 0.5 s between reservoirs 2 and 3, while 3000 V (1239 V/cm) was used for separations between reservoirs 4 and 5. Reservoir 1 was left floating at all times. Reservoir 2 contained a mixture of 10 μM Arg-FITC, Tyr-FITC (FITC labeled tyrosine) and fluorescein in pH 9.1 carbonate buffer, whereas all other reservoirs were filled with the buffer solution. The detector was located 1.6 cm from the injection point. The plateaus of three curves in the figure confirm that the geometrical area of the double T, i.e. the 220 μm offset between the side channels connecting reservoirs 3 and 4 in the Jet-3 device, essentially defines the injection volume as long as the injection voltage is high enough for a certain injection time.

Figures 4.4a and 4.5 demonstrate that geometrically defined injections can be obtained by either fixing injection voltage or injection time, so long as the injected volume is large enough. However, there is a discrepancy between the time required experimentally and that predicted. For example, the separation between the outside walls of the two "stems"

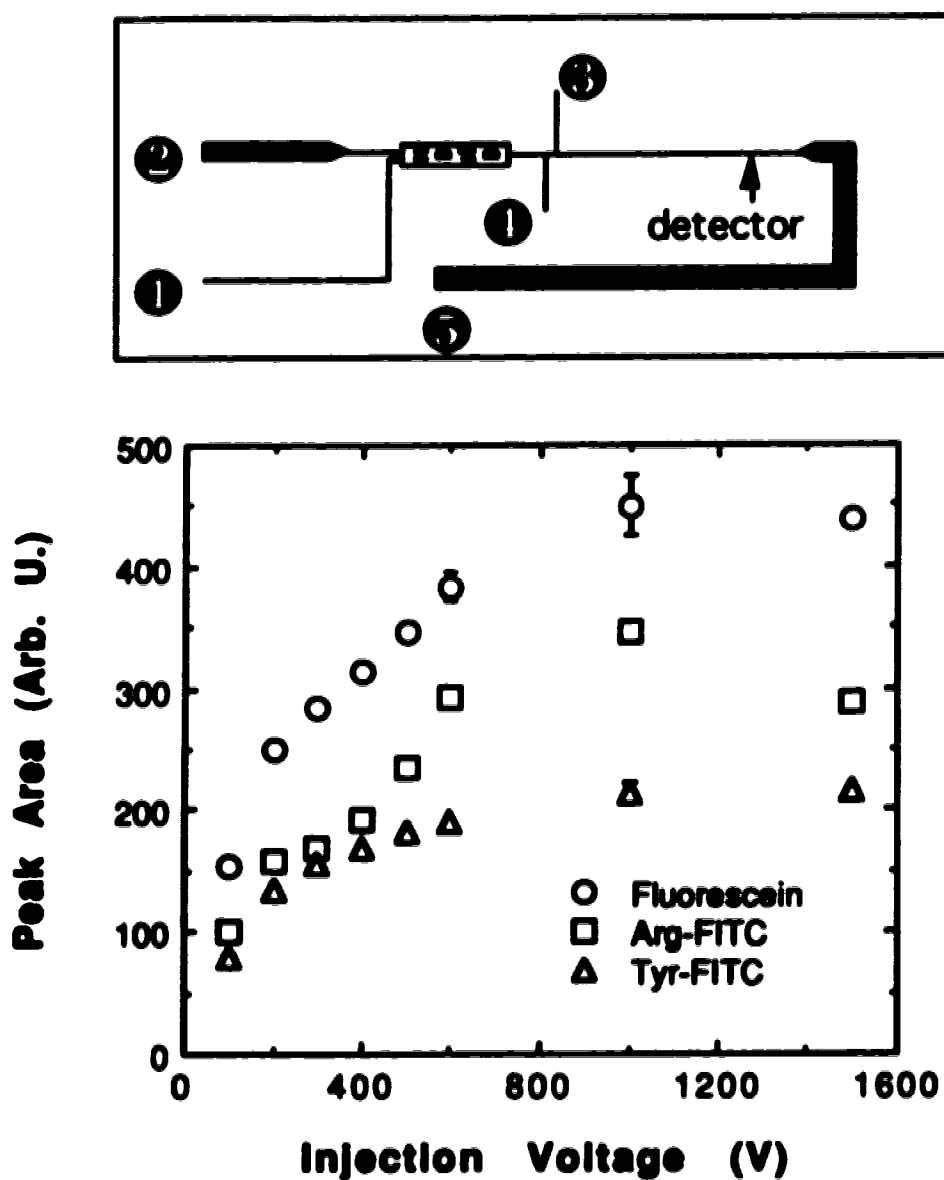


Figure 4.5 Geometrically defined injections were performed on a Jet-3 device, which layout is shown on the top. 10 μ M Arg-FITC, Tyr-FITC and fluorescein in pH 9.1 carbonate buffer was used. Injection voltages were applied between reservoirs 2 and 3 for 0.5 s, while a separation voltage of 3000 V (1239 V/cm) was used between 4 and 5.

of the double T in Jet-1 was 150 μm . To travel such a distance Arg-FTTC should take about 0.7 s, based on the mobility of $9.36 \times 10^{-5} \text{ cm}^2/\text{Vs}$ (pH 8.0 buffer). The mobility was determined in this device from the relationship between migration time and separation voltage (20). Experimentally, Arg-FTTC took ~7 s to reach a plateau. This discrepancy between the time required experimentally and that predicted suggests the volume includes both the geometrical volume of the double T intersection and the volume due to diffusional or other contributions.

The actual situation is shown in the photomicrographs in figure 4.6. These photos were taken when 50 μM fluorescein was driven from reservoir 1 to 2 of Jet-1 by applying 500 V between the two reservoirs. While positioned on an Olympus BH-2 microscope stage, the device was flooded with 488 nm light from a beam expanded Ar ion laser. Figure 4.6a shows there is no fluorescein at the intersection when the buffer was flowing in channel 3-4 before the injection. Figure 4.6b shows the fluorescein sample plug at the intersection about 2 s after the injection was started. A series of pictures was taken while the injection voltage was applied. These pictures clearly indicated that the injection volume was constant after about 7 s. The sample plug shapes after a 7s and 50 s injection are shown in figure 4.6c and figure 4.6d. The sample plug lengths in the pictures 4.6c and 4.6d were estimated at 300 μm based on the geometrical dimension of the channel.

The sample plug length can also be theoretically calculated using equation [4.16] (12, 13, 20).

$$H = \frac{2Dt_m}{d_{id}} + \frac{\omega_{inj}^2}{12d_{id}} + \frac{\omega_{det}^2}{12d_{id}} + \frac{2Dt_{inj}}{d_{id}} \quad [4.16]$$

where, H is the height equivalent to a theoretical plate (HETP), D is the diffusion coefficient, t_m is the migration time, d_{id} is the distance from injection to the detection point, ω_{inj} and ω_{det} are the lengths of the injection plug and detector cell, respectively, and t_{inj} is time between applications of the separation voltage (i.e. period of injection and delay times). This expression assumes a rectangular shape for the injection plug and

(a)



(b)

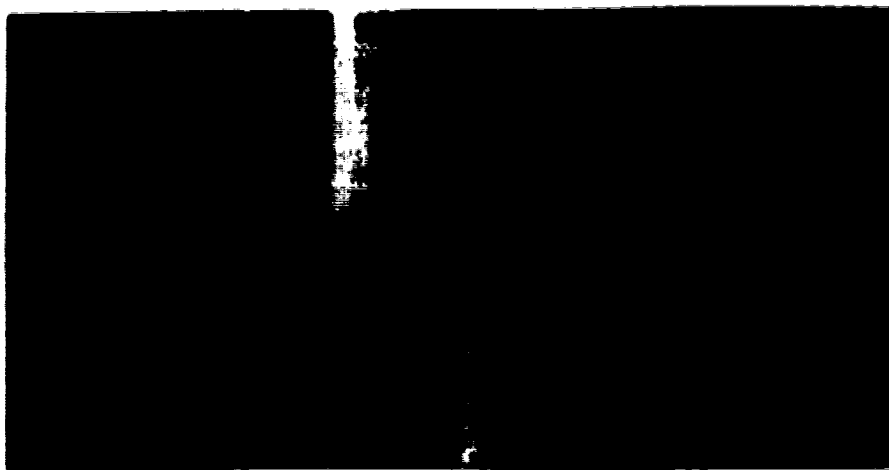


Figure 4.6 Photomicrographs of the injection area of the Jet-1 device. (a) The buffer was flowing in the channel 3-4 before the injection. (b) About 2 s after the injection was started. 50 μM fluorescein in pH 8.0 buffer was used. The injection was from reservoir 1 to 2, performed by applying 500 V between the two reservoirs. Pictures have been smoothed with software called "Adobe Photoshop".

(c)



(d)



Figure 4.6 Photomicrographs of the injection area of the Jet-1 device. (c) About 7 s after the injection was started. (c) After a 50 s injection. 50 μM fluorescein in pH 8.0 buffer was used. The injection was from reservoir 1 to 2, performed by applying 500 V between the two reservoirs. Pictures have been smoothed with software called "Adobe Photoshop".

detector volume, but makes no allowance for possible absorption effects on the walls of the glass. H and t_m were calculated as $2.87 \mu\text{m}$ and 19.6 s from the statistical moment analysis of the Arg-FITC peak in the electropherogram that was obtained in Jet-1 when the injection time was 10 s . Using $3.41 \times 10^{-6} \text{ cm}^2/\text{s}$, 2.3 cm , $100 \mu\text{m}$, and 12.4 s for D , d_{id} , ω_{det} , and t_{inj} respectively, the injection width ω_{inj} was calculated to be $721 \mu\text{m}$, which is much larger than actually observed in the picture. However, if we assume the injector acts as a mixing chamber rather than a rectangular plug, which means the dispersion from the injection is ω_{inj}/d_{id} instead of $\omega_{inj}/12d_{id}$ (22), then ω_{inj} would be calculated to be $208 \mu\text{m}$, which is smaller than the volume we observed. We can conclude the injector acted neither as a true plug injector nor as a mixing chamber. If we use the ω_{inj} of $300 \mu\text{m}$ we observed, the coefficient in front of d_{id} is 2.08 rather than 12 or 1.

An advantage of the double T injection scheme is that biases in injected sample volume using electromigration injection should essentially be avoided. Electroosmotic injection normally gives differing amounts injected because of differing mobilities (18). With long injection times in Jet-1 the sample concentrations in the injection section should virtually be equal to the bulk concentrations. Figure 4.7 shows the comparison of a double T injection (i.e. injection from reservoir 2 to 1 in Figure 4.1) with standard electroosmotic injection around a corner (i.e. injection from reservoir 2 to 4.). To compare the data for the two components the peak area has been normalized for migration time and concentration, since the area is governed by equation [4.17],

$$A = klt_m C \quad [4.17]$$

where A is peak area, k is a factor for the geometry, l is the length of the plug, C is the concentration, and t_m is the migration time (13). When a double T injection was used, the normalized peak areas for the two components injected differed by a factor of about 2. The differences remaining arise from experimental error in the concentrations, and the differences in the fluorescence quantum yield and labelling reaction yield.

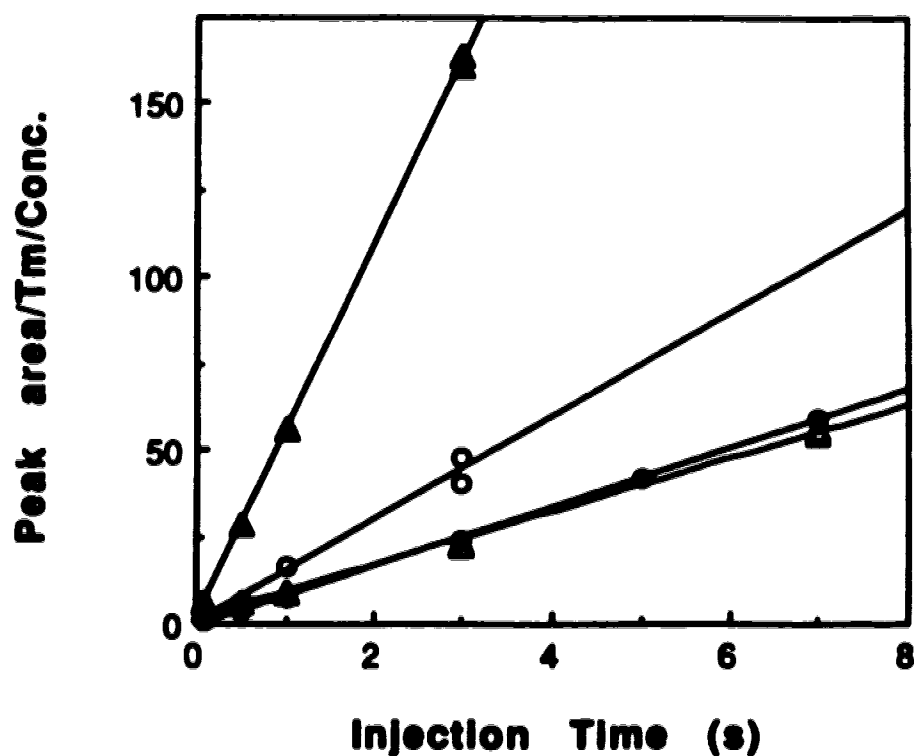


Figure 4.7 10 μM Arg-FITC and 20 μM Tyr-FITC in 0.05 M TRIS and boric acid buffer, pH 8.0 was used. Angle injection was performed by applying 2000 V (675 V/cm) between reservoirs 2 and 4, while H shape injection was by equivalent potential between 2 and 1 (1483 V). A separation voltage of 4000 V was used between 3 and 4. (Δ) angle injection, Arg-FITC; (\circ) Double T injection, Tyr-FITC; (\bullet) angle injection, Tyr-FITC; (\triangle) Double T injection, Arg-FITC. Lines are the least square fit of the data.

Using a spectrofluorophotometer, the emission spectrum peak ratio between Tyr-FITC and Arg-FITC is 1.6 times, which includes both the quantum yield and the reaction yield ratio since we prepared solutions using the same labelling reaction. In contrast, with angle injection (electrokinetic injection) the signal for Tyr-FITC is much smaller than for Arg-FITC, since the more mobile Arg-FITC has a longer injected plug than Tyr-FITC. In fact, since Tyr was twice as concentrated as Arg the mobility difference substantially overwhelmed the concentration difference.

The analysis of the same set of data in figures 4.4 and 4.5 gave the optimum injection parameters for the highest separation efficiency. Only the analysis of the data for fluorescein and Arg-FITC in figure 4.5 is shown in figure 4.8. The highest separation efficiency was obtained when injection voltages were 200 V (178 V/cm). It decreased when injection voltages were more than 300 V (266 V/cm), because overloading took place due to a longer sample plug that resulted from a higher injection voltage. Unfortunately, this means that the separation channel was overloaded when geometrically defined injection parameters were used. However, overloading due to large sample plug could be compensated by using a longer separation channel, so that the ratio of sample plug length to channel length is more reasonable. This should be considered when designing new devices.

In fact, the separation efficiency for both fluorescein and Arg-FITC also decreased when the injection voltages were 100 V (89 V/cm). This could be due to distortions in the idealized plug shape of the sample injection, especially when the sample plug was very small. The distance Arg-FITC travelled after 0.5 s injection at 100 V was 71 μm , which is much smaller than the offset (220 μm) between two stems of the double T injector in Jet-3. However, the distortion in the sample plug shape could have much less effect on the separation efficiency when a larger sample plug is injected. When 200 V (178 V/cm) was used for the injection, the plug would be 142 μm long, so that distortion in the plug shape might be relatively less important.

Nevertheless, the injected sample volume at these conditions was

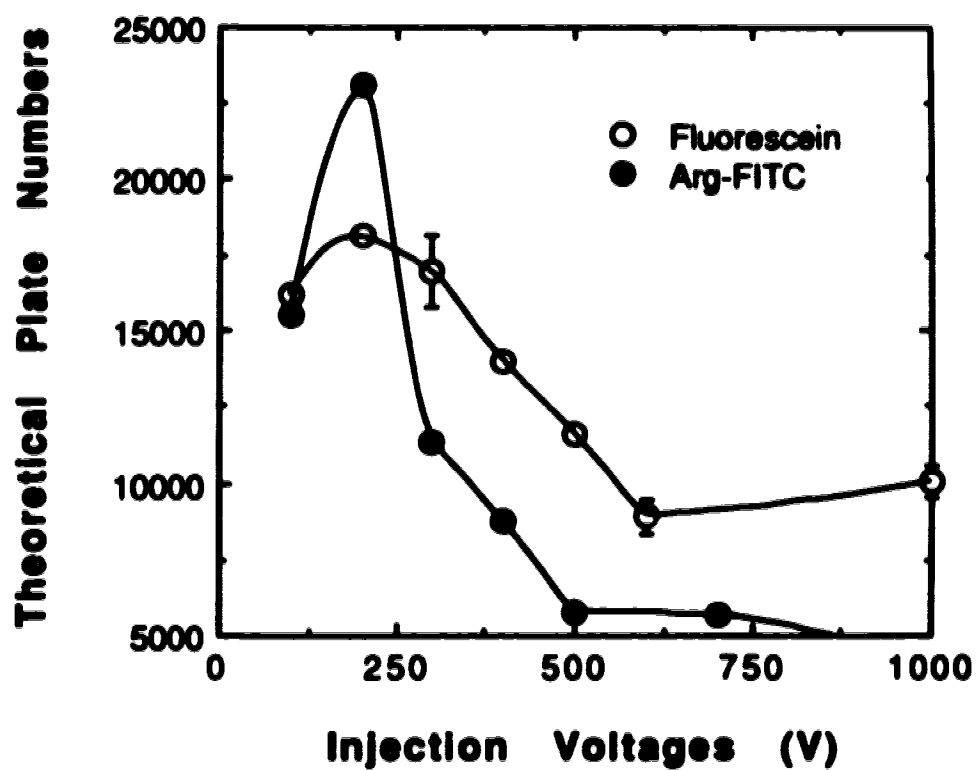


Figure 4.8 The relationship between theoretical plate numbers and injection voltages. Conditions are the same as in figure 4.5. Curves are drawn for clarity.

quite reproducible. Figure 4.9 shows two essentially identical electropherograms using the same injection conditions (100 V, 0.5 s), and an electropherogram using a different injection condition (200 V, 0.5 s).

The maximum separation efficiency we have achieved on Jet-3 was 23,000 plates for Arg-FITC over a 1.6 cm separation distance when 2000 V (826 V/cm) was applied between 4 and 5 for separation and 200 V (178 V/cm) between 2 and 3 was for 0.5 s injection. The efficiency was 17 plates/V, which is higher than the 5 plates/V we achieved in Jet-1 devices. However, it is still lower than 20-30 plates/V reported in conventional CE or in devices recently developed at Ciba-Geigy (14).

4.3.4 Fast separation of 6 amino acids.

Separation of Arg-FITC, Phe-FITC (FITC labeled phenylalanine) and Glu-FITC on Airport devices is relatively easy because these three have different charges in the buffer solution (20). In order to show the ability to effect separation of species with the same charge 3 other amino acids, alanine (Ala), aspartic acid (Asp), and tyrosine were used as well. The electropherograms of the 6 amino acids in pH 8 tris, boric acid buffer are shown in Figure 4.10. The injection was made using the angle injection method, with 2kV applied for 3 s between reservoirs 2 and 4. The separations were complete within as little as 40 seconds, except for resolving Ala-FITC from Phe-FITC. These separations were performed in Jet-1 which had relatively low efficiency. More efficient separations on even faster time scale have recently been performed in other devices (14). However, these were not the subject of this thesis.

4.3.5 Channel dimension change

It is known that the separation efficiency decreases when the column dimensions abruptly increase in HPLC, however there are no studies on this subject in conventional CE. It is useful to know the magnitude of the efficiency loss over channel dimension changes because it may sometimes be necessary to change channel dimensions in μ -TAS

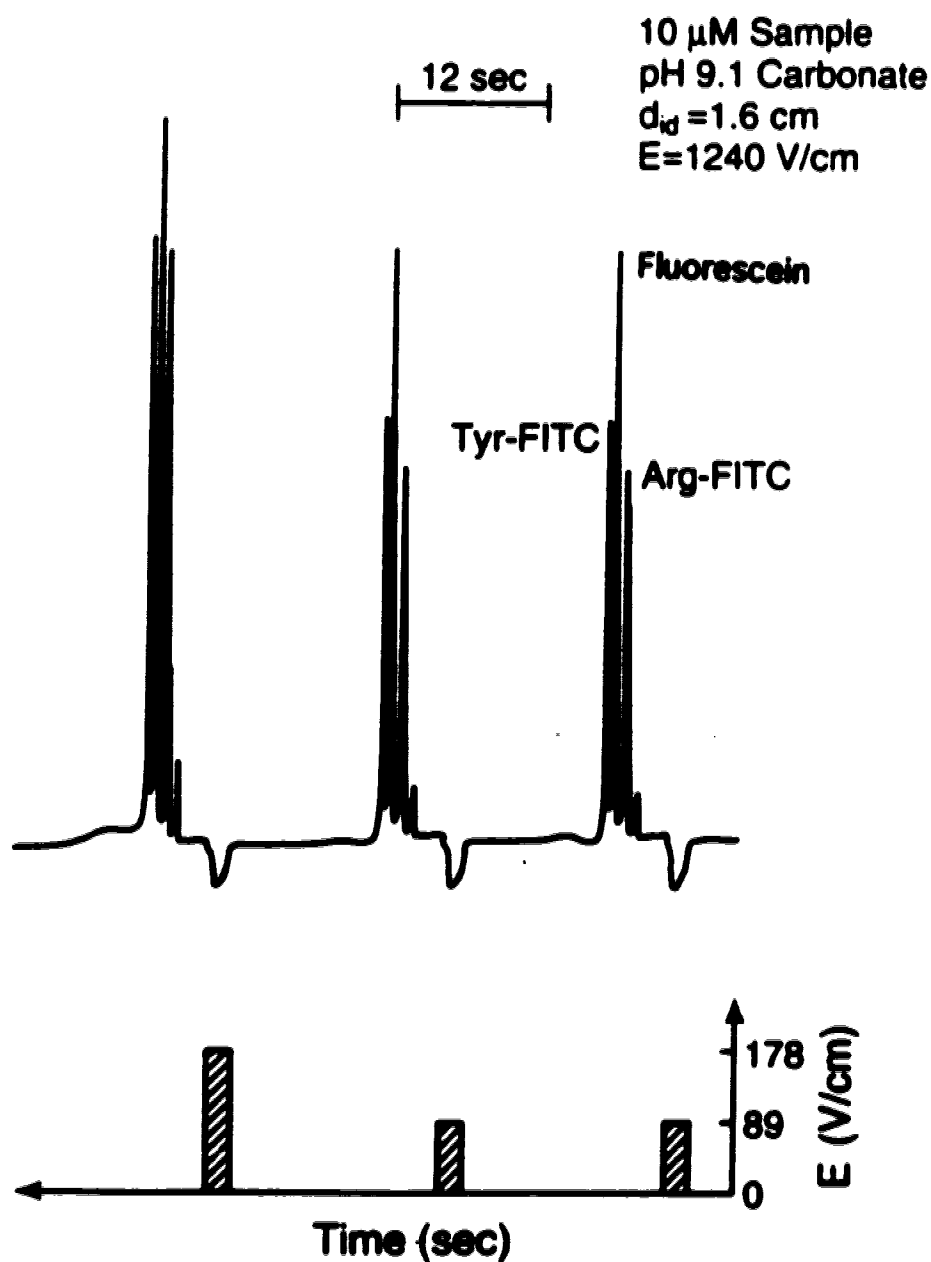


Figure 4.9 Repetitive injections performed on a Jet-3 device. As indicated, the injection voltage for the first two electropherograms was 100 V (89 V/cm), while that for the third one was 200 V (178 V/cm). Other conditions are the same as in figure 4.5. The time interval between electropherograms includes both injection time and delay time. 30 mM carbonate buffer was used.

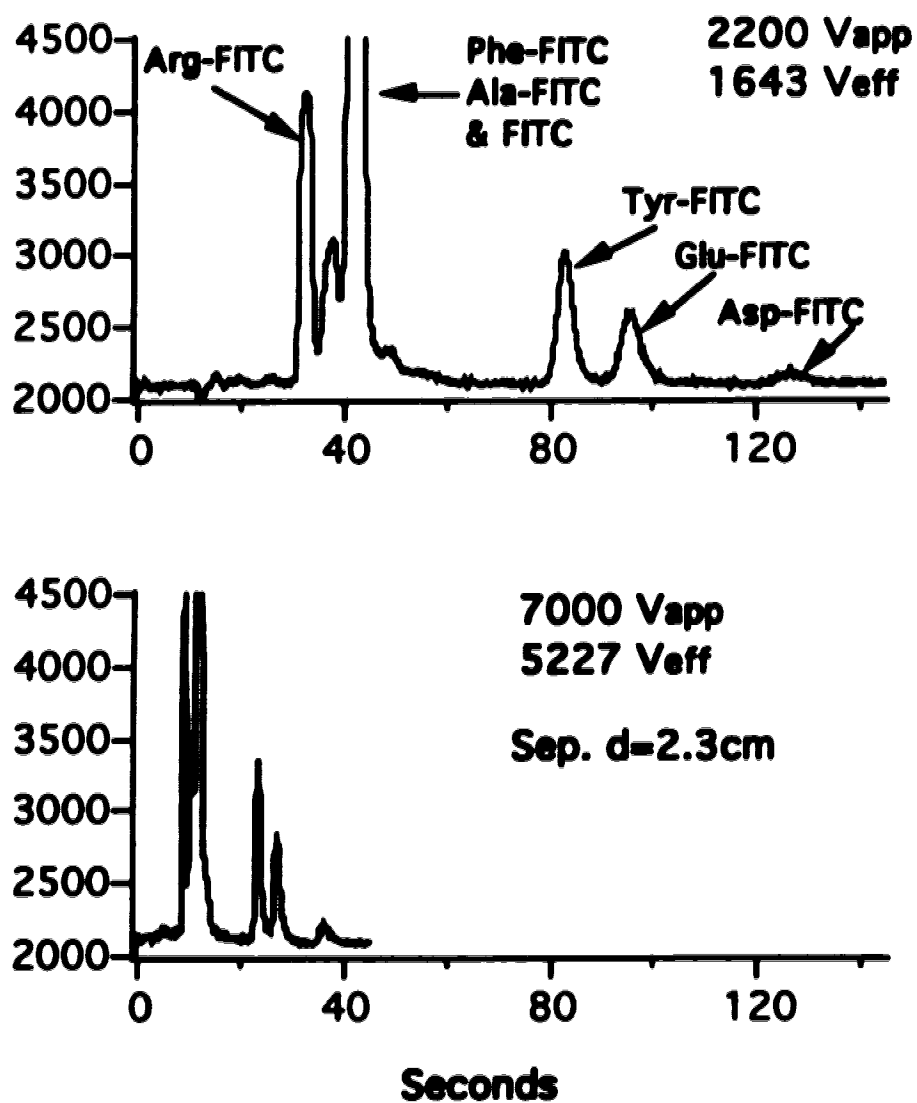


Figure 4.10 Electropherograms of separations of a mixture of 6 amino acids in pH 8.0 TRIS/boric acid buffer. Angle injection of the sample was used.

devices. Figure 4.11 shows a significant loss of separation efficiency when the width of the separation channel changes abruptly from 30 μm to 300 μm . This is at a place immediately past the indicated detector position in figure 4.1, where the channel opens up. The theoretical plate height is constant along the capillary, as it should be before the point in the channel where the dimensions change. It then increased 2.6 times immediately after the channel size increased, then increased 6.2 times 1 mm into the 300 μm channel. The signal can not be detected 1 cm after the dimension change. The abrupt change in Jet-1 device could be expected to give parabolic flow and so greatly degrade efficiency. A graduated increase in channel size was designed for Jet-2, unfortunately Jet-2 was not made because of some defects in the master mask.

4.3.6 Leakage suppression

Both studies on Airport and CETAS devices indicated that sample in the injection capillary contaminated, and even mixed into the buffer in the separation capillary when effecting separation (12, 13, 20). This was caused by diffusional leakage and convective mixing taking place in the intersection. The leakage phenomenon increased the background signal and decreased the dynamic range of detection. Active voltage control of each reservoir ought to solve this problem, because it can be arranged to push samples back towards the sample reservoir to suppress leakage while performing separations. Figure 4.12 shows the background can be driven to a very low level with active voltage control.

For the experiments shown in Figure 4.12 sample solution was present in reservoir 2, which was held at ground. As shown in the inset of the figure at the top, samples were injected across the double T towards reservoir 1, which was at -3kV. The times of injection were varied because the distances the sample was pushed back towards reservoir 2 during the separation step varied with the potentials applied. During separation the voltages of reservoirs 2, 3, and 4 were controlled, while reservoir 1 was left floating (i.e. no electrical contact), as shown in figure 4.3b. Consequently, flow of solution from the sample channel was controlled. However,

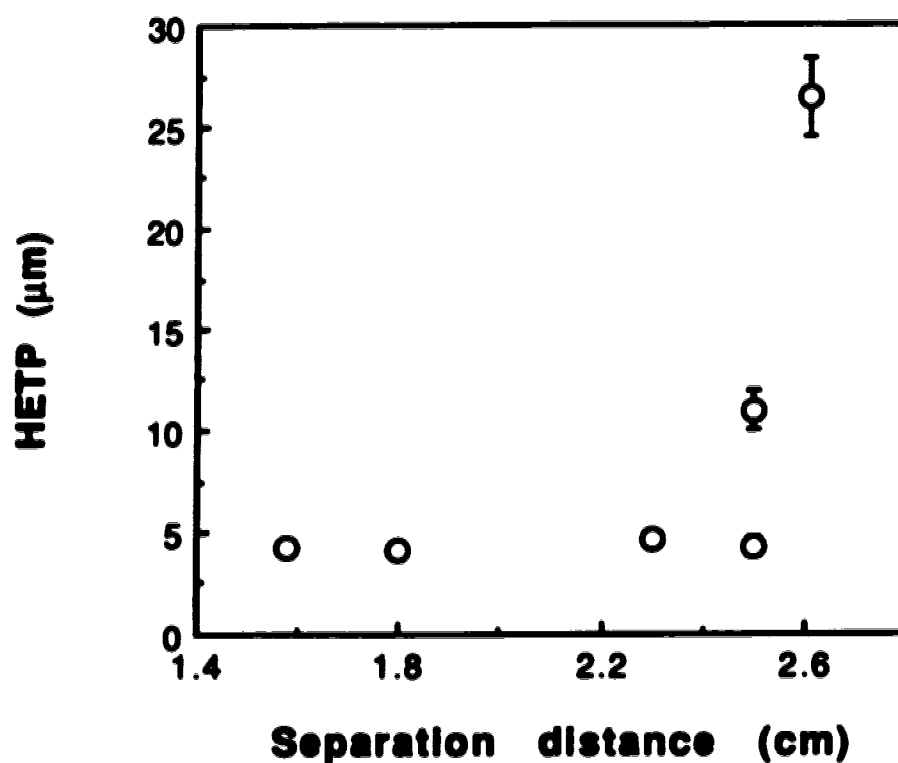


Figure 4.11 Separation efficiency loss over a channel dimension change. 50 μM fluorescein in 0.05 M TRIS and boric acid, pH 8.0 buffer was used. The 30 μm wide channel opened up abruptly to 300 μm at a separation distance of 2.5 cm. Injection voltage of 200 V was applied for 0.5 s between reservoirs 1 and 2, while 4000 V was used as the separation voltage over reservoirs 3 and 4.

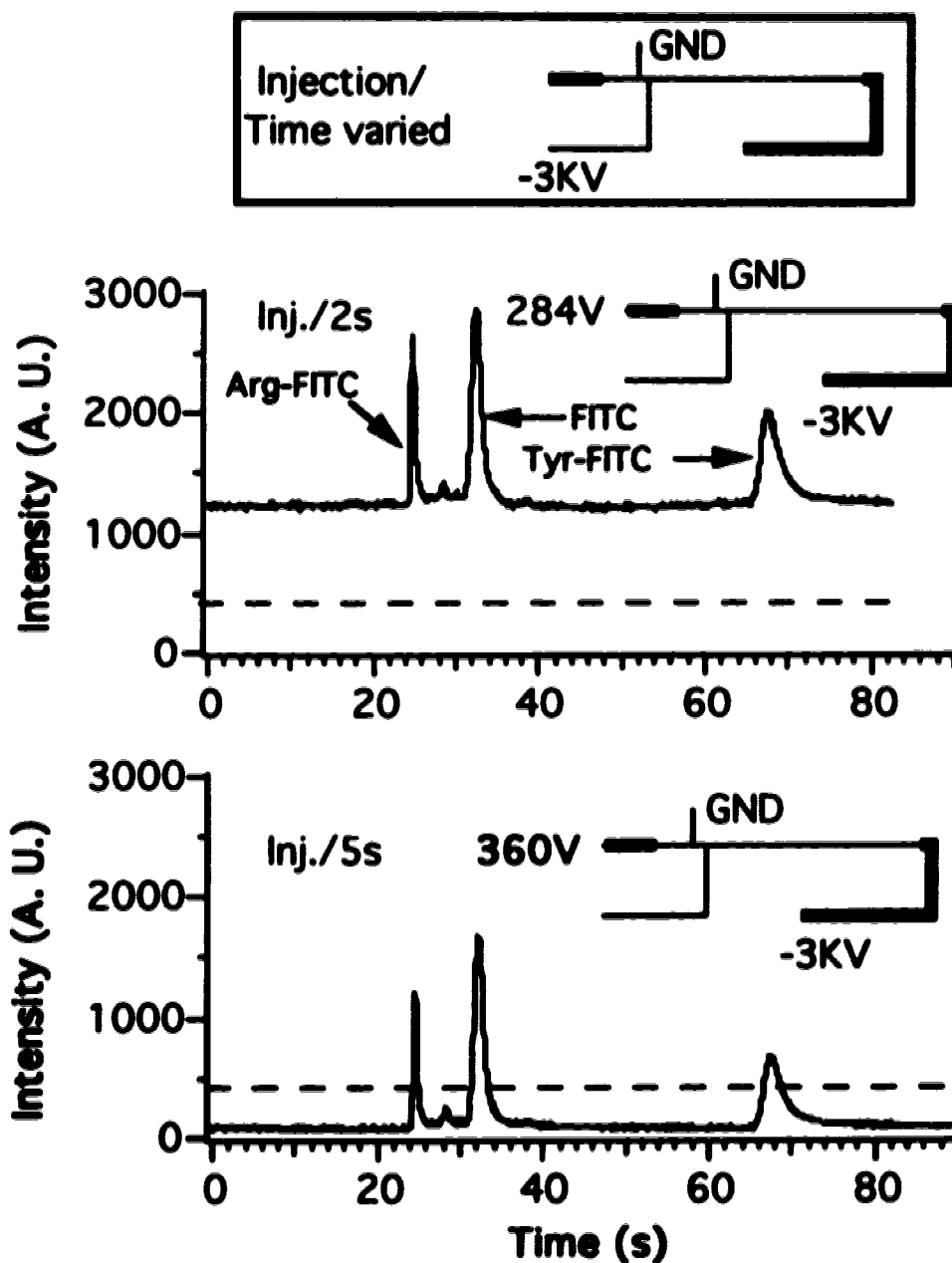


Figure 4.12 Separation of 20 μM Arg-FITC and 40 μM Tyr-FITC in 0.064 M carbonate buffer, pH 9.1 with voltage control of background leakage from the sample channel. The dashed lines indicate the background level without active voltage controls. The inset in the box shows the injection potentials. The injection times varied as indicated.

leakage from the injection waste channel, *i.e.* from reservoir 1, would still occur, just as was seen for the experiments performed in CETAS (12). Because of the long distance of channel 1 relative to channel 2 we expected leakage from channel 1 to be much smaller. Additionally, since reservoir 1 contained buffer the only source of dye was the excess which was introduced during the injection step. There should be relatively little contribution to the fluorescence background from leakage out of channel 1.

In the first electropherogram of Figure 4.12, 284 V was applied to reservoir 3 during the separation. The background level is also shown with a dashed line in the figure which was obtained at the same conditions except reservoir 2 was disconnected. Resistance simulation discussed in section 4.3.2 indicates that the potential at the intersection with the sample channel (*i.e.*, point "a" in the figure 4.3b) should be (-17 ± 12) V. Since the sample channel was at ground, this should mean there is a net flow out of the sample channel, as evidenced by the higher background in the electropherogram than that when reservoir 2 was disconnected. A negative current calculated for I_2 using equation [4.12] also confirmed this flow direction. When the potential at reservoir 3 increases, the potential at the injection point will eventually become positive, which should electroosmotically push sample solution back towards reservoir 2. As shown in Figure 4.12, higher voltage at reservoir 3 does lower the background fluorescence, indicating flow from reservoir 2 is slowed and then prevented or even reversed. In fact it is reversed, since the background level when 360 V was applied to reservoir 3 was much lower than when reservoir 2 was left floating. This result also explains the need for longer injection periods when the separation potential on channel 3 was increased.

The data in Figure 4.12 confirm that there is leakage from the side channel during the separation. Figure 4.13 shows the intensity of background fluorescence during separation as a function of the potential applied to reservoir 3. A potential of about 350 V is required at reservoir 3 to prevent the leakage from the side channel, which is slightly higher than the theoretically predicted value (334 ± 14) V in section 4.3.2.

The background level attained with 360 V applied to reservoir 3

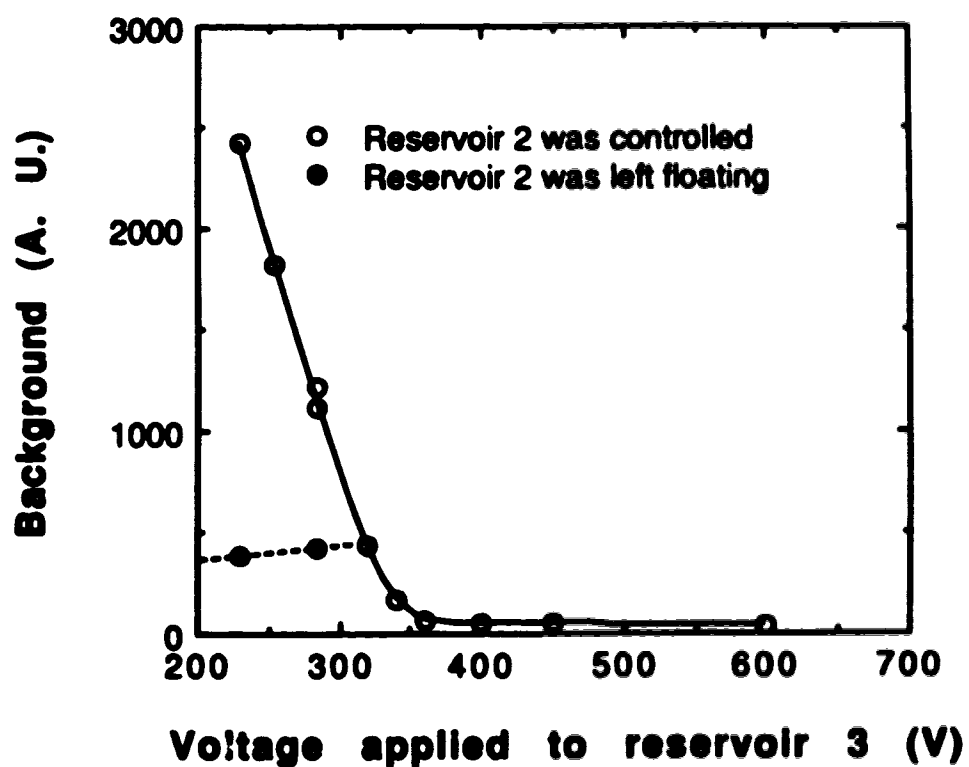


Figure 4.13 The effect of the active voltage control on the background. The background signals when reservoir 2 was left floating are also shown for comparison. Injection and separation conditions are the same with figure 4.12.

during separation substantiates our contention that there is relatively little leakage from reservoir 1, even though it is floating. Since some dye must be present in this channel, introduced by the injection step, there should be some contribution to background. However, Figure 4.12 shows it is no more than about 3% of the signal, similar to the value obtained in CETAS (12). Since the leakage from the sample channel is so much higher this suggests a strategy to control or reduce leakage. As in CETAS it appears it may be useful to have a sample introduction channel which is not too much shorter than the separation channel. This will mean that the back pressure or resistance of the channel to solvent flow is similar to the separation channel and reduce the tendency to have large flows. Conversely, a short side channel may leak excessively because of its low resistance to flow.

The advantage of active voltage control demonstrated here principally lies in the ability to increase the dynamic range of detection. When μ -TAS devices are used with real samples, low concentration components in them would not be detected, because leakage of higher concentration components would give a background that would overwhelm smaller signals.

4.3.7 Calibration curve and the use of a standard

In chemical analysis calibration is a necessary step for accurate measurements. We examined different concentrations of Arg-FITC and Tyr-FITC ranging from 0.05 μ M to 100 μ M in 0.064 M carbonate, pH 9.1. The injection and separation schemes are the same as those described above for suppressing leakage by active voltage control. The potential of reservoir 3 was fixed at 380 V to ensure no leakage at the intersection from the sample channel. The injection time lasted for 5 s. A fairly linear relationship between peak area (or peak height, although it is not shown) and concentration was obtained for concentrations less than 20 μ M, as shown in Figure 4.14a. However, the plots deviate at higher concentrations as shown in the inset, most likely due to quenching, which usually occur at high concentrations of fluorescent compound (23). Self-

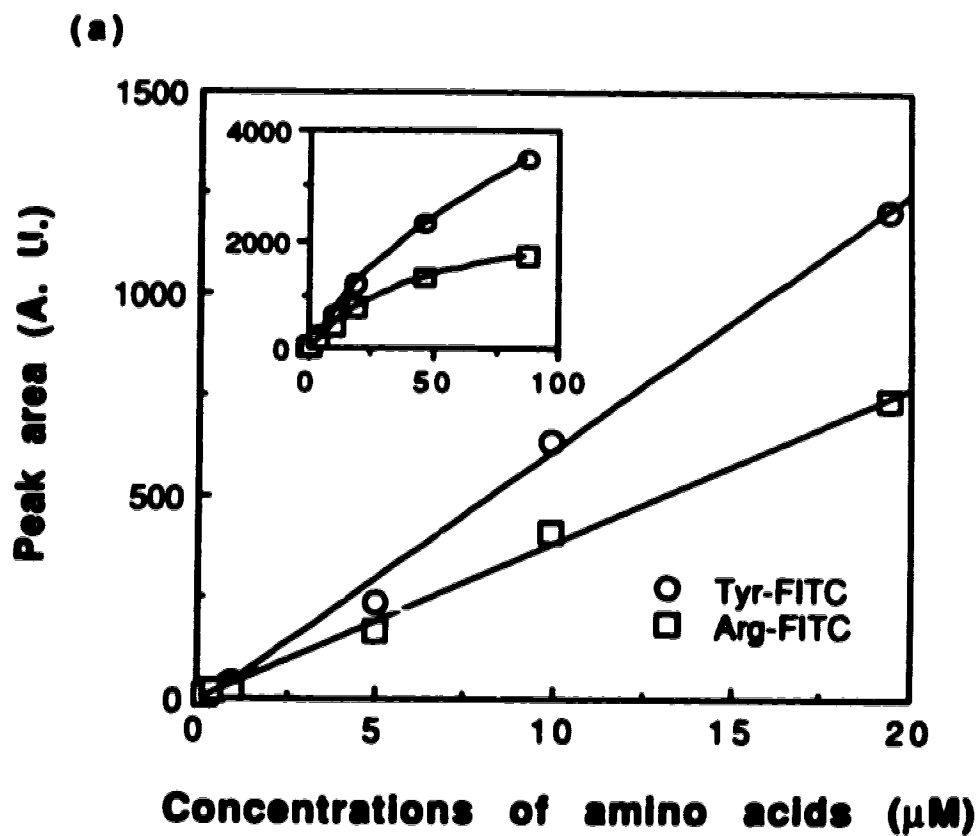


Figure 4.14 (a) Linear relationship between peak areas and amino acid concentrations up to 20 μM . The inset shows the deviation at higher concentrations. Injections and separations were performed as for figure 4.12.

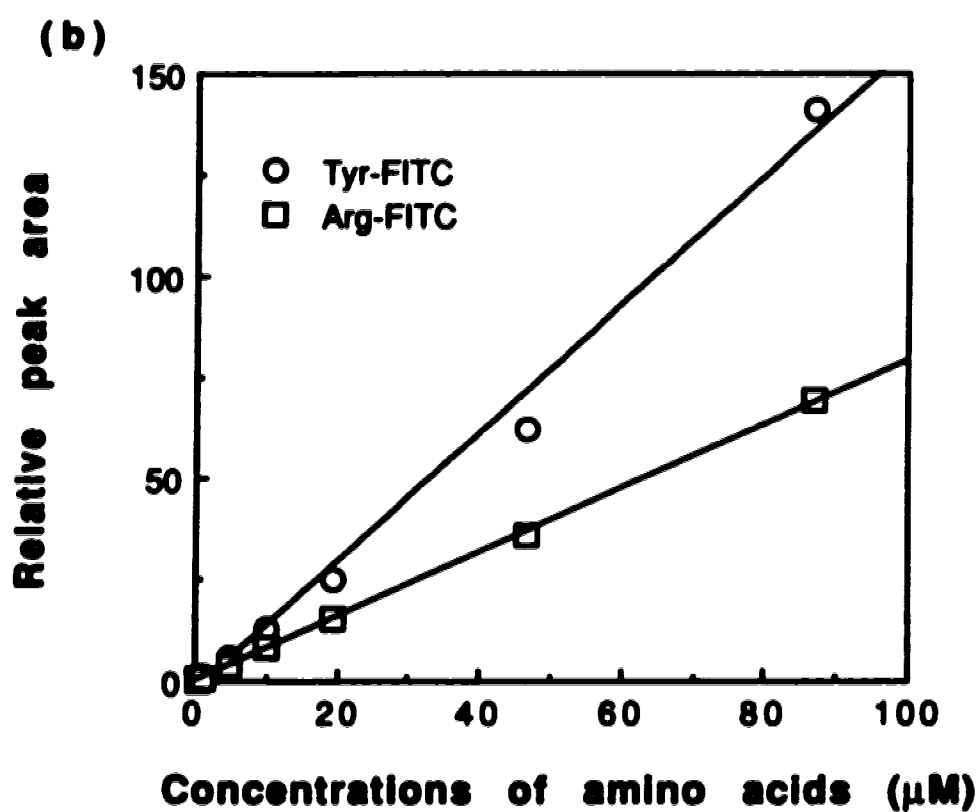


Figure 4.14 (b) Peak areas in figure 4.14a have been normalized to the response for aniline standard and linear relationship has been extended to 100 μM .

absorption is negligible according to the calculation based on the absorption coefficient, the concentration of fluorescein, and light path length.

In order to correct quenching, aniline (AN) was used as a form of internal standard. Aniline was derivatized in the same way as other amino acids, and included in the amino acid mixture. Dilution of the mixture to obtain lower concentrations of amino acids proportionally changed the concentration of aniline. This was different from the conventional technique using an internal standard, as the same amount of an internal standard is usually added into each sample. To correct for quenching the internal standard should have about the same concentration as the sample. This may not always be convenient, but it does offer two benefits. First it will correct the injection volume if electroosmotic mobility changes during the experiments. Secondly, it extends the linear range because AN-FITC should have similar self-absorption and quenching as FITC labeled amino acids. Figure 4.14b shows the extended calibration curve in which peak areas of amino acids were ratioed by aniline peak areas. The slopes of logarithm plots of the same set of data are 1.18 and 0.98 for Tyr-FITC and Arg-FITC respectively. The linearity of the response indicates the effectiveness of the standard.

In order to estimate the detection limit, the noise of the background in electropherograms has been analyzed. The noise of the background is 1.9 ± 0.3 and 2.3 ± 0.3 (arbitrary unit) respectively for those electropherograms of $1 \mu\text{M}$ and $0.2 \mu\text{M}$ amino acid solutions. If we assume that the signal larger than 3 times of the noise is detectable, the detection limit was calculated to be about $0.04 \mu\text{M}$ based on the corresponding peak height of each solution. This detection limit was slightly underestimated, as there was no noticeable peaks in the electropherograms obtained for the $0.05 \mu\text{M}$ amino acid solutions.

4.4 Conclusions

The double T injection designed in both Jet-1 and Jet-3 devices is able to define injection volumes geometrically. This offers μ -TAS devices

an advantage over conventional electromigration injection in CE, because it avoids the need to correct for the bias in sample injection volume due to different ionic mobilities. Geometrically defined injections also prevented the changes of injection volume with the capillary conditions, which was affected by surface absorptions. As a result, flow injection analysis systems integrated with a μ -TAS device could be made reliable in terms of the injection volume. The results described for calibration curves as a function of concentration demonstrate that μ -TAS devices should be capable of quantitative chemical analysis.

The injection volume defined by a double T is larger than the real geometrical volume, as diffusion and convection taking place during injection contribute to the sample size as well. Therefore, it is possible to overload the separation channel if it is very short. The appropriate sample injection volume is from 0.1% to 1% of the separation channel volume (23). This must be considered when new devices are to be designed.

Voltage control of multiple reservoirs shows that the leakage due to diffusion and convection can be suppressed if it is a problem for a given application. Since multiple channel voltage control can be used to effect dilutions, as shown in the next chapter, this indicates the power of electroosmotic pumping as a tool in a μ -TAS environment, and confirms it can meet the initially proposed expectations.

In addition, the resistance simulation is very effective in predicting the potential at a particular point and selecting an appropriate potential for each reservoir. When leakage suppression using multiple channel voltage control is necessary, it is important to use the resistance simulation to choose appropriate voltages.

4.5 References

1. Mikkers, F. E. P.; Everaerts, F. M.; Verheggen, Th. P. E. M., *J. Chromatogr.*, **1979**, *169*, 11-20.
2. Jorgenson, J.; Lukacs, K. D., *Anal. Chem.* **1981**, *53*, 1298-1302.
3. Jorgenson, J.; Lukacs, K. D., *Science*, **1983**, *222*, 266-272.
4. Grossman, P. D.; Colburn, J. C., Eds, *Capillary Electrophoresis*:

- Theory and Practice*, Academics Press: San Diego, CA, 1992.
5. Kuhr, W. G., *Anal. Chem.* 1990, 62, 403R-414R.
 6. Kuhr, W. G.; Monnig, C. A., *Anal. Chem.* 1992, 64, 389R-407R.
 7. Ewing, A.; Wallingford, R. A.; Olefirowicz, T. M., *Anal. Chem.* 1989, 61, 292A-303A.
 8. Bushey, M. M.; Jorgenson, J. W., *Anal. Chem.* 1990, 62, 978-984.
 9. Bushey, M. M.; Jorgenson, J. W., *J. Microcolumn Sep.*, 1990, 2, 293-299.
 10. Lemmo, A. V.; Jorgenson, J. W., *Anal. Chem.* 1993, 65, 1576-1581.
 11. Olefirowicz, T. M.; Ewing, A., *Anal. Chem.* 1990, 62, 1872-1876.
 12. Harrison, D. J.; Manz, A.; Fan, Z.; Lüdi, H.; Widmer, H. M., *Anal. Chem.*, 1992, 64, 1926-1932.
 13. Seiler, K.; Harrison, D. J.; Manz, A., *Anal. Chem.*, 1993, 65, 1481-1488.
 14. Harrison, D. J.; Fluri, K.; Seiler, K.; Fan, Z.; Effenhauser, C. S.; Manz, A., *Science*, 1993, 261, 895-897.
 15. Manz, A.; Fettingner, J. C.; Verpoorte, E.; Lüdi, H.; Widmer, H. M.; Harrison, D. J., *Trends Anal. Chem.* 1991, 10, 144-149.
 16. Manz, A.; Harrison, D. J.; Verpoorte, E.; Fettingner, J. C.; Lüdi, H.; Widmer, H. M., *J. Chromatogr.*, 1992, 593, 253-258.
 17. Rose, P. J.; Jorgenson, J., *Anal. Chem.* 1988, 60, 642-648.
 18. Huang, X.; Gorgon, M. J.; Zare, R. N. *Anal. Chem.* 1988, 60, 377-380.
 19. Huang, X.; Coleman, W. F.; Zare, R. N. *J. Chromatogr.* 1989, 480, 95-110.
 20. Fan, Z.; Harrison, D. J., *Anal. Chem.* 1993, 65, in press.
 21. Harrison, D. J.; Glavina, P. G.; Manz, A., *Sensors and Actuators*, 1993, B10, 107-116.
 22. Sternberg, J.C. *Adv. Chromatogr.* 1988, 2, 206-270.
 23. Skoog, D. A.; Leary, J. J., *Principles of Instrumental Analysis*, 4th Ed, Saunders College Publishing: Orlando, FL, 1992, Chapter 9, 174-195.
 24. M. J. Gordon, X. Huang, S. L. Pentoney Jr., R. N. Zare, *Science*, 1988, 242, 224-228.

Chapter 5

A Micromachined Mixing Chamber in a Miniaturized Capillary Electrophoresis System

5.1 Introduction

Capillary electrophoresis (CE) has created much research interest since Jorgenson and Lukacs showed its power in separation efficiency and resolution (1, 2). Most efforts addressed biological applications such as separation and characterization of amino acids, peptides and proteins, as may be seen in a recent book (3). Detection was often accomplished using an on-column fluorescence detector because of its high sensitivity. Since most biological compounds lack or have low native fluorescence, a fluorescent tag was usually added to analytes prior to separation (4). However, off-column labelling has some limitations as Rose and Jorgenson have pointed out (5). First, some labelled compounds decompose over time with the rate of decomposition being compound dependent. This causes problems not only with quantitative analysis but with qualitative analysis as well. Decomposition changes the mobilities of analyte ions, for the fluorescent tag changes the net charge of sample molecules. Besides, multiple labelling could take place for large molecules due to the presence of several amino groups. As a result, a single compound could yield multiple peaks.

On-column derivatization is certainly one of the solutions. There are three schemes that have been studied, pre-capillary (6), on-capillary (7, 8), and post-capillary (5, 9-13). Pre-capillary methods introduced a labelling agent and had the derivatization take place at the very beginning of the separation capillary (6). One should distinguish it from the term "off-column" mentioned above. Only the injected sample was labelled and the reactions took place inside the separation capillary for the pre-capillary

derivatization, whereas all samples in the sample reservoir were labelled and the reactions occurred in a conventional container for the off-column derivatization. For the on-capillary scheme, a labelling agent was either present in the buffer (7) or immobilized on the capillary walls (8), so that the derivatization reactions were performed during the separation. Post-capillary methods mixed a fluorophore with the effluent at the end of the separation capillary where the labelling reactions took place immediately.

Both pre-capillary and on-capillary derivatization prevent labelled compounds from decomposing in a short separation time, but they can not avoid multiple labelling (5). Post-column derivatization is thus most interesting. Jorgenson *et al.* have developed a coaxial post-capillary reactor in which a concentric capillary with a larger diameter was used for the introduction of the labelling agent at the end of the separation capillary (5, 9). A fluorogenic agent, o-phthalaldehyde (OPA), flowing in the outer capillary mixed with the effluent at the end of the inner capillary (*i.e.*, the separation capillary). Amino acids in the effluent reacted with OPA to form fluorescent compounds, which were detected. Alternatively, Rose used a stationary solution reactor which contained the fluorophore agent and functioned as a waste reservoir as well (10). The fluorescence was detected just beyond the capillary tip with the aid of optical fibers. Post-capillary derivatization could also be achieved using a gap junction reactor in which two capillaries were separated by a 50 μm gap while the labelling agent was introduced into the gap (11). A more conventional approach has also been reported, in which a syringe pump was used to mix the fluorophore agent with the column effluent via a relatively large diameter three-way connector (12). Recently, Dasgupta *et al.* utilized a membrane sleeving two capillaries for the introduction of a reagent, although it was developed as a suppressed conductimetric detector (13).

All these configurations for post-capillary derivatization included connectors with different size from the separation capillary and thus inevitably resulted in dead volumes. The separation efficiency was therefore considerably sacrificed. Micromachining, which involves integrated circuit fabrication technology, is capable of fabricating micron scale capillaries and connectors without dead volumes. Several

miniaturized capillary electrophoresis systems in glass chips have been fabricated using this technique (14-16). They have shown very little, if any, dead volumes.

This chapter presents the study on a micromachined mixing chamber which might be used as a micro-reactor for pre-capillary or post-capillary derivatization. The chamber was incorporated with a miniaturized capillary electrophoresis system including sample pretreatment, injection, separation, and detection. This system was designed as a part of the plan to realize the concept of miniaturized total chemical analysis systems (μ -TAS) discussed in chapters 1, 3, 4. A mixing chamber used for sample pretreatment such as dilution and derivatization is an essential component of a μ -TAS device when it is utilized for chemical analysis. Such a mixing chamber could have significant influence on the performance, *e. g.*, separation efficiency, of a μ -TAS device.

5.2 Experimental Section

Corning 7740 (Pyrex) was obtained from Paragon Optical Co. (Reading, PA) and was annealed at 570 °C for 6 hours before use. The glass devices were fabricated at Alberta Microelectronic Centre (Edmonton, Canada) using the micromachining technology described in chapter 3.

Amino acids, fluorescein and fluorescein-5-isothiocyanate (FITC) were used as received from Sigma. A pH 8.0 buffer of 0.05 M boric acid and 0.05 M tris(hydroxymethyl) aminomethane (TRIS), as well as a pH 9.1 buffer of 0.032 M sodium carbonate were used. All chemicals are of reagent grade and all solutions were prepared in deionized, double-distilled water. Amino acids were derivatized with FITC in the same way as in chapter 4. Solutions were filtered with Miller-GV sterilizing filter unit with 0.22 μ m membrane (Millipore, Bedford, MA) before injecting to capillaries.

The apparatus was the same one used for the work described in chapter 3. The detections were performed by a laser-induced fluorescence detector. Fluorescence emission was collected with a 10:1 microscope objective and directed onto a photomultiplier tube using a 1 mm diameter pinhole at the image plane and an optical band-pass interference filter

(from 508 nm to 533 nm). The peak parameters, such as peak area and the number of theoretical plates, were calculated from statistical moment analysis. Labview programs (National Instruments Corp., Austin, TX) written locally were used for calculations, data acquisition and instrument control.

5.3 Results and Discussion

5.3.1 Device

Using the micromachining technology detailed in chapter 3, a miniaturized capillary electrophoresis system with a mixing chamber has been fabricated in a glass chip. Figure 5.1 shows the layout and dimensions of the glass device called Jet-3. All channels of single line width are 30 μm wide, whereas the blackened bulky lines are 300 μm wide. The different size of the channel between 2 and 5 ensured a maximum potential drop on the effective separation distance that is from the injection point to the detector. The depth of all channels is 10 μm . The box between points "a" and "b" in figure 5.1 was used as a mixing chamber. Islands inside the chamber were intended to facilitate mixing. The chamber was 4.5 mm long and 170 μm wide. The three channels around the double islands were 30 μm wide, while the two channels around the single island were 60 μm wide. The volume of the chamber was calculated to be $3.6 \times 10^{-3} \text{ mm}^3$ based on its geometry. The offset between the side channels connected to reservoirs 3 and 4 is 220 μm , which was used for double T injections discussed in the previous chapter. The size of the whole device was 2.2 cm x 4.7 cm. The numbers given for the reservoirs in the figure will be used for reference in the discussion.

A part of the mixing chamber is shown in the scanning electron micrograph in figure 5.2. The figure illustrates clear-cut edges and corners, which indicates chambers with various shapes can be readily fabricated.

As in chapter 4, the distance of each channel can be expressed by the equivalent length, which was calculated by converting the width of channels to 30 μm wide based on the cross sectional area. It should be noted that

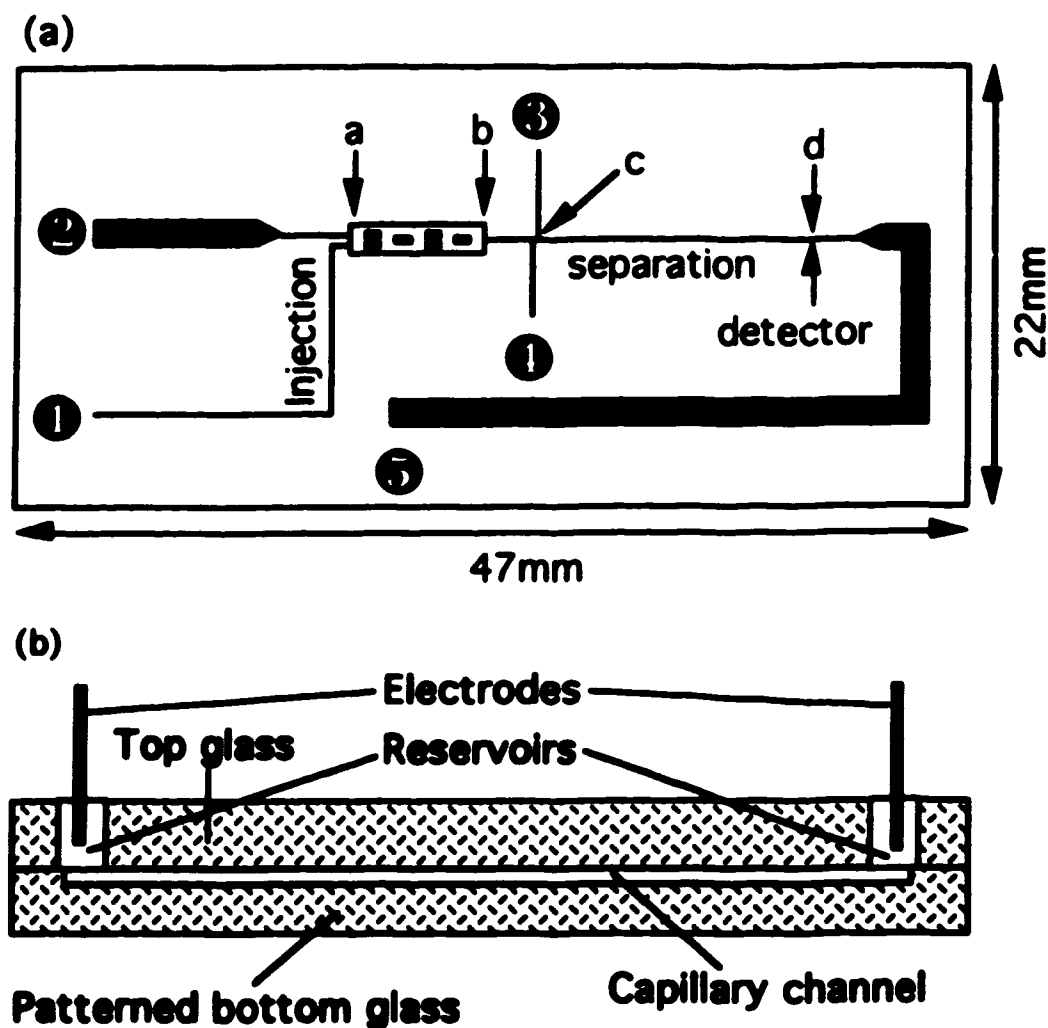


Figure 5.1 (a) The top view of the layout and dimensions of Jet-3 devices. The box between points "a" and "b" was used as a mixing chamber. The offset between the two side channels connected to reservoirs 3 and 4 is 220 μm . The locations of a, b, c, d and the numbers of the reservoirs are used for reference in the discussion. (b) The cross section view of the device. The bottom glass plate with etched capillaries was thermally bonded with a cover plate. Holes in the cover plate were aligned with the capillaries to provide an access for introducing solutions and applying voltages.

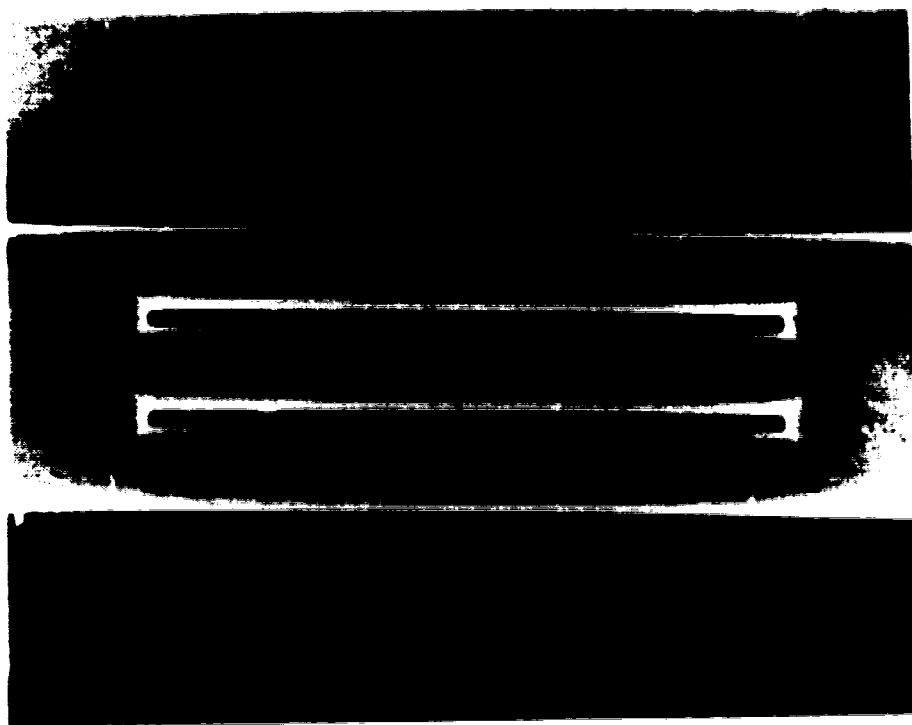


Figure 5.2 The scanning electron micrograph of a part of the mixing chamber in a Jet-3 device. The clear-cut edges and corners are illustrated.

some short channels inside the chamber are in parallel while others are in series, so that the conversion for the mixing chamber used a simulated resistor circuit and the calculation was done according to the relationship between the overall resistance and the resistance of each resistor.

5.3.2 Mixing

As discussed for other μ -TAS devices in chapters 3 and 4, electroosmotic flow under an electrical field was used to pump samples for mixing and injections while electrophoresis was for separations.

Samples were usually introduced through reservoirs 1 and 2, while other reservoirs and channels were filled with a buffer. To drive two samples through the chamber for mixing, one potential was applied to reservoir 1, and another potential was applied to 2, while reservoir 3 was grounded. Both samples in reservoirs 1 and 2 flowed into the chamber and mixed with each other due to diffusion and convection. After a certain time, the mixture in the mixing chamber consists of a fixed portion of each sample. The fraction of each sample in the mixture depends on its own flow rate, which is determined by the applied electrical fields as discussed below. When mixing was completed, these potentials were switched off. Then, a potential between reservoirs 4 and 5 was turned on to flush the double T injector and the separation channel, so that any samples diffused into those area at mixing would be cleared away. The mixture in the chamber was then injected through the double T injector using two injection potentials applied to reservoirs 1 and 2 in the same way as for mixing, but for a shorter period. The sample plug in the double T injection port should then represent the contents in the mixing chamber. The application of a voltage between reservoirs 4 and 5 then caused the separation.

As an example, 200 V (178 V/cm) between reservoirs 2 and 3, and 400 V (152 V/cm) between 1 and 3 was applied at the same time for 5 minutes of mixing. Reservoir 1 contained 10 μ M fluorescein, while reservoir 2 contained 10 μ M FITC labelled arginine (Arg-FITC) and tyrosine (Tyr-FITC). Then 2000 V (826 V/cm) between 4 and 5 was used to flush the double T injection port and the separation channel. Immediately after, 200

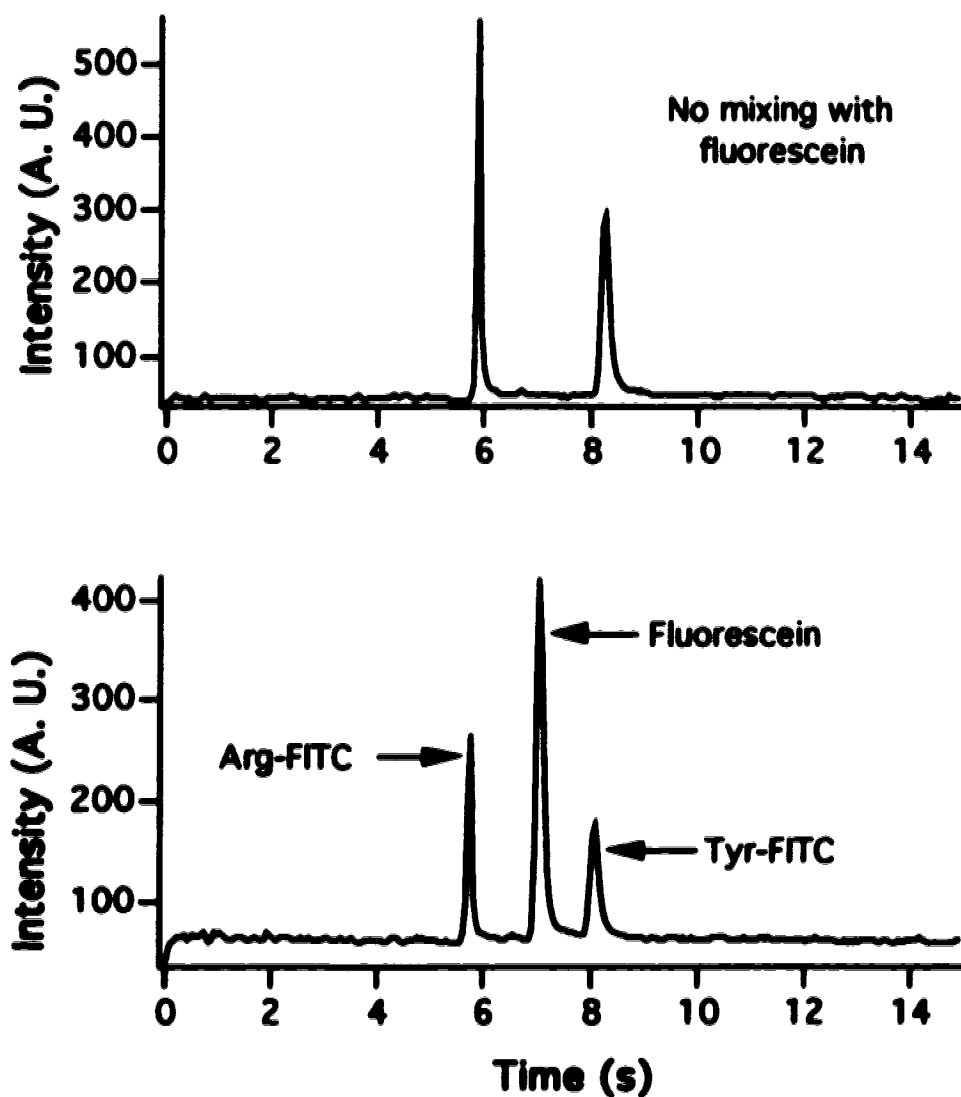


Figure 5.3 Electropherograms of separation of two amino acids without mixing with fluorescein (top) and with mixing (bottom). Two $10\ \mu\text{M}$ amino acids in pH 9.1 carbonate buffer was placed in reservoir 2, whereas $10\ \mu\text{M}$ fluorescein in the same buffer was in reservoir 1. Mixing was performed by applying 200 V and 400 V to reservoir 2 and 1 while reservoir 3 was grounded. Application of 2000 V between 4 and 5 was used for separation.

(178 V/cm) V between 2 and 3, and 400 V (152 V/cm) between 1 and 3 was again applied at the same time for a 0.5 s injection period. Application of 2000 V (826 V/cm) between 4 and 5 then resulted in the electropherogram at the bottom of figure 5.3. As a comparison, an electropherogram without mixing is also shown in figure 5.3. This was done by simply applying 200 V (178 V/cm) between 2 and 3 for 0.5 s for injection and 2000 V (826 V/cm) between 4 and 5 for the separation. No mixing was performed in advance and no voltage was applied to reservoir 1 at any time.

The fraction of each component in the mixing chamber can be adjusted by changing the mixing voltage applied to reservoir 1 while keeping the other parameters the same. As shown in figure 5.4, the fluorescein content increased with the mixing voltage applied to reservoir 1, whereas the Arg-FITC content decreased. In fact there is an interplay between both mixing voltages applied to reservoirs 1 and 2, which controls the effectiveness of mixing. This can be theoretically predicted using simulation of the channel resistances, as discussed in chapter 4.

Figure 5.5 shows a simulated electrical circuit of Jet-3 for the mixing configuration. The lengths of the channels correspond proportionally to the resistances of the channels. While the channels had different geometries, their lengths have been expressed as the length equivalent to a 10 μm deep, 30 μm wide channel. Point "a" is at the head of the chamber, as shown in figure 5.1. When V_2 and V_1 are applied to reservoirs 2 and 1 while 3 is grounded, the potential at point "a" in the figure (V_a) can be calculated from equation [5.1]. The derivation followed the same procedures for equation [4.15] in chapter 4.

$$V_a = \frac{V_1 R_2 R_3 + V_2 R_1 R_3}{R_1 R_2 + R_1 R_3 + R_2 R_3} \quad [5.1]$$

Where R_1 , R_2 , R_3 are the resistances of the resistors representing the corresponding channel sections, as indicated in figure 5.5.

When V_2 was fixed at 200 V, the relationship between V_a and V_1 was described by equation [5.2] after the values of R_1 , R_2 , R_3 were substituted into equation [5.1].

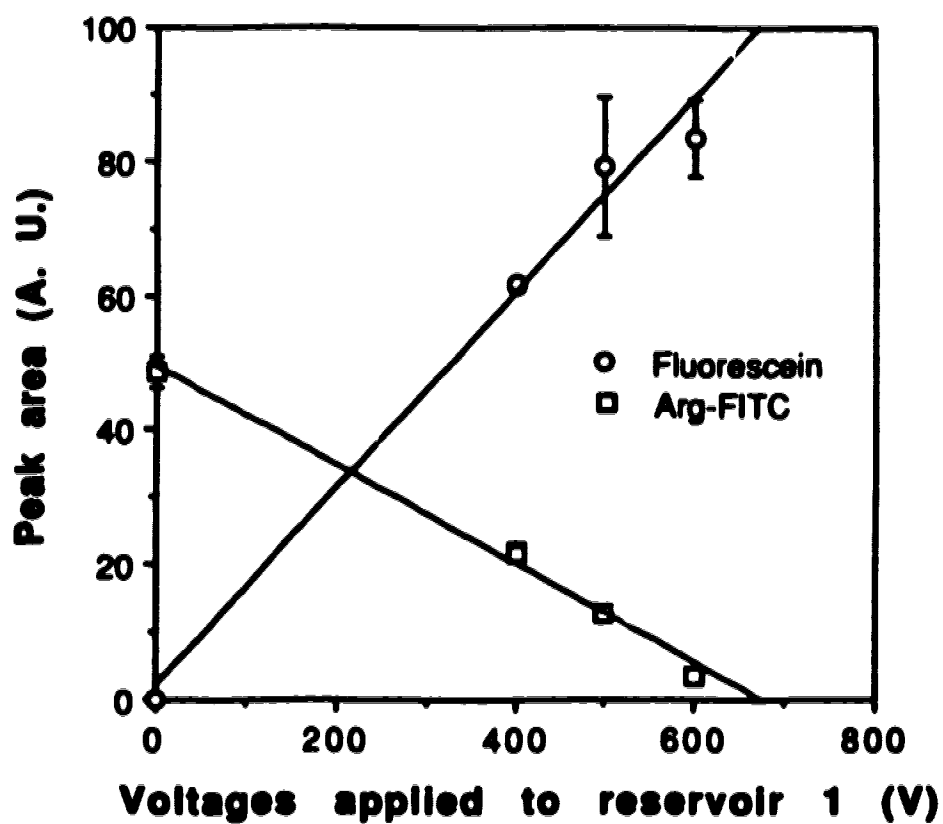


Figure 5.4 The relationship between peak areas and mixing voltages applied to reservoir 1. Other conditions are the same as in figure 5.3.

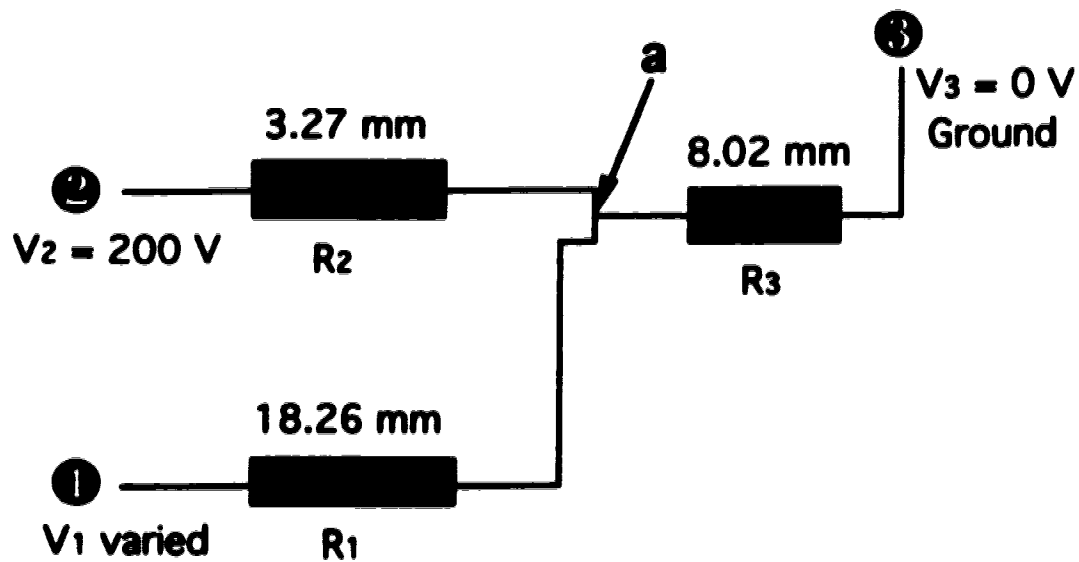


Figure 5.5 The simulated resistance circuit of mixing chamber configuration. The resistances are represented by the equivalent lengths of the channels. The point "a" is at the inlet of the chamber as shown in figure 5.1.

$$V_a = 0.113 V_1 + 126 \quad [5.2]$$

If one requires

$$V_a \leq V_1,$$

then V_1 must be larger than 142 V (54.1 V/cm) using equation [5.2]. That means the potential at reservoir 1 has to be higher than 142 V in order to drive the sample in reservoir 1 to the mixing chamber. If the voltage applied to reservoir 1 is less than 142 V, the electroosmotic flow in the channel connecting reservoir 1 is in the opposite direction, from point "a" to 1. Similarly, if one requires

$$V_a \leq 200 \text{ V } (V_2)$$

then V_1 must be less than 655 V (249 V/cm) using equation [5.2]. If the voltage applied to reservoir 1 is larger than 655 V, V_a is then higher than 200 V, which means that the electroosmotic flow is in the undesired direction, from point "a" to reservoir 2. Therefore, it can be concluded that the mixing voltage applied to reservoir 1 has to be in a range between 142 ± 6 V and 655 ± 9 V for the conditions we used (200 V for reservoir 2 and ground for reservoir 3). The standard deviations were calculated using the error propagation analysis as in chapter 4. The upper limit in figure 5.4 roughly agrees with this calculation.

The completeness of mixing was examined empirically by comparing the peak areas after different periods of mixing. With 400 V (152 V/cm) applied to reservoir 1 and 200 V (178 V/cm) to reservoir 2 during mixing, the peak areas obtained were the same after 5 or 7 minute mixing periods. With 500 V (190 V/cm) on reservoir 1, 2 minutes did not give complete mixing, but the electrophrogram obtained after 3 minutes was same as that after 4 minutes of mixing. The shorter mixing time required at 500 V (190 V/cm) can be explained by the fact that less time was required to flush the chamber at higher flow velocity. The mixing time used with 600 V (228 V/cm) on reservoir 1 was also 3 minutes, but a shorter mixing time was not

tried. With 100 V (38.1 V/cm) on reservoir 1 there was no fluorescein peak after 18 minutes of mixing, which is explained by the calculations above. Only one peak was observed when 800 V (305 V/cm) was applied to reservoir 1 as the mixing voltage, which also agrees with the prediction above. Mixing time could be decreased by simultaneously increasing the mixing voltages applied to reservoirs 1 and 2, as evidenced by the fact that fluorescein in the mixing chamber was removed within 20 s when 2000 V (762 V/cm) was applied between reservoirs 2 and 3.

The mixing chamber could be used as a microreactor for pre-capillary derivatization and possibly post-capillary derivatization. Reaction in the chamber, however, was not pursued at this point. Mixing has been described using two intersecting channels rather than a chamber (16), but longer residence time in a chamber like the one in Jet-3 may give better mixing and more time for a given reaction.

5.3.3 Leakage

Leakage is a phenomenon in which the sample in the side channel leaks at the intersection into the main channel when the separation is effected, as discussed in chapters 3 and 4. It was a problem in the μ -TAS devices we have prepared because it increased the background and decreased the dynamic range of detection (14-16). Both diffusion and convection at the intersection of channels contribute to leakage (15). Unlike a T injector in CETAS devices (14) and a cross injector in Airport devices (15), the two injection channels connected to the inlet of the chamber in Jet-3 are in parallel rather than intersecting, so that the increased distance between the two channels might reduce both diffusion and convection effects. In addition the reduced velocity in the larger chamber should reduce the viscous drag effect that causes convective leakage.

The magnitude of leakage due to diffusion and convection has been characterized by the ratio between the background due to leaking dye and the signal for the dye solution. The minimum ratios we have reported in Airport and CETAS devices are 3% (14, 15). At the T intersection

connecting reservoir 3 in the Jet-3 device the ratio was again 3%, as discussed below.

To evaluate leakage, buffer solution was first directed from reservoir 1 to 5 using 1773 V (416 V/cm, all electrical fields following refer to that in the 30 μm wide channel section), with 0.05 mM fluorescein present in the side channel connected to reservoir 3. The background intensity observed under these conditions can be seen in the inset of figure 5.6a. This intensity roughly indicated the signal due to the leaking fluorescein from the side channel, although it included the signal due to scattered light as well. Fluorescein was then driven from reservoir 3 to 5 using 1000 V (416 V/cm), to establish the signal for the 0.05 mM solution, as seen in figure 5.6a. The ratio of the two signals indicates an upper limit of 3.1% leakage occurred from the side channel connected to reservoir 3.

The leakage induced in the mixing chamber was tested in a similar way. A 0.5 mM fluorescein solution in reservoir 2 was driven to reservoir 5 with 1000 V. The chamber was then flushed by applying 2000 V (470 V/cm) between reservoirs 1 and 5, leaving 2 floating, causing a decrease in signal as seen in figure 5.6b. The background indicates the signal resulting from the leakage at the inlet of the chamber from reservoir 2, plus any additional background sources. The ratio of the background to the maximum signal is 0.9%, which indicates the chamber configuration caused less leakage. However, it is an overestimate of leakage due to two factors. The first is that the additional background sources such as scattered light were not measured, but typically would give at least 50 % of the background signal observed. In addition, quenching occurred when the concentrations of FITC labelled amino acids were above 20 μM , as shown in chapter 4. For 0.1 mM of amino acids the peak heights were reduced to 42-43% of the value expected from linear extrapolation of the calibration curves (figure 4.14) obtained from lower concentrations. This means that the amount of leakage was significantly overestimated, since the signal from the dye in the 0.5 mM solution would be at least 40% larger if no quenching took place.

A better estimate of the leakage induced in the chamber was obtained from the following experiments and analysis. After 2000 V was used for flushing the chamber shown in figure 5.6b, other flushing voltages were

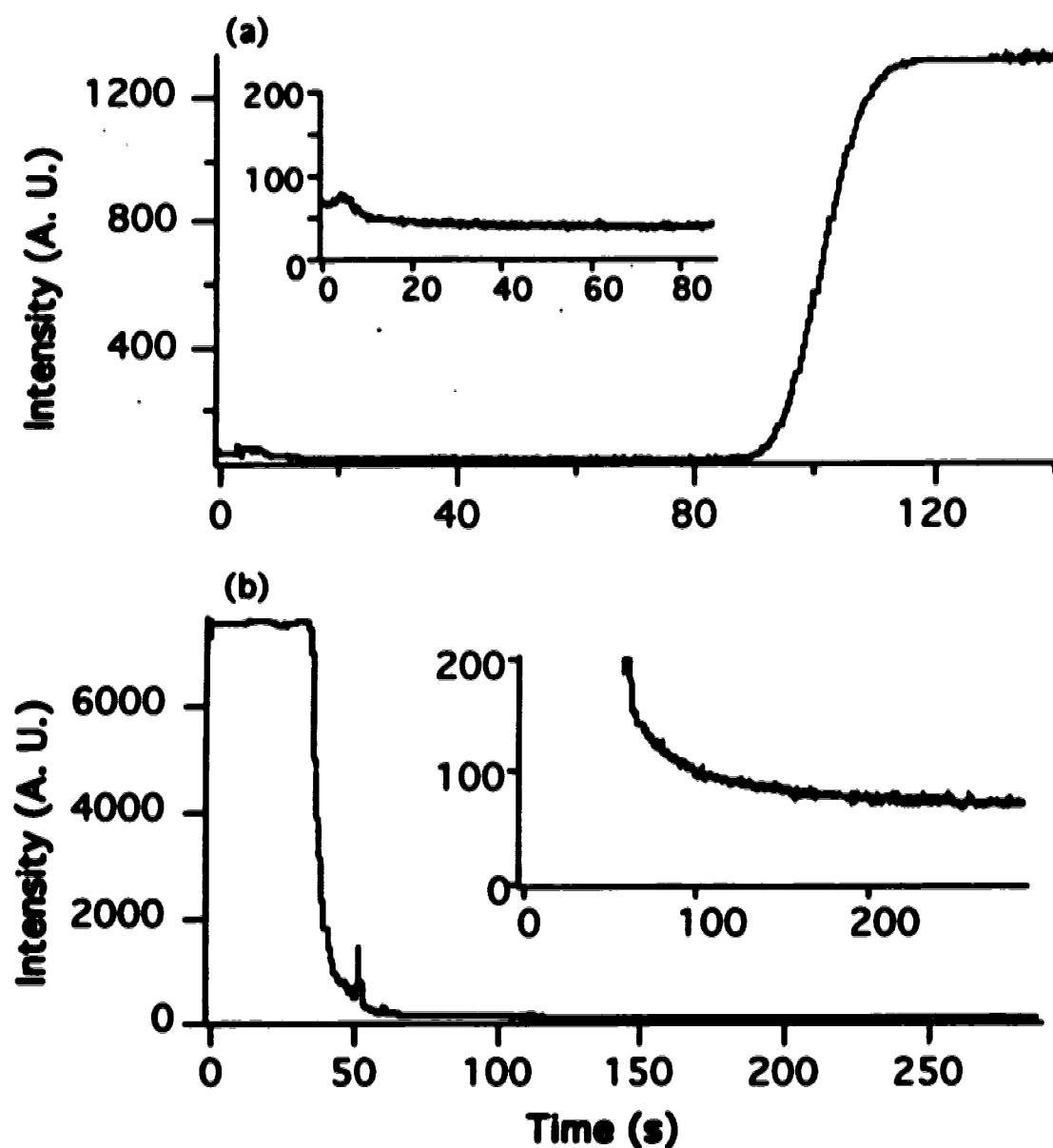


Figure 5.6 Comparison of leakage magnitudes between a T injector (a) and the chamber (b). (a) 0.05 mM fluorescein was driven from reservoir 3 to reservoir 5 by applying 1000 V (416 V/cm) between two reservoirs. (b) 0.5 mM fluorescein was removed from the mixing chamber by applying 2000 V (470 V/cm) between reservoirs 1 and 5. pH 9.1 carbonate buffer was used. The insets show the backgrounds on an expanded scale.

applied between reservoirs 1 and 5. Figure 5.7 shows the background levels at the different flushing voltages. As discussed in chapter 3, the intensity of a dye increased with the flow rate, since less dye was bleached by the laser. Therefore, the change in intensity at different flushing voltages is correlated to the amount of dye present in the buffer. The backgrounds were analyzed in a span of 50 s before and after stepping from 500 V (117 V/cm) to 1500 V (352 V/cm), as there is the biggest change between them in the data set. The background signals were 56.7 ± 1.3 and 62.0 ± 1.5 , respectively. The difference between them (5.3) is about 4 times larger than their standard deviations. This roughly indicates the amount of leaking dye is in the range of 1-2 times the detection limit of the apparatus used. Based on the experiments described to obtain the calibration curves in figure 4.14, the detection limit of our apparatus is slightly more than 50 nM. Therefore the concentration of fluorescein in the chamber due to leaking from the reservoir 2 must be in the range of 70 nM. In other leakage experiments the channel cross-sections were equal, whereas in this study the mixing chamber was 10 times larger in cross-section than the side channel. Even with the same leakage rate this would lead to a further 10-fold dilution of the leaking component. Nevertheless, the small amount of leakage observed indicates there is very little mixing of the solution in the floating side channel with the main stream.

5.3.4 Dispersion in the chamber

Dispersion (bandbroadening) took place when fluids passed through the chamber in Jet-3, just as occurs in connectors or mixing chambers in liquid chromatography. The degree of dispersion is important to know, for a similar chamber might be used in μ -TAS devices for post-capillary derivatization in the future. Using the frontal analysis technique dispersion in the chamber has been quantitatively measured.

Frontal analysis was performed using the following steps. First, 50 μ M fluorescein in reservoir 2 was driven through the chamber to reservoir 5 by applying 1138 V (416 V/cm) between the two reservoirs. The buffer in reservoir 1 was then used to flush fluorescein from the chamber and

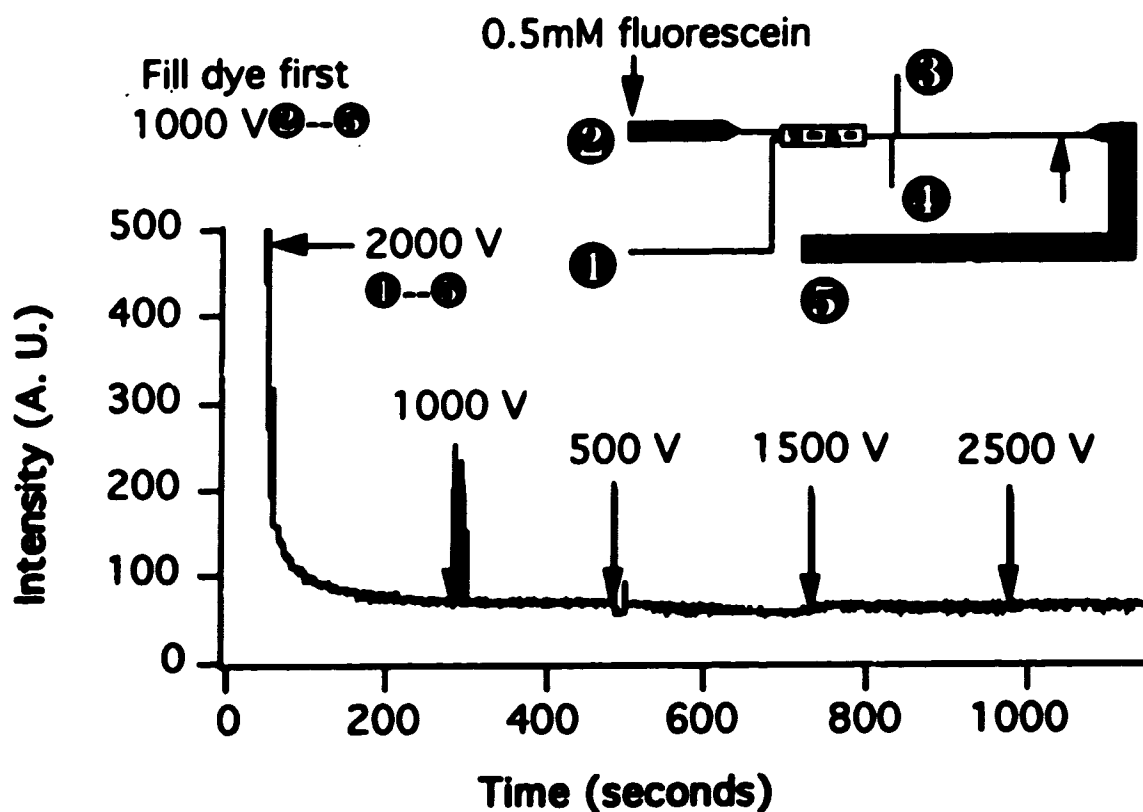


Figure 5.7 The effect of voltages applied between reservoirs 1 and 5 on the magnitude of the leakage at the inlet of the mixing chamber from the channel connected to reservoir 2. 0.5 mM fluorescein was present in reservoir 2 and in the channel between reservoir 2 and the inlet of the chamber, while other reservoirs and channels were filled with a buffer. pH 9.1 carbonate buffer was used.

separation channel into reservoir 5. Reapplication of the potential between reservoirs 2 and 5 then produced a front of fluorescein moving from the inlet of the chamber to the detector. This last step is shown in figure 5.8a. A similar frontal analysis was performed for fluorescein injected via the T injector defined between reservoirs 3 and 5 using 1000 V (416 V/cm) and is shown in figure 5.8b.

In chromatography, differentiation of a frontal analysis chromatogram gives an elution chromatogram (17). Analogously, differentiation of a frontal analysis electropherogram in capillary electrophoresis gives a migration electropherogram. The derivatives of the two electropherograms in figure 5.8 are shown in figure 5.9. Statistical moments reported below are based on analysis of the derivative electropherograms. The second moment or peak variances, σ^2 , were used, because the overall variance due to several bandbroadening processes can be obtained by summing the variances from each process (18). The overall variances can be described by the following equation for the sample flowing from the inlet of the chamber (the injection point for the top electropherogram of figure 5.9) to the detector.

$$\sigma^2_{ad} = \sigma^2_{ab} + \sigma^2_{bc} + \sigma^2_{cd} \quad [5.3]$$

The subscripts refer to the distances between locations indicated in figure 5.1. σ^2_{cd} includes any contribution from the detector as well. Peak variance in figure 5.9a of $1.22 \pm 0.29 \text{ s}^2$ represents the dispersion over the distance "ad" (i. e., σ^2_{ad}), while σ^2_{cd} of $0.07 \pm 0.01 \text{ s}^2$ was obtained from figure 5.9b. The standard deviation in these data was obtained from 3 electropherograms measured under the same conditions. The contribution from the detector to σ^2_{cd} can be estimated from the detection volume. 100 μm is taken for the length of the detector cell based on the magnification of the objective and the slit size, although the laser spot could be as small as 40 μm . The resulting variance, σ^2_{det} , is calculated to be 0.01 s^2 for these conditions. This means that $(\sigma^2_{cd} - \sigma^2_{det})$ represents the peak variance due to the distance "cd". σ^2_{bc} can be calculated from equation [5.4], because the theoretical plate height over "bc" and "cd" should be the same.

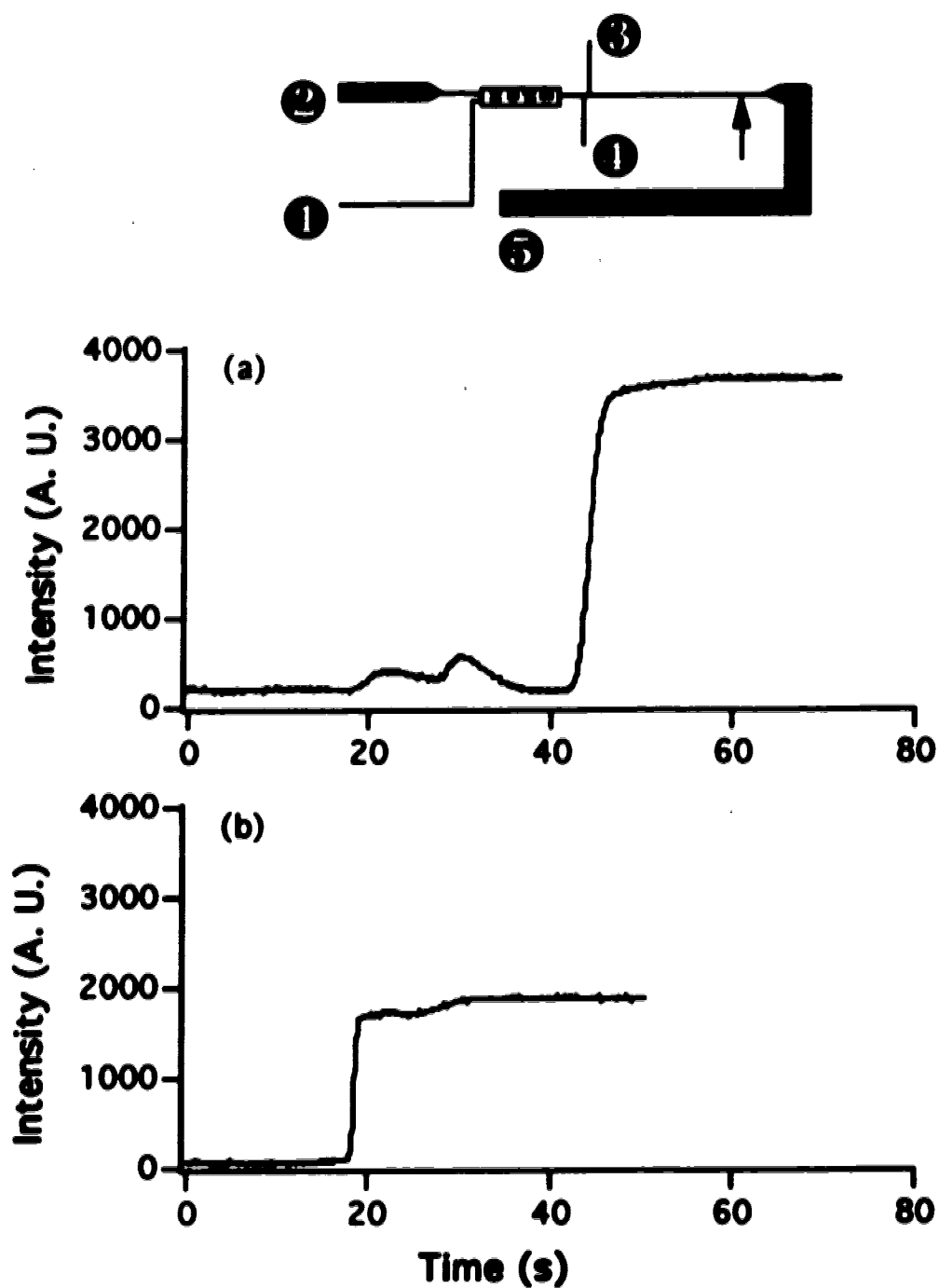


Figure 5.8 The frontal analysis electropherograms of 50 μM fluorescein through the chamber (a) and a T injector (b) at an electrical field of 416 V/cm. See the text for the detail.

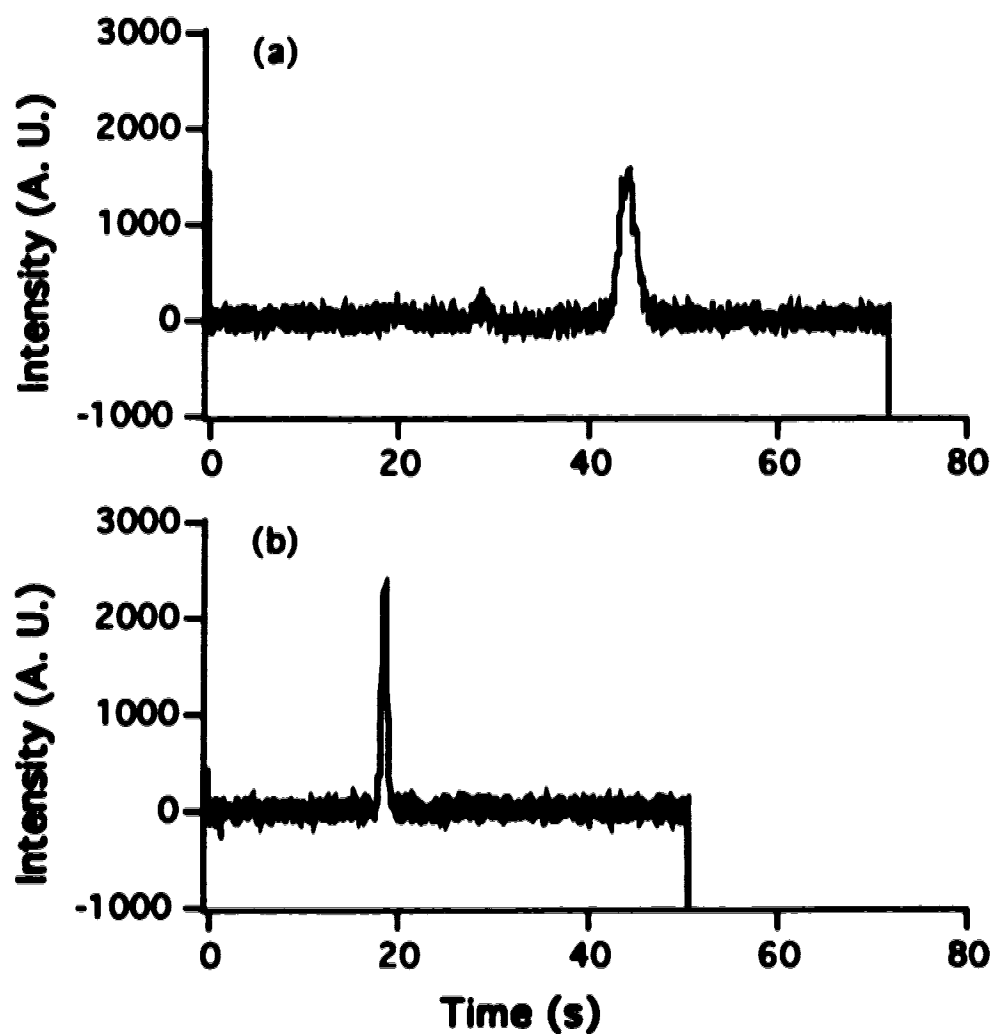


Figure 5.9 The migration electropherograms by differentiating two frontal electropherograms in figure 5.8. 50 μ M fluorescein through the chamber (a) and a T injector (b) at an electrical field of 416 V/cm.

$$\sigma_{bc}^2 = \frac{d_{bc}}{d_{cd}} \times (\sigma_{cd}^2 - \sigma_{det}^2) \quad [5.4]$$

Here d_{bc} and d_{cd} are the distance between "bc" and "cd", 0.31 cm and 1.6 cm respectively. From equations [5.3] and [5.4], σ_{ab}^2 , which was contributed by the mixing chamber, was calculated to be $1.14 \pm 0.30 \text{ s}^2$. That means that about 93% of the total variance over distance "ad" was due to the mixing chamber. In other words, the mixing chamber contributed considerably to bandbroadening.

There are several models to describe the degree of bandbroadening resulting from connectors in liquid chromatography (18). We used the mixing chamber model for the calculation of the degree of dispersion resulting from the chamber in Jet-3. This model assumes turbulent flow or forced mixing is taking place. The equation describing the dispersion from a mixing chamber is

$$\sigma^2 = \left(\frac{V}{F} \right)^2 \quad [5.5]$$

where V is the volume of the mixing chamber ($3.6 \times 10^{-3} \text{ mm}^3$), and F is the volume flow velocity in the chamber.

It was difficult to calculate F due to the irregular shape of the chamber. However, F in the chamber should be equal to F in the $30 \text{ }\mu\text{m}$ wide channel section, which can be obtained from the linear flow velocity (v) and the cross sectional area of the $30 \text{ }\mu\text{m}$ wide channel section ($2.0 \times 10^{-4} \text{ mm}^2$, assuming a trapezoid shape with $30 \text{ }\mu\text{m}$ wide at the top and $10 \text{ }\mu\text{m}$ at the bottom). The v can be obtained from the apparent electrophoretic mobility (μ) and the electrical field (E) in that channel section (416 V/cm, 1136 V between reservoirs 2 and 5). The μ was obtained using the following equation.

$$\frac{d}{t_m} = v = \mu E \quad [5.6]$$

Where d is the separation distance and t_m is the migration time. For the electropherogram in figure 5.9b, d and t_m are 1.6 cm and 18.9 s, while E is 416 V/cm (1000 V between reservoirs 3 and 5). Substituting these values into equation [5.6] gave a μ of $2.04 \times 10^{-4} \text{ cm}^2/\text{s}\cdot\text{V}$. v and F were then calculated to be 0.85 mm/s and $1.7 \times 10^{-4} \text{ mm}^3/\text{s}$ in the 30 μm wide channel section, based on the discussion above.

The dispersion in the chamber was calculated to be 448 s^2 using equation [5.5], which was based on the mixing chamber model. This value is much larger than the experimental value ($1.14 \pm 0.30 \text{ s}^2$). This was expected because the mixing chamber model describes a situation in which turbulent flow takes place, or forced mixing is employed in a laminar flow (18). Stirring was not done in the chamber of Jet-3. However, the plug flow profile resulting from electroosmotic flow in CE may reduce the mixing effects as well, when compared to a parabolic flow profile in liquid chromatography.

The time for fluorescein to diffuse from the edge to the center of the mixing chamber (85 μm) was calculated to be 10 s using $3.41 \times 10^{-6} \text{ cm}^2/\text{s}$ as its diffusion coefficient. Consequently, diffusion could completely account for mixing. The diffusion chamber model is probably more suitable to the chamber we used (18), however, the complexity in the chamber structure in the Jet-3 devices made it difficult to use the mathematical equations of the model. Therefore, it was not pursued.

5.4 Conclusion

The study in this chapter has shown that the mixing chamber in Jet-3 is capable of effecting mixing. The fraction of each component in the mixture could be dynamically controlled by adjusting the voltages applied to sample reservoirs. This indicates that a dilution procedure could be performed using the mixing chamber. The results in figures 5.3 and 5.4 also suggest that a controlled amount of an internal standard or a reactive reagent could be introduced into a real sample in real time, if necessary.

As explained in the Introduction, post-capillary derivatization is a desirable scheme for biological applications of capillary, electrophoresis. The

mixing chamber in Jet-3 might be used for this purpose, although this particular design resulted in a large dispersion. A better design, for example, a diamond shape rather than a rectangular shape, might be used to maintain laminar flow if a post-capillary derivatization scheme is used. However, there is always a trade-off between reaction residence time and separation efficiency loss. A smaller reactor would result in less efficiency loss, but have a shorter residence time for reactions. Therefore, a fast derivatization reaction is definitely desired.

5.5 References

1. Jorgenson, J.; Lukacs, K. D., *Anal. Chem.* **1981**, *53*, 1298-1302.
2. Jorgenson, J.; Lukacs, K. D., *Science*, **1983**, *222*, 266-272.
3. Grossman, P. D.; Colburn, J. C., Eds, *Capillary Electrophoresis: Theory and Practice*, Academic Press: San Diego, CA, **1992**.
4. Yeung, E. S.; Kuhr, W. G., *Anal. Chem.* **1991**, *63*, 275A-282A.
5. Rose Jr., D. J.; Jorgenson, J. W., *J. Chromatog.*, **1988**, *447*, 117-131.
6. Pentoney, S. L.; Huang, X.; Burgi, D. S.; Zare, R. N., *Anal. Chem.* **1988**, *60*, 2625-2629.
7. Swaile, D. F.; Sepaniak, M. J., *J. liquid Chromatog.*, **1991**, *14*, 869-893.
8. Amankwa L. N.; Kuhr, W. G., *Anal. Chem.* **1992**, *64*, 1610-1613.
9. Nickerson, B.; Jorgenson, J. W., *J. Chromatog.*, **1989**, *480*, 157-168.
10. Rose Jr., D. J., *J. Chromatog.*, **1991**, *540*, 343-353.
11. Albin, M.; Weiberger, R.; Sapp, E.; Moring, S., *Anal. Chem.* **1991**, *63*, 417-422.
12. Tsuda, T.; Kobayashi, Y.; Hori, A.; Matsumoto, T.; Suzuki, O., *J. Chromatog.*, **1988**, *456*, 375-381.
13. Dasgupta, P. K.; Bao, L., *Anal. Chem.* **1993**, *65*, 1003-1011.
14. Harrison, D. J.; Manz, A.; Fan, Z.; Lüdi, H.; Widmer, H. M., *Anal. Chem.*, **1992**, *64*, 1926-1932.
15. Fan, Z.; Harrison, D. J., *Anal. Chem.*, **1993**, accepted.
16. Harrison, D. J.; Fluri, K.; Seiler, K.; Fan, Z.; Effenhauser, C. S.; Manz, A., *Science*, **1993**, *261*, 895-897.

17. Conder, J. R.; Young, C. L., *Physicochemical Measurement by Gas Chromatography*, John Wiley and Sons: NY, 1979, Chapter 9.
18. Sternberg, J.C. *Adv. Chromatogr.* **1968**, *2*, 206-270.

Chapter 6

Conclusions and Future Directions

A summary will be given in this chapter of the contribution of this thesis to certain scientific fields. Also presented are the conclusions drawn on the basis of this work and future directions of the research projects involved in this thesis. For clarity, they will be discussed in terms of the individual projects, which are an implantable glucose sensor and miniaturized capillary electrophoresis systems.

6.1 An implantable glucose sensor

6.1.1 A summary of the study on Nafion

The study on Nafion membranes used for an implantable glucose sensor was described in chapter 2 of this thesis, while the review of this subject and the techniques used for measuring membrane thickness were introduced in chapter 1. This work contributed a small component compared to all the efforts which have been made to treat diabetes during the last 3 decades. A few critical parameters have been given in this thesis for one type of implantable glucose sensor, that is, a Nafion encapsulated glucose sensor pioneered by Harrison *et al.* (1-4). These parameters include the permeability and diffusion coefficient of glucose in Nafion membranes, and the selectivity of the membrane against interfering species in blood samples, such as ascorbic acid. In addition, the influence of membrane preparation conditions on these parameters was evaluated.

The results present quantitative guidelines for designing an implantable glucose sensor using Nafion. For example, a thinner Nafion membrane used for a sensor offered a larger permeability and thus a larger sensitivity. The required thickness for a given sensitivity can be determined

once one knows the diffusion coefficients of glucose and O_2 . Curing at high temperatures gave a more stable film with less solubility in aqueous solutions, compared to curing at room temperature. Recently, Moussy *et al.* have used this fact to increase the lifetime of implanted glucose sensors (4).

This work has also contributed to the study of chemically modified electrodes. The results indicated that ellipsometry is a good method to measure membrane thicknesses for electrochemistry because it is accurate and nondestructive. The comparison among the diffusion coefficients of neutral molecules, cations and anions in Nafion elucidated the different mass transport mechanisms they experienced, and provided further understanding of the Nafion membrane structures and morphology. These results could also be used for other purposes, because Nafion membranes have been extensively used for fuel cells (5) and as coatings for other sensors.

6.1.3 Future directions

As discussed by Reach and Wilson (6), the obstacles to realizing continuous blood glucose monitoring with an implanted glucose sensor are implantability including biocompatibility and biostability, *in vivo* calibration, and interferences. Although new technologies for implanted sensors continue to be reported, it is often the case that they do not overcome these problems (7). Therefore, to demonstrate the implantation of a glucose sensor that functions properly *in vivo* in a long term remains a major challenge.

As a result, the evaluation of a Nafion encapsulated glucose sensor in animals and eventually humans, and the sensor modifications needed to overcome problems encountered when implanted are definitely future directions. In fact, Dr. Moussy in our research group has been pursuing this direction. Nafion encapsulated glucose sensors have been implanted in a dog and functioned for more than 10 days (4). Modifications of the sensor for long term implantation and further experiments are being undertaken.

Like other polymer coatings used in glucose sensors, Nafion membranes do not have selectivity against neutral interfering species, as

shown in chapter 2. Electroactive neutral species in the human body will cause a response at such an implanted glucose sensor. One example is acetaminophen, a widely used analgesic drug. The implantation of a glucose sensor in patients would be accompanied by a restriction on the use of this drug. One possible solution is to use another membrane as an inner coating, as discussed in chapter 1. The inner membrane needs to allow H_2O_2 diffuse but reject other neutral species such as acetaminophen. Moussy *et al.* have used electrodeposited poly(o-phenylenediamine) as an inner coating, which was able to reduce about 70% of interference due to acetaminophen (4). Wilson *et al.* have also reported they are studying other coatings for this purpose (6). A systematic effort to evaluate a number of possible polymers would be an appropriate area of study.

6.2 Miniaturized capillary electrophoresis systems

6.2.1 A summary

Miniaturized capillary electrophoresis systems studied in this thesis experimentally demonstrate the concept of miniaturized total chemical analysis systems (μ -TAS). As discussed in chapter 1, a μ -TAS was proposed incorporating sample pretreatment and separation within an integrated system. Such a μ -TAS device should have advantages over conventional chemical sensors in terms of accuracy, selectivity, and durability. The μ -TAS devices described in this thesis establish that it is possible to make such integrated systems function for chemical analysis. This suggests a promising direction for developing chemical sensors.

The μ -TAS devices were fabricated using micromachining technology. This shows the potential of micromachining to miniaturize bench-top instruments for proposed integrated systems. We have proven it is possible to integrate flow injection analysis (FIA) with capillary electrophoresis (CE) in planar devices.

Several μ -TAS devices with a variety of features have been studied in this thesis. The performance of these devices, and the conclusions drawn on

the basis of them, have been discussed in chapters 3, 4, and 5, and will be summerized below.

Chapter 3 detailed the device fabrication method known as micromachining. The selection and annealing treatment of glass substrate showed significant effects on the etching quality of a device. The very rapid separation of amino acids, as fast as 3 seconds, was first demonstrated in such a CE-based μ -TAS device. This indicates the potential of these μ -TAS devices to compete with chemical sensors in terms of total analysis time. A cross injector formed at the intersection of two etched capillaries was integrated in a device called "Airport". However, the cross injector did not define injection volumes geometrically as was hoped, because fluids mixed at the intersection due to diffusion and convection. It was also demonstrated that sample leaks into the separation channel when a separation was being effected. This leakage phenomenon increased the background and decreased the dynamic range of the detection.

To solve problems encountered with the Airport devices, two devices, Jet-1 and Jet-3, were designed and fabricated. As discussed in chapter 4, a double T injector was included in both devices, although it had different configurations. Both double T injectors showed their ability to define injection volume geometrically when injection time was long enough or injection voltage was high enough. However, the actual injected sample volumes were larger than the geometrical volume of the injector, because diffusion and other, as yet unidentified effects during injection also contributed to the injected volume. To suppress the leakage at an intersection, applying appropriate voltages to all the reservoirs was demonstrated to be effective. The resistance simulation was proven to be useful for this purpose. In addition, linear calibration curves over 3 orders of magnitude were obtained for amino acids tagged with a fluorophore.

A mixing chamber integrated in Jet-3 was demonstrated for sample pretreatment, specifically mixing with a reagent, as discussed in chapter 5. The chamber was able to mix samples effectively and to adjust dynamically the fraction of each sample in the mixture. This indicates such a chamber could be used for pre- or post-capillary derivatizations. Bandbroadening in the chamber was investigated and quantitatively analyzed. The study

showed that this particular chamber made a considerable contribution to the loss of separation efficiency, so that a chamber with a better design is desired for post-capillary applications.

Combined with other efforts by Harrison's group and our collaborators at CIBA-GEIGY in Switzerland (8-12), the results in this thesis indicated that it is feasible to realize the concept of μ -TAS for a real chemical analysis. These μ -TAS devices did and will demonstrate advantages over both chemical sensors and bench-top instruments. Advantages over conventional CE include FIA type sample injection, efficient heat dissipation, ability to do dilution or mixing, fast separation, and so on.

6.2.3 Future directions

There is still much to do to develop μ -TAS devices for real chemical analyses. Many problems and questions need to be addressed first. The following aspects are some of those we are now in a position to consider.

(1) Injection

The injectors integrated in all μ -TAS devices we have studied made a considerable contribution to the loss of separation efficiency. One injector reported in reference 12 showed its superiority in this respect. However, the reason behind this was not clear. It has been observed that the channel dimension and length had some effects on the performance of an injector, because the resistance of a channel decides the back pressure, which influences the flow rate (11). An injector with balanced channel resistances should be tested. An injector with a smaller injection channel may be tested as well, because it probably causes less leakage due to a larger resistance and less contact with the separation channel. More importantly, the relationship between the injector configuration and its performance needs to be quantified.

Active voltage control was quite effective in suppressing leakage at the intersections in a device with a simple pattern. However, it could be very

difficult to use this for a device with a large manifold of capillaries as complex as that in figure 1.5, because it will be complicated to apply voltages to all reservoirs and to perform dynamic voltage control. Flow direction and flow rate in each channel section may influence each other. Experimental demonstration of this technique in such a complex μ -TAS device is desired, and the delicacy required of the voltage control needs to be sorted out.

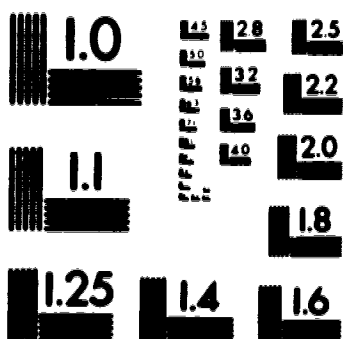
(2) Detection

All μ -TAS devices discussed in this thesis used fluorescence detection, because it is relatively simple to use and widely applied in conventional CE. Many other detection methods used in CE, *e. g.* electrochemistry and UV-visible absorbance, might be integrated in μ -TAS devices as well. In fact, an electrical chemical detector was fabricated in the CETAS device (10, 11), but its performance has not been pursued extensively. One interesting project being undertaken in Harrison's group is to integrate a waveguide within a μ -TAS device, so that the detector will be inside the μ -TAS device.

In terms of using electrochemical detection in μ -TAS devices, it is first necessary to decide where to locate the detector, inside or outside separation system. Ewing *et al.* decoupled the CE voltage from the electrochemical detection voltage, so that there is no electrical interference with each other (13). The detections were made just beyond the end of the separation capillary, but such a scheme introduced loss of separation efficiency. If an electrochemical detector is placed inside the separation system, the potential drop over the electrodes due to the CE separation voltage could interfere with the electrochemical detection. However, micromachining technology provides a means to place two electrodes so close that a potential drop between two electrodes might be negligible. In fact, Pt electrode pairs separated by 20 μm have been made in the CETAS device (10) and other devices (8). Unfortunately their performance has not been reported to date. These questions need to be addressed experimentally.

3 of/de 3

PM-1 3 1/2" x 4" PHOTOGRAPHIC MICROCOPY TARGET
NBS 1010a ANSI/ISO #2 EQUIVALENT



PRECISIONSM RESOLUTION TARGETS

(3) Application

It has been shown that μ -TAS devices may be very promising for a variety of applications. However, quantitative chemical analysis of a real, relatively complex sample with a μ -TAS device has not been demonstrated. Such an example will be discussed below.

Capillary electrophoresis has been extended for inorganic ion analysis and a review of this subject has appeared recently (14). For example, Swaile and Sepaniak added a chelation agent into the mobile phase to detect Ca^{2+} and Mg^{2+} in blood serum (15). Fluorescence detection was employed, because the ligand, 8-hydroxyquinoline-5-sulphonic acid (HQS), does not fluoresce except when it complexes a metal. This example might be explored in a μ -TAS device as a post-capillary derivatization scheme, since the complexation reaction is fast. This example can also be extended to water analysis, because the concentrations of metal ions are one indicator of water quality, such as hardness.

6.3 References

1. Harrison, D. J.; Turner, R. F. B.; Baltes, H. P., *Anal. Chem.*, **1988**, *60*, 2002-2007.
2. Turner, R. F. B.; Harrison, D. J.; Rajotte, R. V.; Baltes, H. P., *Sensors and Actuators*, **1990**, *B1*, 561-564.
3. Turner, R. F. B.; Harrison, D. J.; Rajotte, R. V., *Biomaterials*, **1991**, *12*, 361-368.
4. Moussy F.; Harrison, D. J.; O'Brien, D. W.; Rajotte, R. V., *Anal. Chem.*, **1993**, *65*, 2070-2077.
5. Eisenberg, A.; Yeager, H. L., Ed., *Perfluorinated Ionomer membranes*, ACS symposium series 180, American Chemical Society: Washington, D. C. **1982**.
6. Reach, G.; Wilson, G. S., *Anal. Chem.*, **1992**, *64*, 381A-386A.
7. Pickup, J., *TIBTECH*, **1993**, *11*, 285-291.
8. Manz, A.; Feltinger, J. C.; Verpoorte, E.; Lüdi, H.; Widmer, H. M.; Harrison, D. J., *Trends Anal. Chem.* **1991**, *10*, 144-149.

9. Manz, A.; Harrison, D. J.; Verpoorte, E.; Fettingner, J. C.; Lüdi, H.; Widmer, H. M., *J. Chromatogr.*, **1992**, *593*, 253-258.
10. Harrison, D. J.; Manz, A.; Fan, Z.; Lüdi, H.; Widmer, H. M., *Anal. Chem.*, **1992**, *64*, 1926-1932.
11. Seiler, K.; Harrison, D. J.; Manz, A., *Anal. Chem.*, **1993**, *65*, 1481-1488.
12. Harrison, D. J.; Fluri, K.; Seiler, K.; Fan, Z.; Effenhauser, C. S.; Manz, A., *Science*, **1993**, *261*, 895-897.
13. Wallingford, F. A.; Ewing, A. G., *Anal. Chem.*, **1987**, *59*, 1762-1766.
14. Romano, J. P., *Am. Lab.*, **1993**, *25(8)*, 48-51.
15. Swaile, D. F.; Sepaniak, M. J., *Anal. Chem.*, **1991**, *63*, 179-184.

Appendix 1

This appendix consists of computer programs used for the work described in this thesis. The software used was Laboratory Virtual Instrument Engineering Workbench (LabVIEW), version 2.2, from National Instrument Corporation (Austin, TX). As claimed in LabVIEW user manuals, LabVIEW is designed to simplify scientific computation, process control, and test and measurement application, as well as for a wide variety of programming applications. Macintosh LC, IICI, and IISI computers were used for programming.

There are 3 programs or virtual instruments (VI) in this appendix. All programs were written by the author on the basis of the initial work by Dr. Kurt Seiler. Each program starts with the front panel that used to control instruments and demonstrate data, and ends up with the block diagram which details all wiring and the sequence of the program execution. In addition to a brief description at the beginning of each program, a few comments are also written in the program, so that it is easier for one to recognize the functions of the routines.

VI 1

A Virtual Instrument for Controlling a Relay Switch System

This LabVIEW program was used as a sub-VI in other programs to control a relay switch system. The relay system consists of a digitally controlled relay unit (Control 488/16, IoTech, Cleveland, OH), a 24 V power supply, and high voltage (HV) relay switches. This VI sent out commands through an interface board (NB-MIO-16L, National Instrument Corporation) to control IoTech relays. Each activated IoTech relay then connected its corresponding HV relay to the 24 V power supply, and the HV relay switch was then activated.

This VI has a connector pane preceding the front panel. The connector panel shows the way to connect the inputs and outputs of this VI when it was used as a sub-VI.

Four relay switches can be controlled by this VI at the same time, as shown in the front panel. The board number in the panel refers to the interface board slot number in the computer. Time taken for switching relays is also indicated. The error indicators in the front panel were used for diagnosing problems when the program did not function properly.

The mechanism of controlling the IoTech relay unit is indicated in the first page of the block diagram. Each I/O channel connected to a relay switch was assigned with a number corresponding to a bit. Two I/O Port VI's are used for the operation, as one port commands only 4 bits. The least significant bit of port 0 was reserved for the strobe line used to activate commands.

Frame 2 in the block diagram was used to start communication with the IoTech unit. The address or the slave setting of the IoTech was physically set at 2, which was added to 64 and sent out. Adding 64 was required by the IoTech unit for displaying communication errors. The assignment of port lines, and the logic is shown below.

	Port 1 (higher bits)				Port 0 (lower bits)			
line	4	3	2	1	4	3	2	1
logic	1	0	0	0	0	1	0	1
decimal	64	0	0	0	0	2	0	/

The decimal sum was 66 and the corresponding binary number was 1000010. The last bit in port 0 was not counted, as it was used as the strobe line.

This VI controls the relay switches in a similar way. For example, when switches connected to I/O channels 1 and 4 need to be turned on, the following logic would be executed.

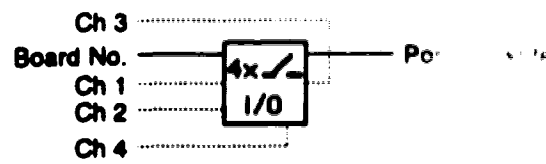
	Port 1 (higher bits)				Port 0 (lower bits)			
line	4	3	2	1	4	3	2	1
logic	0	1	1	1	0	0	1	1
decimal	0	32	16	8	0	0	1	/

This execution was performed by frame 4. The logic of the individual bits is shown in the outside of the frames, and was printed with frame 0. Channels 1 and 4 were turned on with decimal 1 and 8, respectively. The decimal numbers had to be converted to ASCII numbers by adding 48 (i.e. $32 + 16$). Then the decimal sum above became 57, corresponding to a binary number 111001. The last bit of port 0 was again used as the strobe line.

It has to be pointed out that the combination of channel assignments can not be larger than 9. For example, channels 1, 2, 3 can be closed at the same time, because the combination of their assignment is 7 (i.e. $1 + 2 + 4$). However, channels 3 and 4 can not be closed at the same time, because their combination of assignment would be 12 (i.e. $4 + 8$). Two digits of such a number needs to activate the strobe line twice to send out commands, so

that twice the time was required to execute the program. In fact a program written by Dr. K. Seiler can operate 8 switches at the same time, but it required about 3 times more time to execute than this program. The time used for program execution needs to be as small as possible, so that the loss of separation efficiency due to diffusion can be maintained at a minimum level.

Connector Pane

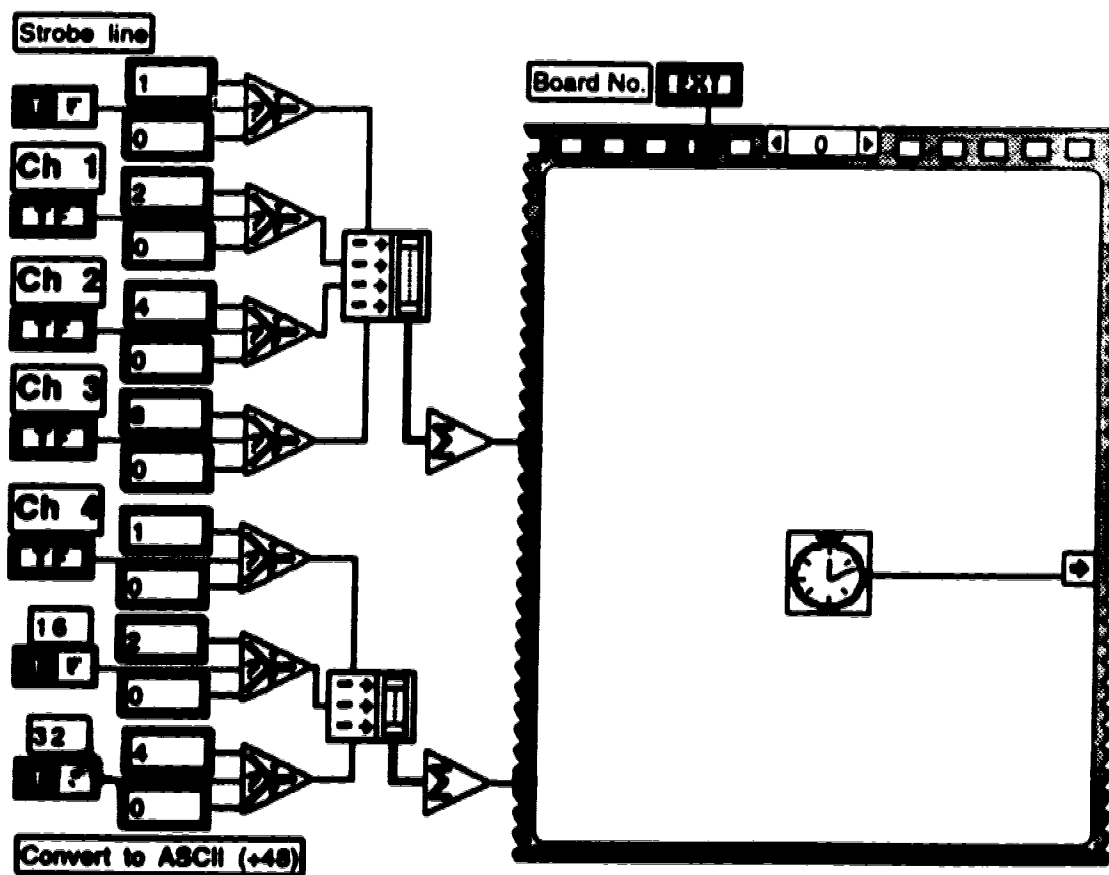


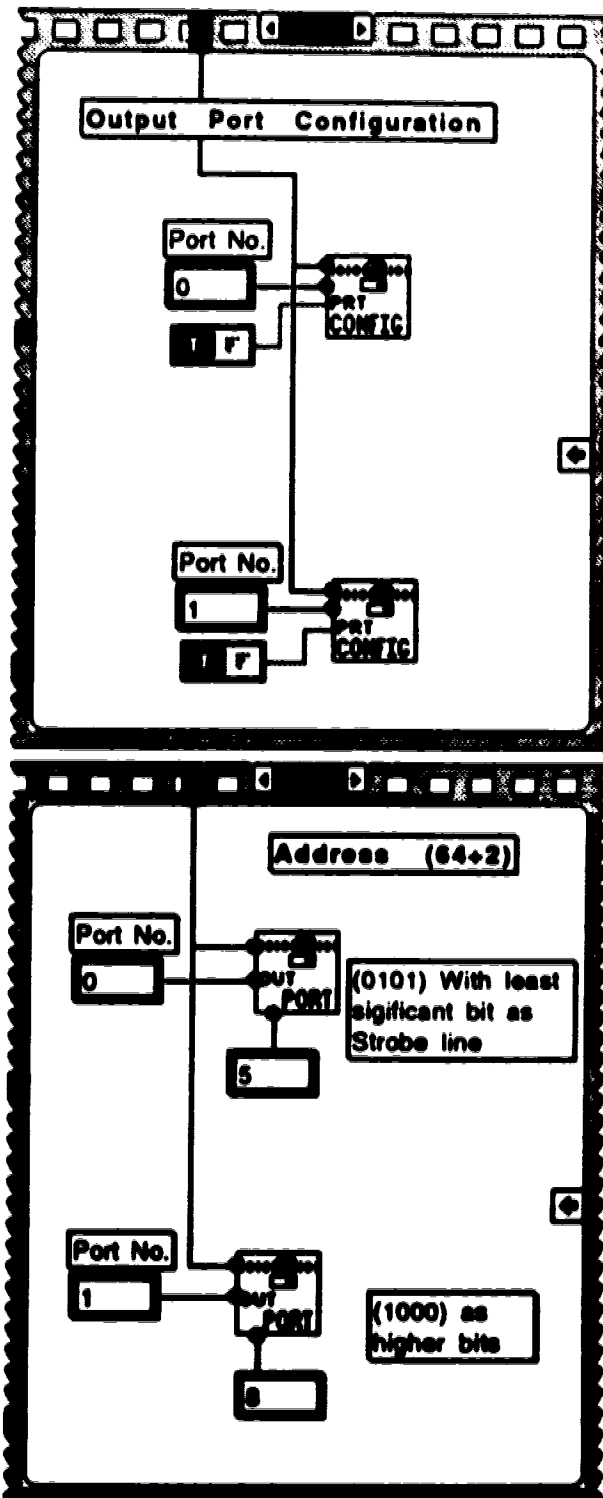
I/O-control

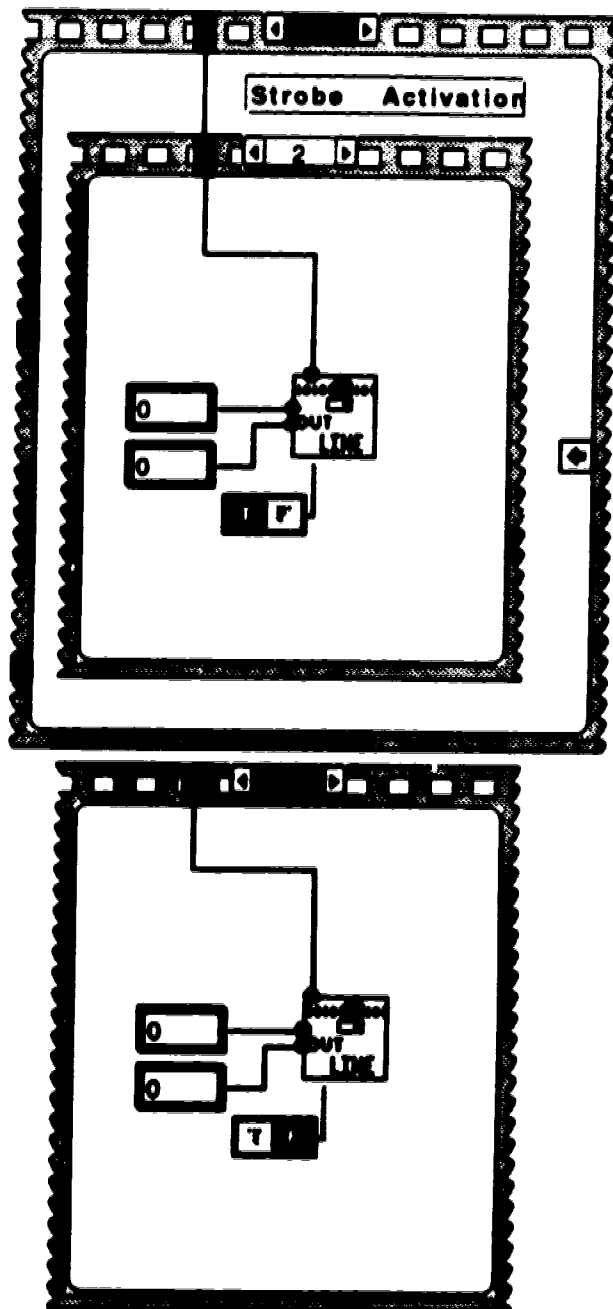
Front Panel

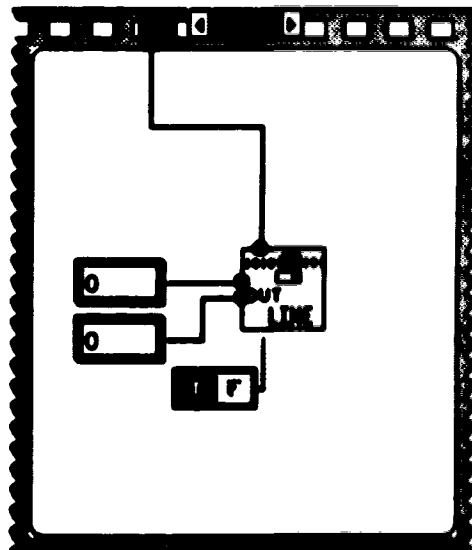
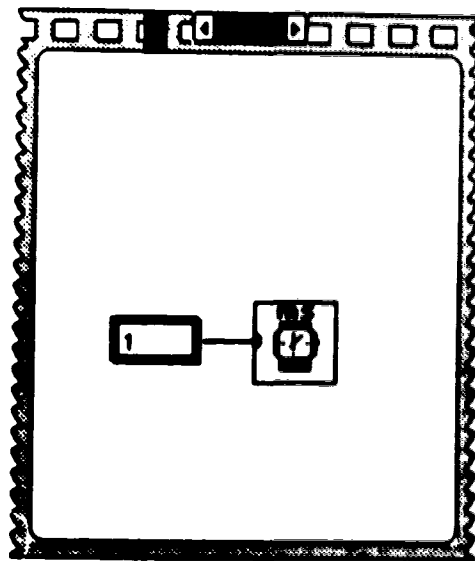
Ch 1	Ch 2	Ch 3	Ch 4
<input type="checkbox"/> on <input type="checkbox"/> off	<input type="checkbox"/> on <input type="checkbox"/> off	<input type="checkbox"/> on <input type="checkbox"/> off	<input type="checkbox"/> on <input type="checkbox"/> off
Board No. <input type="text" value="6.00"/>		time elapsed(ms) <input type="text" value="0.00"/>	
<input type="checkbox"/>	Port 0 write <input type="text" value="0.00"/>	Port 1 write <input type="text" value="0.00"/>	

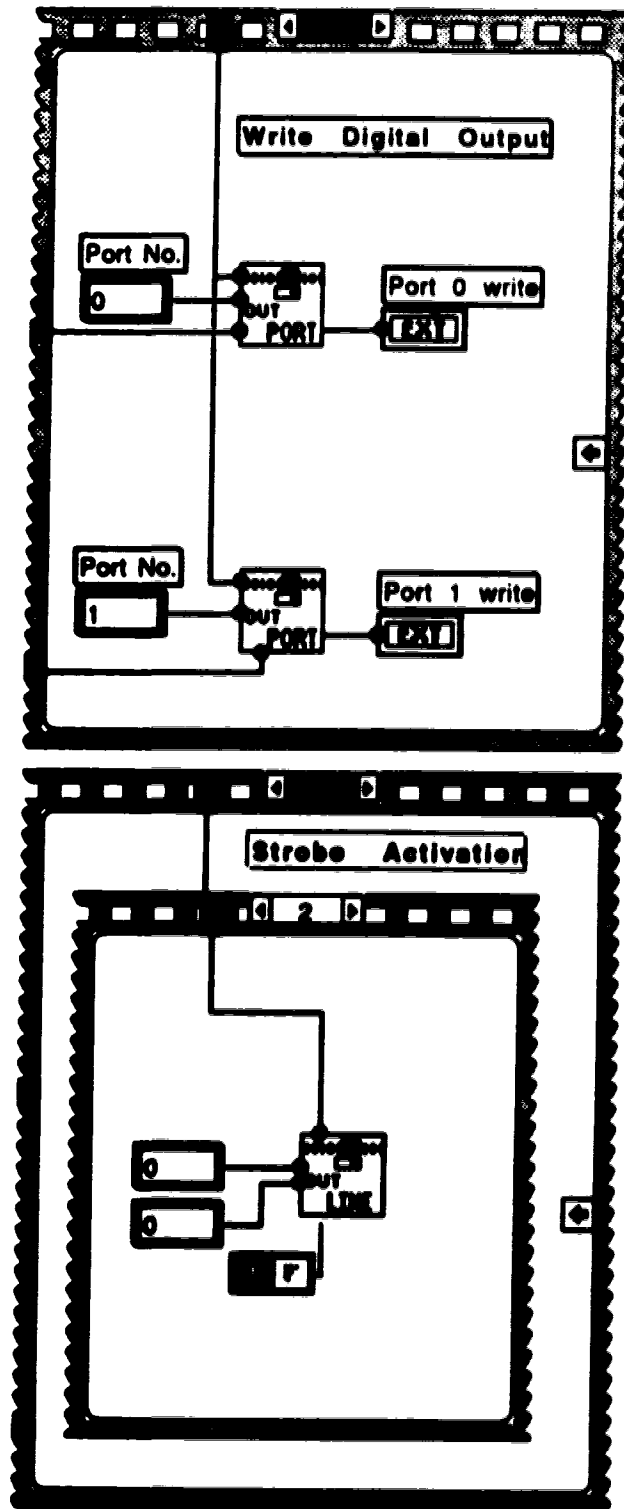
Block Diagram

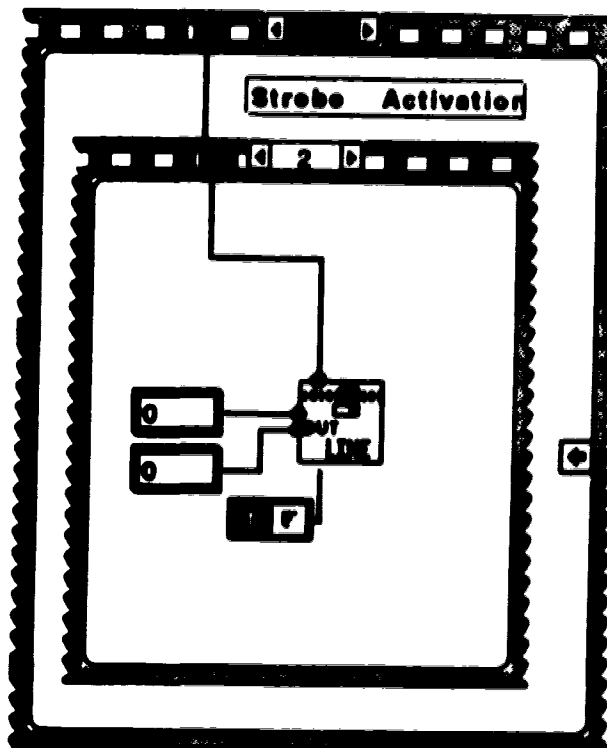
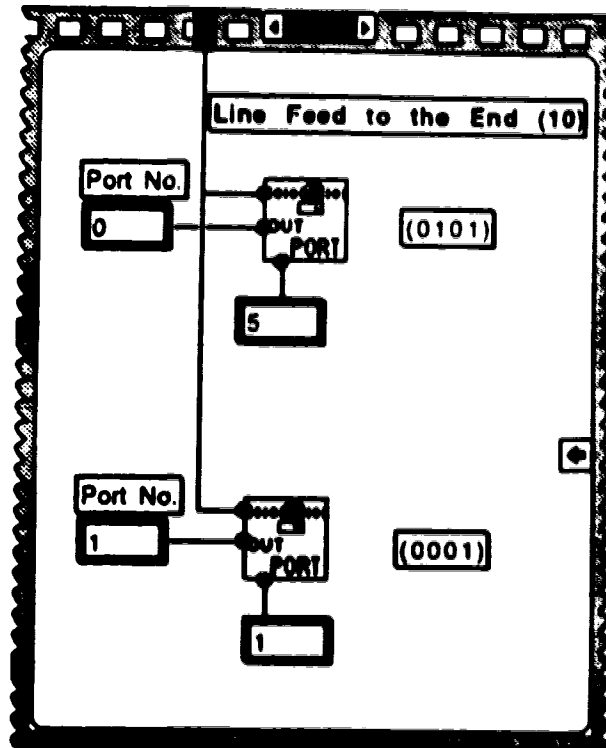


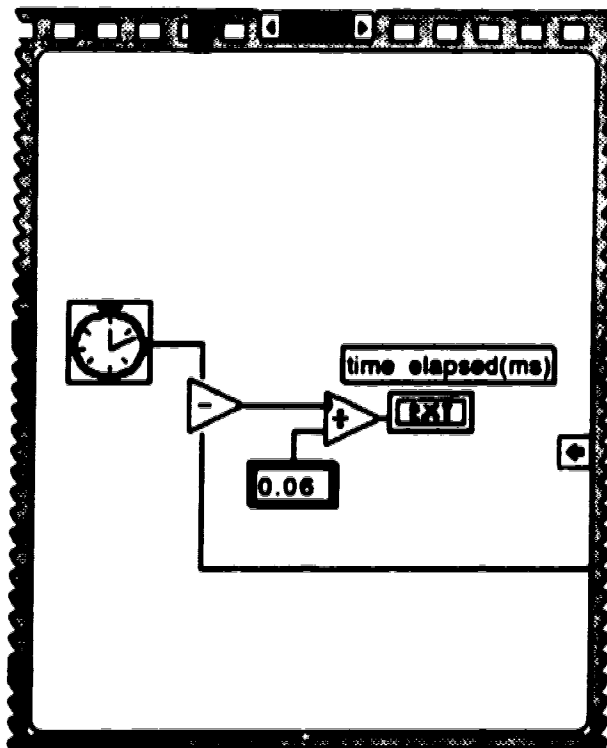












VI 2

A Virtual Instrument for the Jet-3 Device

This LabVIEW program was used for the experiments performed in Jet-3 devices, which includes a mixing chamber discussed in chapter 5. This program, after some modifications, was also used for running experiments in Airport devices of chapter 3 and in Jet-1 devices of chapter 4. Experiments of leakage suppression using active voltage control, as discussed in chapter 4, were also performed by this virtual instrument.

As shown in the front panel, two injection voltages furnished by two high voltage (HV) power supplies were used to drive two samples through the mixing chamber. One of the two HV power supplies was also used for the separation, by switching its output to another reservoir with a relay. The voltage used is identified as "Separation V". Both "Inj. AO Channel" and "Sep. AO Channel" in the front panel refer to the analog output channel number of the computer interface board commanding injection and separation voltages. "Checkstop" was a boolean control button used for stopping execution of the program after a full electropherogram appeared in the chart. "Gain" was set to obtain an appropriate magnitude of the signal. The choices of the gain are 1, 2, 4, 8 for the NB-MIO-16H interface board, and 1, 10, 100, 500 for the NB-MIO-16L board. "Sample interval" indicated data sampling frequency. The error indicators were used for diagnosing problems when the program did not function properly. The acquired electropherogram was stored in a newly created file called by "filename".

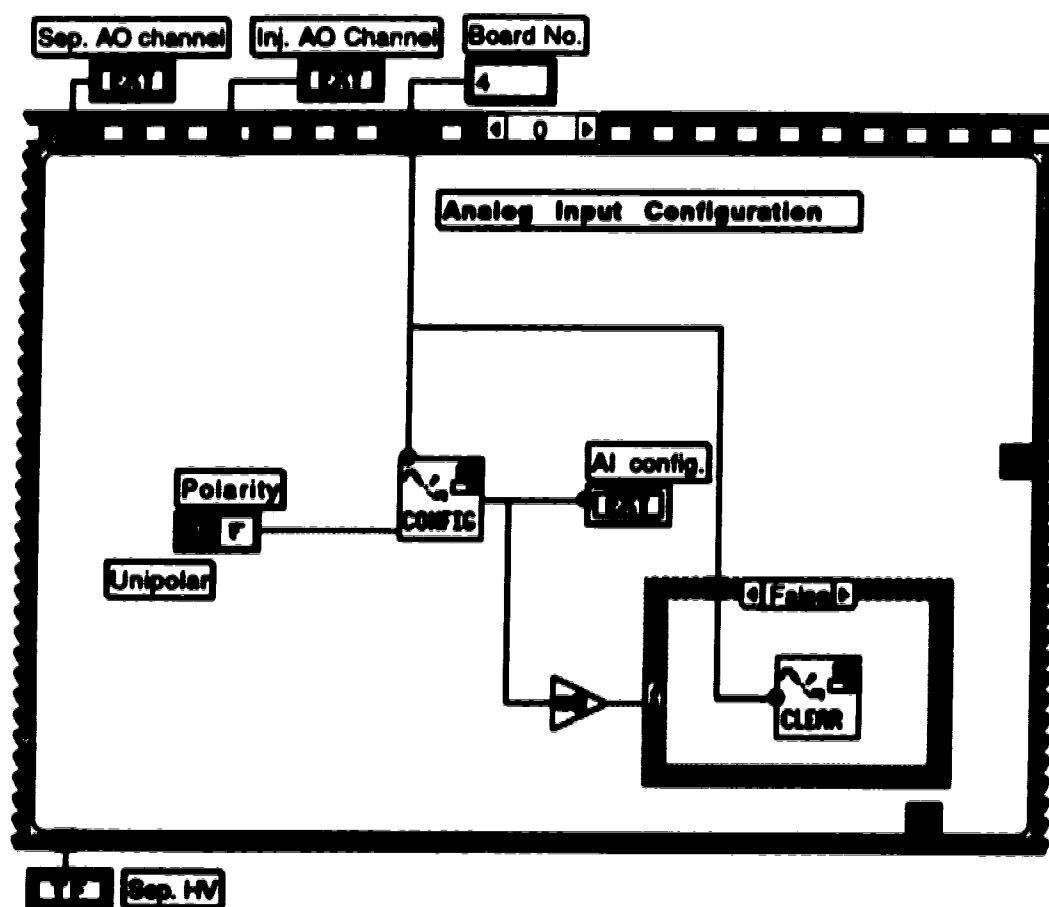
There are two periods of waiting time used in the block diagram. The waiting time used for switching relay is set to 10 ms , as it was determined that the relay switches took about 5-7 ms to reach a stable connection. The waiting time used for a desired voltage is set to 100 ms, as

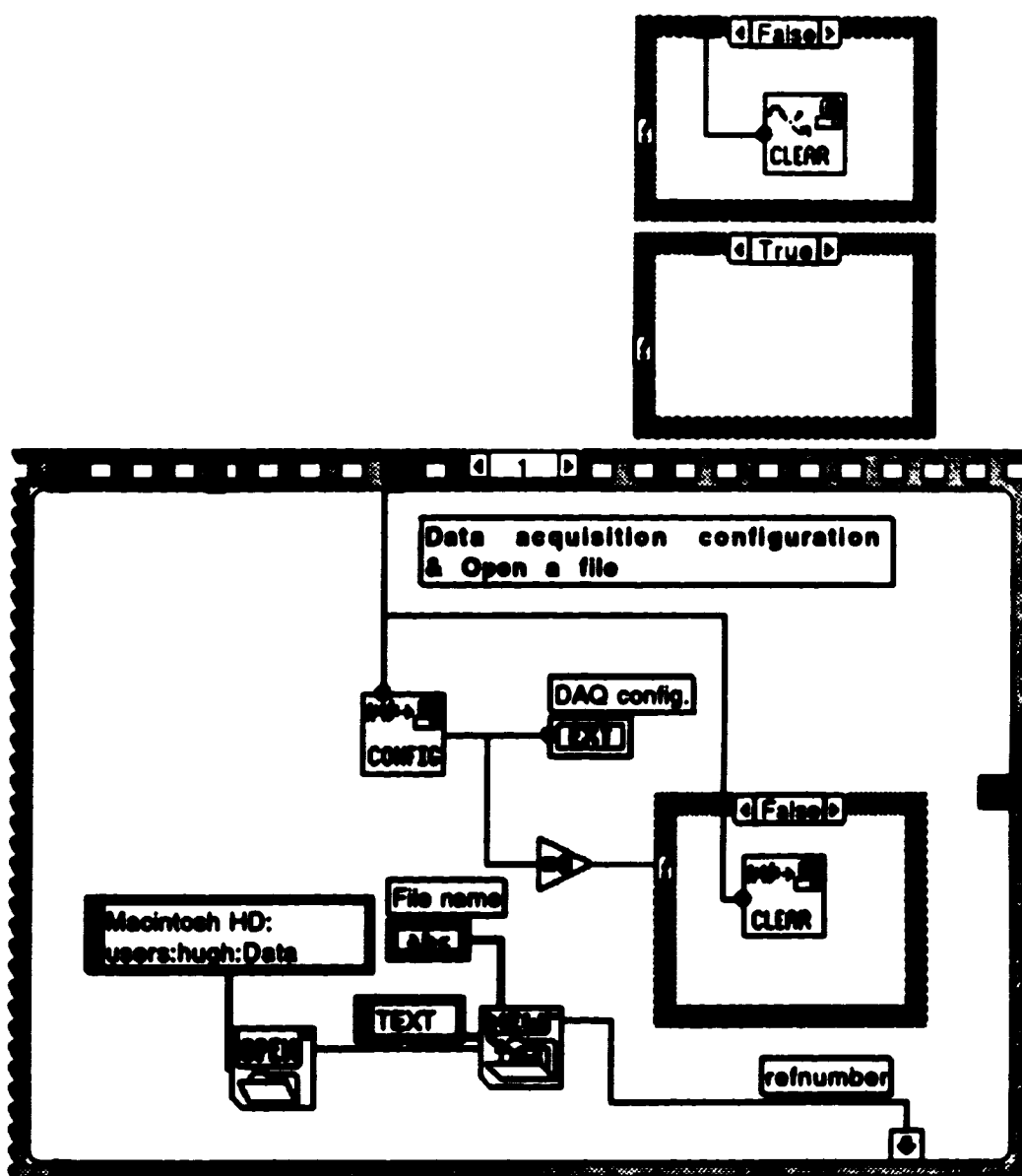
it was determined that the power supplies took about 100 ms to reach 90% of the assigned value.

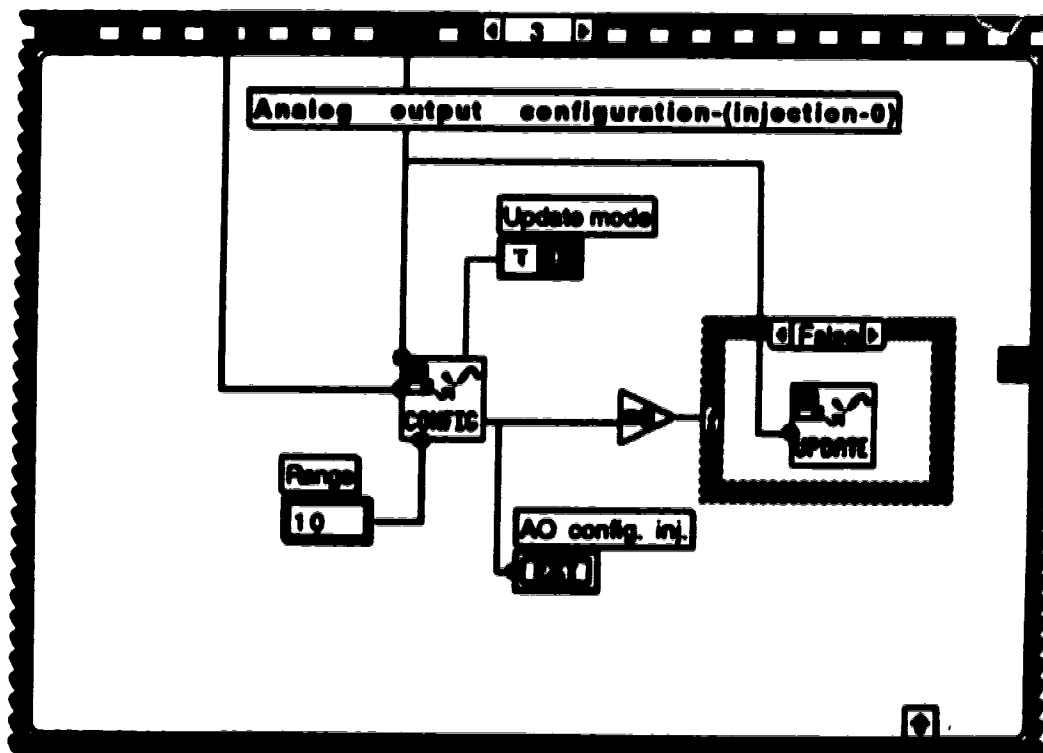
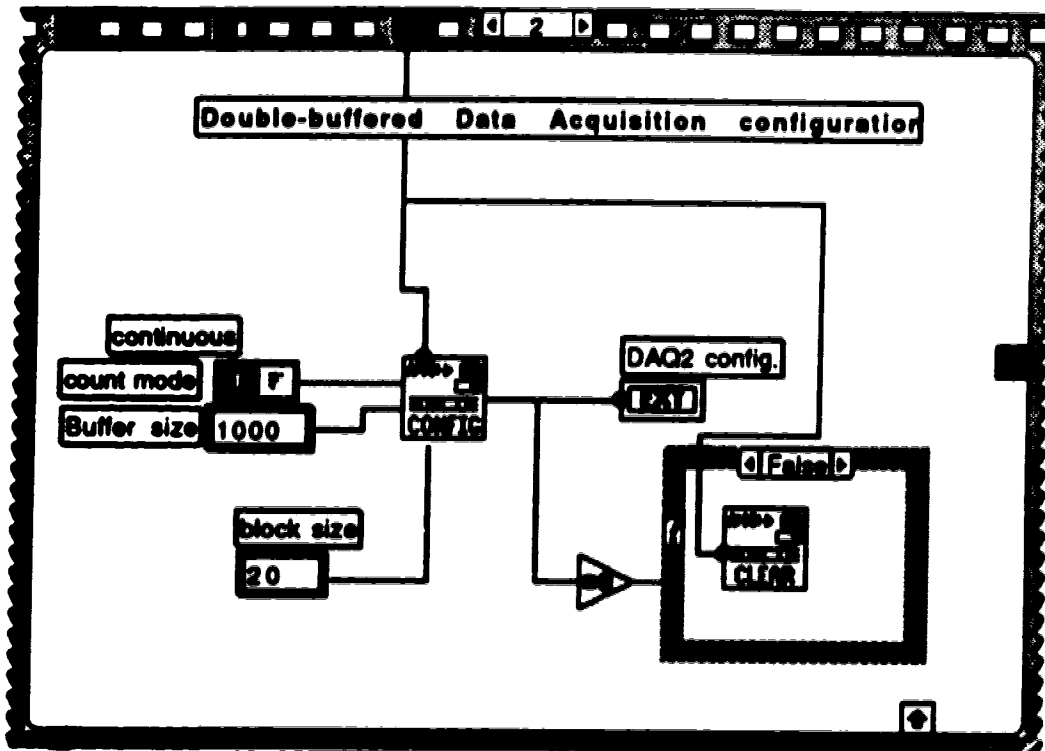
Front Panel

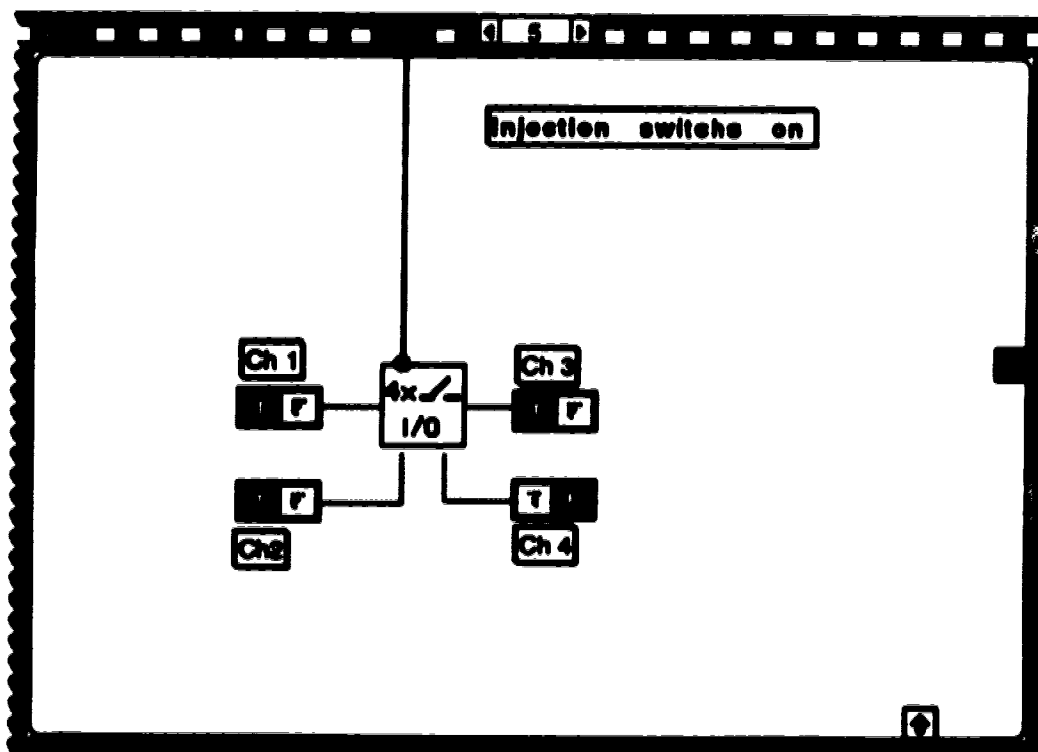
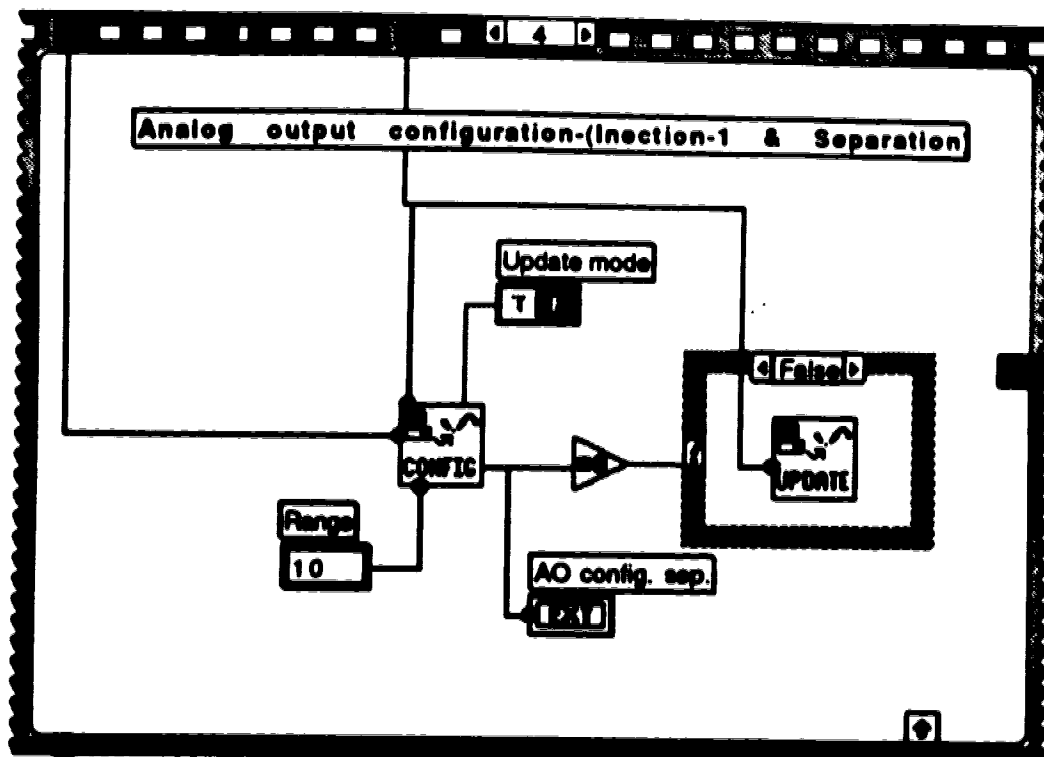
Inj. HV		Inj. AO Channel		Injection Voltage-0		Injection Time	
<input type="checkbox"/>		<input type="text" value="0.00"/>		<input type="text" value="100.00"/>		<input type="text" value="1.00"/>	
				Injection Voltage-1			
				<input type="text" value="100.00"/>			
Sep. HV		Sep. AO channel		Separation V		Check stop	
<input type="checkbox"/>		<input type="text" value="1.00"/>		<input type="text" value="500.00"/>		<input type="checkbox"/>	
Gain		Sample interval		File name			
<input type="text" value="1.00"/>		<input type="text" value="50.00"/>		<input type="text" value="dat1"/>			
						<input type="text" value="0.00"/> s	
						AI config.	
						<input type="text" value="0.00"/>	
						DAQ config.	
						<input type="text" value="0.00"/>	
						DAQ2 config.	
						<input type="text" value="0.00"/>	
						AO config. inj.	
						<input type="text" value="0.00"/>	
						AO write inj.	
						<input type="text" value="0.00"/>	
				AO config. sep.			
				<input type="text" value="0.00"/>			
				AO write sep.			
				<input type="text" value="0.00"/>			
				DAQ2start			
				<input type="text" value="0.00"/>			
				DAQ2get			
				<input type="text" value="0.00"/>			
				Write File			
				<input type="text" value="0.00"/>			

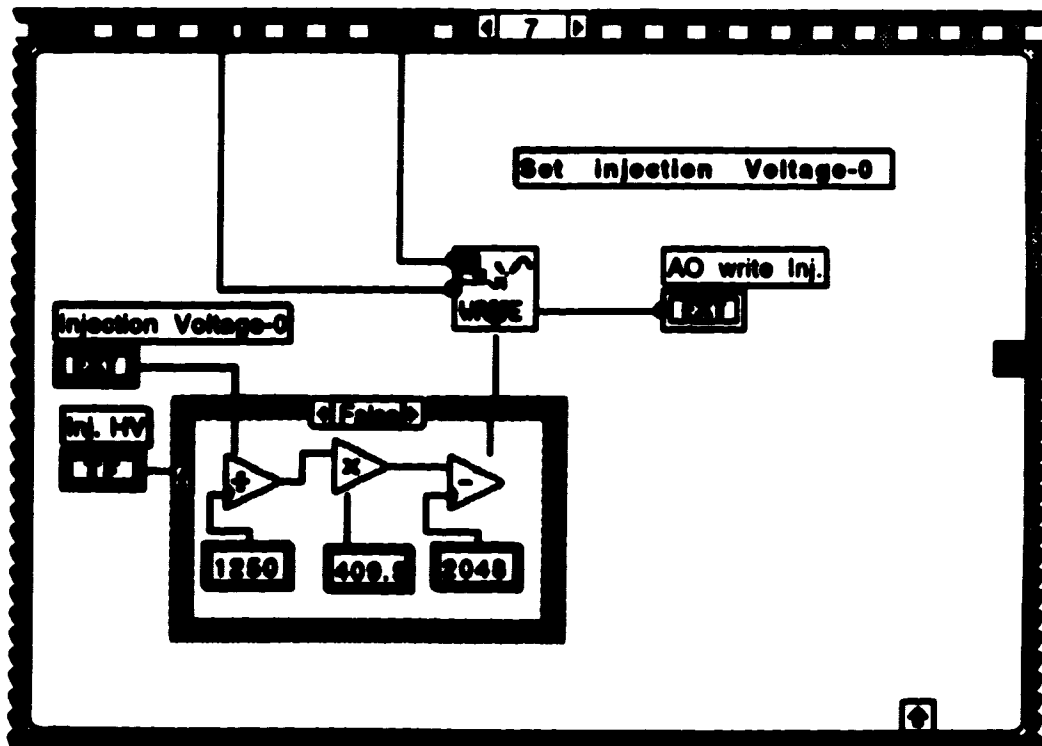
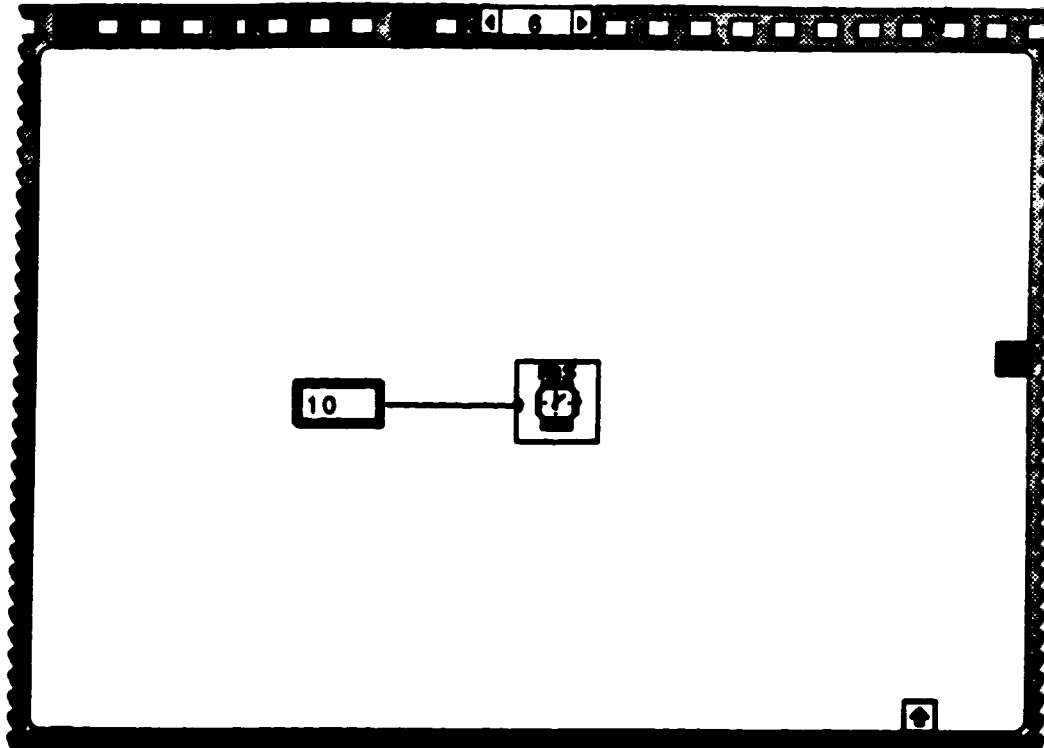
Block Diagram

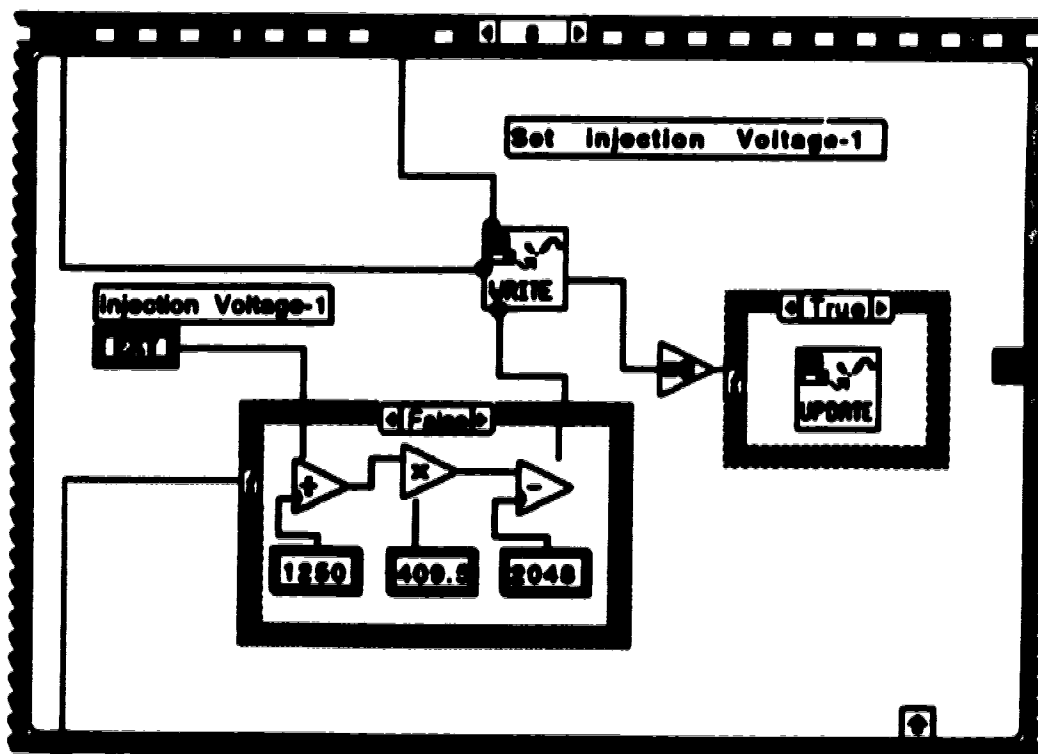
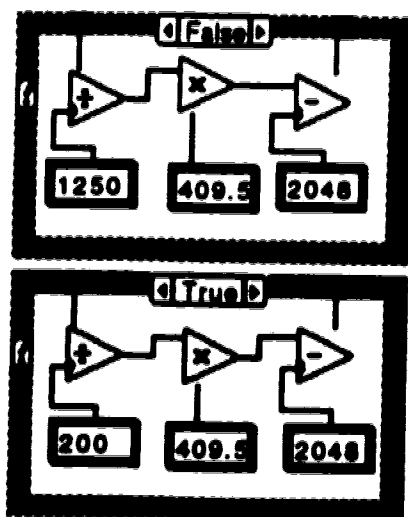


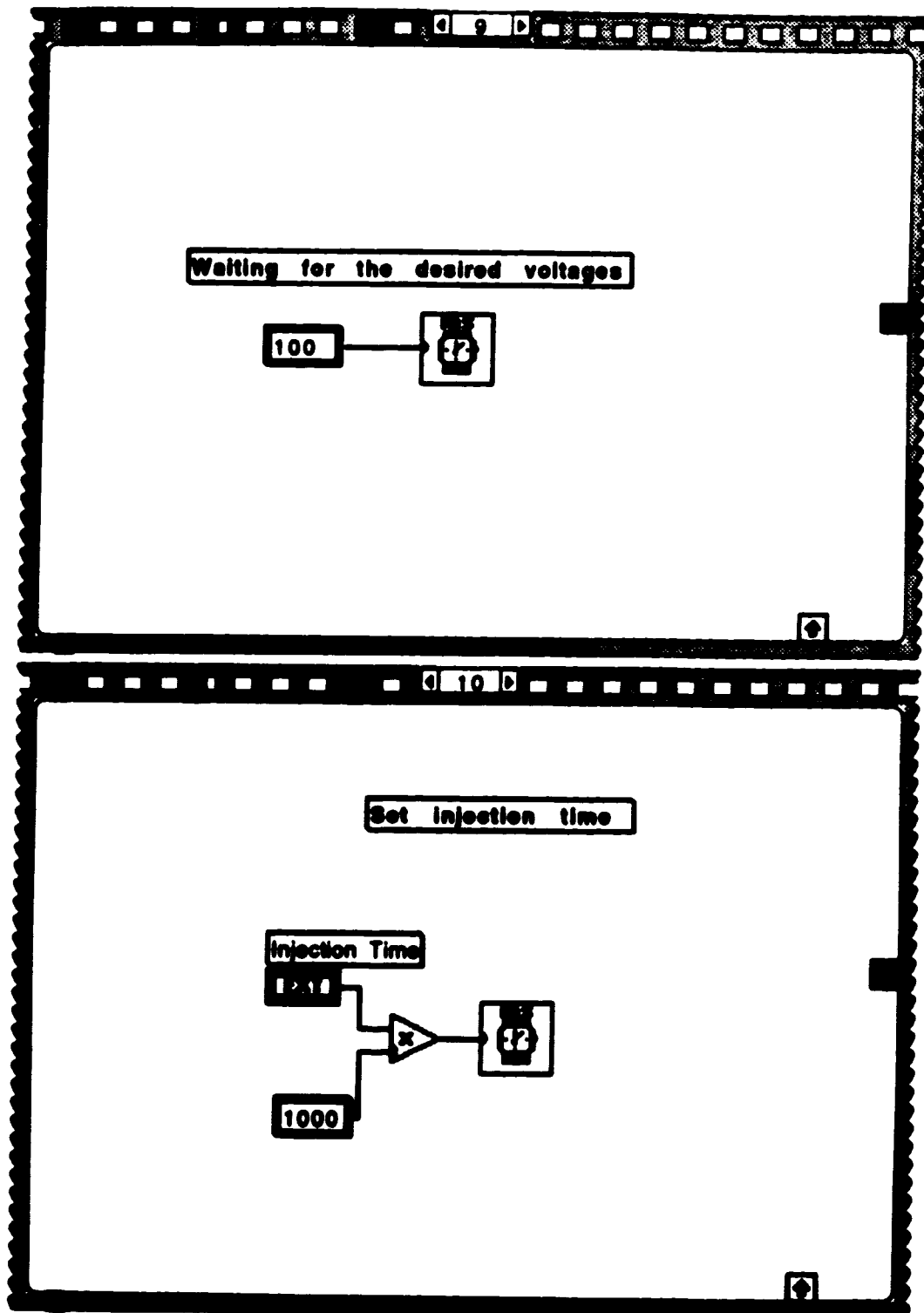


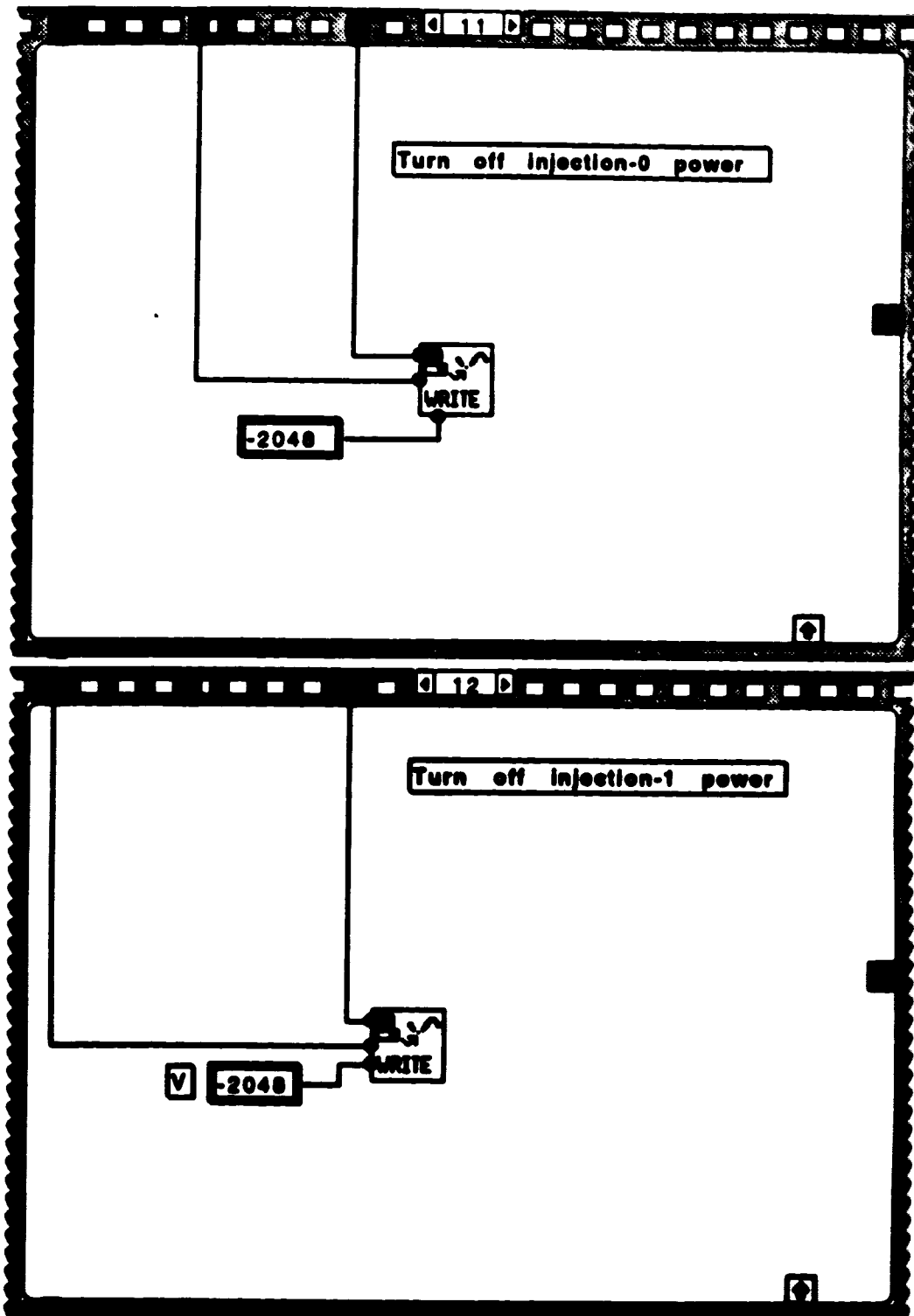


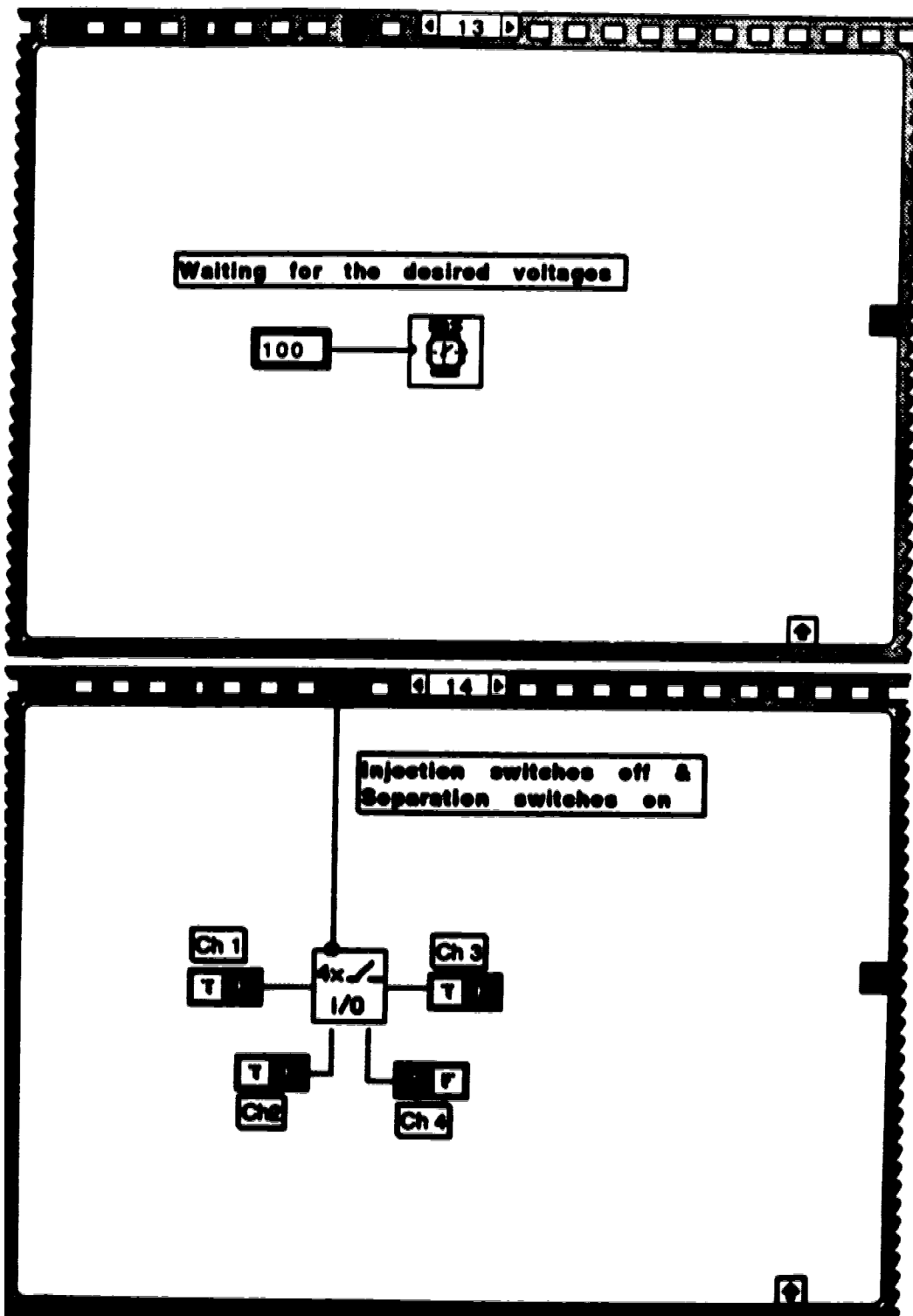


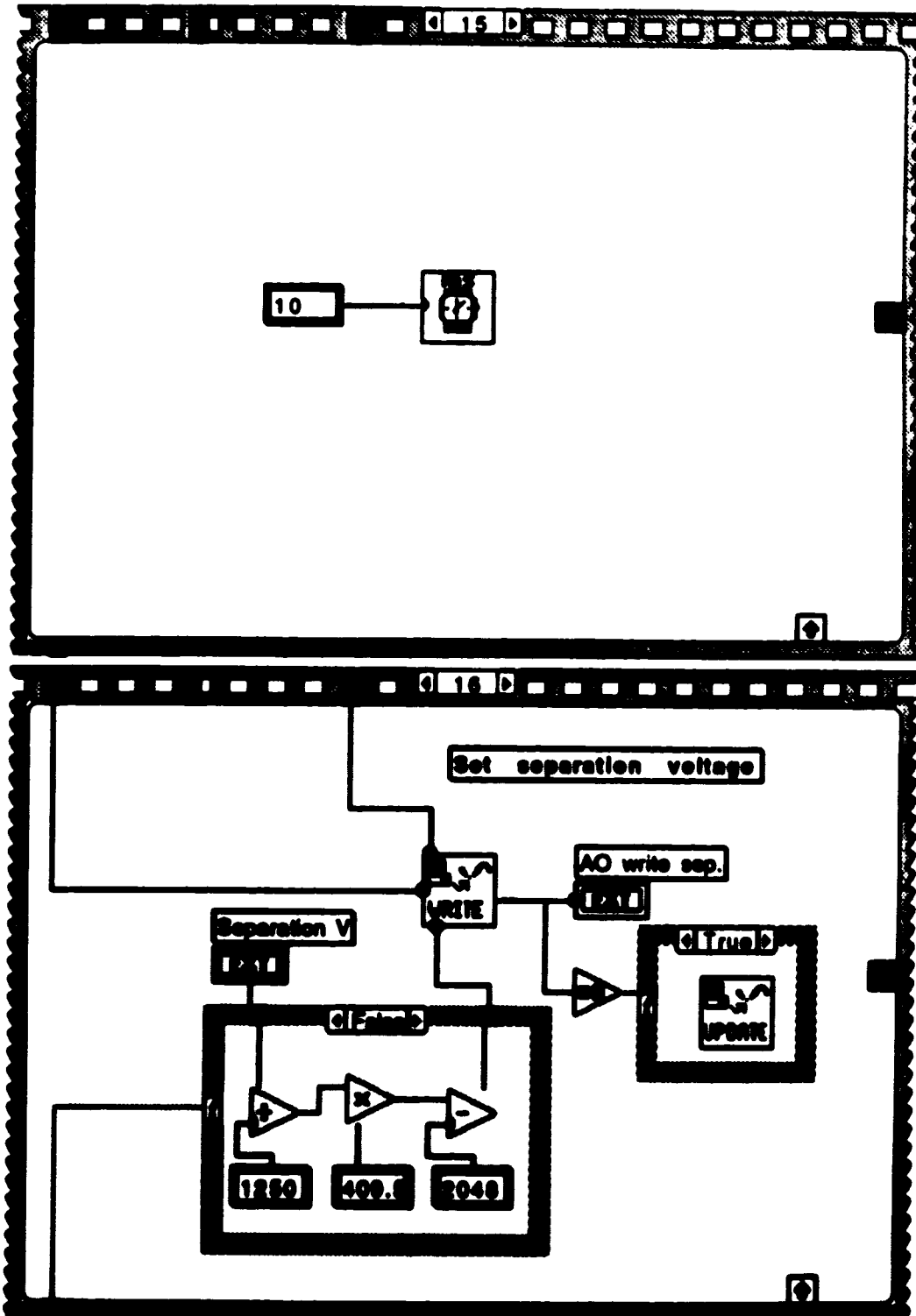


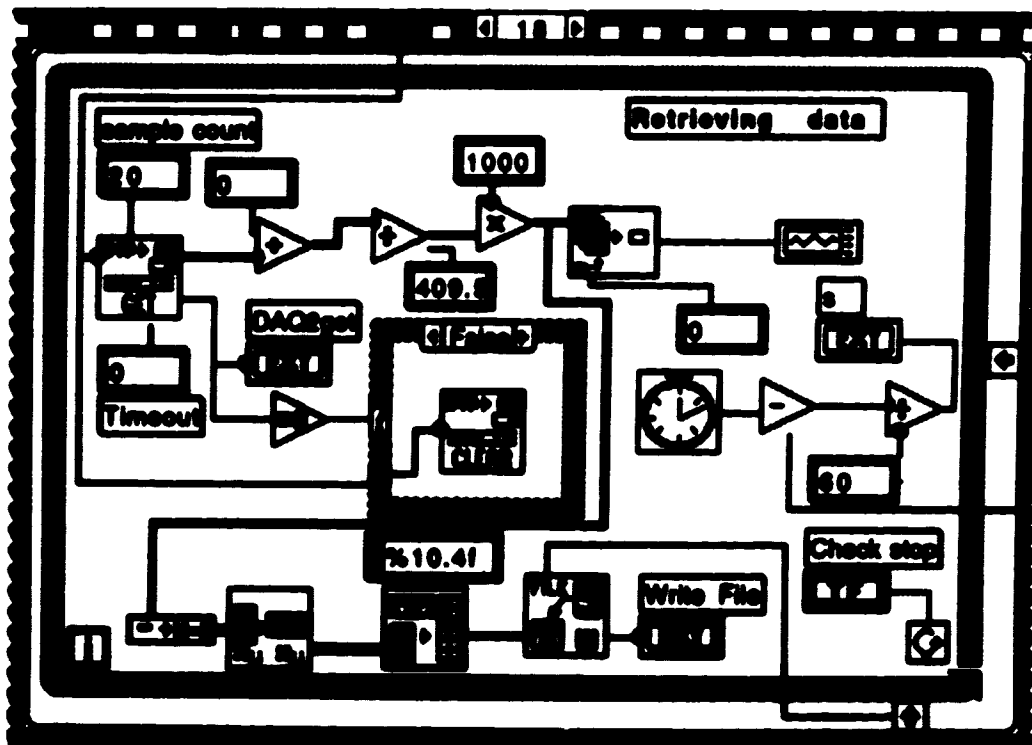
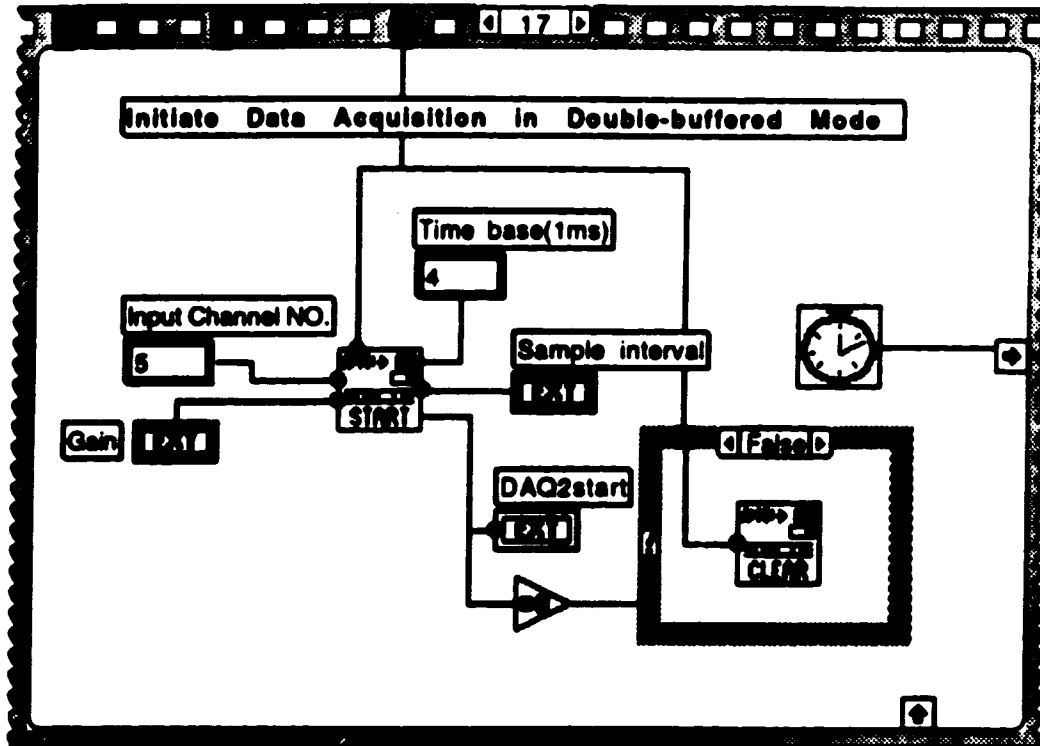


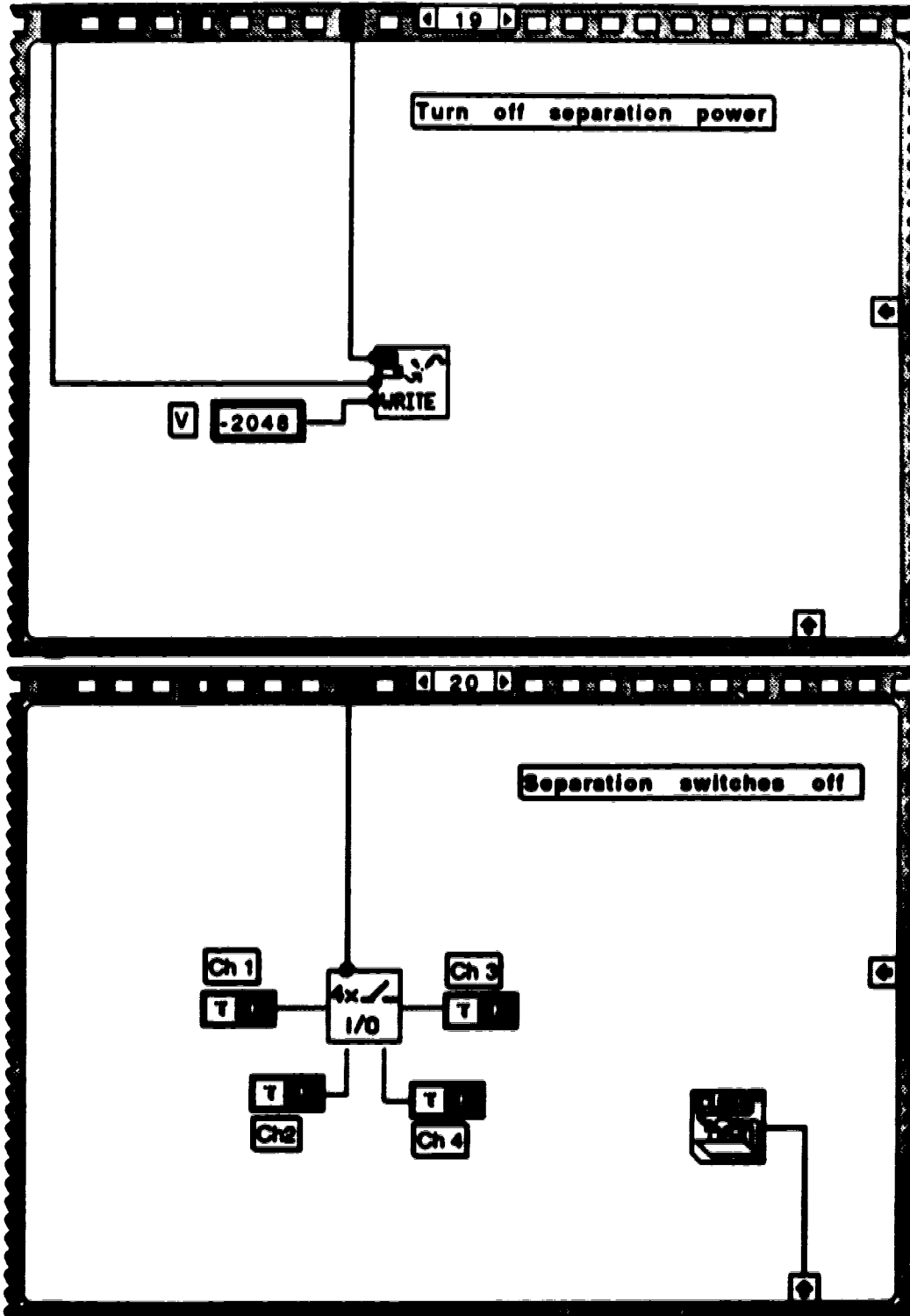










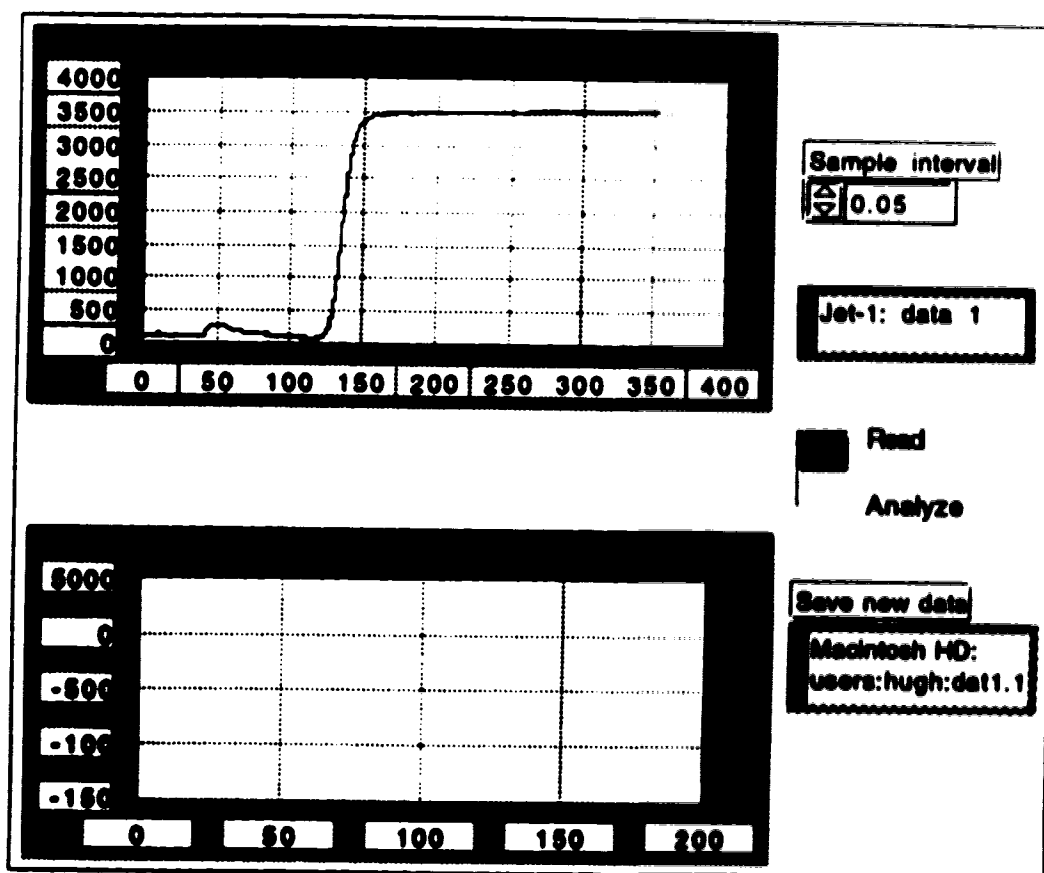


VI 3

A Virtual Instrument for Differentiating Frontal Electropherograms

This LabVIEW program was used for studying the dispersion of a sample plug passing through the mixing chamber of a Jet-3 device, as discussed in chapter 5. Frontal electropherograms of a sample through the chamber were obtained using the frontal analysis technique. Differentiation of such a frontal electropherogram gave a migration electropherogram, which can be analyzed to obtain statistical moments indicating the degree of the bandbroadening.

This program involves two processes, "Read" and "Analyze", as shown in the frontal panel. The VI first reads a frontal electropherogram from a file, for example, "data 1" in disk "Jet-1" indicated in the panel. An example of such an electropherogram is shown in the top chart. "Sample interval" refers to the data sampling frequency as in VI 2. This value is used to convert the points in the x axis of the chart into the right time scale. The frontal electropherogram is then analyzed by this VI, and a migration electropherogram appears in the bottom chart and is stored in a new file. The resulting migration electropherogram can be analyzed using another program to obtain statistical moments. That program was prepared by Dr. K. Seiler and is not reproduced here.

Front Panel

Appendix 2

This appendix consists of Jet-1 and Jet-3 configurations, which are proportional to the real layout in the master masks. The scale of the proportion of each layout is shown in the figure. The mixing chamber in Jet-3 devices is also shown. These layout patterns were designed by a software "LEDIT".

Figure A1 shows the layout of Jet-1. Each end of the channels were numbered for references in the following discussion. The widths reported below are the feature widths in the master mask. The channel connected to 1 is 5 μm wide and 18 mm long, while the channel connected to 2 is 30 μm wide and 4 mm long. The width of the bulky channels connected to 3 and 4 is 280 μm , whereas the width of the narrow channel between them is 10 μm . The bulky channel at 3 is 8 mm long, and that at 4 is 33 mm long. The channel between these is 27 mm long. The distance between the intersection connected to 2 and the end of the bulky channel connected to 3 is 2 mm. The offset between the two side channels connected to 1 and 2 is 130 μm from the outside edge to the outside edge. The size of the whole device is 2.2 cm x 4.7 cm.

Figure A2 shows the layout of Jet-3. All narrow channels are 10 μm wide, whereas the bulky channels are 280 μm wide. The bulky channel at 2 is 8 mm long, and that at 5 is 33 mm long. The distance between the end of the bulk channel at 2 and the head of the mixing chamber is 2.5 mm, while that between the end of the bulk channel at 5 and the end of the mixing chamber is 20 mm. The length of the channel between the intersection connected to 4 and the end of the mixing chamber is 3 mm. The offset between the side channels connected to 3 and 4 is 200 μm from the outside edge to the outside edge. Both channels connected to 3 and 4 are 4 mm long, while the channel connected to 1 is 18.5 mm long. The size of the whole device is again 2.2 cm x 4.7 cm. The detail of the mixing chamber is also shown at the bottom of the figure. The chamber is

4.5 mm long and 150 μm wide. The single islands inside the chamber are 500 μm long and 70 μm wide, while each of the double islands is 500 μm long and 60 μm wide. Three channels around the double islands are 10 μm wide, while two channels around the single channel are 40 μm .

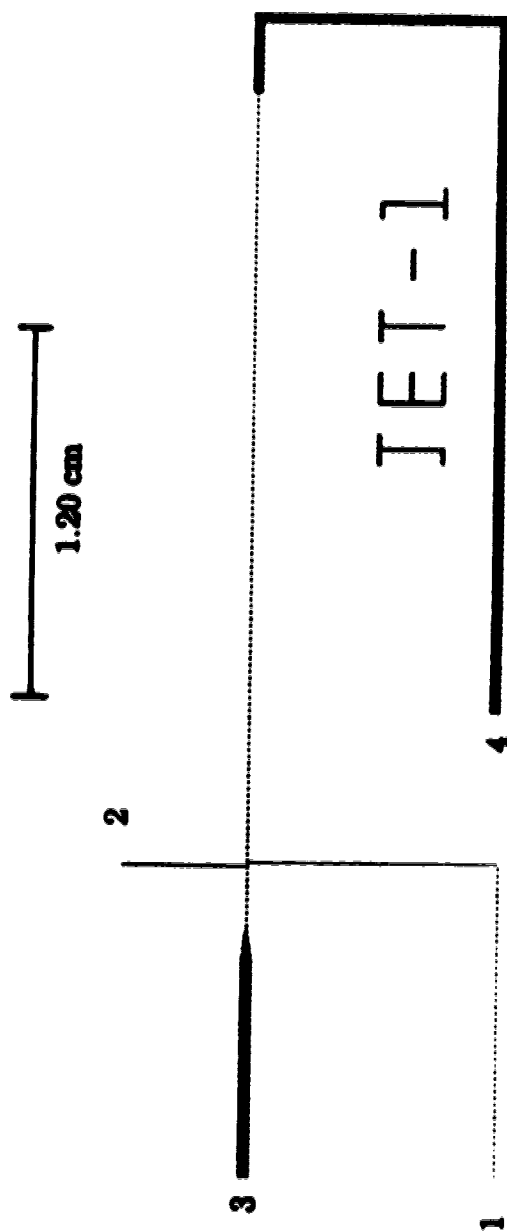


Figure A1 The layout of Jet-1 devices.

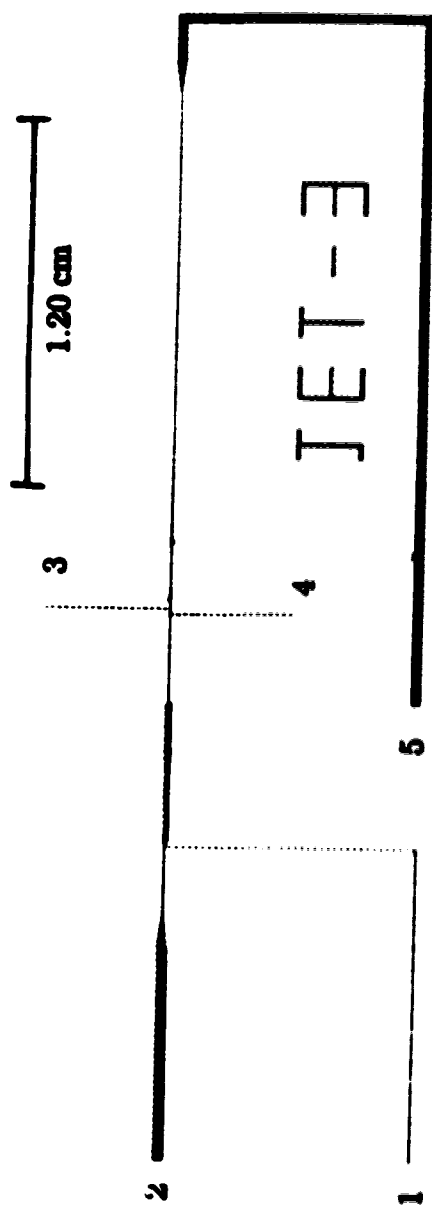


Figure A2 The layout of Jet-3 devices (top) and the mixing chamber in these devices (bottom).

END

2 7 - 0 8 - 9 6

FIN